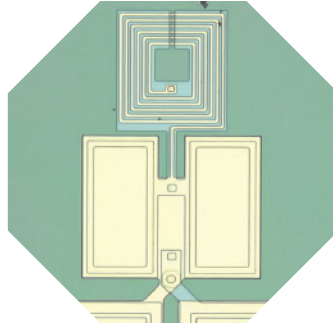


11010
01011
1010
0011



Microwave-coupled superconducting devices for sensing and quantum information processing

Visa Vesterinen



Microwave-coupled superconducting devices for sensing and quantum information processing

Visa Vesterinen

A doctoral dissertation completed for the degree of Doctor of Science (Technology) to be defended, with the permission of the Aalto University School of Science, at a public examination held at the lecture hall AS1 at the Aalto University School of Science (Espoo, Finland) on 18 June 2015 at noon.



ISBN 978-951-38-8311-9 (Soft back ed.)
ISBN 978-951-38-8312-6 (URL: <http://www.vtt.fi/publications/index.jsp>)

VTT Science 96

ISSN-L 2242-119X
ISSN 2242-119X (Print)
ISSN 2242-1203 (Online)

Copyright © VTT 2015

JULKAISIJA – UTGIVARE – PUBLISHER

Teknologian tutkimuskeskus VTT Oy
PL 1000 (Tekniikantie 4 A, Espoo)
02044 VTT
Puh. 020 722 111, faksi 020 722 7001

Teknologiska forskningscentralen VTT Ab
PB 1000 (Teknikvägen 4 A, Esbo)
FI-02044 VTT
Tfn +358 20 722 111, telefax +358 20 722 7001

VTT Technical Research Centre of Finland Ltd
P.O. Box 1000 (Tekniikantie 4 A, Espoo)
FI-02044 VTT, Finland
Tel. +358 20 722 111, fax +358 20 722 7001

Cover image: optical micrographs by Andrey Timofeev and Pasi Lähteenmäki.

Juvenes Print, Tampere 2015

Microwave-coupled superconducting devices for sensing and quantum information processing

Visa Vesterinen. Espoo 2015.

Abstract

Superconducting circuits and devices have unique properties that make them interesting from both theoretical and practical perspective. In a superconductor cooled below its critical temperature, electrons bound in Cooper pairs have the ability to carry current without dissipation. A structure where the Cooper pairs are coherently tunneling across a weak link is called a Josephson junction (JJ). The dissipationless and non-linear character of the JJ has found applications, e.g., in microwave amplifiers and quantum circuits. These two subjects are closely related since superconducting quantum bits (qubits) are artificial atoms with a transition spectrum in the microwave range. Mediated by microwave photons, qubit readout in circuit quantum electrodynamics (cQED) architecture requires signal boosting with a low-noise preamplifier. In this thesis, a new type of ultrasensitive JJ microwave amplifier was characterized and its noise performance was found to be close to a bound set by quantum mechanics. The amplifier uses the intrinsic negative differential resistance of a current-biased JJ.

This work also addressed a challenge related to the scalability of the cQED architecture when the qubits are weakly anharmonic. In a frequency-crowded multi-qubit system, driving individual qubits may cause leakage into non-computational levels of the others. Leakage-avoiding single-qubit Wah-Wah control was implemented. At maximum gate speed corresponding to the frequency crowding, microwave control of two transmon qubits on a 2D cQED quantum processor was decoherence limited. The results disclose the usefulness of Wah-Wah in a future quantum computing platform.

Quasiparticles are excitations from the paired superconducting ground state of conduction electrons. As the third topic, the generation-recombination dynamics of quasiparticles was employed in sensing. In electrodynamic terms, superconducting thin films have kinetic inductance from the inertia of the Cooper pairs and resistive dissipation from the quasiparticles. If the film is a part of an electrical resonator, quasiparticle density steers its microwave eigenfrequency and quality factor. In this work, submillimetre-wave radiation and external magnetic field were first converted into quasiparticle-generating temperature variations and screening currents in a superconductor, respectively. In the two devices called kinetic inductance bolometer and magnetometer, the corresponding changes in resonator parameters

were read out to extract the encoded signal. Sensor characterization indicated potential for high sensitivity and low noise. Future applications of the bolometer and the magnetometer include security screening and biomagnetism, respectively. Here, multiplexability in frequency domain facilitates the scale-up to large sensor arrays.

Preface

This study was carried out at VTT Technical Research Centre of Finland Ltd during the years 2011-2015. The work was mostly funded by the Academy of Finland, and a grant from the Research Foundation of Helsinki University of Technology supported my research visit to Delft University of Technology, the Netherlands. The research work in this thesis made use of the Aalto University Low Temperature Laboratory infrastructure.

I am grateful to my thesis advisors at VTT, Prof. Heikki Seppä and Dr. Juha Hassel, for continuous support, ideas and encouragement. I am indebted to my co-authors and several other colleagues who provided help and expertise. I thank Mikko Kiviranta and Dr. Andrey Timofeev especially for sharing their knowledge on experimental techniques. I've also had a great pleasure working with Prof. Arttu Luukanen, Hannu Sipola, Leif Grönberg, and my office mates Dr. Juho Luomahaara and Nikolai Beev. Assistance from VTT technicians, Paula Holmlund in particular, was invaluable during the experimental projects. I also thank the group bosses Dr. Panu Helistö and Dr. Timo Varpula for taking care of administrative duties.

Many people outside VTT contributed to this work. First, fruitful collaboration with Pasi Lähteenmäki and Prof. Pertti Hakonen at Low Temperature Laboratory, Aalto University is gratefully acknowledged. Secondly, I thank the people of the Quantum Transport group in Delft for warm hospitality during my research visit in the winter 2013-2014. I thank Asst. Prof. Leo DiCarlo for accepting me as a visitor in his superconducting quantum circuits team. My gratitude extends to the co-workers Dr. Olli-Pentti Saira, Dr. Diego Ristè, Dr. Gijs de Lange, Dr. Alessandro Bruno, Dr. Stefano Poletto and Christian Dickel. Olli-Pentti was my instructor in the Wah-Wah project, and he also provided helpful comments on the "quantum" parts of the thesis manuscript.

I wish to thank my supervising professors at Aalto University, Sebastiaan van Dijken (in the first year and a half) and Pertti Hakonen (starting from 2012) for guidance and advice. Finally, I would like to thank family, relatives and friends for their support.

Espoo, 20 April, 2015,

Visa Vesterinen

Academic dissertation

Thesis advisors	Research Prof. Heikki Seppä Sensors and circuits VTT Technical Research Centre of Finland Ltd Espoo, Finland
	Dr. Juha Hassel Sensors and circuits VTT Technical Research Centre of Finland Ltd Espoo, Finland
Preliminary examiners	Dr. Olivier Buisson Institut NÉEL - CNRS Grenoble, France
	Prof. Alexander Shnirman Karlsruhe Institute of Technology Karlsruhe, Germany
Opponent	Prof. Vitaly Shumeiko Chalmers University of Technology Gothenburg, Sweden
Supervising professor (14.02.2011-06.09.2012)	Prof. Sebastiaan van Dijken Department of Applied Physics Aalto University Espoo, Finland
Supervising professor (07.09.2012-)	Prof. Pertti Hakonen Department of Applied Physics Aalto University Espoo, Finland

List of publications

This thesis is based on the following original publications which are referred to in the text as I–V. The publications are reproduced with kind permission from the publisher.

- I Lähteenmäki, P.*, Vesterinen, V.*, Hassel, J., Seppä, H., & Hakonen, P. J. (2012). Josephson junction microwave amplifier in self-organized noise compression mode. *Sci. Rep.* **2**, 276. 5 pages + supplement 23 pages.
- II Vesterinen, V., Hassel, J., & Seppä, H. (2013). Tunable Impedance Matching for Josephson Junction Reflection Amplifier. *IEEE Trans. Appl. Supercond.* **23**, 1500140. 4 pages.
- III Timofeev, A. V., Vesterinen, V., Helistö, P., Grönberg, L., Hassel, J., & Luukanen, A. (2014). Submillimeter-wave kinetic inductance bolometers on free-standing nanomembranes. *Supercond. Sci. Technol.* **27**, 025002. 7 pages.
- IV Luomahaara, J., Vesterinen, V., Grönberg, L., & Hassel, J. (2014). Kinetic Inductance Magnetometer. *Nat. Commun.* **5**, 4872. 7 pages.
- V Vesterinen, V., Saira, O.-P., Bruno, A., & DiCarlo, L. (2014). Mitigating information leakage in a crowded spectrum of weakly anharmonic qubits. arXiv:cond-mat/1405.0450. *Submitted for publication in Physical Review X*. 5 pages + supplement 8 pages.

*equal contribution

Author's contributions

- I The author conducted the numerical simulations and made the analytical mixing analysis. The author wrote the first version of the manuscript, including supplementary material, together with M.Sc. Pasi Lähteenmäki.
- II The author planned the work together with the other authors. The author simulated and designed the circuit. The author was responsible for the design and construction of the experimental setup. The author performed the measurements, analysed the data, and wrote the manuscript.
- III The author contributed to the theoretical analysis. The author commented on the manuscript, and wrote a part of the appendix. The author did not contribute to the design and fabrication of the free-standing membranes.
- IV The author took part in theoretical modelling and device design. The author contributed to the manuscript whose principal writer was Dr. Juho Luomahaara.
- V The author carried out the experiments and the data analysis under the supervision of Dr. Olli-Pentti Saira. The author wrote the first version of the manuscript, including some parts of supplementary material.

List of abbreviations

ac	Alternating current
BCS	Bardeen-Cooper-Schrieffer
CPB	Cooper pair box
cQED	Circuit quantum electrodynamics
dc	Direct current
DRAG	Derivative removal by adiabatic gate
EPS	Error per computational step
GBP	Gain-bandwidth product
GR	Generation-recombination
HEMT	High-electron-mobility transistor
IF	Intermediate frequency
J-C	Jaynes-Cummings
JJ	Josephson junction
JPA	Josephson parametric amplifier
KID	Kinetic inductance detector
KIM	Kinetic inductance magnetometer
LO	Local oscillator
MEG	Magnetoencephalography
NEP	Noise-equivalent power
NETD	Noise-equivalent temperature difference
NMR	Nuclear magnetic resonance

PCB	Printed circuit board
RB	Randomized benchmarking
RCSJ	Resistively and capacitively shunted junction
rms	root mean squared
RF	Radio frequency
RSJ	Resistively shunted junction
SJA	Single junction amplifier
SNR	Signal-to-noise ratio
SPAM	State preparation and measurement
SQUID	Superconducting quantum interference device
ULF MRI	Ultra-low-field magnetic resonance imaging
Wah-Wah	Weak anharmonicity with average Hamiltonian

List of symbols

α_d	a constant in $j^* = \alpha_d j_d$
α_i	current non-linearity
α_k	kinetic inductance fraction
α_p	power non-linearity
α_q	anharmonicity
β	DRAG parameter
β_c	Stewart-McCumber parameter
Δ, Δ_0	superconducting gap (at zero temperature)
δ	angular frequency offset
ϵ_r	relative permittivity
Γ	reflection coefficient
γ	qubit decay rate
κ	resonator linewidth
κ_i, κ_e	internal and external decay rate of a resonator
Λ	in-plane penetration depth
λ, λ_0	magnetic penetration depth (at zero temperature)
λ_1, λ_2	coupling strength of a microwave drive to the transition $ 0\rangle \leftrightarrow 1\rangle$ ($ 1\rangle \leftrightarrow 2\rangle$)
ν	signal angular frequency
ν_c	low-pass corner angular frequency
Φ	magnetic flux
Φ_a	external magnetic flux

ϕ	phase of qubit rotation
$\sigma = \sigma_1 - i\sigma_2$	complex conductivity
σ_n	normal state conductivity
σ_q	standard deviation of a Gaussian microwave pulse
$\hat{\sigma}_m, m \in \{x, y, z\}$	Pauli matrices
τ	dimensionless time
τ_r	recombination time
τ_{th}	thermal time constant
θ	qubit rotation angle
φ	Josephson junction phase difference
Ω_I, Ω_Q	in- and out-of-phase quadrature envelope
ω	angular frequency
$\hat{\Pi}$	projection operator
ω_{01}	qubit transition angular frequency
ω_{12}	leakage transition angular frequency
ω_i	idler angular frequency
ω_J	Josephson angular frequency
ω_p	Josephson plasma angular frequency
ω_{pump}	pump angular frequency
ω_r, ω_{r0}	resonance angular frequency (at zero I_s)
ω_{rf}	radio angular frequency
2χ	transmon-cavity dispersive shift
A	area
A_m	sideband modulation amplitude
A_θ	pulse amplitude at rotation angle θ
\hat{a}^\dagger, \hat{a}	creation (annihilation) operator of an intra-cavity photon
\vec{B}, \vec{B}_0	magnetic flux density
ΔB	dynamic range in units of B

C	capacitance
C_{Σ}	sum of capacitances
C_c	coupling capacitance
C_e	external resonator capacitance
C_g	gate capacitance
C_J	Josephson capacitance
C_{th}	heat capacity
d	film thickness
E^*	kinetic scaling energy
\vec{E}	electric field
E_C	charging energy
E_J	Josephson energy
E_{ij}	transition energy between quantum states i and j .
E_m	discrete energy spectrum with m an integer
E_r	energy stored in a resonator
f	frequency
G	heat conductance
G_a	power gain
g	qubit-cavity coupling strength
I, I^*	current, scaling current
I_b	bias current
I_c	critical current
I_d	depairing current
j_d, j_{d0}	depairing current density (at zero temperature)
I_n	noise current
I_s	screening current
j, j^*	current density, scaling current density
\vec{k}	momentum

L	inductance or self-inductance
L_g	geometric inductance
L_J	Josephson inductance
L_k, L_{k0}	kinetic inductance (at zero temperature)
L_{par}	parasitic inductance
L_s	kinetic surface inductance
L_{tot}	total inductance
L_w	bonding wire inductance
l	mean free path of electrons
m	integer
N_0	single-spin density of states at Fermi level
n	number of Cooper pairs
n_g	offset charge
$\langle n_{\text{ph}} \rangle$	mean occupation of a cavity
n_{qp}	quasiparticle density
n_s	density of paired electrons
P_{rf}	RF power
Q_i, Q_e, Q_t	internal, external, and total quality factor
q, q_{rms}	external parameter
\vec{q}	added momentum
R	resistance
R_b	bias resistance
R_d	differential resistance
R_i, R_e	internal and external resistance of a resonator
R_s	kinetic surface resistance
S_{11}, S_{21}	scattering parameters
$S_B^{1/2}$	magnetometer resolution
S_I	current spectral density

S_p	power spectral density
T	temperature
T_1	qubit relaxation time
T_2	qubit dephasing time
T_a	amplifier noise temperature
T_n	total input noise temperature
T_{res}	resonator temperature
T_{src}	source temperature
t	time
t_0	center time
t_b	buffer time
t_g	gate time
t_{meas}	measurement time
t_s	computational step time
V, V_{rms}	voltage
V_b	bias voltage
V_{out}	demodulated output voltage
v	dimensionless Josephson voltage
W	loop edge length
w	trace width
X	reactance
Z	impedance
Z_0	characteristic impedance
Z_{res}	resonator impedance
Z_s	kinetic surface impedance

Contents

Abstract	i
Preface	iii
Academic dissertation	iv
List of publications	v
Author's contributions	vi
List of abbreviations	vii
List of symbols	ix
1 Introduction	2
2 Superconducting devices and circuits	5
2.1 Josephson effect	5
2.2 Dissipative devices	7
2.3 Quantum limited amplifiers	9
2.4 Dispersive devices	10
2.5 Quantum elements	20
3 Results	31
3.1 Radio-frequency Josephson amplifier	31
3.2 Kinetic inductance sensing	37
3.3 Addressability of quantum bits	48
4 Summary and conclusions	53
References	56
Appendices	71
Appendix A: KIM dynamic range	71
Appendix B: Errata	72
Publications I-V	

1. Introduction

Cooling materials to temperatures near absolute zero ($-273.15\text{ }^\circ\text{C}$) has certain benefits. One is reduction of thermal fluctuations and associated noise at energy scale $k_B T$, with k_B the Boltzmann constant and T the temperature. Some metals and compounds enter superconducting state below a material-dependent critical temperature¹ T_c [1, 2]. Here, despite Coulombic repulsion between electrons it becomes energetically favourable for charge-carrying electrons to form Cooper pairs. There are two hallmark properties of superconductivity. Superconductors carry electrical current without presenting any dc resistance (up to the depairing current density j_d) and they repel magnetic fields (forcing exponential decay of the field inside, with the length scale given by the magnetic penetration depth λ).

Low temperature enables fundamental investigations of quantum mechanics. The explanation of superconductivity by Bardeen, Cooper and Schrieffer (BCS) [1, Chap. 3] is a quantum theory where microscopic Cooper pairs form a bosonic condensate described using a macroscopic wavefunction. The well-defined phase of this wavefunction gives rise to phenomena called the Josephson effect [3] and flux quantization [4]. The Josephson effect describes coherent Cooper pair tunnelling across a weak link, such as a thin insulating barrier separating two superconducting leads. This element is called the Josephson junction. Magnetic flux threading a superconducting loop is always an integer multiple of the flux quantum $\Phi_0 \approx 2.07\text{ fWb}$. In the presence of an external magnetic field the quantization is enforced by a dissipationless flow of screening currents on the material surface.

This work deals with experimental studies and theoretical analysis of superconducting circuits and devices. In some devices fundamental physical phenomena are observed, while others are sensitive instruments of practical importance. Common factors are operation at radio frequencies² (RF) and use of resonant structures or circuits.

The devices of fundamental interest are discussed first. A quantum computer is a distant goal of the scientific community [5]. It consists of quantum bits (qubits) that can take a binary state 0 or 1 like a classical bit, or any superposition of the two. Using a computing resource called quantum entanglement, the device can solve certain hard problems faster than a

¹In this work T_c ranges from 1.2 K in Al to 14 K (15.5 K) in NbN (NbTiN).

²Radio frequencies of this work range from 100 MHz to 8 GHz.

classical computer. There are many competing quantum computing platforms. Superconducting systems have recently shown an improving degree of scalability and controllability [6]. To build a superconducting qubit [7], the macroscopic quantum behaviour of the Cooper pairs is complemented with the Josephson effect. Protecting the delicate nature of the qubit requires a sub-K temperature³ and isolation from environmental noise. This work has addressed technical issues related to (i) qubit state readout fidelity, and (ii) coherent single-qubit control.

A signal from the quantum state readout is weak and requires boosting by a low-noise preamplifier. To this end, Publications I-II propose and demonstrate a near quantum-limited microwave amplifier from a single dc-biased Josephson junction. The amplifier has not actually been tested in qubit readout because the first, narrowband devices have not been frequency tunable. However, the device is an interesting object in its own right. It competes against a broad class of RF pumped parametric amplifiers [8, 9, 10] and a microstrip superconducting quantum interference device (SQUID) amplifier [11].

The work on single-qubit control (Publication V) has experimentally validated the performance of a so-called Wah-Wah technique. Theoretically described in Ref. [12], Wah-Wah facilitates quantum processor scalability. Many qubits, including transmons [13] used in this work, are only weakly anharmonic. They are quantum objects whose multi-level spectra consist of almost equidistant energy levels. One pair of levels defines the qubit. Hence, pulsed microwave control targeting a qubit transition may have spectral weight on an unwanted leakage transition. This is a problem especially in frequency-crowded multi-qubit systems. Unlike a previous control method [14] that only avoids leakage in the addressed qubit, Wah-Wah also mitigates the leakage error induced in a frequency neighbour qubit. This allows a reduction in the number of control lines, since cross-talk can be tolerated.

The superconducting sensing devices are discussed next. Above absolute zero, not all conduction electrons are paired. Competing dynamic random processes of Cooper pairs breaking into quasiparticles and the quasiparticles recombining back are present [15, 16]. The fermionic quasiparticles are excitations with energy above Δ , the superconducting gap⁴. The Cooper pairs have inertia that becomes observable in a thin film. The film has kinetic impedance to which the Cooper pairs (quasiparticles) contribute in the form of inductance (resistance). The kinetic impedance, in which the inductance dominates due to a low level of dissipation, reacts to a change in quasiparticle density.

One practical application of the kinetic inductance is sensing of radiation at Cooper-pair-breaking frequencies $\omega > 2\Delta/\hbar$, with \hbar the reduced Planck's constant. A milestone paper in 2003 [17] has demonstrated that

³In this work, $T = 20$ mK has been achieved in a dilution refrigerator.

⁴It takes an energy 2Δ to break a Cooper pair with a photon.

a thin-film sensor can be embedded as part of an RF resonator to realize a so-called dispersive readout. The device is called a kinetic inductance detector (KID). The resonant enhancement of the small impedance variation improves sensitivity. Furthermore, the readout can be frequency multiplexed in large arrays where each sensor/resonator system is assigned a unique eigenfrequency. KID arrays for imaging of THz radiation, which is relevant to astrophysicists, are currently being tested in ground-based telescopes [18, 19].

The sensors in Publications III-IV can be considered spin-offs of the mature KID technology. They similarly utilize the electrodynamic response of thin films and the resonant circuitry for readout. However, the Cooper-pair-breaking mechanisms are different. First, Publication III is an experimental study of bolometric radiation detection [20, 21]. Arriving photons heat a thermally isolated membrane. Temperature rise creates quasiparticles in a thin superconducting meander line deposited on the membrane, and the corresponding enhancement of kinetic inductance is read out. The bolometer has been designed for the THz range. Although its sensitivity does not meet the requirements of astrophysics, the detector operates at higher temperature than the KID. This is advantageous for some terrestrial applications.

Secondly, Publication IV proposes and demonstrates a sensitive kinetic inductance magnetometer from a relatively large superconducting loop. As noted above, screening currents arise to maintain flux quantization when an external magnetic field is applied. The flow of supercurrent, i.e., finite momentum of Cooper pairs, reduces Δ and the associated pairing energy of electrons. The supercurrent is thus indirectly responsible for the quasiparticle generation. Kinetic inductance magnetometry using these principles has been demonstrated in Refs. [22, 23, 24]. However, this work tremendously improves sensitivity since the pair breaking is distributed across the entire loop instead of being geometrically constricted. Magnetometer performance has been benchmarked against an established type of a superconducting flux detector, a low- T_c SQUID [25]. The ultrasensitive SQUID uses flux quantization in a different way, i.e., in conjunction with the Josephson effect.

2. Superconducting devices and circuits

Chapters 2.1-2.5 provide an overview of the theoretical background to superconducting devices and circuits, beginning with the Josephson effect and the dynamics of Josephson junctions and circuits (Publications I, II, and V). Secondly, amplification of weak RF signals is discussed (Publications I-II). The third topic is the electrodynamic response of superconducting thin films, including an aspect of electrical RF techniques and measurements (Publications III-IV). Next, the discussion on the Josephson junction is extended to cover a quantized charge regime. This forms a basis for understanding superconducting qubits (Publication V). The last topic addresses an on-chip platform where the qubits are operated.

2.1. Josephson effect

2.1.1. Josephson junction

Josephson junctions (JJs) are weak links between superconductors [3, 26]. Often realized as a thin aluminium oxide (AlO_x) insulating barrier, the link allows Cooper pair tunnelling in a quantum phase-coherent manner. Josephson current and voltage (I and V) relations are interlinked by the dynamics of the wavefunction phase difference φ across the junction:

$$I = I_c \sin \varphi \quad (2.1)$$

$$\hbar \frac{d\varphi}{dt} = 2eV, \quad (2.2)$$

where I_c is the critical current, and e the elementary charge. In electrical circuit diagrams the tunnelling element described by the relations (2.1)-(2.2) is depicted with a cross \times . The insulating barrier also forms a parallel-plate-style Josephson capacitance C_J which shunts the junction. As such, the JJ is a dissipationless and non-linear circuit element. In the so-called zero voltage state, $V \propto \partial_t \varphi = 0$, the JJ can sustain a flow of supercurrent $|I| < I_c$. In this work, I_c ranges from 40 nA to 20 μA .

2.1.2. SQUID

A superconducting quantum interference device (SQUID) combines the Josephson effect and the magnetic properties of a superconducting loop. The mag-

netic flux Φ threading the loop is quantized, i.e., it may only take discrete values. This follows from the properties of the quantum wavefunction describing the Cooper pair condensate. More specifically, Φ can be expressed through a formula containing a closed contour integral of the wavefunction phase gradient. The uniqueness of the wavefunction forces the integral to be a multiple of 2π , and the flux discretizes as $\Phi = 2\pi m\hbar/(2e) = m\Phi_0$, with m as an integer. The quantized flux is a superposition of externally applied flux Φ_a and flux induced by screening currents flowing in the material. If the loop were interrupted by two JJs 1 and 2, a SQUID would be formed.

SQUID Josephson dynamics responds to flux applied to the loop. In this context, a measurable quantity is the effective critical current of the SQUID $\max\{I_{c1} \sin \varphi_1 + I_{c2} \sin \varphi_2\}$. Throughout this work the junctions are assumed to be identical ($I_{c1} = I_{c2} = I_c$). This simplifies the relations for the junction phases and the total flux

$$\varphi_2 - \varphi_1 = 2\pi(m - \Phi/\Phi_0) \quad (2.3)$$

$$\Phi = \Phi_a + LI_c(\sin \varphi_1 - \sin \varphi_2)/2, \quad (2.4)$$

with the SQUID loop self-inductance L (Fig. 2.1a). In the case of a small loop, L is neglected and $\Phi \approx \Phi_a$. Quantum interference within the SQUID is now understood as sinusoidal modulation $\max\{I_c(\sin \varphi_1 + \sin \varphi_2)\} \approx 2I_c|\cos(\pi\Phi_a/\Phi_0)|$. Finite L reduces the modulation depth, the peak-to-peak value of flux-tunable effective critical current¹.

The sensitivity of the SQUID to an applied flux as weak as a fraction of Φ_0 enables magnetometry [25, 27]. In practice, this is accomplished by a mutual coupling of the SQUID loop to a flux transformer with a larger pick-up area for the external field. Other applications of the SQUID are diverse, ranging from voltage measurement of low-impedance sources [28] to noise thermometry [29]. The operation of the SQUID as a flux-tunable non-linear inductor is explained next.

2.1.3. Josephson inductance

In this section, the inductance of the Josephson junction is derived. The Josephson current relation in Eq. (2.1) is differentiated as:

$$\frac{dI}{dt} = I_c \cos \varphi \frac{d\varphi}{dt} \Leftrightarrow V = \frac{\Phi_0}{2\pi I_c \cos \varphi} \frac{dI}{dt} \equiv L_J(\varphi) \frac{dI}{dt}. \quad (2.5)$$

This defines a Josephson inductance $L_J(\varphi)$ containing a weak non-linearity $\cos \varphi = \sqrt{1 - (I/I_c)^2}$, $|I| \ll I_c$. Together L_J and C_J set a characteristic plasma frequency $\omega_p = 1/\sqrt{L_J C_J}$ for the Josephson junction. Its typical magnitude is tens of GHz. In Eq. (2.5), I_c can be that of a SQUID, i.e., flux tunable and maximally two times the critical current of a single JJ.

¹Asymmetric junctions similarly reduce the SQUID modulation depth.

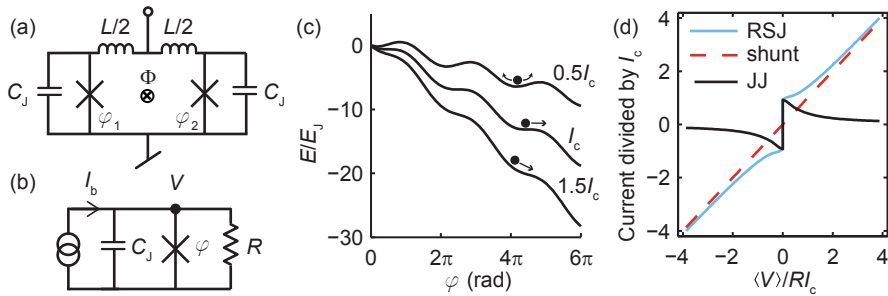


Figure 2.1: Elementary Josephson devices. (a) SQUID is a superconducting loop L interrupted by two Josephson junctions (identical here). (b) RCSJ circuit diagram. (c) Potential energy landscape of (b). The potential resembles a washboard tilted by bias current (labels). By mechanical analogue, the phase is a moving mass $(\Phi_0/2\pi)^2 C_J$. At $|I_b| < I_c$ motion is with high probability confined to plasma oscillations across a potential energy minimum. At $|I_b| > I_c$ phase evolves and $|\langle V \rangle| > 0$. (d) Current-voltage characteristics of RSJ [overdamped junction in (b)]. Bias current (blue) is the sum of currents flowing through the shunt (red) and the junction (black).

2.2. Dissipative devices

Resistance is a source of dissipation and current (or voltage) fluctuations in electrical circuits. Besides explaining the dynamics of a resistively shunted JJ, this chapter gives a frequently used expression for the noise generated by a resistor.

2.2.1. Resistively shunted junction

When subject to dc current biasing, the JJs in a circuit can be lifted from the zero voltage state to a finite voltage state. In the context of this work, a resistor R is placed parallel to the junction to control Josephson dynamics under bias. The circuit is called RCSJ [1, Chap. 6], resistively and capacitively shunted junction (Fig. 2.1b, note C_J). The bias current (I_b) splits into two arms, one containing the junction and the other the shunt R . Differential equation of the time evolution of the phase across the junction is

$$\beta_c \frac{d^2 \varphi}{d\tau^2} + \frac{d\varphi}{d\tau} + \sin \varphi = \frac{I_b + I_n}{I_c}, \quad (2.6)$$

where $\tau = 2\pi I_c R t / \Phi_0$ is dimensionless time, $\beta_c = 2\pi I_c R^2 C_J / \Phi_0$ the Stewart-McCumber parameter, and I_n current noise from the resistor. Eq. (2.6) can be regarded as an equation of motion where effective potential energy is $E_J(1 - \cos \varphi - \varphi I_b / I_c)$, with $E_J = \Phi_0 I_c / (2\pi)$ the Josephson energy (Fig. 2.1c).

I_n follows a spectrum that is temperature and frequency dependent. The Callen and Welton formula for current spectral density reads [30]

$$S_I(\omega) = \frac{2\hbar\omega}{R} \coth\left(\frac{\hbar\omega}{2k_B T}\right). \quad (2.7)$$

The spectral density simplifies to Johnson-Nyquist thermal noise $4k_B T/R$ when $\hbar\omega \ll 2k_B T$, and to the so-called quantum noise $2\hbar\omega/R$ in the opposite limit. The quantum fluctuations play a role even at zero temperature. It can be noted that noise power spectral density $S_p = RS_I$ is independent of the value of R .

The RCSJ model describes the Josephson effect semiclassically. RCSJ is valid for large junctions, but it breaks down in the sub- μm regime where single-electron charging effects in C_J arise. Small junctions are given proper quantum mechanical treatment later (Sect. 2.5.1). It should also be noted that fluctuations influence the Josephson phase dynamics. For instance, thermal fluctuations in current-biased junctions with $\beta_c < 1$ are observed as the rounding of the transition between the zero and finite voltage states. However, the devices of this work are not operated near the transition.

It will be shown that the differential resistance of a junction in the finite voltage state is negative. This is derived from Eq. (2.6) with I_n neglected for simplicity. Small bias currents $|I_b| < I_c$ only induce a constant phase $\varphi = \arcsin(I_b/I_c)$ and the average junction voltage $\langle V \rangle = RI_c \langle d\varphi/d\tau \rangle$ remains zero (Sect. 2.1.1). By contrast, at $I_b > I_c$ the system enters a state of almost linear phase evolution²

$$\varphi \simeq \omega_J t + \varphi_J. \quad (2.8)$$

Because of the linear slope ω_J (Josephson frequency), the finite voltage state is often called the running state. The additional term φ_J contains sinusoidal oscillations at integer multiples of ω_J , with a progressively decreasing amplitude of the harmonics. By differentiation of Eq. (2.8), $\langle V \rangle = \omega_J \Phi_0 / 2\pi$. The dc relationship between $\langle V \rangle$ and I_b forms an IV curve that is useful in the analysis of the circuit at frequencies $\omega \ll \omega_J$. The devices of this work have $\beta_c < 1$ where the IV curve is non-hysteretic. The particular case $\beta_c \approx 0$ (overdamped junction) has an analytically solvable $\langle V \rangle$: the effect of C_J is suppressed, hence the name RSJ (resistively shunted junction). RSJ has the IV curve $\langle V \rangle = R\sqrt{I_b^2 - I_c^2}$. The bias current splits as

$$I_b = \langle I \rangle + \langle V \rangle / R, \quad (2.9)$$

implying a junction current $\langle I \rangle = \langle I_c \sin \varphi \rangle = I_b - \sqrt{I_b^2 - I_c^2}$ (Fig. 2.1d). The corresponding differential resistance of the junction is

$$R_d = \frac{\partial \langle V \rangle}{\partial \langle I \rangle} = \frac{RI_b^2}{I_c(\sqrt{I_b^2 - I_c^2} - I_b)}, \quad (2.10)$$

²Without loss of generality a positive I_b is assumed here.

negative at all bias points $I_b > I_c$. In the RSJ model, this negativity is always masked by the shunt since $R < |R_d|$. In other words, the combination of the two resistances in parallel has a positive value.

In Publications I-II (Chapter 3.1) frequency selective damping [31] of the JJ has been introduced to reveal the negative³ R_d on demand. The device is called a single junction amplifier (SJA). In an electrical circuit, a signal reflecting from a negative resistance experiences gain. With proper impedance matching of the JJ to a standard $Z_0 = 50 \Omega$ microwave environment, amplification of weak signals was accomplished. General amplifier concepts are reviewed next.

2.3. Quantum limited amplifiers

Linear amplification of electrical signals using non-linear circuits is discussed in this chapter. Detecting weak signals is easier with a preamplifier that has a low input noise temperature (T_a) [32, Chap. 10] and provides sufficient power gain ($G_a > 10$). To understand the noise temperature, consider the textbook definition with Johnson-Nyquist noise from an impedance matched source resistor at physical temperature T [Eq. (2.7)]. The noise added by the amplifier is converted to a rise of the resistor temperature: noise power spectral density is $S_p = k_B(T + T_a)$ at the input of the amplifier. Besides being of practical importance, amplifiers may turn into intriguing quantum objects at low temperature. There are quantum mechanical lower bounds for the noise added by a linear amplifier, independent of physical implementation [33, 34]. In the quantum regime the noise is expressed through the number of quanta $k_B T_a / (\hbar\omega)$. RF amplifiers are categorized as phase sensitive and phase preserving. The former is ideally noiseless and amplifies only a single signal quadrature. The latter amplifies both quadratures and optimally adds half a quantum of noise, which is equal to the magnitude of vacuum fluctuations. The SJA is a phase-preserving amplifier.

Each amplifier is optimal only across a certain frequency band and at a fixed impedance level. In this work microwave amplifiers for the standard impedance Z_0 are considered. Near quantum-limited amplifiers have previously been realized by pumping non-linear Josephson inductance (Sect. 2.1.3) with microwaves. This is analogous to optical parametric amplification in materials with non-linear refractive index [35]. An example of RF pumped devices is a Josephson parametric amplifier (JPA) [8], a non-linear resonator coupled to an RF environment. Considering a JPA, the quantum concepts of amplification can be illustrated [36]. A pump tone at ω_{pump} arrives at the JPA input together with a signal at ω_{rf} . The pump supplies energy for the amplification of a reflected signal, and dynamics at an idler frequency $\omega_i = 2\omega_{\text{pump}} - \omega_{\text{rf}}$ arises in the process as well (this is called four-wave mixing). A phase-sensitive JPA has the pump at $\omega_{\text{pump}} = \omega_{\text{rf}}$,

³ $R_d < 0$ will occur at finite β_c as well.

and $\omega_i = \omega_{\text{rf}}$. The pump phase determines the amplified and deamplified signal quadratures [37]. On the other hand, at $\omega_{\text{pump}} \neq \omega_{\text{rf}}$ the JPA is phase preserving. The idler is a separate frequency from which vacuum input noise is mixed to ω_{rf} , hence the quantum limit of added noise.

2.4. Dispersive devices

In contrast to Chapter 2.2, dissipation is minimized here by working with mainly reactive impedance elements. Superconductors are inherently suitable for this purpose.

2.4.1. Kinetic impedance

The superconducting state of a material responds to changes in various environmental conditions: static magnetic field, paramagnetic impurities, temperature, electromagnetic radiation, dc and ac bias currents, to name but a few. This section deals with the electrodynamic response of superconductors. As a main result, thin-film circuit elements not relying on the Josephson effect are introduced. In this context, the materials of this work (e.g., NbN) were "dirty" superconductors, simplifying the discussion throughout this section. Simply put, Cooper pair size is limited by the mean free path of electrons l , much shorter than the BCS coherence length. Furthermore, the electrodynamic response is local, since the magnetic penetration depth λ exceeds the length scale set by l . The long penetration depth correlates with a high normal state resistance of the material, typically associated with a large amount of disorder scattering of electrons.

With these assumptions in place, the current density \vec{j} and the electric field \vec{E} can be related as $\vec{j} = \sigma \vec{E}$ in the superconductor. This looks similar to Ohm's law for normal conductors. However, the conductivity σ is complex-valued and describes the charge carried by both paired and unpaired electrons. In this section the kinetic impedance of superconductors is derived from σ . Secondly, it will be explained how the sensitivity of the kinetic impedance to external conditions opens new applications in sensing. Thirdly, a readout method for such sensors is described.

Complex conductivity

Conductivity is divided into real and imaginary parts as $\sigma = \sigma_1 - i\sigma_2$, arising from quasiparticles and Cooper pairs, respectively. The basic properties of σ are captured by a simple two-fluid model [2, Chap. 3] that assumes low frequency $\omega \ll \Delta/\hbar$. The Cooper pair breaks into two quasiparticles when absorbing a quantum at $\omega > 2\Delta/\hbar$. To account for this effect, a more comprehensive microscopic treatment has been derived by Mattis and Bardeen [38]. The Mattis-Bardeen theory presents the conductivities scaled

by the normal state conductivity σ_n :

$$\frac{\sigma_1}{\sigma_n} = \frac{2\Delta_0(e^{\hbar\omega/\Delta_0} - 1)}{\hbar\omega} \int_{\Delta/\Delta_0}^{\infty} \frac{g_1(x)}{(1+e^x)(1+e^{x+\hbar\omega/\Delta_0})} dx$$

$$- \frac{\Delta_0}{\hbar\omega} \int_{\min\{(\Delta-\hbar\omega)/\Delta_0, -\Delta/\Delta_0\}}^{\Delta/\Delta_0} \tanh\left(\frac{x}{2} + \frac{\hbar\omega}{2\Delta_0}\right) g_1(x) dx \quad (2.11)$$

$$\frac{\sigma_2}{\sigma_n} = \frac{\Delta_0}{\hbar\omega} \int_{\max\{(\Delta-\hbar\omega)/\Delta_0, -\Delta/\Delta_0\}}^{\Delta/\Delta_0} \tanh\left(\frac{x}{2} + \frac{\hbar\omega}{2\Delta_0}\right) g_2(x) dx \quad (2.12)$$

$$g_1(x) = \frac{x(x + \hbar\omega/\Delta_0) + (\Delta/\Delta_0)^2}{\sqrt{x^2 - (\Delta/\Delta_0)^2} \sqrt{(x + \hbar\omega/\Delta_0)^2 - (\Delta/\Delta_0)^2}} \quad (2.13)$$

$$g_2(x) = \frac{x(x + \hbar\omega/\Delta_0) + (\Delta/\Delta_0)^2}{\sqrt{(\Delta/\Delta_0)^2 - x^2} \sqrt{(x + \hbar\omega/\Delta_0)^2 - (\Delta/\Delta_0)^2}}. \quad (2.14)$$

The energy scale is set by Δ_0 , superconducting gap at zero temperature. The integration variable x is dimensionless energy. For the materials of this work the gap is in the range $\Delta_0/h \simeq 90 - 500$ GHz, with h the Planck's constant.

To move from bulk to confined geometries of practical importance, consider a film of thickness d . The surface impedance⁴ of this film can be written as [39, 40]

$$Z_s = \sqrt{\frac{i\mu_0\omega}{\sigma}} \coth\left(\sqrt{i\mu_0\omega\sigma}d\right), \quad (2.15)$$

with μ_0 the vacuum permeability. Due to the low loss of the superconductor, the imaginary part of conductivity dominates. The imaginary conductivity is related to the magnetic penetration depth through the London theory [1, Chap. 2]:

$$\sigma_2 = \frac{1}{\mu_0\omega\lambda^2}. \quad (2.16)$$

The frequency factor inside the hyperbolic cotangent in Eq. (2.15) can be rewritten using Eq. (2.16):

$$Z_s = \sqrt{\frac{i\mu_0\omega}{\sigma}} \coth\left(\frac{d}{\lambda} \sqrt{\frac{i\sigma}{\sigma_2}}\right). \quad (2.17)$$

To simplify Z_s further, a lower bound for λ is derived from the Mattis-Bardeen theory. When quasiparticle distribution is thermal [$e^x \gg 1$ in Eqs. (2.11)-(2.12)] and $k_B T, \hbar\omega \ll \Delta$, analytical conductance formulae can be obtained [41]. The reactive part is $\sigma_2/\sigma_n = \pi\Delta_0/(\hbar\omega)$. This provides a link

⁴The unit of the surface impedance is Ω/\square .

to magnetic penetration depth at zero temperature

$$\lambda_0 = \sqrt{\frac{\hbar}{\pi\mu_0\Delta_0\sigma_n}} \quad (2.18)$$

from Eq. (2.16). Later, it will be shown that λ_0 is the lower bound since λ increases with temperature.

In this work the relevant microstructures are so thin that $d \simeq 100 \text{ nm} \ll \lambda_0 \leq \lambda$. Hence, Eq. (2.17) yields the so-called kinetic surface impedance $Z_s \approx 1/(d\sigma)$. The resistive part is described by $R_s = \text{Re}\{Z_s\} \approx \sigma_1/(d\sigma_2^2)$ and the reactive part by the surface inductance

$$L_s = \text{Im}\{Z_s\}/\omega = \frac{\mu_0\lambda^2}{d}. \quad (2.19)$$

The thin films are fabricated as strips of width w . When the width is smaller than the in-plane penetration depth (Pearl length [42]) $\Lambda \approx \lambda^2/d$, the distribution of current flowing along the strip is homogeneous instead of peaking at the edges. Kinetic impedance per unit length can thus be written as $(R_s + i\omega L_s)/w$. Multiplying by the total strip length yields an impedance $R + i\omega L_k$, with L_k the kinetic inductance. As the geometric inductance L_g associated with the energy stored in a magnetic field is not contained in σ or L_k , it is useful to define the kinetic inductance fraction α_k , the ratio between kinetic and total inductance. By reducing the dimensions of the strip cross-section, L_k can be made comparable to or even higher than L_g .

To become measurable, the impedance element defined by the strip can be embedded into a resonant structure. Shunting by a capacitor forms a conventional RLC circuit [32, Chap. 6] with an eigenfrequency $\omega_r \ll \Delta/\hbar$. This type of a circuit appears frequently in this thesis. The inductive part of the film impedance tunes the eigenfrequency by the relationship $\omega_r \propto \sqrt{\alpha_k/L_s}$, with α_k dependent on the particular geometry. The dissipative losses of the film are best described with an internal quality factor

$$Q_i = \frac{\omega_r L_s}{\alpha_k R_s} \approx \frac{\sigma_2}{\alpha_k \sigma_1}. \quad (2.20)$$

Weakened superconductivity as a detector

Weakening of superconductivity due to external conditions turns a superconducting film into a sensor or a detector. An external parameter steers σ which can be observed in the electrical readout of the film impedance. At the microscopic level, the weakening of the superconductivity originates from (i) absorption of radiation⁵ at frequencies $\omega > 2\Delta/\hbar$, or (ii) Cooper pair breaking becoming otherwise thermodynamically favourable. In both cases, pair breaking dynamics affect the densities of paired electrons and quasiparticles (n_s and n_{qp} , respectively).

⁵Kinetic inductance detector (KID) [17] relies on this mechanism.

To gain more insight into mechanism (ii), the fundamental nature of the Cooper pair has to be understood. It is formed by two electrons with opposite momenta $\pm\vec{k}$ and spin. Pair breaking is associated in some cases with the loss of time-reversal symmetry [43]. For example, consider externally applied static electromagnetic fields. First, a magnetic field \vec{B} causes the time-reversed states to be dephased differently. Second, an electric field \vec{E} accelerates the superfluid into a finite velocity, and the added momentum \vec{q} also breaks the symmetry since $\vec{q} + \vec{k}$ is no longer opposite to $\vec{q} - \vec{k}$. Paramagnetic impurities also weaken superconductivity in a way that can be treated analogously [43].

The weakening of superconductivity can be related to observable quantities. From the conductivity point of view, it is noted that the magnetic penetration depth λ increases and σ_2 is modified accordingly in Eq. (2.16). In addition, the increasing n_{qp} strengthens the ac loss modelled by σ_1 . For the purpose of this work, temperature and dc current responses of σ are described next in more detail.

Temperature dependence

To study the temperature dependence of superconducting properties, a good starting point is the suppression of the energy gap. In the BCS theory this a generic curve numerically solved from a self-consistent equation of Δ/Δ_0 as a function of T/T_c [44] (Fig. 2.2a). The zero-temperature limit is $\Delta_0 \approx 1.76k_B T_c$. The Mattis-Bardeen theory at low frequency can be used together with the BCS gap to model the temperature dependency of σ . λ is a tangible quantity related to σ_2 through Eq. (2.16). λ increases with T and its behaviour near T_c is divergent. Note that the kinetic inductance can be written as $L_k = L_{k0}(\lambda/\lambda_0)^2$ [Eqs. (2.18)-(2.19)], with L_{k0} the zero-temperature value. Temperature variations of dissipation are such that σ_1 vanishes exponentially at low temperature and converges to normal state conductance σ_n when approaching T_c .

An analytical expression that coincides with the Mattis-Bardeen result at low frequency is [1, Chap. 3]

$$\lambda = \lambda_0 \left[\frac{\Delta}{\Delta_0} \tanh \left(\frac{\Delta}{2k_B T} \right) \right]^{-1/2} \quad (2.21)$$

where the BCS gap enters as $\Delta/(2k_B T) \approx 1.76(\Delta/\Delta_0)/(2T/T_c)$ (Fig. 2.2b).

Current dependence

It is useful to recall that magnetic flux expulsion is based on screening currents on the surface of the superconductor. It is therefore understandable that superconductivity is perturbed in a fundamentally similar way by current biasing and applied magnetic fields [43]. Here, the characteristic depairing

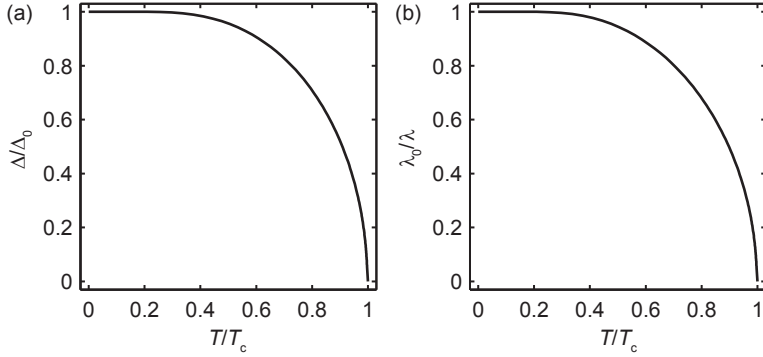


Figure 2.2: Superconductor responding to temperature. (a) Superconducting gap of the BCS theory. (b) Inverse of magnetic penetration depth from Eq. (2.21).

energies scale quadratically as $\propto j^2$ and $\propto B^2$. The condensation energy of the superfluid is consumed by the inertia of the Cooper pairs or the expulsion of the magnetic field, respectively.

The supercurrent density cannot exceed a depairing value j_d which maximizes to j_{d0} at zero temperature. Theoretical formula [45]

$$j_{d0} = 0.75\Delta_0^{3/2} \sqrt{\frac{N_0\sigma_n}{\hbar}} \quad (2.22)$$

contains N_0 , single-spin density of states at Fermi level. At j_{d0} the kinetic energy of the superfluid measures half of the condensation energy that the Cooper pairs have at rest [46]. The Bardeen equation for j_d temperature dependence is

$$j_d = \frac{j_{d0}}{2\sqrt{2}} \left[1 - \left(\frac{T}{T_c} \right)^2 \right]^{3/2}. \quad (2.23)$$

There is a reasonable agreement between this formula and thin films measured at temperatures $T/T_c \simeq 0.2 - 1$ [45].

The flow of supercurrent enhances the kinetic inductance by a quadratic factor⁶

$$L_k \mapsto L_k \left[1 + \left(\frac{j}{j^*} \right)^2 \right], \quad |j| < j_d \quad (2.24)$$

where the absence of a linear term indicates independence of current direction. The normalizing current density is $j^* = \alpha_d j_d$, with α_d a constant. Theoretically $\alpha_d \simeq 2.3$ [21], but a value 3.4 has been measured for NbN

⁶In Publication IV the symbol L_{k0} has been adopted for kinetic inductance at finite temperature and zero current. Due to the low temperature of the experiment $T/T_c \approx 0.3$ it is, however, interchangeable with the definition of this chapter.

in Publication IV⁷The modelling of losses expressed through the current dependence of σ_1 is a complicated task which involves non-equilibrium superconductivity [46].

2.4.2. Resonant matching network

Superconducting sensors and detectors relying on kinetic impedance were studied in Publications III-IV (Chap. 3.2). Detector impedance is denoted as $Z = R + iX$, and its readout has to be carefully planned for several reasons. Firstly, the voltage level across the detector is low due to the combination of a small magnitude of Z and a low current handling capacity [note the depairing current in Eq. (2.23)]. Secondly, long electrical lines connecting to a low-temperature setup have parasitic capacitance. Thirdly, operability may benefit from a large number of sensors, for which a compact readout is desirable⁸. A solution to all three is resonant enhancement of Z variations. The corresponding measurement is said to be dispersive.

Dispersive measurement

The dispersive measurement reads out the variations of a dominantly reactive impedance, $|X| \gg R$. In brief, Z is made compatible with the Z_0 environment where scattering parameter (S-parameter) measurement [32, Chap. 4] is a standard RF technique. Here, an RF excitation signal is transmitted through a chain of components (Fig. 2.3a): an attenuated transmission line reaching the cold parts of a cryocooler where the detector is located, and an output line that includes amplification. The detector is connected to the transmission line through a resonant matching network from reactive elements such as interdigital or parallel-plate capacitors (Fig. 2.3b). The combination forms a shunt impedance Z_{res} , a narrowband resonator. Changes in Z modify its eigenfrequency and quality factor.

In this section, expressions for the resonator parameters are derived. The lumped element equivalent of the system is an R_i - L - C circuit externally loaded with the transmission line (Fig. 2.3c). Low internal loss is accounted for by the resistor R_i . The loading is analyzed by converting the series impedance from a coupling capacitor C_c and terminations $Z_0/2$ into parallel admittance (Fig. 2.3d):

$$\frac{1}{R_e} + i\omega C_e \approx (\omega C_c)^2 \frac{Z_0}{2} + i\omega C_c, \quad (2.25)$$

where $(Z_0/2)^2 \ll 1/(\omega C_c)^2$ is assumed. The loaded resonator has the

⁷This discrepancy could be attributed to (i) a defect in the fabricated NbN current loop that locally decreases the critical current density, or (ii) geometry-dependent current-crowding effects. [47]

⁸A large number of wires presents a significant heat load for the cryocooler.

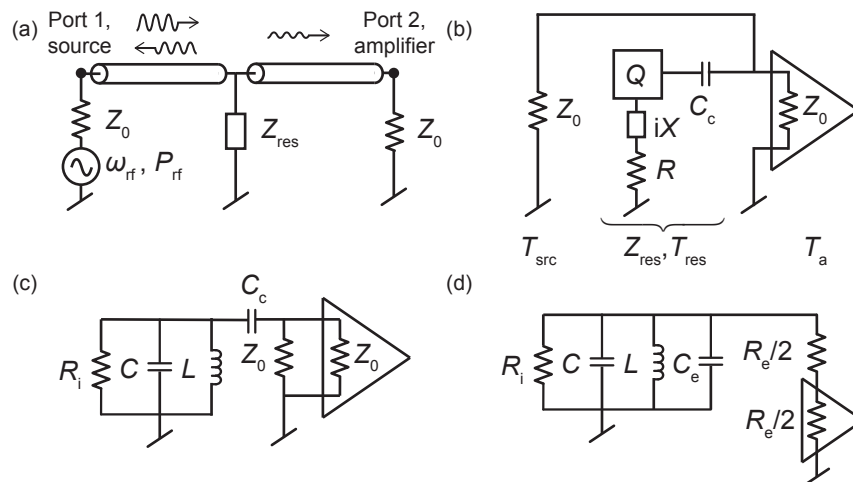


Figure 2.3: Circuit diagram of dispersive measurement. (a) An S-parameter measurement of a transmission line shunted by a resonator Z_{res} . S_{11} describes the relative amplitude and phase of a power wave reflected back to the source at port 1. S_{21} depicts transmission from port 1 to an amplifier at port 2. The RF environment has the characteristic impedance $Z_0 = 50 \Omega$. (b) An equivalent of (a) with the voltage generator idle, Z_{res} decomposed, and the amplifier explicitly drawn. The measured element $Z = R + iX$, $R \ll |X|$ is matched to Z_0 by a resonant matching network Q and a coupling capacitor C_c . The amplifier has an input noise temperature T_a , and the source (resonator) is at the physical temperature T_{src} (T_{res}). (c) Together Z and Q form a lumped element R_i - L - C resonator. (d) External loading by C_c and the transmission line is converted from a series to parallel impedance configuration to facilitate the analysis on the resonance.

eigenfrequency and total quality factor

$$\omega_r = \frac{1}{\sqrt{L(C + C_c)}} \quad (2.26)$$

$$\frac{1}{Q_t} = \left(\frac{1}{R_i} + \frac{1}{R_e(\omega_r)} \right) \sqrt{\frac{L}{C + C_c}} \equiv \frac{1}{Q_i} + \frac{1}{Q_e}. \quad (2.27)$$

Internal and external losses are described by the quality factors

$$Q_i = R_i \sqrt{(C + C_c)/L} \quad (2.28)$$

$$Q_e = 2(C + C_c)/(\omega_r Z_0 C_c^2), \quad (2.29)$$

respectively. Note that $R_e(\omega_r)$ has been calculated from Eq. (2.25).

To understand the transmission (S_{21}) measurement in Fig. 2.3a the shunt impedance is written near the resonance as

$$Z_{\text{res}} \approx \frac{Z_0 Q_e}{2Q_i} (1 + 2iQ_i(\omega - \omega_r)/\omega_r). \quad (2.30)$$

The S_{21} is the frequency response from a source to a preamplifier

$$S_{21} = \frac{2Z_{\text{res}}}{2Z_{\text{res}} + Z_0}. \quad (2.31)$$

Off the resonance $|S_{21}| \approx 1$ and the excitation signal travels basically unperturbed past the resonator. By contrast, on the resonance $S_{21}(\omega_r) = Q_t/Q_i < 1$. Some of the input power P_{rf} reflects back to the source, according to parameter S_{11} . To fulfil the power balance, the fraction of power dissipated in the shunt is considered:

$$P_{\text{rf}}(1 - |S_{21}|^2 - |S_{11}|^2) = \frac{2Q_t^2 P_{\text{rf}}}{Q_i Q_e} = \frac{\omega_r E_r}{Q_i} \equiv E_r \kappa_i, \quad (2.32)$$

This relation ties the measurement strength to the energy stored in the resonator E_r . The energy is expressed as the resonator voltage V_{rms} :

$$E_r = V_{\text{rms}}^2 (C + C_c). \quad (2.33)$$

Power at the preamplifier input is (see Fig. 2.3d)

$$\frac{V_{\text{rms}}^2}{2R_e(\omega_r)} = \frac{\omega_r E_r}{2Q_e} \equiv \frac{E_r \kappa_e}{2}. \quad (2.34)$$

The resonator linewidth resolvable in a transmission measurement is $\kappa = \kappa_i + \kappa_e$, the sum of the internal decay rate [see Eq. (2.32)] and the rate at which energy is exchanged with the environment. Measurement speed and bandwidth are related to the latter.

The effectiveness of the dispersive measurement relies on a high responsivity and a low noise level. The responsivity is understood as the

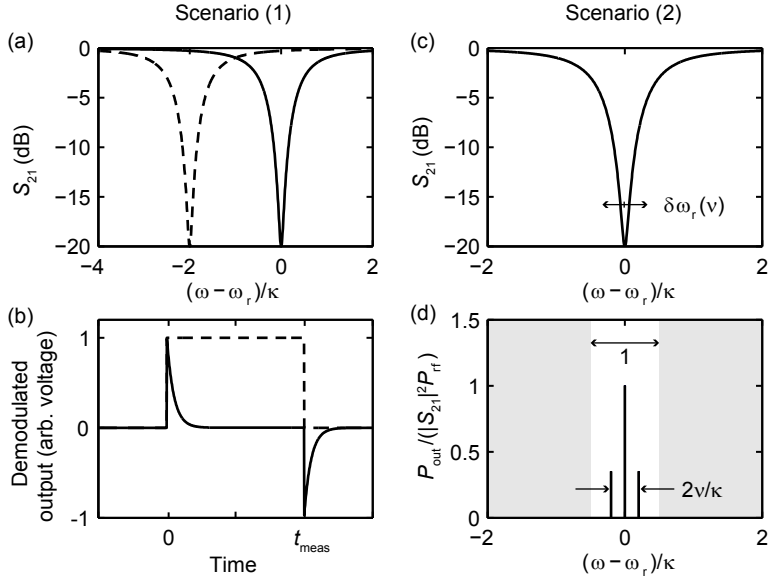


Figure 2.4: Dispersive measurement scenarios in frequency and time domain. The carrier at ω_r has the power P_{rf} , and noise is neglected for clarity. (a,b) An on-off measurement where the resonator eigenfrequency is either nominal (solid line) or clearly shifted (dashed line). The transmission spectrum (a) has distinct dips. The resonator position is resolvable in a demodulated time trace (b) where the measurement duration is t_{meas} . The solid trace in (b) has an exponential time constant $2/\kappa$. (c,d) A detector measurement where a weak sinusoidal modulation of the resonator eigenfrequency (c) generates information-carrying sidebands at $\omega_r \pm \nu$. The sidebands and the carrier are visible in the output power spectrum (d). In (d) the greyed region shows where the detected signal is low-pass filtered by the resonator. In (a) and (c) $Q_t/Q_i = 0.1$ is an arbitrary choice.

magnitude of an induced voltage change across the preamplifier input due to a change in Z . In this work two scenarios are relevant: (1) Z jumps by a discrete value and the eigenfrequency moves by κ or more (Fig. 2.4a,b). The measurement has an on-off character that emerges in a particular situation (discussed in Sect. 2.5.1). (2) The measurement is optimized to resolve small variations δZ that mainly translate into $\delta\omega_r \ll \kappa$ around the nominal ω_r (Fig. 2.4c,d). In both scenarios the noise is quantified by $k_B T_n$, power spectral density referred to the preamplifier input. An obvious contribution is noise added by the amplifier T_a (Chap. 2.3). Commercial cryogenic RF semiconductor amplifiers⁹ have $T_a < 10$ K. Reducing T_a to a sub-K level with a custom preamplifier has been one topic of this work (Chap. 3.1). A circulator [32, Chap. 9] in front of the preamplifier can improve impedance matching and protect the resonator from amplifier noise back-action.

Another term relevant for T_n is thermal noise from the source (and R_i) at physical temperature T_{src} (T_{res}). By noting how the thermal noise is coupled to the preamplifier at ω_r , a lower bound

$$T_n \geq T_a + \left(\frac{Q_t}{Q_i}\right)^2 \left(T_{\text{src}} + \frac{2Q_i}{Q_e} T_{\text{res}}\right) \quad (2.35)$$

can be written. The source line from room temperature is cryo-attenuated to obtain T_{src} equal to the lowest physical temperature¹⁰. Besides T_a , T_{src} and T_{res} any excess noise mechanisms, perhaps intrinsic to the measured element Z , should be included in T_n . One example is generation-recombination noise following a Lorentzian spectrum [16].

Responsivity and noise are combined to analyse the measurement fidelity. In essence, a high fidelity means a short integration time to resolve a signal from the noise. In the on-off scenario (1) a signal-to-noise ratio (SNR) of unity is achieved by integrating over a measurement time

$$t_{\text{meas}} = \frac{2k_B T_n}{E_r \kappa_e}, \quad (2.36)$$

see Fig. 2.4b. In the detector scenario (2) the impedance variation is caused by an external parameter q . The fidelity is described by the smallest resolvable signal amplitude q_{rms} of an oscillation at angular frequency ν . A 1 Hz detection bandwidth and SNR = 1 are assumed. When interrogating the resonator with an RF tone ω_{rf} , the q -oscillation creates sidebands $\omega_{\text{rf}} \pm \nu$ around the carrier (Fig. 2.4d). Their strength is maximal if the carrier is aligned with the nominal eigenfrequency ω_r . Unless stated otherwise, perfect alignment is assumed throughout this work.

To extract q_{rms} , the RF signal from the detector is amplified and demodulated. In a demodulated linear picture, signal voltage amplitude at ν is

⁹Cryogenic semiconductor amplifiers are often based on high-electron-mobility transistors (see, e.g., the products of Low Noise Factory, Sweden).

¹⁰In the quantum regime $T_{\text{src}} = \hbar\omega_r/(2k_B)$; the same applies to T_{res} .

proportional to

$$\sqrt{Z_0 P_{\text{rf}}} \frac{\partial S_{21}}{\partial q} q_{\text{rms}} = \sqrt{Z_0 P_{\text{rf}}} \left(\text{Re} \left\{ \frac{\partial S_{21}}{\partial q} \right\} + i \text{Im} \left\{ \frac{\partial S_{21}}{\partial q} \right\} \right) q_{\text{rms}}, \quad (2.37)$$

where S_{21} is given by Eq. (2.31). The in-phase quadrature [real part of Eq. (2.37)] responds to changes in the quality factor. The out-of-phase quadrature (imaginary part) responds to changes in the eigenfrequency. The latter effect is typically more prevalent. However, the validity of Eq. (2.37) is compromised at large ν and/or q_{rms} . On one hand, when ν exceeds the resonance linewidth κ information in the sidebands is filtered: the -3 dB low-pass corner is $\nu_c = \kappa/2$. On the other hand, large q_{rms} beyond the dynamic range of the sensor breaks the linear description of the system. This is witnessed as a constant downward shift in ω_r and extra sidebands (e.g., $\omega_{\text{rf}} \pm 2\nu$). Relating the ideal signal in Eq. (2.37) to noise and integration time yields

$$q_{\text{rms}}^2 = \frac{2k_B T_n}{t_{\text{meas}} E_r (\kappa^2 / \kappa_e) |\partial S_{21} / \partial q|^2} \quad (2.38)$$

where $t_{\text{meas}} = 0.5$ s corresponds to Nyquist sampled 1 Hz.

Both measurement scenarios [Eqs. (2.36) and (2.38)] would improve if the resonator was coupled more strongly to the feedline, or excited with higher RF power. However, there are trade-offs ranging from the onset of non-linear behaviour to protecting the quantum nature of the measured element. These are discussed in the context of individual applications.

Frequency division multiplexing

An advantage of dispersive measurement is that multiple resonators with different eigenfrequencies can be coupled to the same feedline (Fig. 2.5). With a frequency separation larger than the linewidth there is little cross-talk between the measured resonators. In principle, all resonators can be read out simultaneously by frequency comb excitation. The number of multiplexable resonators is restricted by preamplifier bandwidth (and possibly that of the optional circulator).

2.5. Quantum elements

2.5.1. Quantum bit

This chapter discusses the fundamentals of a quantum bit (qubit), a well-defined pair of energy levels. Many quantum systems, such as atoms and ions, have a discrete multi-level spectrum E_m , and the qubit is usually formed from the two lowest-energy levels. If the corresponding transition energy $E_{01} = E_1 - E_0$ is well above the thermal energy $k_B T$ the qubit can be passively initialized to ground state with high probability. Passive means waiting a time much longer than the energy relaxation time constant

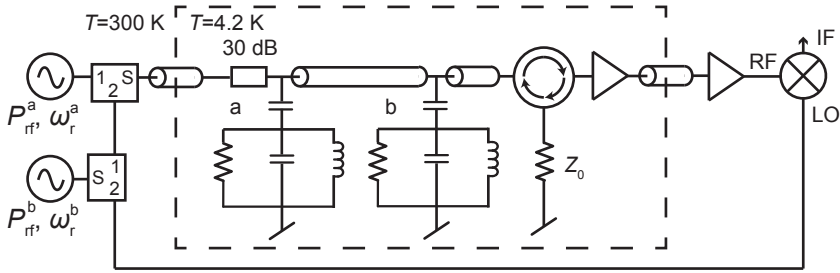


Figure 2.5: Frequency multiplexed dispersive measurement. Two resonators are simultaneously read out by sending tones down the feedline at their nominal eigenfrequencies ω_r^a, ω_r^b . In this example, the local oscillator (LO) of a demodulating mixer is a copy of one carrier. Intermediate frequencies (IF) are 0 Hz and $|\omega_r^a - \omega_r^b|/(2\pi)$. Source noise from room temperature is attenuated by a factor at least as large as the temperature ratio. A circulator in front of a cold preamplifier does impedance matching and suppresses amplifier back-action. Power splitters/combiners [32, Chap. 7] have a sum port (S) and two equivalent ports 1, 2.

T_1 , which is discussed later in the context of decoherence. The qubit is addressed by a drive at the transition frequency $\omega_{01} = E_{01}/\hbar$, and it can interact with other quantum elements near this frequency. Realizable in a superconducting system, millikelvin temperatures allow tuning the transition frequency to $\omega_{01}/(2\pi) = 4 - 8$ GHz range, which is popular due to the availability of off-the-shelf microwave hardware, while keeping the thermal excitations at an acceptable level.

The qubit transition energy must also be unique so that qubit control does not drive any other transitions of the system, causing leakage out of the computational subspace. A quantized harmonic oscillator at angular frequency ω_r , a superconducting LC circuit for instance, does not satisfy this criterion due to its equal spacing of energy levels $\hbar\omega_r$ (Fig. 2.6a). The spectrum must possess a sufficient degree of anharmonicity

$$\alpha_q = (E_{12} - E_{01})/\hbar \quad (2.39)$$

which describes the frequency offset to the nearest leakage transition $E_{12} = \hbar\omega_{12}$. To this end, some superconducting qubits harness non-linear Josephson inductance (Sect. 2.1.3) to make the level spacing of an LC oscillator unequal (Fig. 2.6b). The anharmonicity limits the speed of qubit control: minimal duration of a control waveform at ω_{01} is $2\pi/|\alpha_q|$ to avoid significant spectral weight at ω_{12} .

Ideally, a large number of control operations (also called gates or unitaries) should fit within the qubit coherence time. Borrowing from nuclear magnetic resonance (NMR) terminology [48], the coherence is measured

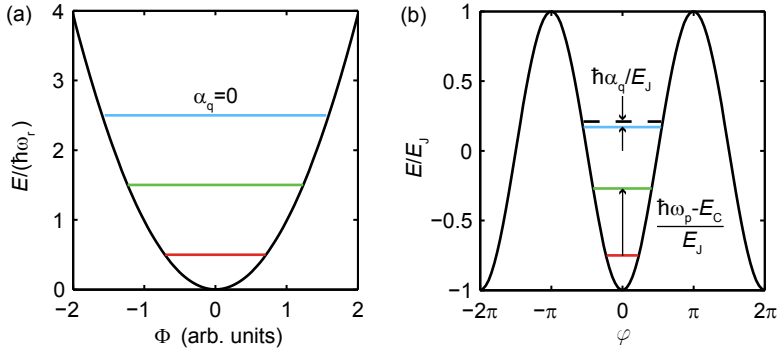


Figure 2.6: Potential landscape and the three lowest-energy levels of superconducting quantum elements. (a) A quantum LC oscillator with the potential $\propto \Phi^2$, squared flux in the inductor. Energy level spacing is $\hbar\omega_r$, one quantum at oscillator eigenfrequency. (b) A transmon qubit in a Josephson cosine potential at $E_J/E_C = 30$, $n_g = 1/2$ (see the main text for definitions). The weak anharmonicity from the Josephson effect is calculated by subtracting $2E_1 - E_0$ (dashed line) from E_2 (blue). The sensitivity to the charge offset is described by the probability of tunnelling to adjacent cosine wells. The probability decays exponentially with E_J/E_C . At the same time, the transmon anharmonicity weakens according to a power law $|\alpha_q/\omega_{01}| \propto (8E_J/E_C)^{-1/2}$.

with the relaxation time T_1 (time for random decay of the excited state) and the dephasing time $T_2 \leq 2T_1$ (time until the phase of the quantum state has randomized). Even though physical qubits are always imperfect, many of them could be wired to an error-detecting and -correcting network that protects quantum data longer than the lifetime of its individual components [6, 49, 50, 51]. Here, the fault tolerance threshold is $\simeq 99\%$ fidelity for local operations on physical qubits [52]. The superconducting transmon qubit has recently reached this threshold [53]. As the transmon has been studied in Publication V, its history and properties are reviewed next.

Cooper pair box

Without Josephson tunnelling there would be no superconducting qubits [54, 7]. The Josephson junction can be pushed to a quantized charge regime by miniaturizing its dimensions. Here, as opposed to Sect. 2.2.1, single-Cooper-pair charging effects are relevant. The number of Cooper pairs n and the junction phase φ form a quantum conjugate pair of variables. To generate an isolated quantum object with a discrete energy spectrum, one or multiple junctions are reactively shunted. In this kind of an "artificial atom", the qubit transition frequency is by design in the microwave domain. The shunt of this work is a capacitor, and the corresponding device is called a Cooper pair box (CPB).

The concept of the CPB is as simple as two superconducting islands connected with a JJ or a SQUID. Electrostatic coupling between the islands determines a capacitance C parallel to the junction capacitance. The CPB interacts with its environment through a gate capacitor C_g . The use of the SQUID, which is assumed in the following¹¹, brings additional controllability at the expense of sensitivity to magnetic flux noise (Fig. 2.7a). The single-electron charging energy of the CPB is defined as $E_C = e^2/(2C_\Sigma)$, where the sum of capacitances is $C_\Sigma = C + 2C_J + C_g$. The CPB Hamiltonian

$$\hat{H}_{\text{CPB}} = 4E_C(\hat{n} - n_g)^2 - E_J \cos \hat{\varphi} \quad (2.40)$$

also contains the Josephson energy associated with Cooper pair tunnelling across the JJs, $E_J = \Phi_0 I_c |\cos(\pi \Phi_a / \Phi_0)| / \pi$. The operator \hat{n} is the number of coherently transferred Cooper pairs. Offset n_g (in multiples of $2e$) is induced by the gate voltage across C_g and fluctuations in the background charge that typically follow a $1/f$ spectrum. To avoid thermal excitations at energy scale $k_B T$, E_C (E_J) is made (kept) large by shrinking C_Σ (controlling the magnitude of I_c)

In the first CPB qubits, the relative strength of the energies was $E_J/E_C \simeq 1$. The offset charge modulates the CPB energy spectrum (eigenvalues of \hat{H}_{CPB}), an effect called charge dispersion. An offset $n_g = 1/2$ constitutes a charge insensitive point [55], which is typically adopted for experiments.

¹¹The single-junction CPB can be recovered with $C_J \mapsto C_J/2$, $I_c \mapsto I_c/2$, and $\Phi_a = 0$.

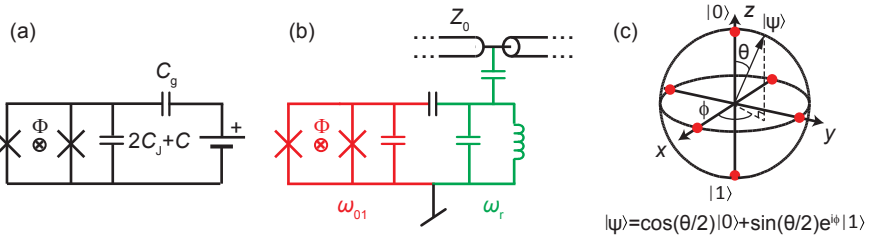


Figure 2.7: (a) Cooper pair box, a quantum element controllable with gate voltage and magnetic flux. (b) Qubit-cavity system. The readout resonator takes a lumped element representation near ω_r . (c) Bloch sphere. Pure quantum states $|\psi\rangle$ are specified by coordinates (ϕ, θ) on the surface of a unit sphere. Six cardinal states are visualized in red. North and south poles correspond to ground and excited state, respectively. Equally weighted quantum superpositions are on the equator.

The corresponding transition energy from the ground to excited state is

$$E_{01} = \sqrt{[4E_C(2n_g - 1)]^2 + E_J^2}, \quad (2.41)$$

tunable by small variations in n_g or by the flux-dependent $E_J(\Phi_a)$. There is enough anharmonicity to operate the CPB as a qubit: in the small- E_J/E_C limit it scales as $\hbar\alpha_q \approx 9E_{01}(E_J/E_C)^{-1} \gg E_{01}$ [13]. The eigenstates of the $n_g = 1/2$ qubit are superpositions of charge states with zero or one excess Cooper pairs in the box.

Transmon

The main drawback of the CPB is its sensitivity to charge fluctuations, which limits the coherence time to $< 1 \mu\text{s}$ [56]. A transmon qubit overcoming this limitation has evolved from the CPB [13, 57]. The transmon has a considerably higher $E_J/E_C \simeq 20 - 100$ achieved, e.g., by enlarging the shunt capacitance C , which lowers the charging energy. In this regime, the charge dispersion is exponentially suppressed as $\exp(-\sqrt{8E_J/E_C})$, and the CPB eigenstates distribute over a broad range of charge states. The vanishing charge dispersion eliminates the need for the gate bias and improves the coherence thanks to insensitivity to background charge fluctuations. The coherence times of transmons hosted by a circuit quantum electrodynamics platform (Sect. 2.5.2) routinely exceed $10 \mu\text{s}$ nowadays [53], enough for coherent protocols consisting of sequential single- and multi-qubit gates (with gate times typically measuring tens of nanoseconds). Theoretically, the transmon should reach the no-pure-dephasing limit of coherence $T_2 = 2T_1$.

The drawback of moving from small E_J/E_C to the transmon regime is reduced anharmonicity. Calculated from the transition energies in large-

E_J/E_C limit

$$E_{ij} \approx \sqrt{8E_C E_J}(j-i) - E_C[j(j+1) - i(i+1)]/2, \quad (2.42)$$

α_q is only of the order of $-E_C/\hbar$ ($|\alpha_q/\omega_{01}| \simeq 4 - 10\%$, see Fig. 2.6b). $\sqrt{8E_C E_J}$ is equivalent to $\hbar\omega_p$, the quantum of Josephson plasma oscillation, in Eq. (2.42). This gives the transmon its longer name: transmission line shunted plasma oscillation qubit. The flux tunable plasma frequency ($\propto \sqrt{|\cos(\pi\Phi_a/\Phi_0)|}$) sets the order of magnitude of ω_{01} . Transmission line is included in the name due to the similar geometry of an interdigital C and a twin-lead transmission line in the first proposal [13].

The origin of the non-vanishing transmon anharmonicity can be understood from the small- φ expansion of the Josephson potential $E_J \cos \varphi \approx E_J(1 - \varphi^2/2 + \varphi^4/24)$ in Eq. (2.40), valid at high E_J/E_C . This gives a harmonic oscillator Hamiltonian with a small Duffing nonlinearity (the φ^4 term) from the Josephson effect. The eigenstates of the Hamiltonian show a weakly anharmonic spectrum [Eq. (2.42)]. The nearby third energy level above the qubit subspace is not entirely useless. It has found use in, e.g., multi-qubit operations [58, 59].

2.5.2. Circuit quantum electrodynamics

Introduction

What kind of platform turns the superconducting qubit into a practical quantum element that can be isolated, controlled, and read out? Circuit quantum electrodynamics (cQED) is a popular architecture that borrows many concepts from cavity quantum electrodynamics, where real atoms couple strongly to photons in an optical cavity [60]. In cQED, superconducting qubits are artificial atoms, and the photons are at microwave frequencies. The dimensionality of the cavity divides cQED into two categories: 2D [61] and 3D [62]. In 2D cQED the cavity is a superconducting microresonator that capacitively couples to a qubit and a microwave feedline. All elements are planar and fabricated on a small-scale electrical chip. This includes flux bias lines for qubit frequency tuning. By contrast, 3D cQED works with three-dimensional cavities. The qubit on a chip is positioned at an electric field node of a selected resonant mode, and its dipole moment establishes the interaction with the cavity. The 2D architecture was employed in this work (Fig. 2.8).

The cavity is an impedance matching network separating the qubit from the noisy $50\ \Omega$ microwave environment (Fig. 2.7b). In electrical terms, it is the real part of the environmental impedance which provides a relaxation channel for the qubit, leading to decoherence. When the qubit and the cavity are sufficiently detuned, the outside world is filtered by a factor of $g^2/(\omega_r - \omega_{01})^2 \ll 1$ where g is the qubit-cavity interaction strength (vacuum Rabi frequency of coherent interaction with a single photon). This is the

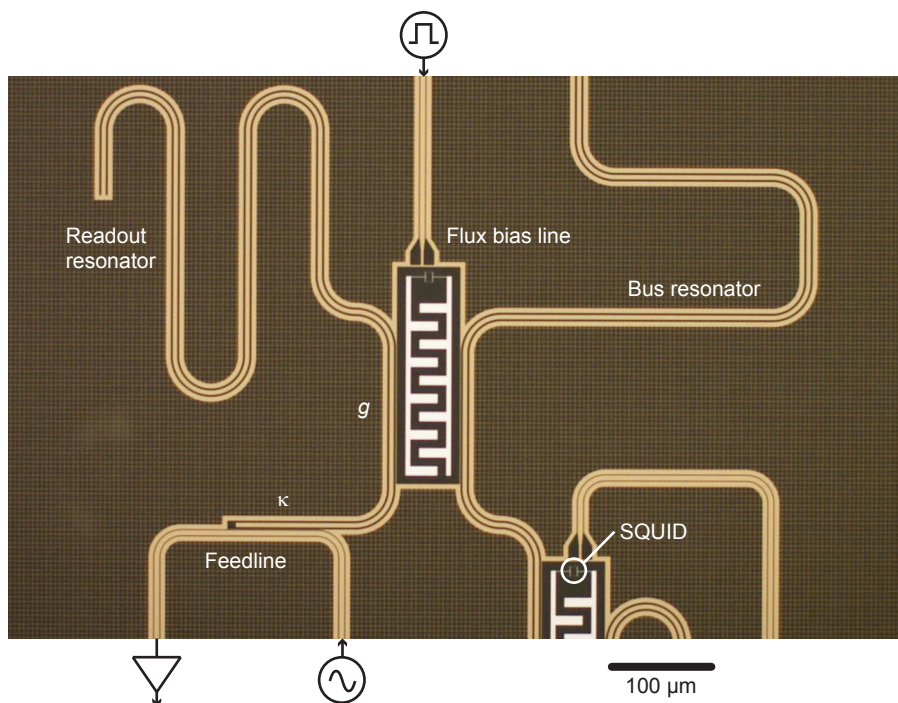


Figure 2.8: Elements of a 2D cQED quantum processor. The device is the same as in Publication V. The substrate is a C-plane sapphire wafer. Transmon qubits (Al, grey) consist of interdigitated electrodes connected by a SQUID. Flux bias lines shorted near the SQUID loop control the transmon frequency by modulating the Josephson energy (z control). Readout near ω_r and xy control at ω_{01} are coupled from the microwave feedline to the qubit through a cavity (a quarter-wavelength transmission line resonator). Multi-qubit operations mediated by a bus resonator have not been conducted in this work. Resonators, control lines and the perforated ground plane are thin-film NbTiN whose kinetic inductance is taken into account. Optical micrograph by Alessandro Bruno, Delft University of Technology.

dispersive regime of cQED. The opposite resonant regime, where the qubit and single-photon states can be exchanged back and forth, is important for local multi-qubit operations [63, 64], which have not been implemented in this thesis. To be detectable, the qubit-cavity interaction has to be strong in comparison with the decay rates of the cavity ($g \gg \kappa$) and the qubit ($g \gg \gamma$). In the first cQED demonstration of the strong dispersive regime, a conventional CPB was coupled to a full-wavelength coplanar waveguide resonator [65].

Readout

Qubit readout is mediated by microwave photons sent to populate the cavity. Multi-qubit 2D processors have evolved from a single-cavity approach [63] to a system with dedicated, frequency multiplexed readout resonators for each qubit [66]. In the dispersive limit the frequencies of the interacting qubit and cavity renormalize by small Lamb shifts [67] (in this work by factors -5×10^{-4} and 3×10^{-4} , respectively) and the system's effective Hamiltonian is of the Jaynes-Cummings [13, 68] form

$$\hat{H}_{J-C} = -\frac{\hbar\omega_{01}}{2}\hat{\sigma}_z + (\hbar\omega_r - \hbar\chi\hat{\sigma}_z)\hat{a}^\dagger\hat{a}. \quad (2.43)$$

Here, $\hat{\sigma}_z$ is the Pauli Z -operator whose expectation value is the outcome of a qubit measurement: $\langle\hat{\sigma}_z\rangle = \pm 1$ for the qubit in ground (excited) state. The operator \hat{a}^\dagger creates and \hat{a} annihilates one cavity photon. $\hat{a}^\dagger\hat{a}$ is called the number operator whose expectation value is $\langle n_{\text{ph}} \rangle$, the mean occupation of the cavity. The qubit-cavity dispersive shift 2χ plays a major role. First, regrouping from the qubit's point of view gives $-\hbar\hat{\sigma}_z(\omega_{01} + 2\chi\hat{a}^\dagger\hat{a})/2$. This is the ac Stark effect where the qubit frequency shifts by $2\chi\langle n_{\text{ph}} \rangle$. Second, in $\hbar(\omega_r - \chi\hat{\sigma}_z)\hat{a}^\dagger\hat{a}$ the resonator frequency experiences a $\mp\chi$ shift depending on the qubit state (ground or excited). This is understood as the development of an intra-cavity coherent state of photons entangled with the qubit. The qubit state can thus be resolved in a microwave transmission measurement near ω_r with high contrast if $|2\chi| > \kappa$ (the on-off dispersive measurement of Sect. 2.4.2). To stay in the linear regime of the Jaynes-Cummings interaction the readout has to be relatively weak, keeping the photon number below a critical value $\langle n_{\text{ph}} \rangle_{\text{crit}} = (\omega_{01} - \omega_r)^2/(4g^2)$ [61] ($\sim 300 - 500$ in this work)¹². This explains the value of the ultralow-noise microwave amplifier in the cQED setup.

Control

The simplest form of coherent qubit control in cQED is a Rabi oscillation induced by microwaves resonant with ω_{01} . In a multi-qubit setting these

¹²High P_{rf} may induce state transitions, so the measurement is no longer quantum non-demolition.

tones also couple off-resonantly to other qubits, causing unwanted effects. Cross-talk can be minimized by using dedicated control lines coupling to single qubits, but at the price of a high number of wires. From the scalability point of view, it is more straightforward to send control tones along the common feedline installed above for readout purposes. However, cross-talk cannot be avoided, since the control reaches all qubits through the readout resonators. A topic of this work has been the mitigation of control errors in this situation by microwave pulse shaping. This section proceeds in the following order. Firstly, design and calibration of the single-qubit control are discussed. Secondly, the unwanted effects are identified with the help of a two-transmon Hamiltonian. Finally, optimal control methods avoiding these effects are introduced.

With a decent qubit readout in place, there is visibility for observing the sinusoidal Rabi oscillations between the ground ($|0\rangle$) and excited ($|1\rangle$) states, say, as a function of the amplitude of a fixed-duration microwave pulse at ω_{01} . The primitives of single-qubit control are "truncated" Rabi oscillations realizing, e.g., unitary $\pi/2$ and π rotations around x and y axes. The axes refer to the Bloch sphere [5] visualization of quantum states (Fig. 2.7c). The rotation angle comes from the time integral of the control envelope, and the axis from the phase relative to the microwave carrier. The optimization of the rotations in a multi-qubit processor is initially done for each qubit separately, without concern for the possible effects inflicted on others. In this work, this has been accomplished by running an "AIXY" sequence [69, Chap. 5] where a qubit is measured after 21 different pairs of applied unitaries. The outcome shows a distinct footprint for various error types such as a detuning from ω_{01} , or over-/under-rotations. In this way, the calibration is measurement based and the imperfections of the control hardware, e.g., finite bandwidth, do not have to be characterized in fine detail.

As noted in Sect. 2.5.1, the error budget of the single-qubit control consists of decoherence and leakage, factors which are balanced by varying the control pulse duration. The leakage implies population transfer to $|2\rangle$, the second excited state. Pulse spectral bandwidth is typically reduced by selecting a Gaussian envelope $\propto \exp(-(t-t_0)^2/2\sigma_q^2)$ with t_0 the centre and σ_q the standard deviation¹³. The control is on during $t \in [t_0 - t_g/2, t_0 + t_g/2]$, with t_g the gate time. To identify control errors, a system Hamiltonian including the control is written for two transmons Q_a and Q_b in a frame rotating with angular frequency ω_{01}^a [12]. The Hamiltonian is truncated at the third

¹³Fourier transforming this Gaussian yields a Gaussian $\propto \exp(-(\omega - \omega_{01})^2\sigma_q^2/2)$ in the frequency domain; note that the role of the standard deviation has inverted.

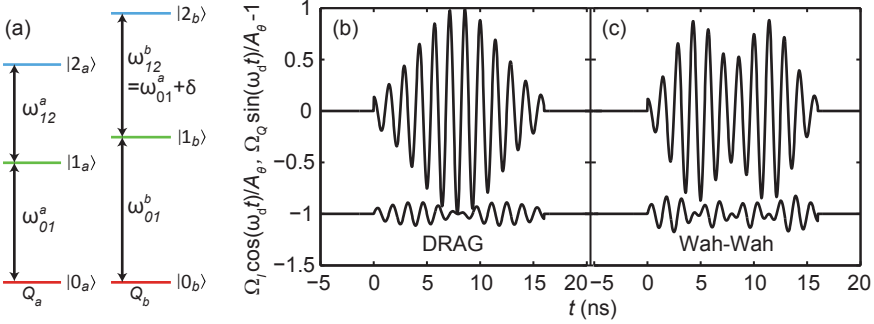


Figure 2.9: (a) Level diagram for transmons Q_a, Q_b (not to scale). A control addressing $|0_a\rangle \leftrightarrow |1_a\rangle$ may drive the internal (and external) leakage transition ω_{12}^a (ω_{12}^b). (b,c) Q_a control pulses at $t_g = 16$ ns, $\sigma_q = t_g/4$ (microwave carrier ω_d not to scale). The out-of-phase quadrature is offset for clarity. The DRAG pulse in (b) suppresses leakage to $|2_a\rangle$. As an improvement over DRAG, the sideband modulated Wah-Wah pulse in (c) does not induce any net leakage from $|1_b\rangle$ to $|2_b\rangle$ either. The choice of the DRAG and Wah-Wah parameters $\beta = 0.75$ ns, $A_m = 0.7$, and $\omega_m/(2\pi) = 100$ MHz is illustrative. The envelopes are cut at $t = 0, t_g$ to avoid the infinitely long tails of the Gaussian.

energy level and the rotating wave approximation is employed:

$$\begin{aligned}
 \hat{H}_{\text{control}}/\hbar &= \alpha_{q,a} \hat{\Pi}_2^a + (\delta - \alpha_{q,b}) \hat{\Pi}_1^b + (2\delta - \alpha_{q,b}) \hat{\Pi}_2^b \\
 &+ \frac{\Omega_I(t)}{2} [\lambda_1^a \hat{\sigma}_{x,1}^a + \lambda_1^b \hat{\sigma}_{x,1}^b + \lambda_2^a \hat{\sigma}_{x,2}^a + \lambda_2^b \hat{\sigma}_{x,2}^b] \\
 &+ \frac{\Omega_Q(t)}{2} [\lambda_1^a \hat{\sigma}_{y,1}^a + \lambda_1^b \hat{\sigma}_{y,1}^b + \lambda_2^a \hat{\sigma}_{y,2}^a + \lambda_2^b \hat{\sigma}_{y,2}^b].
 \end{aligned} \tag{2.44}$$

The anharmonicities are $\alpha_{q,k} = \omega_{12}^k - \omega_{01}^k$, $k \in \{a, b\}$. The projection operators are $\hat{\Pi}_l^k = |l_k\rangle \langle l_k|$, and the Pauli X and Y operators are $\sigma_{x,l}^k = |l_k\rangle \langle l-1_k| + |l-1_k\rangle \langle l_k|$ and $\sigma_{y,l}^k = i |l_k\rangle \langle l-1_k| - i |l-1_k\rangle \langle l_k|$. $\Omega_I(t)$ and $\Omega_Q(t)$ are the in- and out-of-phase pulse envelopes of a drive centred at ω_{01}^a , and λ_l^k is the coupling strength of this drive to the $|l-1_k\rangle \leftrightarrow |l_k\rangle$ transition. In the dispersive regime of cQED the driving can be treated separately from the readout [the Jaynes-Cummings Hamiltonian in Eq. (2.43)], but the filtering effect of the cavities is contained in the coefficients λ_l^k . Finally, $\delta = \omega_{12}^b - \omega_{01}^a$ is a parameter whose smallness describes susceptibility to leakage in Q_b when controlling Q_a (Fig. 2.9a).

The simple Gaussian envelope for an x -rotation by θ enters \hat{H}_{control} as $\Omega_I = A_\theta \exp(-(t-t_0)^2/2\sigma_q^2)$, $\Omega_Q = 0$. In principle, inserting a zero-average envelope to Ω_Q will not affect the rotation angle or axis. The unwanted transitions driven by the Q_a control in the Hamiltonian [Eq. (2.44)] are explained

next in detail. (I) At an offset $\alpha_{q,a}$ there is *internal* leakage to $|2_a\rangle$. (II) At a large offset $\omega_{01}^b - \omega_{01}^a = \delta - \alpha_{q,b}$ the subspace $|0_b\rangle \leftrightarrow |1_b\rangle$ is driven. (III) At an offset δ there is *external* leakage to $|2_b\rangle$ which can be the most relevant of these three if $|\delta| < |\alpha_{q,a}|$.

A DRAG¹⁴ pulse shaping technique addressing the internal leakage problem (I) has been developed in Ref. [14] and demonstrated in Refs. [70, 71]. The out-of-phase quadrature is $\Omega_Q = \beta \partial \Omega_I / \partial t$ while Ω_I is the plain Gaussian to the first order [72] (Fig. 2.9b). β is the DRAG coefficient, theoretically

$$\beta = \frac{(\lambda_2/\lambda_1)^2}{4\alpha_q}. \quad (2.45)$$

In practice, β is optimized by running the "AllXY" measurement. In one of the first demonstrations that compared an optimal DRAG pulse to the unshaped Gaussian pulse [71], DRAG reduced the error per gate by a factor of 15 at $\sigma_q = 4$ ns, the shortest gate width attainable with the used experimental instrumentation. The speed improvement of decoherence-limited control was ~ 3 in that particular experiment.

In a two-qubit system where the external Q_b leakage (III) comes into play, DRAG could be retuned to avoid either internal or external leakage, but not both at the same time. This is a serious limitation, but the next generation of pulse shaping has suggested a sideband modulation of the Ω_I Gaussian together with $\Omega_Q = \beta \partial \Omega_I / \partial t$ (as in DRAG) to avoid leakage in both qubits simultaneously [12]. The new technique nicknamed Wah-Wah (weak anharmonicity with average Hamiltonian) was experimentally tested in this work (Chap. 3.3). Wah-Wah control envelopes for a gate $0 \leq t \leq t_g$ are

$$\Omega_I(t) = A_\theta e^{-(t - \frac{t_g}{2})^2 / (2\sigma_q^2)} \left[1 - A_m \cos \left(\omega_m \left(t - \frac{t_g}{2} \right) \right) \right] \quad (2.46)$$

$$\Omega_Q(t) = \beta \partial \Omega_I / \partial t, \quad (2.47)$$

with the sideband modulation frequency ω_m and amplitude A_m (Fig. 2.9c). Again, the pulse parameters A_m, ω_m can be derived from theory, but they are optimized in practice with an iterative procedure.

¹⁴DRAG stands for derivative removal by adiabatic gate.

3. Results

This is an overview of Publications I-V. Results from Publications I and II demonstrating the single junction amplifier are presented in Chap. 3.1. Kinetic inductance devices are discussed next. The bolometer of Publication III and the magnetometer of Publication IV are in Sects. 3.2.1 and 3.2.2, respectively. Finally, work on quantum bits (Publication V) is described in Chap. 3.3.

3.1. Radio-frequency Josephson amplifier

Ultralow-noise Josephson microwave amplifiers are often used to improve the readout fidelity of qubits [73, 74]. Other low-temperature setups would also benefit from an SNR improvement: one example is sensing the motion of a nanoelectromechanical resonator [75]. This chapter gives an overview of SJA (Sect. 2.2.1), whose performance is compared to traditional JPA (Chap. 2.3) which similarly has a resonant feature that narrows bandwidth. An essential difference between the two devices is centre frequency of gain, which is fixed in SJA but flux tunable in JPA.

3.1.1. Operating principle

The SJA has three building blocks: (i) a Josephson junction dc biased to finite voltage state, (ii) a bandstop filter from a resonant RLC shunt tuned to microwave frequency (3 GHz in this work), and (iii) a matching network to Z_0 environment. There are three separate frequency bands of amplifier dynamics: dc, filter stopband $\omega_{\text{rf}} \approx 1/\sqrt{LC}$, and ω_J (in rising order). Josephson phase dynamics [Eqs. (2.1)-(2.2)] mixes the low and high frequency signals, and creates sidebands such as $\omega_J \pm \omega_{\text{rf}}$ across the Josephson frequency. The junction and the shunt are on the same microchip (Fig. 3.1a,b). Since the LC part of the shunt is an electrical short at low and high frequencies, Josephson phase dynamics yields an IV curve from the standard RCSJ model [Eq. (2.6), Fig. 3.1c,d]. Hence, the junction exhibits negative differential resistance R_d that is damped by R (as in RCSJ) at all frequencies outside the filter stopband. Being damped at a specific frequency means that the resistive part of overall system impedance is positive.

3.1. Radio-frequency Josephson amplifier

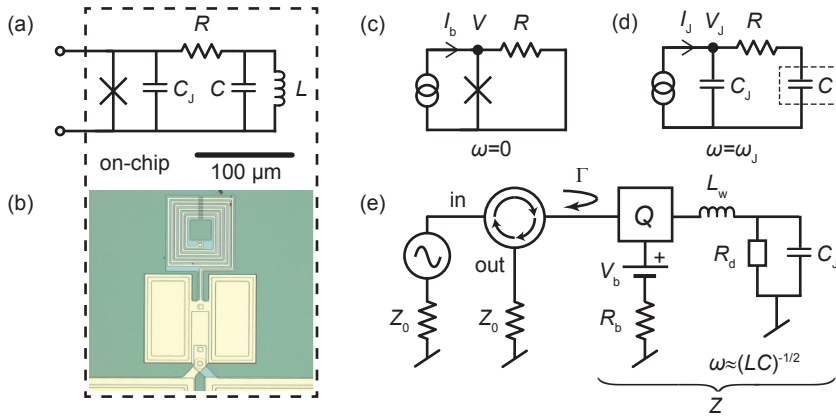


Figure 3.1: Single junction amplifier. (a) A Josephson junction (Nb-Al/AIO_x-Nb) and a bandstop shunt on a microchip. (b) In a corresponding optical micrograph (Pasi Lähteenmäki, Aalto University) a Nb spiral inductor $L \simeq 0.7$ nH and parallel-plate capacitors $C \simeq 4$ pF are identifiable. The JJ is the dot nearest to the bondpads at the bottom. (c-e) Circuit diagrams for three frequency bands. Amplifier dynamics is governed by non-overlapping dc (c), signal (e), and Josephson frequency bands (d) (in rising order). A static bias current $|I_b| > I_c$ lifts the junction to the finite voltage state in (c). The IV curve is non-hysteretic since $\beta_c \simeq 0.3$. Josephson oscillations I_J, V_J arise in (d) where a large C may be dropped out of the picture. Near the shunt eigenfrequency the junction is replaced with a negative differential resistance R_d in (e). A matching network Q not only transforms R_d into Z close to $-Z_0$, which provides gain in reflection, but also isolates a dc supply $V_b \approx R_b I_b$ from the RF circuit. Bondwires to the chip have a total inductance of L_w .

On the relatively narrow stopband the negative resistance is visible to off-chip elements. The microwave environment provides additional damping to keep the system stable. The chip is connected to external RF and dc lines through a reactive matching network (Fig. 3.1e) whose simplest form is a standard bias-T (as in Publication I). The network transforms R_d into Z , which is close to $-Z_0$. This provides gain for signals reflected from the SJA, as noted from the definition of the reflection coefficient [32, Chap. 2]

$$\Gamma = \frac{Z - Z_0}{Z + Z_0}. \quad (3.1)$$

Z is the impedance looking out of a circulator into the SJA (Fig. 3.1e). The power gain of the SJA is $G_a = |\Gamma|^2$. The matching network also isolates the dc supply for junction biasing from the RF circuit.

3.1.2. Characterization

Linear SJA operation requires a stable bias point $I_b > I_c$, which is found by output RF spectroscopy (Fig. 2 in Publication I). During an I_b sweep various branches of amplifier dynamics are identified. Impedance mismatch or saturation give a faint response or no features above system noise floor. Instability (insufficient damping of R_d at low I_b) is witnessed as deterministic ringing with multiple harmonics. In contrast, a stable impedance matched bias point amplifies input noise without generation of harmonics. Hence, the output spectrum shows near the LC eigenfrequency a single peak whose shape resembles that of power gain.

This section proceeds with a summary of results from Publications I-II. Amplifier noise temperature as a main topic of Publication I is discussed first. Secondly, gain-bandwidth product and dynamic range from both publications are presented.

Publication I: noise

Noise added by the SJA originates from the shunt resistor [$R \simeq 4 \Omega$ in Eq. (2.7)]. Noise at signal frequency (direct noise) is blocked by the band-stop filter, but noise on the Josephson band is mixed down by the non-linear dynamics and reaches the output. The lowest measured SJA noise at 70 mK base temperature was $1.6\hbar\omega$, about three times the quantum limit. Unexpectedly, this occurred at $I_b = 8.2I_c$ ($I_c \simeq 17 \mu\text{A}$) where a simple noise model (see the Supplement of Publication I) predicts 17 added quanta (approximately linear growth of noise spectral density with I_b). A "self-organizing" mechanism was proposed to explain this discrepancy (Fig. 3.2). Noise processes alter the Josephson phase dynamics in a way that compresses noise at output without an equal degradation of gain for the useful signal. The compression requires a high I_b and gain in excess of ~ 20 dB

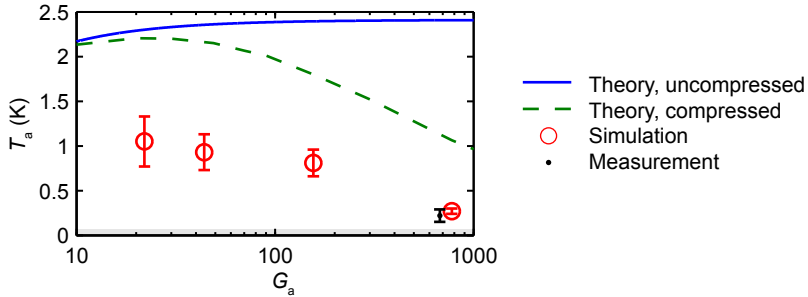


Figure 3.2: Noise compression as a function of SJA gain (Publication I). SJA input noise temperature $T_a = 220 \pm 70$ mK (black) was measured with a SNR improvement technique [8, 10]. The quantum limit at the operating frequency $\omega_{\text{rf}}/(2\pi) \approx 2.9$ GHz is $T_a = 70$ mK (grey). At high gain, noise from simple theory is $T_a = 2.4$ K (blue), but simulation (red) predicts lower values. A revised model (green) builds compression dynamics between ω_{rf} , ω_J , and a single sideband pair $\omega_J \pm \omega_{\text{rf}}$. However, a full description would need the entire set of sidebands ($\omega_J + m\omega_{\text{rf}}$, $m \in \mathbb{Z}$) that grows in size with I_b/I_c .

(experimentally, $G_a \simeq 28$ dB has been achieved). The compression mechanism was reproduced in a numerical simulation of amplifier dynamics, and first steps were taken towards an analytical description.

An alternative route to low noise is low I_b where one quantum of noise (half a quantum per nearest Josephson sideband $\omega_J \pm \omega_{\text{rf}}$) is added according to theory and simulation (see the Supplement of Publication I). This regime is currently experimentally unexplored. As discussed next, the low I_b is attractive also because of a potentially high gain-bandwidth product GBP.

Publication I: gain-bandwidth product and dynamic range

Theory predicts in the Supplement of Publication I that

$$\text{GBP} = 2/[|R_d|(C + C_J)] \quad (3.2)$$

$$\frac{R_d}{R} \approx -\frac{2v^2[1 + (\beta_c v)^2]^2}{1 + 3(\beta_c v)^2} \text{ at } v = \frac{\langle V \rangle}{RI_c} \geq 3. \quad (3.3)$$

Notably, $v \approx I_b/I_c$ here¹. In the first equation low $|R_d|$ gives a high GBP. In the second equation this correlates with a low $|I_b|$. The impedance matching network in front of the SJA has thus be designed to support such a bias point. Here, the main complications are related to parasitic impedances. As explicitly shown in Fig. 3.1e, the chip is wire-bonded to a circuit board and

¹IV point is close to the one determined by the linear shunt, $\langle V \rangle \approx RI_b$.

this adds a series inductance L_w of a couple of nH. At GHz frequencies L_w and $C_J \simeq 0.4$ pF are non-negligible parasitics. As no particular attention was paid to impedance matching in Publication I, only high bias points $I_b \approx (6-8)I_c$ were stable. Measured GBP was $2\pi \times 40-50$ MHz, in line with the theory where $|R_d| \simeq 1.4$ k Ω from Eq. (3.3) was plugged into Eq. (3.2).

The dynamic range of an amplifier is expressed through the -1 dB compression point of input power. Here, compression indicates saturation where the gain is no longer linear. Physically, this happens in the SJA when a notable fraction of power supplied by the dc bias is consumed as microwave amplification. The compression point was -160 dBm at the above bias point. The typical value for the traditional JPA is -130 dBm [76].

Publication II: improvements

The first improvement demonstrated in Publication II is related to the matching network. To effectively counteract the parasitics, varactor diodes (1 – 10 pF capacitors tunable with dc voltage) were added to a printed circuit board (PCB, Fig. 3.3a). The varactors enabled stable operation across a wide range of I_b points in a nominally identical SJA sample. The main differences between the two experiments include resistor material (Mo instead of TiW) and base temperature (4.2 K). At the lowest $I_b \approx (4-5)I_c$, a $GBP = 2\pi \times 100$ MHz was measured (Fig. 3.3b). Here, the GBP was limited by the bandwidth of the matching network rather than $|R_d|$ in Eq. (3.2). In terms of GBP, the SJA slightly outperformed the traditional JPA [76]. The shift in the bias point increased the -1 dB compression point to -117 dBm.

Furthermore, Publication II successfully sought an alternative to the circulator for characterization of stability and GBP. Non-reciprocal circulators are in general bulky, magnetic and expensive. An asymmetric branch-line coupler [32, Chap. 7] from quarter-wavelength elements suppressed the back-action of a follower amplifier. As the coupler is a reciprocal element, this came at the expense of SNR reduction, instead of improvement, for the useful signal. More specifically, a large attenuator (not shown in Fig. 3.3a) had to be placed at the PCB input port into which most of the amplified signal was guided. The coupler bandwidth was ~ 500 MHz, which did not restrict the SJA operation.

3.1.3. Comparison with microstrip SQUID

Another variant of dc biased Josephson amplifier is SLUG, superconducting low-inductance undulatory galvanometer [77]. It is based on a SQUID quasistatically biased to the finite voltage state at a certain flux offset. It amplifies signals from a low-impedance source. Using a resonant transmission-line matching technique, the device was recently demonstrated to work in the 50Ω environment at GHz frequencies [78]. The GBP was about $2\pi \times 120$ MHz. Similarly to the SJA, the SLUG has potential for wideband

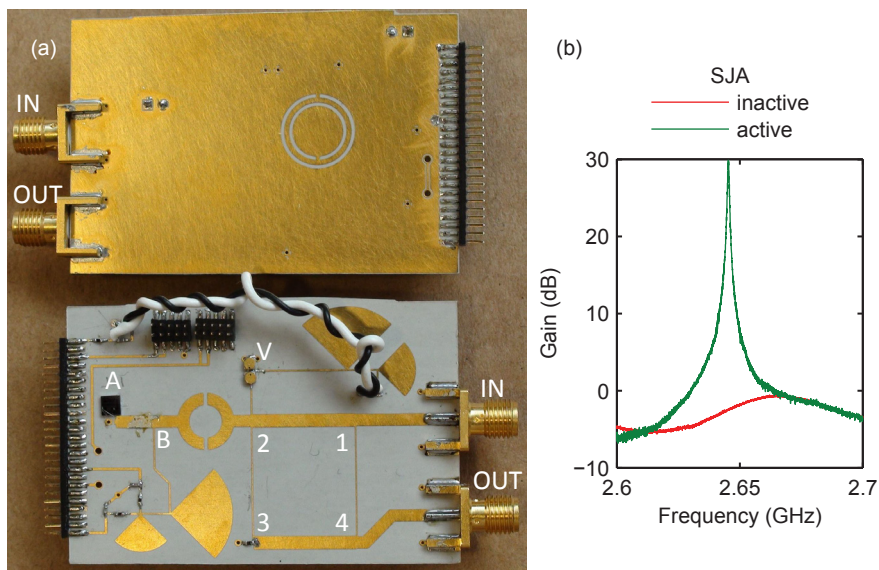


Figure 3.3: Tunable impedance matching of the SJA (Publication II). (a) Microstrip-based [32, Chap. 3] transmission lines and filters on a $62 \text{ mm} \times 41 \text{ mm}$ PCB (thickness 0.76 mm , relative permittivity $\epsilon_r = 2.94$). An amplifier chip (A) is connected to a branch-line coupler 1 – 2 – 3 – 4 through a bias-T (B). The 2 – 6 GHz custom bias-T consists of a high-pass filter (featuring split-ring resonators on ground plane) and an RF choke (radial stubs). Varactor diodes (V) are tunable capacitors for impedance matching. (b) Measured reflection gain referenced to port 2 with the SJA inactive at $I_b = 0$ (red) or at a high-gain point $I_b = 4.5I_c$ (green). The input power at port IN was -145 dBm .

operation upon optimization of the input matching network. Due to noise from the resistive shunts across the Josephson junctions, the theoretical lower bound of added noise is one quantum for the SLUG. Its -1 dB compression point lies somewhere between -110 and -90 dBm according to simulations. The dynamic range is thus 1 – 2 orders of magnitude higher than that of the SJA. One competitive advantage of the SLUG is transmission mode of operation. Unlike the reflection amplifiers, it is a directional device providing isolation in the reverse direction of signal propagation, i.e., from amplifier output to input.

3.2. Kinetic inductance sensing

Over the past decade, kinetic inductance sensing has substantially gained maturity. A driving force has been the tremendous sensitivity of Cooper-pair-breaking astrophysical KIDs [17]. Dispersive measurement together with software radio techniques has allowed a frequency multiplexed readout of kilopixel arrays [79]. However, the world market for these specialized instruments is limited. Emerging kinetic impedance technologies include tunable nanoinductors [80], wideband parametric amplifiers [81, 82], and frequency comb generators [83]. They all harness the current nonlinearity [Eq. (2.24)] in superconductors where the electron-phonon scattering rate is high (e.g., NbN and NbTiN).

Two sensors of this work can be added to the list. Firstly, a bolometric radiation detector has been demonstrated in Publication III. The kinetic inductance bolometer is a complementary device to KIDs. Secondly, a kinetic inductance magnetometer has been studied theoretically and experimentally in Publication IV.

3.2.1. Kinetic inductance bolometer

Astrophysical KIDs operated at a sub-K temperature require sophisticated cryocoolers. Cooling far below T_c exponentially suppresses² n_{qp} and the KID noise floor may reach a level below the photon noise of incoming cold³ radiation [85]. To image the cold objects of the Universe, the instrument has to be launched to space or operated at a high altitude where atmospheric THz transmission is sufficient. One might ask what THz radiation detectors can do in terrestrial conditions, where the background is hot ($T = 250 - 300$ K) and water vapour absorption limits the imaging distance. One practical application of the $0.1 - 1$ THz regime is security screening [86] due to a combination of a short wavelength and relatively good penetration through dielectrics. Despite continuous effort [87, 88], the use of semiconductor technology for this frequency band and application remains unprac-

²In practice, KID RF readout sustains an excess quasiparticle population [84].

³Cosmic microwave background has $T = 2.73$ K.

tical. The sensitivity requirements of passive THz imaging are more easily met with superconducting detectors.

There are two types of radiation detector that convert incoming photons to heat [20]. A calorimeter resolves the energy of single photons. In contrast, a bolometer integrates arriving photon flux. Both detectors have to be thermalized to a surrounding bath (substrate), but sufficiently isolated for the generated heat to localize and the temperature to rise. In this work, kinetic inductance was used as a thermometer [Eq. (2.21)] in a bolometric application [89, 90, 91] (Publication III, Fig. 3.4a,b). A superconducting meander inductor (NbN, $d = 100$ nm) was patterned on a suspended 1 mm^2 membrane (SiN). Narrow supporting legs reduced thermal conduction between the membrane and surrounding substrate (Si). A resistive grid (TiW) on top absorbed THz photons⁴. The operation point was close to $T_c \sim 6$ K where λ and L_k had strong, even divergent, temperature sensitivity (Fig 2.2b). The benefit of using a compound superconductor NbN is T_c control in fabrication to achieve sensitive bolometry at a specific cryocooler base temperature. Other groups have recently demonstrated similar bolometers from NbTiN [92], YBCO⁵ [93], and Nb [94].

The meander inductor was resonantly matched to an RF environment (the dispersive measurement in Sect. 2.4.2). Due to small dimensions compared with the guided readout wavelength $\sim 1 \text{ m}$ at $\omega_r/(2\pi) \sim 100$ MHz, the circuit had a lumped element character. Capacitors (parallel plates off the membrane) and the inductor ($L = L_k + L_g$ including a geometric component L_g) form an inherently multiplexable resonator for use in a focal plane array. Bolometer thermal physics is governed by the membrane heat capacity C_{th} and the total leg thermal conductivity G . Their ratio gives the thermal time constant τ_{th} , which was the longest time scale of the system (Fig. 3.4c). Thereby, it set the signal bandwidth to video-rate $\nu_c/(2\pi) = 1/(2\pi\tau_{\text{th}}) \approx 25$ Hz. The other time scales are the electrical time constant of the resonator defining the readout speed, and the quasiparticle recombination time, which tells how fast L_k responds to temperature variations.

On the theory side, the limits of the dispersive measurement were analysed. The RF carrier of the dispersive measurement is partially dissipated on the membrane [Eq. (2.32)] since the meander inductor is lossy. The readout-induced heating generates electro-thermal feedback. In addition, the RF current through the meander hits the non-linear L_k [Eq. (2.24)] and the carrier is partially rectified. Both the heating and the current rectification give rise to Duffing non-linearities in the resonator [95]. In a normalized

⁴Any direct breaking of Cooper pairs in the meander would be unintentional. Note that NbN has a large gap, and its surface impedance is mainly reactive.

⁵YBCO stands for yttrium-barium-copper-oxide, a high- T_c superconductor.

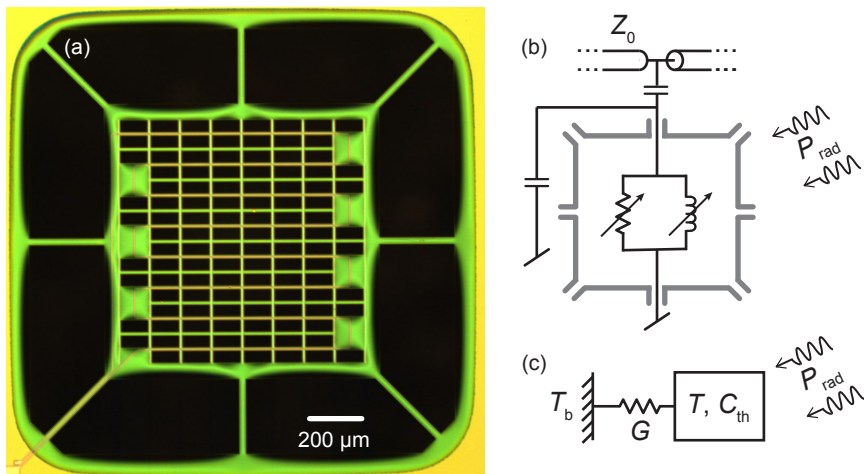


Figure 3.4: Kinetic inductance bolometer. (a) An optical micrograph (Andrey Timofeev, VTT) with the colours: Si substrate (dark yellow), SiN+SiO membrane (green), NbN meander (brown), TiW absorber grid (light yellow), and holes (black). (b) Membrane thermometry. Incident THz radiation at power P_{rad} heats the membrane. The kinetic impedance of the superconducting meander line responds to the temperature. Capacitors off the membrane resonantly match the meander to a Z_0 environment for dispersive readout. (c) A thermal model where the membrane connects to a bath at temperature T_b through a conductance $G \simeq 18$ nW/K. The thermal time constant is $\tau_{\text{th}} = C_{\text{th}}/G \approx 6.4$ ms, with $C_{\text{th}} \simeq 120$ pJ/K the heat capacity.

3.2. Kinetic inductance sensing

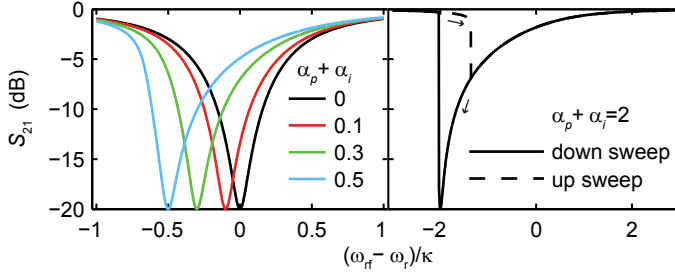


Figure 3.5: Non-linear resonator response during dispersive readout. Using Eqs. (3.4)-(3.5) the transmission measurement is modelled at readout powers below (left panel) and above (right panel) the bifurcation threshold $\alpha_p + \alpha_i \approx 0.8$. The non-linearity is assumed to be purely reactive. In practice, the readout power dependence of the quality factor makes the S_{21} dip shallower when P_{rf} is increased [96].

frequency coordinate x derived from physical carrier ω_{rf} ,

$$S_{21} = \frac{Q_t/Q_i + 2ix}{1 + 2ix} \quad (3.4)$$

$$x = \frac{\omega_{\text{rf}} - \omega_r}{\kappa} + \frac{\alpha_p + \alpha_i}{1 + 4x^2}, \quad (3.5)$$

where dimensionless α_p (α_i) from heating (current) describes the non-linearity, and ω_r is eigenfrequency at low measurement power. Increasing linearly with the power,

$$\alpha_p = \frac{Q_t^3 P_{\text{rf}}}{Q_i Q_e G L} \frac{\partial L}{\partial T}, \quad \alpha_i = \frac{2Q_t^2 P_{\text{rf}}}{Q_e \omega_r E^*} \quad (3.6)$$

bend the resonance dip of $|S_{21}|$ toward a lower frequency (Fig. 3.5a). The model assumes that L_k responds to P_{rf} much stronger than Q_i and Q_t . Note the appearance of G and the divergence of $(\partial_T L)/L$ near T_c : α_p is expected to dominate in the bolometer. The kinetic scaling energy is $E^* \propto L_k (I^*/\alpha_k)^2$ [Eq. (2.24)], and the quality factors have been defined in Eqs. (2.27)-(2.29). Low readout power $\alpha_p + \alpha_i \leq 0.1$ was used in the characterizations of this work. Exploring the opposite Duffing regime could be worthwhile in future, since at high P_{rf} preamplifier noise is more easily overcome. Trade-offs are bifurcation at $\alpha_p + \alpha_i > 0.8$ (Fig. 3.5b), and α_p -related reduction of imaging speed and dynamic range.

Single-bolometer experiments are summarized in the following. Firstly, the thermal behaviour of the resonator was investigated. L_k and Q_i were extracted from the S_{21} measurements. In Fig. 3.6 they are further compared to the kinetic impedance from the BCS and the Mattis-Bardeen theory. Secondly, suitability for radiation detection was determined from noise-

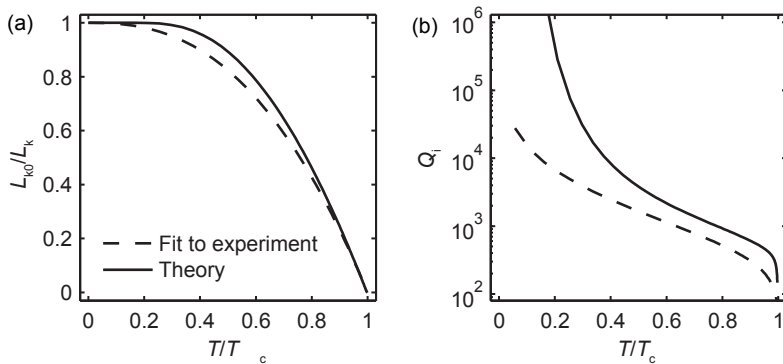


Figure 3.6: Fits to measured resonator parameters (Fig. 2 in Publication III) and a comparison to the BCS and the Mattis-Bardeen theory [Eqs. (2.11)-(2.12) and (2.19)-(2.20)]. (a) Thin-film kinetic inductance. (b) Internal quality factor. The model takes into account the variation of α_k and ω_r with T . The low measured Q_i was likely to be caused by the dielectric loss of SiO_2 in the parallel-plate capacitors.

equivalent power (NEP), noise-equivalent temperature difference (NETD)⁶, and THz spectral response measurements. NEP is measured by recording the noise spectrum of a demodulated carrier. The carrier is at the eigenfrequency of an unilluminated bolometer. The result was $\text{NEP} \approx (3.5 \pm 2.0) \text{ fW Hz}^{-1/2}$, in line with the theoretical NEP from phonons [97] $\sqrt{4k_B T^2 G} = 5.8 \text{ fW Hz}^{-1/2}$. Generation-recombination (GR) noise was estimated to be more than three orders of magnitude below the phonon noise. The sum of thermal Johnson noise and preamplifier input noise was $0.01 \text{ fW Hz}^{-1/2}$, a good number despite the lack of a cryogenic preamplifier. For comparison with astrophysical detectors, a GR-limited $\text{NEP} \simeq 4 \times 10^{-4} \text{ fW Hz}^{-1/2}$ has recently been measured for an aluminium KID at $T = 100 \text{ mK}$ [85]. However, due to the warm terrestrial background, ultra-high sensitivity is not required in the current application.

NETD is a more relevant figure of merit in terrestrial imaging. NETD measurement with an aqueous blackbody calibrator [98] showed that a $6.3 \pm 2.0 \text{ mK}$ temperature difference is resolvable at 1 s integration time. This is slightly higher than the NETD of a superconducting hotspot microbolometer [99], 125 mK at 30 ms integration time. However, keeping the NETD of an entire imaging system at a low level is easier with the kinetic inductance bolometer: frequency multiplexing allows scale-up to a full focal plane array to avoid mechanically scanned optics [100]. The hotspot microbolometer is a detector suitable for comparison since it similarly has a terrestrial application and a relaxed cryocooler base temperature requirement.

⁶NETD is the temperature change of radiation source that corresponds to $\text{SNR} = 1$.

The spectral response was measured using amplitude-modulated illumination from a 0.2 – 1.4 THz photomixer. A reflective backshort at three quarters of wavelength distance ($450 \mu\text{m}$) made the spectral response periodic (310 GHz interval). The average over the usable spectral bandwidth 312 – 623 GHz gave an absorption efficiency of 11%, limited by non-optimized matching of the TiW grid to the vacuum impedance.

3.2.2. Kinetic inductance magnetometer

Motivation

Section 2.1.2 introduced flux quantization in a superconducting loop, and SQUID magnetometry with loops interrupted by two Josephson junctions. The tremendous sensitivity of the SQUID magnetometer is balanced by challenges in operability, and complexity in fabrication. In a system of multiple SQUIDs, e.g., biomagnetic setups, each one is read out through dedicated wiring. The dynamic range of the SQUID is limited by the Φ_0 -periodicity of its operating point, calling for linearization by a flux-locked loop [25]. At the cost of electronics complexity, flux-quanta counting and dynamic field compensation methods can further extend the dynamic range [101]. Since flux trapped in the superconductor couples to JJs reducing the modulation depth, the SQUID may recover poorly from external field pulses unless proper shielding is introduced [102, 103]. The pulses can originate either from the environment or from intentional magnetic manipulation of samples. The manipulation is an essential part of ultralow-field magnetic resonance imaging (ULF MRI), a biomagnetic technique [104, 105]. Furthermore, the SQUID is susceptible to RF interference over a wide band of frequencies [106, 107]. The interference increases the sensor white noise level, and may have an adverse effect on the flux-to-voltage transfer function. Fabrication of the SQUID magnetometers is a multi-step process in which junction quality and reproducibility are not easily guaranteed. One complication is the thin oxide layer for the JJ.

This section demonstrates a sensitive magnetometer avoiding the Josephson effect altogether by harnessing kinetic inductance. At the heart of the sensor is a loop of superconducting thin film just like in the SQUID, but not interrupted by JJs. When an external flux is threading the loop, flux quantization generates a circulating screening current I_s which nulls the magnetic field inside the superconductor. As the superposition of the external and self-induced flux⁷ must be quantized,

$$LI_s - \Phi_a = m\Phi_0, \quad m \in \mathbb{Z}. \quad (3.7)$$

The relation to average magnetic flux density is $B_0 = \Phi_a/A$, with A the loop area. The loop inductance L is the sum of geometric (L_g) and kinetic

⁷When looking at a loop from above, a Φ_a into the plane of the loop generates a anticlockwise circulating I_s .

(L_k) terms. The kinetic component responds non-linearly to the screening current, as recalled from Eq. (2.24). The inductance variation is read out using the standard dispersive framework (Fig. 3.7). This is the main idea behind the kinetic inductance magnetometer (KIM) in Publication IV.

Readout

KIM readout is similar to that of the bolometer in the previous section. The loop is embedded into a lumped element RF resonator (ω_{r0} is the eigenfrequency at zero I_s). To avoid multiple layers in fabrication, capacitors are formed from planar, interdigitated fingers. In this work, resonator material was thin-film ($d = 165$ nm) NbN with $T_c = 14$ K. The dispersive S_{21} measurement responds to the flux threading the loop. More specifically, an increasing magnitude of I_s due to Φ_a will shift down the resonator eigenfrequency and degrade its intrinsic quality factor, effects which move the S_{21} resonance dip and slightly change its form, respectively (Sect. 2.4.2, Fig. 3.8). For the loop pictured in Fig. 3.7c some superconductor parameters were extracted from the measured S_{21} : $L_k(I_s = 0) = 147$ nH and $\lambda = 1100$ nm [Eq. (2.19)]. There was a discrepancy between the measured penetration depth and the theoretical estimate 710 nm [Eq. (2.18)]. Examples of quantities with uncertainties that could have contributed to the discrepancy are the gap Δ , the simulated L_g , and the film thickness d .

In the following, the upper bound of KIM readout power is discussed. The Duffing non-linearity term α_p in Eq. (3.6) can be neglected since the KIM is strongly thermalized to a substrate. According to experiments at high P_{rf} , a depairing mechanism typically kicked in before resonance bending from α_i was observed. The RF excitation generates an ac current through L that adds to the circulating I_s . When the total current exceeds the depairing value I_d , the material is driven (partly) normal. At P_{rf} just below the threshold, KIM responsivity maximizes to

$$\left. \frac{\partial V_{out}}{\partial B_0} \right|_{\omega_{rf}=\omega_r}^{\max} \approx \frac{Q_i \sqrt{Q_e}}{Q_i + Q_e} \sqrt{\frac{\omega_r Z_0}{2L_{tot}}} \frac{|I_s| (I_d - |I_s|) A}{I^{*2} (1/\alpha_k + 3(I_s/I^*)^2)}. \quad (3.8)$$

Here, V_{out} is the demodulated output voltage, and $L_{tot} = L/4 + L_{par}$ with L_{par} the parasitic inductance (Fig. 3.7a). Many variables in Eq. (3.8) are temperature dependent (Sect. 2.4.1), but the KIM experiment was conducted at the fixed temperature of a liquid helium bath. The signal bandwidth extends from $\nu = 0$ (static applied field) to a characteristic low-pass corner frequency ν_c of the system dynamics. In practice, the resonator linewidth determines the corner as $\nu_c = \kappa/2$. By plugging in typical numbers $\omega_r/2\pi = 100$ MHz and $Q_t = 10^3$, a KIM bandwidth $\nu_c/2\pi = 50$ kHz suitable for many purposes is obtained.

3.2. Kinetic inductance sensing

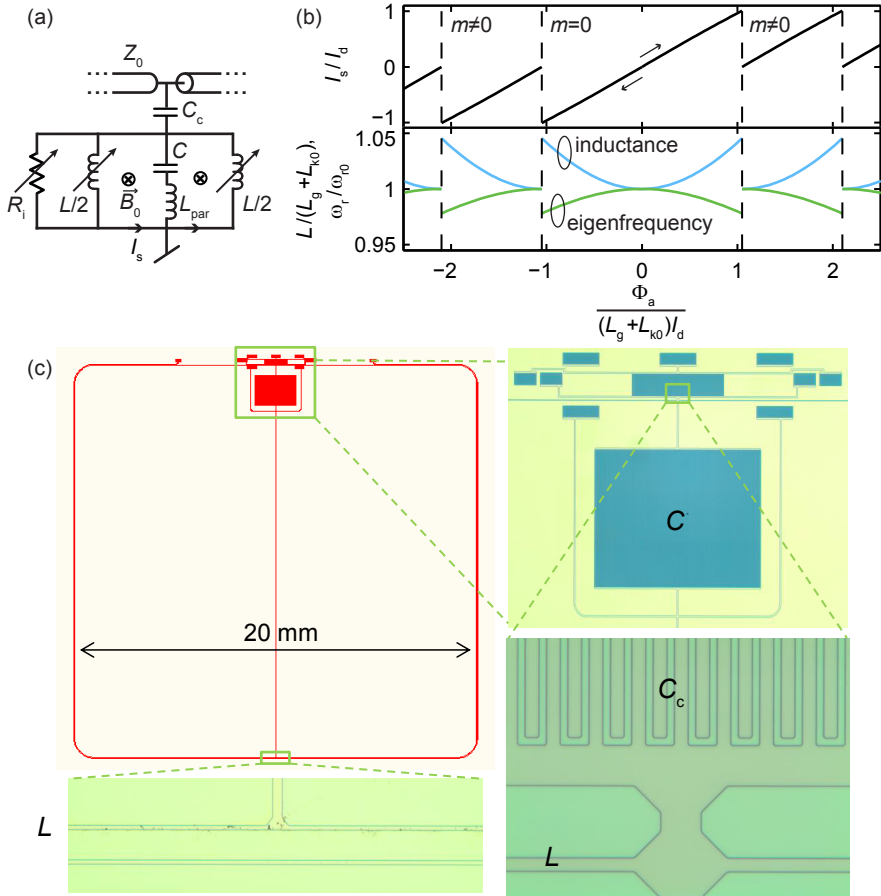


Figure 3.7: Kinetic inductance magnetometer. (a) Circuit diagram. Flux quantization in a superconducting loop generates a shielding current I_s that enhances the loop inductance L . The inductance is read out with dispersive measurement. (b) Theoretical up- and downward sweeps of Φ_a starting from $\Phi_a = 0$, $m = 0$. The calculation assumes $I_d = 0.3I^*$, $\alpha_k = 0.5$, $LI_d \gg \Phi_0$, and $P_{rf} \approx 0$. The shielding current resets when its magnitude exceeds the geometry- and material-dependent depairing value. An RF current superimposed on I_s would lower the reset tolerance if the measurement power was turned on. (c) NbN device layout on Si substrate and optical micrographs (Juho Luomahaara, VTT). The loop area is $A = 20 \times 20 \text{ mm}^2$, the narrowest trace width is $w = 5 \text{ }\mu\text{m}$, and the capacitor gap is $3 \text{ }\mu\text{m}$.

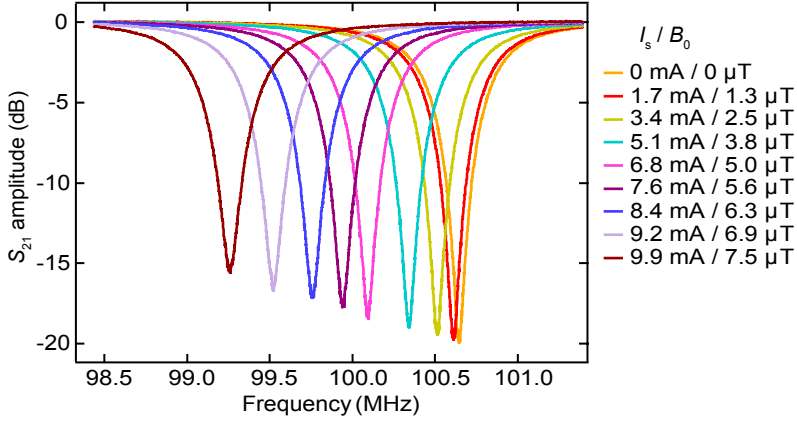


Figure 3.8: Low-power transmission measurement as a function of applied magnetic field. The operating temperature was $T = 4.2$ K. I_s circulating in the loop shifts the eigenfrequency and degrades the quality factor. In this device reset to $\omega_{r0}/(2\pi) = 100.7$ MHz occurred when $|I_s| \approx I_d = 10$ mA.

Noise and dynamic range

To be useful for applications, the KIM should perform comparably to state-of-the-art SQUIDs, which dominate the market of ultra-sensitive magnetometers. Suitability for similar tasks, such as biomagnetism, should be evaluated. As noted above, the KIM has a relatively wide bandwidth. Low-frequency noise is also of great importance: SQUIDs for biomagnetism have $S_B^{1/2} \sim 1$ fT/Hz $^{1/2}$ resolution and a 1 Hz $1/f$ corner [108]. The intrinsic noise mechanisms of the KIM include thermal noise from resistive circuit elements ($S_{B,th}^{1/2}$), and generation-recombination (GR) noise from quasiparticle dynamics ($S_{B,gr}^{1/2}$). The relevant proportionalities of these two are

$$S_{B,th}^{1/2} \propto \frac{1}{A} \sqrt{\frac{L_{tot}}{\omega_r Q_i}}, \quad (3.9)$$

$$S_{B,gr}^{1/2} \propto \frac{L_{k0} I^*}{A} \sqrt{\frac{\tau_r n_{qp}}{4wd\sqrt{A}}}, \quad (3.10)$$

with the loop volume $4wd\sqrt{A}$, the quasiparticle recombination time τ_r , and $L_{tot}, L_{k0} \propto \sqrt{A}$. Note that Eq. (3.9) assumes maximal P_{rf} . Noise can be reduced by growing the loop size. Interestingly, the expected constancy of $\omega_r Q_i$ in Eqs. (3.8) and (3.9) [2, Chap. 3] suggests that the responsivity and noise are independent of the resonator eigenfrequency.

A summary of external noise sources that are related to the readout hardware is presented in Table 3.1. Measures implemented to make the first noise measurements more reliable are marked with \checkmark . The noise spec-

3.2. Kinetic inductance sensing

Table 3.1: Reducing the effect of electronics on KIM noise. EMI = electromagnetic interference, HEMT = high-electron-mobility transistor, IF = intermediate frequency.

Non-ideality	Countermeasure	
Carrier phase noise	Single source for excitation and reference	✓
Rectification of carrier amplitude noise	Stable RF generator	✓
Thermal noise from room temperature	Feedline attenuated at low temperature	✓
Ambient magnetic fields and EMI	Shielded environment	✓
Noise from DC flux bias	Persistent current mode of operation	✓
Noise of the first preamp	Cryogenic preamp, e.g., HEMT	
Non-optimal source impedance for the first preamp	Circulator placed in front of the preamp	
$1/f$ noise added in demodulation	Low-noise mixer, or finite IF by sideband modulating the carrier, or carrier cancellation allowing more RF preamplification before the mixer saturates	

trum was recorded in a shielded environment in three scenarios where the spectral density progressively decreases: (i) KIM highly responsive to Φ_a , (ii) KIM unresponsive ($I_s = 0$), and (iii) KIM removed from the system. An elevated spectrum of (i) in comparison with (ii) can be explained by the amplitude noise of the carrier meeting the kinetic inductance non-linearity. In addition, local coupling of random flux to the loop contributes here as well. This noise could originate from the movement of trapped vortices [109], or microscopic fluctuators in the substrate and interfaces [110, 111]. Scenario (iii) constitutes a lower bound set by the readout chain.

In the first measurements, the noise spectra showed a white noise region above 1 kHz and a 400 Hz $1/f$ corner (see Fig. 4 in Publication IV). The $1/f$ part, similar throughout (i)-(iii), is likely to have been added by a demodulating mixer. The white regions of (i) and (ii) were indistinguishable from each other, amounting to $32 \text{ fT/Hz}^{1/2}$. The KIM acted as a mismatched source for the first preamplifier, which explains why the white noise had a slightly lower level in (iii). The main conclusion is that the intrinsic KIM contribution, theoretically dominated by Johnson noise at $S_{B,\text{th}}^{1/2} = 2 \text{ fT/Hz}^{1/2} \approx 100 S_{B,\text{gr}}^{1/2}$ in this specific device, was masked by the noise of the room temperature electronics. Reaching the intrinsic noise floor by utilizing all of the methods in Table 3.1 is an avenue for future work and would enable fair comparison with the SQUID magnetometer.

The KIM dynamic range is limited by responsivity degradation when the applied field moves the resonance dip off the fixed carrier frequency (see Fig. 3 in Publication III). Derived in Appendix A, the dynamic range corre-

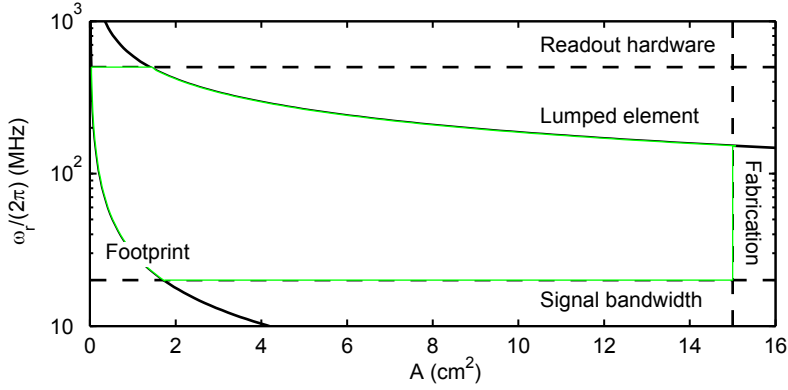


Figure 3.9: KIM eigenfrequency and loop area. Feasible parameters are bounded in green, and labels outside indicate which tolerance or criterion is not met (see the main text for definitions). High A lowers the intrinsic noise. Upper and lower solid curves scale as $\propto A^{-1/2}$ and $\propto A^{-3/4}$, respectively. $\omega_r Q_t$ is assumed to be constant throughout. Materials and geometry are as in Publication IV, except that $L_{\text{par}} = 0$ and $Q_i = Q_e$. Readout wavelengths are longer than $20\sqrt{A}$. As arbitrary choices, the hardware operates below 500 MHz, $A \leq 15 \text{ cm}^2$, and the bandwidth requirement is $\nu_c/(2\pi) = 2 \text{ kHz}$.

sponding to the half-responsivity bandwidth is

$$\Delta B \approx \frac{4L_{\text{tot}}I^{*2}}{\sqrt{3}Q_t A I_s} \left(1/\alpha_k + 3(I_s/I^*)^2\right), \quad (3.11)$$

which assumes $I_s > 0$. A high critical current density of the material increases the dynamic range. Using the device and operation parameters of Publication IV yields 790 nT, somewhat larger than the measured 600 nT. In the absence of a feedback scheme the dynamic range of a typical SQUID is only $\sim 1 \text{ nT}$.

Design guidelines

The KIM design factors are listed from a physical and practical perspective. KIM design essentially involves selecting a loop size and an eigenfrequency (Fig. 3.9). The KIM will benefit from a sufficient α_k that requires a small cross-section of the superconducting strip. The square $W \times W$ loops of this work had rounded corners, trace width $w \ll W$, thickness $d \ll w, \lambda$, and L_{k0} from Eq. (2.19). The geometric inductance of the square loop can be approximated as [112, Chap. 5.4.] $L_g \approx 2\mu_0 W [\text{arsinh}(2W/w) - 1]/\pi$. For greater accuracy, L_g could be solved by numerical simulation, e.g., with *FastHenry* software [113]. Besides improving α_k , narrowing the trace also helps resist the trapping of flux vortices when the superconductor crosses

T_c at a finite magnetic field. The critical field for vortex trapping is of the order of Φ_0/w^2 [114]. A trade-off related to the smallness of the cross-section is GR noise in Eq. (3.10), which may rise to an observable level.

From the readout perspective, the loop has to behave as a lumped element, which means small dimensions compared to carrier wavelength. This will limit the product of the KIM eigenfrequency and the loop size:

$$\omega_r W \ll 2\pi c_0 / \sqrt{(1 + \epsilon_r)/2}, \quad (3.12)$$

with c_0 the speed of light in vacuum and ϵ_r the relative permittivity of the substrate (Si had $\epsilon_r = 11.9$ in this work). In practice, the readout hardware will support a certain frequency band, which typically spans a decade at most. The lower bound for ω_r may also arise from the signal bandwidth requirement ν_c (note low-pass filtering at $\omega_r < 2\nu_c Q_t$), or capacitance density (the footprint of the capacitors must not exceed the loop area).

3.3. Addressability of quantum bits

The topic of Publication V was the experimental demonstration of the Wah-Wah method [12], which speeds up single-qubit operations in a frequency-crowded quantum processor (Sect. 2.5.2). When microwave control is sent through a common feedline, it also reaches unaddressed qubits causing phase shifts of the quantum state and leakage out of the qubit two-level subspace. This chapter explains how leakage was first witnessed and subsequently cured with Wah-Wah.

To study leakage, two transmons Q_a, Q_b on a 2D cQED processor (Fig. 3.10) were operated as three-level systems, or qutrits [115]. Frequency multiplexed transmon readouts were made sensitive to the second excited state by interrogating the cavities at $(\omega_r + \chi)/(2\pi) \simeq 7.7 - 7.8$ GHz corresponding to a transmon in $|1\rangle$, and recording both signal quadratures. Anharmonicities were measured with two-tone spectroscopy [57], and unitary rotations were calibrated for both $|0\rangle \leftrightarrow |1\rangle$ and $|1\rangle \leftrightarrow |2\rangle$ subspaces. In the $|1\rangle \leftrightarrow |2\rangle$ calibration the qutrit is first excited to $|1\rangle$ by a π pulse at ω_{01} , and "AIXY" (see Sect. 2.5.2) is then performed with ω_{12} pulses. The readout and the unitaries provide a toolbox for extracting qutrit level populations at the instance of the measurement, and thus witnessing leakage to $|2\rangle$.

To create intentional frequency crowding as in Fig. 2.9a, one transmon (Q_a) was held at its flux insensitive point $\omega_{01}^a/(2\pi) \simeq 6.3$ GHz while the other (Q_b) was shifted to operating points where $\delta/(2\pi) = 57, -60$, or -81 MHz. These offsets were much smaller than the anharmonicity $\alpha_q/(2\pi) \simeq -350$ MHz, so the control speed barrier was $t_g = 2\pi/|\delta| \simeq 12 - 18$ ns (results from the first δ point are shown). At gate times approaching this barrier, leakage during Q_a control was characterized with level population measurements. Here, the control was truncated at the nanosecond resolution of pulse synthesis. State tomography [5] after the truncation

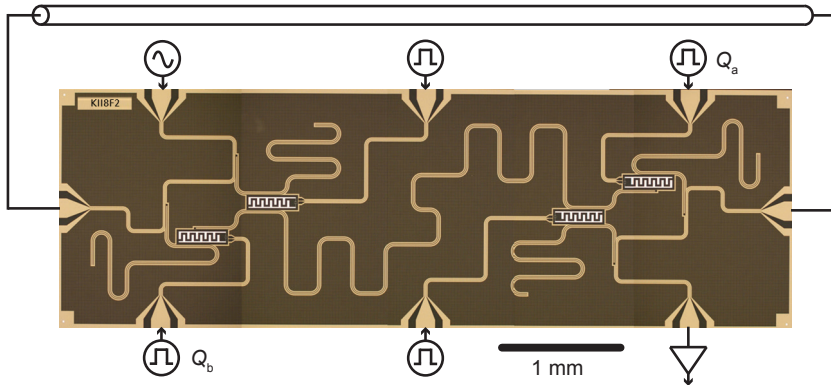


Figure 3.10: Four-qubit 2D cQED processor for the Wah-Wah experiment. The $2 \times 7 \text{ mm}^2$ chip was operated at $T = 20 \text{ mK}$. The elements are described in the zoom-in Fig. (2.8). The flux bias lines of transmons Q_a and Q_b are labelled, and the inactive transmons are far detuned. The common feedline for readout and control contains a short coaxial cable connecting the side terminals off-chip. A full wiring diagram and a list of device parameters is presented in the Supplement of Publication V. Optical micrograph by A. Bruno, Delft University of Technology.

yields the time evolution of transmon level populations (Fig. 3.11 a). According to the results, the DRAG pulse shaping technique mitigated internal Q_a leakage (Fig. 3.11b), but was incapable of simultaneously preventing external Q_b leakage. In Fig. 3.11c 50 % population transfer from $|1_b\rangle$ to $|2_b\rangle$ is witnessed after just four Q_a pulses.

Both leakage types were suppressed with Wah-Wah, which adds sideband modulation to the pulse envelope [Eqs. (2.46)-(2.47), Fig. 3.11 d]. The intuition behind Wah-Wah is engineered pulse spectral density at multiple unwanted transition frequencies. The sideband modulation was initially hand-optimized, but simulating Hamiltonian dynamics [Eq. (2.44)] was found to accelerate the search (Fig. S3 in the Supplement of Publication V). There is no unique pair of Wah-Wah parameters, but an entire optimum manifold of ω_m and A_m that changes shape according to δ . Importantly, Wah-Wah parameters are also different for each rotation angle.

In this work, Wah-Wah was used in conjunction with $\pi/2$ and π rotations, which are perhaps the most common single-qubit unitaries. Applying them around $\pm x$, $\pm y$ axes can take the quantum state to six cardinal points: poles of the Bloch sphere ($|0\rangle$, $|1\rangle$), and four superpositions on the equator (Fig. 2.7c). The idea of randomized benchmarking (RB [116, 117]) is to characterize single-qubit gate error by applying standard unitaries and the identity (idling for an equal t_g) in random order. Each RB sequence ends with the transmon ideally at $|0\rangle$ or $|1\rangle$, and the measured fidelity to the ex-

3.3. Addressability of quantum bits

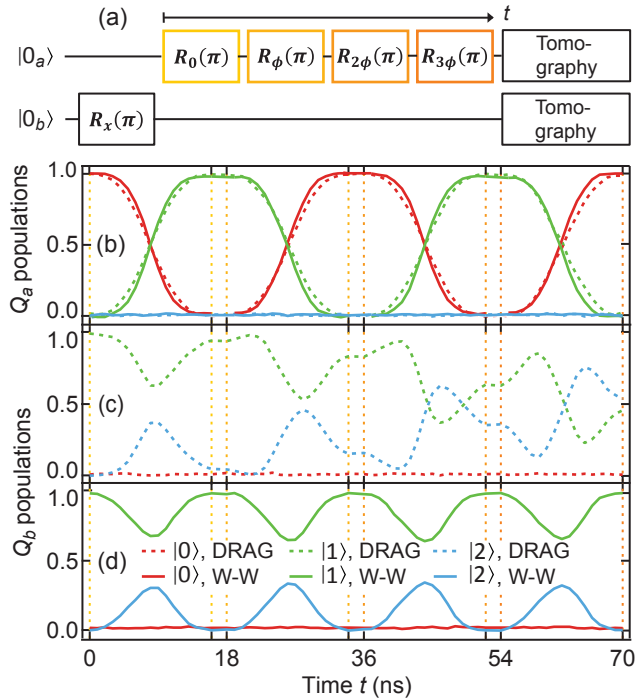


Figure 3.11: Measured evolution of level populations in Q_a and Q_b during four consecutive Q_a π pulses with either optimal DRAG or Wah-Wah envelopes. (a) Pulse sequence. Pulses ($t_g = 16$ ns) are followed by a $t_b = 2$ ns buffer. $R_\phi(\theta)$ denotes rotation θ at phase ϕ ($\phi = 0$ is rotation around x). (b) Evolution of Q_a levels. Neither DRAG (dashed curves) nor Wah-Wah (solid curves) pulses drive the leakage transition in Q_a . (c-d) Evolution of Q_b levels during DRAG (c) and Wah-Wah (d) Q_a pulses. DRAG pulsing drives the Q_b leakage transition. The net effect is controlled with the relative phase between subsequent pulses. The Wah-Wah pulses populate $|2_b\rangle$ temporarily, returning the population to $|1_b\rangle$ by the end of each pulse.

pected outcome decays with increasing number of gates in the sequence. If the benchmarking is properly averaged and repeated over multiple randomizations, an exponential fit to the decay gives an estimate for the error per gate. In this work a closely related quantity, average error per computational step (EPS), was used instead (see the Supplement of Publication V for a definition). The extracted value is not sensitive to state preparation and measurement (SPAM) errors [118] that limit the accuracy of the level population measurements.

The purpose of running RB was to show with high accuracy that the fidelity of Wah-Wah control is limited by decoherence, while DRAG pulses of equal duration induce significant error. To this end, the buffer time t_b between pulses was varied. Firstly, the individual RB, where only one transmon is pulsed, gave decoherence-limited baselines of Q_a and Q_b (EPS vs. $t_g + t_b$ extrapolates to origin). Secondly, at high t_b exceeding the gate time, RB sequences on the transmons were symmetrically interleaved⁸ with pulses on Q_a and Q_b applied in an alternating fashion (Fig. 3.12a). This allows compensation for deterministic phase shifts [120] in pulse synthesis; thus the possible increase in the EPS, when comparing with the baseline, is from the leakage. RB measurements showed that when Wah-Wah pulsing on Q_a was turned on, Q_b EPS remained at the decoherence baseline. In contrast, DRAG pulsing on Q_a increased Q_b EPS noticeably (Fig. 3.12b). As deduced from a series of experiments (see also Fig. S4 in the Supplement of Publication V), the Q_b EPS difference from the leakage grew with decreasing t_g , as expected from the broadening of the pulse spectral bandwidth. Q_b DRAG pulsing did not induce leakage in Q_a , as expected from a large frequency difference between ω_{01}^b and ω_{12}^a (Fig. 3.12c). Hence, Q_b pulses did not need Wah-Wah sideband modulation.

Similar conclusions on Wah-Wah superiority over DRAG were drawn from quantum process tomography [121] (see Fig. 4 in Publication V, and Fig. S5 in its Supplement).

⁸This method should not be confused with interleaved RB in Ref. [119].

3.3. Addressability of quantum bits

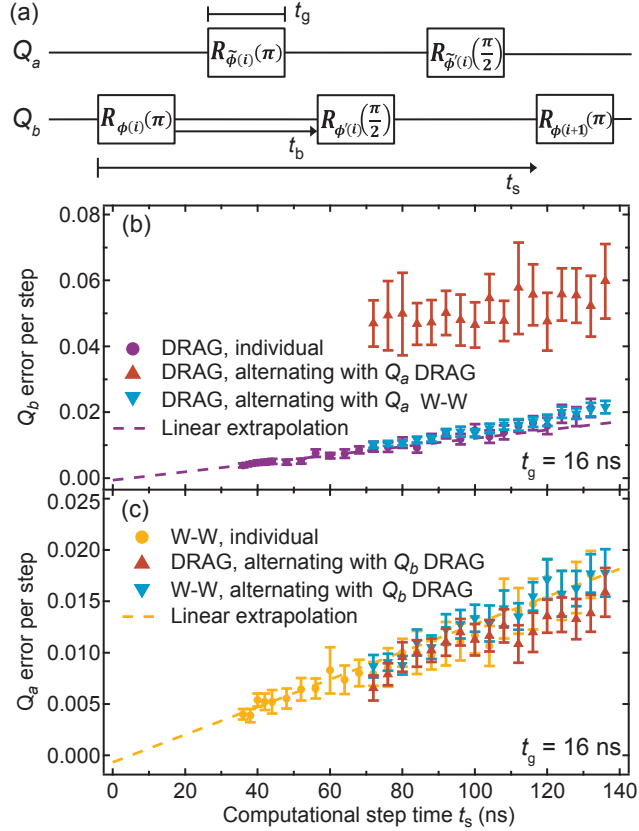


Figure 3.12: Randomized benchmarking. (a) An alternating RB gate sequence that can be reduced to individual RB by idling on either transmon. The computational step time is $t_s = 2t_g + 2t_b$, where a step consists of a π , $\pi/2$ pulse pair and variable buffers. $R_\phi(\theta)$ denotes rotation θ at phase ϕ ($\phi = 0$ is rotation around x). (b,c) EPS of optimal transmon control vs. t_s , at fixed $t_g = 16$ ns. The individual RB constitutes a decoherence limited baseline in both panels, since the EPS extrapolates to origin. In (b) Q_b EPS increases due to leakage induced by alternating Q_a DRAG pulses. However, when the alternating Q_a pulses have Wah-Wah sideband modulation, the Q_b EPS is indistinguishable from the decoherence baseline. In (c) Q_a control is also decoherence limited. There are no observable Q_a EPS differences when changing the Q_a pulse shaping technique or switching between the two Q_b sequences, i.e., idling and DRAG pulsing.

4. Summary and conclusions

The single junction amplifier (SJA) is a dc biased, selectively damped Josephson junction (JJ) that provides microwave gain in reflection. Demonstrated and analysed in this work, the first SJAs were proof-of-concept devices. In practical applications such as quantum bit readout, the SJA faces competition against a broad class of RF pumped amplifiers and the microstrip SQUID amplifier. Some highlights of recent work include directional amplification to avoid placement of a circulator between source and amplifier [122], strong environmental coupling in JPA to increase dynamic range and bandwidth [123], and a travelling wave Josephson amplifier [124]. A crucial improvement of the SJA would be a tunable bandstop filter in order to move the centre frequency of the gain curve. In other Josephson amplifiers frequency is tuned with flux-biased superconducting quantum interference device(s) [SQUID(s)]. The bandstop filter tunability could be implemented with a varactor diode.

From the design perspective, the SJA benefits from straightforward Langevin simulation of the electric circuit. However, a full analytical description of the system, including a JJ in the finite voltage state, is elusive. By contrast, developing the theory of an RF pumped amplifier is easier since the junctions are in the zero voltage state. In spite of the listed drawbacks, the SJA showed unexpected features of non-linear Josephson dynamics. At a "self-organized" SJA operating point the noise performance was near the quantum limit.

New kinetic impedance devices were demonstrated in this work. They harness the temperature or dc current sensitivity of the kinetic impedance in superconducting thin films. The kinetic inductance bolometer is a lightweight membrane heated by THz radiation. A superconducting meander line with a high fraction of kinetic inductance probes the membrane temperature, and the inductance is read out by a dispersive measurement. Employed frequently in this work, the dispersive readout involves a resonant matching network. The network transforms a change in impedance to changes in the eigenfrequency and quality factor of an RF resonator, quantities observable in RF transmission measurements.

The bolometer experiments indicated suitability for terrestrial THz imaging. Future bolometers on a focal plane array will have to be designed together with optics in order to build, e.g., a security screening device. Con-

4. Summary and conclusions

cealed objects are detected because their radiation temperature is lower than that of the human body. The instrument is passive, requiring no coherent target illumination, and the acquired images are easy to interpret. The dispersive readout facilitates scale-up to large arrays due to the frequency multiplexability of the bolometers. It is anticipated that the bolometer noise, dominated by phonons, can be lowered by narrowing membrane suspensions while retaining mechanical robustness and high device yield. This, however, would require simultaneous reduction of membrane heat capacity in order not to reduce imaging speed. Electromagnetic simulations may facilitate optimization of the geometry of the resistive absorber of THz radiation. Uncooled semiconductor modules as passive THz receivers are only gradually becoming competitive against cryogenic sensors. Here, the key issues are related to transistor speed and low-frequency noise [88].

This work improved the state-of-the-art in kinetic inductance magnetometry. The kinetic inductance was distributed across a large superconducting pick-up loop for the magnetic field. Flux quantization in the loop generates a circulating shielding current that enhances the kinetic inductance. Kinetic inductance magnetometer (KIM) readout is similar to that of the bolometer, and shares its many advantages. For instance, frequency multiplexing may find use in biomagnetic measurements such as magnetoencephalography (MEG) [125] and its combination with ultralow-field magnetic resonance imaging (ULF MRI) [126, 103]. These techniques non-invasively map the temporal activity and structural data of the human brain, respectively.

The KIM has potential to challenge low- T_c SQUID sensors. While follow-up experiments are required to reach the intrinsic noise floor of the KIM, it was shown that the KIM is a versatile device. Inexpensive wafer-scale fabrication is possible. Unlike the SQUID, the KIM has a wide dynamic range, and its sensitivity to RF interference is negligible. These properties ease operation outside a magnetically shielded environment, and allow magnetic manipulation of measured samples (as in ULF MRI) without detector saturation. Ultrasensitive atomic magnetometers operated near room temperature [127, 128] are not practical enough at present to replace cryogenic sensor systems.

As a final topic of this work, superconducting transmon quantum bits (qubits) on a 2D circuit quantum electrodynamics (cQED) processor were studied. The transmons have a weakly anharmonic energy spectrum that originates from the Josephson effect. The drawback of the presence of a nearby third energy level is susceptibility to leakage outside the qubit subspace. The leakage induced by single-qubit microwave control pulses was investigated. The shorter the pulse duration, the larger the spectral weight at unwanted transitions. To maximize the number of control operations that fits within the qubit coherence time, pulse shaping is utilized.

The Wah-Wah (weak anharmonicity with average Hamiltonian) pulse shaping technique was demonstrated successfully. Wah-Wah mitigates not only internal leakage in the qubit addressed by the control, but also external

leakage in its frequency neighbour qubit. This is an asset for quantum processor scalability, as the control can be sent through a common feedline. Hence, Wah-Wah reduces the number of control lines connected to a cQED device. Wah-Wah has found immediate use in a five-transmon experiment that implements bit-flip error detection [50].

References

- [1] Tinkham, M. (1996). *Introduction to Superconductivity*. McGraw-Hill, New York, 2nd edition.
- [2] Van Duzer, T. & Turner, C. W. (1999). *Principles of Superconductive Devices and Circuits*. Prentice-Hall, Upper Saddle River, NJ, 2nd edition.
- [3] Josephson, B. D. (1962). Possible new effects in superconductive tunnelling. *Phys. Lett.*, **1**, 251 – 253.
URL [http://dx.doi.org/10.1016/0031-9163\(62\)91369-0](http://dx.doi.org/10.1016/0031-9163(62)91369-0)
- [4] Deaver, B. S. & Fairbank, W. M. (1961). Experimental Evidence for Quantized Flux in Superconducting Cylinders. *Phys. Rev. Lett.*, **7**, 43–46.
URL <http://link.aps.org/doi/10.1103/PhysRevLett.7.43>
- [5] Nielsen, M. A. & Chuang, I. L. (2000). *Quantum Computation and Quantum Information*. Cambridge University Press, Cambridge.
- [6] Devoret, M. H. & Schoelkopf, R. J. (2013). Superconducting Circuits for Quantum Information: An Outlook. *Science*, **339**, 1169–1174.
URL <http://dx.doi.org/10.1126/science.1231930>
- [7] Clarke, J. & Wilhelm, F. K. (2008). Superconducting quantum bits. *Nature*, **453**, 1031.
URL <http://dx.doi.org/10.1038/nature07128>
- [8] Castellanos-Beltran, M. A. & Lehnert, K. W. (2007). Widely tunable parametric amplifier based on a superconducting quantum interference device array resonator. *Appl. Phys. Lett.*, **91**, 083509.
URL <http://dx.doi.org/10.1063/1.2773988>
- [9] Bergeal, N., Schackert, F., Metcalfe, M., Vijay, R., Manucharyan, V. E., Frunzio, L., Prober, D. E., Schoelkopf, R. J., Girvin, S. M., & Devoret, M. H. (2010). Phase-preserving amplification near the quantum limit with a Josephson ring modulator. *Nature*, **465**, 64–68.
URL <http://dx.doi.org/10.1038/nature09035>

- [10] Hatridge, M., Vijay, R., Slichter, D. H., Clarke, J., & Siddiqi, I. (2011). Dispersive magnetometry with a quantum limited SQUID parametric amplifier. *Phys. Rev. B*, **83**, 134501.
URL <http://link.aps.org/doi/10.1103/PhysRevB.83.134501>
- [11] Mück, M. & McDermott, R. (2010). Radio-frequency amplifiers based on dc SQUIDS. *Supercond. Sci. Technol.*, **23**, 093001.
URL <http://stacks.iop.org/0953-2048/23/i=9/a=093001>
- [12] Schutjens, R., Abu Dagga, F., Egger, D. J., & Wilhelm, F. K. (2013). Single-qubit gates in frequency-crowded transmon systems. *Phys. Rev. A*, **88**, 052330.
URL <http://dx.doi.org/10.1103/PhysRevA.88.052330>
- [13] Koch, J., Yu, T. M., Gambetta, J., Houck, A. A., Schuster, D. I., Majer, J., Blais, A., Devoret, M. H., Girvin, S. M., & Schoelkopf, R. J. (2007). Charge-insensitive qubit design derived from the Cooper pair box. *Phys. Rev. A*, **76**, 042319.
URL <http://link.aps.org/doi/10.1103/PhysRevA.76.042319>
- [14] Motzoi, F., Gambetta, J. M., Rebentrost, P., & Wilhelm, F. K. (2009). Simple Pulses for Elimination of Leakage in Weakly Nonlinear Qubits. *Phys. Rev. Lett.*, **103**, 110501.
URL <http://link.aps.org/doi/10.1103/PhysRevLett.103.110501>
- [15] Wilson, C. M. & Prober, D. E. (2004). Quasiparticle number fluctuations in superconductors. *Phys. Rev. B*, **69**, 094524.
URL <http://link.aps.org/doi/10.1103/PhysRevB.69.094524>
- [16] de Visser, P. J., Baselmans, J. J. A., Diener, P., Yates, S. J. C., Endo, A., & Klapwijk, T. M. (2011). Number Fluctuations of Sparse Quasiparticles in a Superconductor. *Phys. Rev. Lett.*, **106**, 167004.
URL <http://dx.doi.org/10.1103/PhysRevLett.106.167004>
- [17] Day, P. K., LeDuc, H. G., Mazin, B. A., Vayonakis, A., & Zmuidzinas, J. (2003). A broadband superconducting detector suitable for use in large arrays. *Nature*, **425**, 817–821.
URL <http://dx.doi.org/10.1038/nature02037>
- [18] Sayers, J., Bockstiegel, C., Brugger, S., Czakon, N. G., Day, P. K., Downes, T. P., Duan, R. P., Gao, J., Gill, A. K., Glenn, J., Golwala, S. R., Hollister, M. I., Lam, A., LeDuc, H. G., Maloney, P. R., Mazin, B. A., McHugh, S. G., Miller, D. A., Mroczkowski, A. K., Noroozian, O., Nguyen, H. T., Schlaerth, J. A., Siegel, S. R., Vayonakis, A., Wilson, P. R., & Zmuidzinas, J. (2014). The status of MUSIC: the multiwavelength sub-millimeter inductance camera. *Proc. SPIE*, **9153**, 915304.
URL <http://dx.doi.org/10.1117/12.2055444>

- [19] Catalano, A., Calvo, M., Ponthieu, N., Adam, R., Adane, A., Ade, P., André, P., Beelen, A., Belier, B., Benoît, A., Bideaud, A., Billot, N., Boudou, N., Bourrion, O., Coiffard, G., Comis, B., D'Addabbo, A., Désert, F.-X., Doyle, S., Goupy, J., Kramer, C., Leclercq, S., Macías-Pérez, J. F., Martino, J., Mauskopf, P., Mayet, F., Monfardini, A., Pajot, F., Pascale, E., Perotto, L., Revéret, V., Rodriguez, L., Savini, G., Schuster, K., Sievers, A., Tucker, C., & Zylka, R. (2014). Performance and calibration of the NIKA camera at the IRAM 30 m telescope. *A&A*, **569**, A9.
URL <http://dx.doi.org/10.1051/0004-6361/201423557>
- [20] Giazotto, F., Heikkilä, T. T., Luukanen, A., Savin, A. M., & Pekola, J. P. (2006). Opportunities for mesoscopics in thermometry and refrigeration: physics and applications. *Rev. Mod. Phys.*, **78**, 217–274.
URL <http://dx.doi.org/10.1103/RevModPhys.78.217>
- [21] Zmuidzinas, J. (2012). Superconducting microresonators: Physics and Applications. *Annu. Rev. Condens. Matter Phys.*, **3**, 169–214.
URL <http://dx.doi.org/10.1146/annurev-conmatphys-020911-125022>
- [22] Meservey, R. & Tedrow, P. M. (1969). Measurements of the Kinetic Inductance of Superconducting Linear Structures. *J. Appl. Phys.*, **40**, 2028–2034.
URL <http://dx.doi.org/10.1063/1.1657905>
- [23] Goodkind, J. & Stolfa, D. (1970). The Superconducting Magnetic Flux Detector. *Rev. Sci. Instr.*, **41**, 799–807.
URL <http://dx.doi.org/10.1063/1.1684651>
- [24] Ayela, F., Bret, J. L., & Chaussy, J. (1995). Absolute magnetometer based on the high-frequency modulation of the kinetic inductance of a superconducting thin film. *J. Appl. Phys.*, **78**, 1334–1341.
URL <http://dx.doi.org/10.1063/1.360307>
- [25] Wellstood, F., Heiden, C., & Clarke, J. (1984). Integrated dc SQUID magnetometer with a high slew rate. *Rev. Sci. Instr.*, **55**, 952.
URL <http://dx.doi.org/10.1063/1.1137871>
- [26] Likharev, K. K. (1986). *Dynamics of Josephson Junctions and Circuits*. Gordon and Breach, New York.
- [27] Ryhänen, T., Seppä, H., Ilmoniemi, R., & Knuutila, J. (1989). SQUID Magnetometers for Low-Frequency Applications. *J. Low Temp. Phys.*, **76**, 287–386.
URL <http://dx.doi.org/10.1007/BF00681735>
- [28] Clarke, J. (1966). A superconducting galvanometer employing Josephson tunnelling. *Phil. Mag.*, **13**, 115–127.
URL <http://dx.doi.org/10.1080/14786436608211991>

- [29] Beyer, J., Drung, D., Kirste, A., Engert, J., Netsch, A., Fleischmann, A., & Enss, C. (2007). A Magnetic-Field-Fluctuation Thermometer for the mK Range Based on SQUID-Magnetometry. *IEEE Trans. Appl. Supercond.*, **17**, 760–763.
URL <http://dx.doi.org/10.1109/TASC.2007.898265>
- [30] Callen, H. B. & Welton, T. A. (1951). Irreversibility and Generalized Noise. *Phys. Rev.*, **83**, 34–40.
URL <http://link.aps.org/doi/10.1103/PhysRev.83.34>
- [31] Seppä, H., Kiviranta, M., & Grönberg, L. (1995). Dc SQUID based on unshunted Josephson junctions: experimental results. *IEEE Trans. Appl. Supercond.*, **5**, 3248–3251.
URL <http://dx.doi.org/10.1109/77.403284>
- [32] Pozar, D. M. (2012). *Microwave Engineering*. John Wiley & Sons, Hoboken, NJ, 4th edition.
- [33] Caves, C. M. (1982). Quantum limits on noise in linear amplifiers. *Phys. Rev. D*, **26**, 1817–1839.
URL <http://link.aps.org/doi/10.1103/PhysRevD.26.1817>
- [34] Clerk, A. A., Devoret, M. H., Girvin, S. M., Marquardt, F., & Schoelkopf, R. J. (2010). Introduction to quantum noise, measurement, and amplification. *Rev. Mod. Phys.*, **82**, 1155–1208.
URL <http://link.aps.org/doi/10.1103/RevModPhys.82.1155>
- [35] Yurke, B. & Buks, E. (2006). Performance of Cavity-Parametric Amplifiers, Employing Kerr Nonlinearities, in the Presence of Two-Photon Loss. *J. Lightwave Technol.*, **24**, 5054–5066.
URL <http://jlt.osa.org/abstract.cfm?URI=jlt-24-12-5054>
- [36] Eichler, C. (2013). *Experimental Characterization of Quantum Microwave Radiation and its Entanglement with a Superconducting Qubit*. PhD Dissertation, ETH Zürich.
- [37] Castellanos-Beltran, M. A., Irwin, K. D., Hilton, G. C., Vale, L. R., & Lehnert, K. W. (2008). Amplification and squeezing of quantum noise with a tunable Josephson metamaterial. *Nature Phys.*, **4**, 929–931.
URL <http://dx.doi.org/10.1038/nphys1090>
- [38] Mattis, D. C. & Bardeen, J. (1958). Theory of the Anomalous Skin Effect in Normal and Superconducting Metals. *Phys. Rev.*, **111**, 412–417.
URL <http://link.aps.org/doi/10.1103/PhysRev.111.412>
- [39] Barends, R. (2009). *Photon-Detecting Superconducting Resonators*. PhD Dissertation, Delft University of Technology.

- [40] de Visser, P. J. (2014). *Quasiparticle dynamics in aluminium superconducting microwave resonators*. PhD Dissertation, Delft University of Technology.
- [41] Gao, J., Zmuidzinas, J., Vayonakis, A., Day, P., Mazin, B., & Leduc, H. (2008). Equivalence of the Effects on the Complex Conductivity of Superconductor due to Temperature Change and External Pair Breaking. *J. Low Temp. Phys.*, **151**, 557–563.
URL <http://dx.doi.org/10.1007/s10909-007-9688-z>
- [42] Pearl, J. (1964). Current distribution in superconducting films carrying quantized fluxoids. *Appl. Phys. Lett.*, **5**, 65–66.
URL <http://dx.doi.org/10.1063/1.1754056>
- [43] Anthore, A., Pothier, H., & Esteve, D. (2003). Density of States in a Superconductor Carrying a Supercurrent. *Phys. Rev. Lett.*, **90**, 127001.
URL <http://link.aps.org/doi/10.1103/PhysRevLett.90.127001>
- [44] Fetter, A. L. & Walecka, J. D. (2003). *Quantum theory of many-particle Systems*. Dover, Mineola, NY.
- [45] Romijn, J., Klapwijk, T. M., Renne, M. J., & Mooij, J. E. (1982). Critical pair-breaking current in superconducting aluminum strips far below T_c . *Phys. Rev. B*, **26**, 3648–3655.
URL <http://link.aps.org/doi/10.1103/PhysRevB.26.3648>
- [46] Clem, J. R. & Kogan, V. G. (2012). Kinetic impedance and depairing in thin and narrow superconducting films. *Phys. Rev. B*, **86**, 174521.
URL <http://link.aps.org/doi/10.1103/PhysRevB.86.174521>
- [47] Hortensius, H. L., Driessen, E. F. C., Klapwijk, T. M., Berggren, K. K., & Clem, J. R. (2012). Critical-current reduction in thin superconducting films due to current crowding. *Appl. Phys. Lett.*, **100**, 182602.
URL <http://dx.doi.org/10.1063/1.4711217>
- [48] Vandersypen, L. M. K. & Chuang, I. L. (2005). NMR techniques for quantum control and computation. *Rev. Mod. Phys.*, **76**, 1037–1069.
URL <http://link.aps.org/doi/10.1103/RevModPhys.76.1037>
- [49] Còrcoles, A. D., Magesan, E., Srinivasan, S. J., Cross, A. W., Steffen, M., Gambetta, J. M., & Chow, J. M. (2015). Demonstration of a quantum error detection code using a square lattice of four superconducting qubits. *Nat. Commun.*, **6**, 6979.
URL <http://dx.doi.org/10.1038/ncomms7979>
- [50] Ristè, D., Poletto, S., Huang, M.-Z., Bruno, A., Vesterinen, V., Saira, O.-P., & DiCarlo, L. (2015). Detecting bit-flip errors in a logical qubit using stabilizer measurements. *Nat. Commun.*, **6**, 6983.
URL <http://dx.doi.org/10.1038/ncomms7983>

- [51] Kelly, J., Barends, R., Fowler, A. G., Megrant, A., Jeffrey, E., White, T. C., Sank, D., Mutus, J. Y., Campbell, B., Chen, Y., Chen, Z., Chiaro, B., Dunsworth, A., Hoi, I.-C., Neill, C., O'Malley, P. J. J., Quintana, C., Roushan, P., Vainsencher, A., Wenner, J., Cleland, A. N., & Martinis, J. M. (2015). State preservation by repetitive error detection in a superconducting quantum circuit. *Nature*, **519**, 66–69.
URL <http://dx.doi.org/10.1038/nature14270>
- [52] Fowler, A. G., Mariantoni, M., Martinis, J. M., & Cleland, A. N. (2012). Surface codes: Towards practical large-scale quantum computation. *Phys. Rev. A*, **86**, 032324.
URL <http://link.aps.org/doi/10.1103/PhysRevA.86.032324>
- [53] Barends, R., Kelly, J., Megrant, A., Veitia, A., Sank, D., Jeffrey, E., White, T. C., Mutus, J., Fowler, A. G., Campbell, B., Chen, Y., Chen, Z., Chiaro, B., Dunsworth, A., Neill, C., O'Malley, P., Roushan, P., Vainsencher, A., Wenner, J., Korotkov, A. N., Cleland, A. N., & Martinis, J. M. (2014). Superconducting quantum circuits at the surface code threshold for fault tolerance. *Nature*, **508**, 500–503.
URL <http://dx.doi.org/10.1038/nature13171>
- [54] You, J. Q. & Nori, F. (2005). Superconducting circuits and quantum information. *Phys. Today*, **58**, 42–47.
URL <http://dx.doi.org/10.1063/1.2155757>
- [55] Vion, D., Aassime, A., Cottet, A., Joyez, P., Pothier, H., Urbina, C., Esteve, D., & Devoret, M. H. (2002). Manipulating the Quantum State of an Electrical Circuit. *Science*, **296**, 886.
URL <http://dx.doi.org/10.1126/science.1069372>
- [56] Wallraff, A., Schuster, D. I., Blais, A., Frunzio, L., Majer, J., Devoret, M. H., Girvin, S. M., & Schoelkopf, R. J. (2005). Approaching Unit Visibility for Control of a Superconducting Qubit with Dispersive Readout. *Phys. Rev. Lett.*, **95**, 060501.
URL <http://link.aps.org/doi/10.1103/PhysRevLett.95.060501>
- [57] Schreier, J. A., Houck, A. A., Koch, J., Schuster, D. I., Johnson, B. R., Chow, J. M., Gambetta, J. M., Majer, J., Frunzio, L., Devoret, M. H., Girvin, S. M., & Schoelkopf, R. J. (2008). Suppressing charge noise decoherence in superconducting charge qubits. *Phys. Rev. B*, **77**, 180502.
URL <http://dx.doi.org/10.1103/PhysRevB.77.180502>
- [58] Fedorov, A., Steffen, L., Baur, M., da Silva, M. P., & Wallraff, A. (2012). Implementation of a Toffoli gate with superconducting circuits. *Nature*, **481**, 170–172.
URL <http://dx.doi.org/10.1038/nature10713>

- [59] Reed, M. D., DiCarlo, L., Nigg, S. E., Sun, L., Frunzio, L., Girvin, S. M., & Schoelkopf, R. J. (2012). Realization of Three-Qubit Quantum Error Correction with Superconducting Circuits. *Nature*, **482**, 382. URL <http://dx.doi.org/10.1038/nature10786>
- [60] Raimond, J. M., Brune, M., & Haroche, S. (2001). Manipulating quantum entanglement with atoms and photons in a cavity. *Rev. Mod. Phys.*, **73**, 565–582. URL <http://link.aps.org/doi/10.1103/RevModPhys.73.565>
- [61] Blais, A., Huang, R.-S., Wallraff, A., Girvin, S. M., & Schoelkopf, R. J. (2004). Cavity quantum electrodynamics for superconducting electrical circuits: An architecture for quantum computation. *Phys. Rev. A*, **69**, 062320. URL <http://dx.doi.org/10.1103/PhysRevA.69.062320>
- [62] Paik, H., Schuster, D. I., Bishop, L. S., Kirchmair, G., Catelani, G., Sears, A. P., Johnson, B. R., Reagor, M. J., Frunzio, L., Glazman, L. I., Girvin, S. M., Devoret, M. H., & Schoelkopf, R. J. (2011). Observation of high coherence in Josephson junction qubits measured in a three-dimensional circuit QED architecture. *Phys. Rev. Lett.*, **107**, 240501. URL <http://dx.doi.org/10.1103/PhysRevLett.107.240501>
- [63] Majer, J., Chow, J. M., Gambetta, J. M., Johnson, B. R., Schreier, J. A., Frunzio, L., Schuster, D. I., Houck, A. A., Wallraff, A., Blais, A., Devoret, M. H., Girvin, S. M., & Schoelkopf, R. J. (2007). Coupling superconducting qubits via a cavity bus. *Nature*, **449**, 443. URL <http://dx.doi.org/10.1038/nature06184>
- [64] Sillanpää, M. A., Park, J. I., & Simmonds, R. W. (2007). Coherent quantum state storage and transfer between two phase qubits via a resonant cavity. *Nature*, **449**, 438. URL <http://dx.doi.org/10.1038/nature06124>
- [65] Wallraff, A., Schuster, D. I., Blais, A., Frunzio, L., Huang, R.-S., Majer, J., Kumar, S., Girvin, S. M., & Schoelkopf, R. J. (2004). Strong coupling of a single photon to a superconducting qubit using circuit quantum electrodynamics. *Nature*, **431**, 162–167. URL <http://dx.doi.org/10.1038/nature02851>
- [66] Groen, J. P., Ristè, D., Tornberg, L., Cramer, J., de Groot, P. C., Picot, T., Johansson, G., & DiCarlo, L. (2013). Partial-Measurement Backaction and Nonclassical Weak Values in a Superconducting Circuit. *Phys. Rev. Lett.*, **111**, 090506. URL <http://link.aps.org/doi/10.1103/PhysRevLett.111.090506>

- [67] Fragner, A., Göppl, M., Fink, J. M., Baur, M., Bianchetti, R., Leek, P. J., Blais, A., & Wallraff, A. (2008). Resolving Vacuum Fluctuations in an Electrical Circuit by Measuring the Lamb Shift. *Science*, **322**, 1357–1360.
URL <http://dx.doi.org/10.1126/science.1164482>
- [68] Jaynes, E. & Cummings, F. (1963). Comparison of quantum and semiclassical radiation theories with application to the beam maser. *Proc. IEEE*, **51**, 89–109.
URL <http://dx.doi.org/10.1109/PROC.1963.1664>
- [69] Reed, M. (2013). *Entanglement and quantum error correction with superconducting qubits*. PhD Dissertation, Yale University.
- [70] Lucero, E., Kelly, J., Bialczak, R. C., Lenander, M., Mariantoni, M., Neeley, M., O’Connell, A. D., Sank, D., Wang, H., Weides, M., Wenner, J., Yamamoto, T., Cleland, A. N., & Martinis, J. M. (2010). Reduced phase error through optimized control of a superconducting qubit. *Phys. Rev. A*, **82**, 042339.
URL <http://dx.doi.org/10.1103/PhysRevA.82.042339>
- [71] Chow, J. M., DiCarlo, L., Gambetta, J. M., Motzoi, F., Frunzio, L., Girvin, S. M., & Schoelkopf, R. J. (2010). Optimized driving of superconducting artificial atoms for improved single-qubit gates. *Phys. Rev. A*, **82**, 040305.
URL <http://dx.doi.org/10.1103/PhysRevA.82.040305>
- [72] Gambetta, J. M., Motzoi, F., Merkel, S. T., & Wilhelm, F. K. (2011). Analytic control methods for high-fidelity unitary operations in a weakly nonlinear oscillator. *Phys. Rev. A*, **83**, 012308.
URL <http://dx.doi.org/10.1103/PhysRevA.83.012308>
- [73] Johnson, J. E., Macklin, C., Slichter, D. H., Vijay, R., Weingarten, E. B., Clarke, J., & Siddiqi, I. (2012). Heralded State Preparation in a Superconducting Qubit. *Phys. Rev. Lett.*, **109**, 050506.
URL <http://dx.doi.org/10.1103/PhysRevLett.109.050506>
- [74] Ristè, D., van Leeuwen, J. G., Ku, H.-S., Lehnert, K. W., & DiCarlo, L. (2012). Initialization by Measurement of a Superconducting Quantum Bit Circuit. *Phys. Rev. Lett.*, **109**, 050507.
URL <http://dx.doi.org/10.1103/PhysRevLett.109.050507>
- [75] Regal, C. A., Teufel, J. D., & Lehnert, K. W. (2008). Measuring nanomechanical motion with a microwave cavity interferometer. *Nat. Phys.*, **4**, 555–560.
URL <http://dx.doi.org/10.1038/nphys974>

- [76] Castellanos-Beltran, M., Irwin, K., Vale, L., Hilton, G., & Lehnert, K. (2009). Bandwidth and Dynamic Range of a Widely Tunable Josephson Parametric Amplifier. *IEEE Trans. Appl. Supercond.*, **19**, 944–947.
URL <http://dx.doi.org/10.1109/TASC.2009.2018119>
- [77] Ribeill, G. J., Hover, D., Chen, Y.-F., Zhu, S., & McDermott, R. (2011). Superconducting low-inductance undulatory galvanometer microwave amplifier: Theory. *Journal of Applied Physics*, **110**, 103901.
URL <http://dx.doi.org/10.1063/1.3660217>
- [78] Liu, Y., Srinivasan, S. J., Hover, D., Zhu, S., McDermott, R., & Houck, A. A. (2014). High fidelity readout of a transmon qubit using a superconducting low-inductance undulatory galvanometer microwave amplifier. *New Journal of Physics*, **16**, 113008.
URL <http://stacks.iop.org/1367-2630/16/i=11/a=113008>
- [79] McHugh, S., Mazin, B. A., Serfass, B., Meeker, S., O'Brien, K., Duan, R., Raffanti, R., & Werthimer, D. (2012). A readout for large arrays of microwave kinetic inductance detectors. *Rev. Sci. Instr.*, **83**, 044702.
URL <http://dx.doi.org/10.1063/1.3700812>
- [80] Annunziata, A. J., Santavicca, D. F., Frunzio, L., Catelani, G., Rooks, M. J., Frydman, A., & Prober, D. E. (2010). Tunable superconducting nanoinductors. *Nanotechnology*, **21**, 445202.
URL <http://stacks.iop.org/0957-4484/21/i=44/a=445202>
- [81] Ho Eom, B., Day, P. K., LeDuc, H. G., & Zmuidzinas, J. (2012). A wideband, low-noise superconducting amplifier with high dynamic range. *Nat. Phys.*, **8**, 623–627.
URL <http://dx.doi.org/10.1038/nphys2356>
- [82] Bockstiegel, C., Gao, J., Vissers, M., Sandberg, M., Chaudhuri, S., Sanders, A., Vale, L., Irwin, K., & Pappas, D. (2014). Development of a Broadband NbTiN Traveling Wave Parametric Amplifier for MKID Readout. *J. Low Temp. Phys.*, **176**, 476–482.
URL <http://dx.doi.org/10.1007/s10909-013-1042-z>
- [83] Erickson, R. P., Vissers, M. R., Sandberg, M., Jefferts, S. R., & Pappas, D. P. (2014). Frequency Comb Generation in Superconducting Resonators. *Phys. Rev. Lett.*, **113**, 187002.
URL <http://link.aps.org/doi/10.1103/PhysRevLett.113.187002>
- [84] de Visser, P. J., Baselmans, J. J. A., Yates, S. J. C., Diener, P., Endo, A., & Klapwijk, T. M. (2012). Microwave-induced excess quasiparticles in superconducting resonators measured through correlated con-

- ductivity fluctuations. *Appl. Phys. Lett.*, **100**, 162601.
 URL <http://dx.doi.org/10.1063/1.4704151>
- [85] de Visser, P. J., Baselmans, J. J. A., Bueno, J., Llombart, N., & Klapwijk, T. M. (2014). Fluctuations in the electron system of a superconductor exposed to a photon flux. *Nat. Commun.*, **5**, 3130.
 URL <http://dx.doi.org/10.1038/ncomms4130>
- [86] Luukanen, A., Appleby, R., Kemp, M., & Salmon, N. (2013). Millimeter-Wave and Terahertz Imaging in Security Applications. In Peiponen, K.-E., Zeitler, A., & Kuwata-Gonokami, M., editors, *Terahertz Spectroscopy and Imaging*, volume 171 of *Springer Series in Optical Sciences*, pages 491–520. Springer Berlin Heidelberg.
 URL http://dx.doi.org/10.1007/978-3-642-29564-5_19
- [87] Samoska, L. (2011). An Overview of Solid-State Integrated Circuit Amplifiers in the Submillimeter-Wave and THz Regime. *IEEE Trans. Terahertz Sci. Technol.*, **1**, 9–24.
 URL <http://dx.doi.org/10.1109/TTHZ.2011.2159558>
- [88] Grossman, E., Leong, K., Mei, X., & Deal, W. (2014). Low-Frequency Noise and Passive Imaging With 670 GHz HEMT Low-Noise Amplifiers. *IEEE Trans. Terahertz Sci. Technol.*, **4**, 749–752.
 URL <http://dx.doi.org/10.1109/TTHZ.2014.2352035>
- [89] McDonald, D. G. (1987). Novel superconducting thermometer for bolometric applications. *Applied Physics Letters*, **50**, 775–777.
 URL <http://dx.doi.org/10.1063/1.98042>
- [90] Seppä, H. (2001). Superconducting transition-edge bolometer in a resistive and in an inductive mode. *IEEE Trans. Appl. Supercond.*, **11**, 759–761.
 URL <http://dx.doi.org/10.1109/77.919456>
- [91] Lindeman, M. A. (2014). Resonator-bolometer theory, microwave read out, and kinetic inductance bolometers. *J. Appl. Phys.*, **116**, 024506.
 URL <http://dx.doi.org/10.1063/1.4890018>
- [92] Lindeman, M. A., Eom, B. H., Day, P. K., Swenson, L. J., Wernis, R., LeDuc, H. G., & Zmuidzinas, J. (2014). AC Bolometer Theory and Measurements of Kinetic Inductance Bolometer-Resonators. *J. Low Temp. Phys.*, **176**, 511–517.
 URL <http://dx.doi.org/10.1007/s10909-013-1008-1>
- [93] Lindeman, M. A., Bonetti, J. A., Bumble, B., Day, P. K., Eom, B. H., Holmes, W. A., & Kleinsasser, A. W. (2014). Arrays of membrane isolated yttrium-barium-copper-oxide kinetic inductance bolometers.

- J. Appl. Phys.*, **115**, 234509.
 URL <http://dx.doi.org/10.1063/1.4884437>
- [94] Arndt, M., Wuensch, S., Kuzmin, A., Anders, S., May, T., Schubert, M., Meyer, H., & Siegel, M. (2015). Novel Detection Scheme for Cryogenic Bolometers With High Sensitivity and Scalability. *IEEE Trans. Appl. Supercond.*, **25**, 1–5.
 URL <http://dx.doi.org/10.1109/TASC.2014.2363413>
- [95] Swenson, L. J., Day, P. K., Eom, B. H., Leduc, H. G., Llombart, N., McKenney, C. M., Noroozian, O., & Zmuidzinas, J. (2013). Operation of a titanium nitride superconducting microresonator detector in the nonlinear regime. *J. Appl. Phys.*, **113**, 104501.
 URL <http://dx.doi.org/10.1063/1.4794808>
- [96] de Visser, P. J., Withington, S., & Goldie, D. J. (2010). Readout-power heating and hysteretic switching between thermal quasiparticle states in kinetic inductance detectors. *J. Appl. Phys.*, **108**, 114504.
 URL <http://dx.doi.org/10.1063/1.3517152>
- [97] Mather, J. C. (1982). Bolometer noise: nonequilibrium theory. *Appl. Opt.*, **21**, 1125–1129.
 URL <http://dx.doi.org/10.1364/AO.21.001125>
- [98] Dietlein, C., Popović, Z., & Grossman, E. N. (2008). Aqueous black-body calibration source for millimeter-wave/terahertz metrology. *Appl. Opt.*, **47**, 5604–5615.
 URL <http://dx.doi.org/10.1364/AO.47.005604>
- [99] Luukanen, A., Grossman, E., Miller, A. J., Heliö, P., Penttilä, J., Sipola, H., & Seppä, H. (2006). An Ultra-Low Noise Superconducting Antenna-Coupled Microbolometer With a Room-Temperature Read-Out. *IEEE Microwave Wireless Comp. Lett.*, **16**, 464–466.
 URL <http://dx.doi.org/10.1109/LMWC.2006.879483>
- [100] Grossman, E., Dietlein, C., Ala-Laurinaho, J., Leivo, M., Grönberg, L., Grönholm, M., Lappalainen, P., Rautiainen, A., Tamminen, A., & Luukanen, A. (2010). Passive terahertz camera for standoff security screening. *Appl. Opt.*, **49**, E106–E120.
 URL <http://ao.osa.org/abstract.cfm?URI=ao-49-19-E106>
- [101] Drung, D. (2003). High- T_c and low- T_c dc SQUID electronics. *Supercond. Sci. Technol.*, **16**, 1320.
 URL <http://stacks.iop.org/0953-2048/16/i=12/a=002>
- [102] Luomahaara, J., Vesanen, P. T., Penttilä, J., Nieminen, J. O., Dabek, J., Simola, J., Kiviranta, M., Grönberg, L., Zevenhoven, C. J., Ilmoniemi, R. J., & Hassel, J. (2011). All-planar SQUIDs and pickup

- coils for combined MEG and MRI. *Supercond. Sci. Technol.*, **24**, 075020.
 URL <http://stacks.iop.org/0953-2048/24/i=7/a=075020>
- [103] Luomahaara, J. (2014). *Advances in superconducting sensors for medical imaging and metrology*. PhD Dissertation, Aalto University.
- [104] McDermott, R., Lee, S., ten Haken, B., Trabesinger, A. H., Pines, A., & Clarke, J. (2004). Microtesla MRI with a superconducting quantum interference device. *Proc. Natl. Acad. Sci. U.S.A.*, **101**, 7857–7861.
 URL <http://www.pnas.org/content/101/21/7857.abstract>
- [105] Kraus, R. H., Jr., Espy, M. A., Magnelind, P. E., & Volegov, P. L. (2014). *Ultra-Low Field Nuclear Magnetic Resonance: A New MRI Regime*. Oxford University Press, New York.
- [106] Ishikawa, N., Nagata, K., Sato, H., Kasai, N., & Kiryu, S. (1993). Effect of RF interference on characteristics of DC SQUID system. *IEEE Trans. Appl. Supercond.*, **3**, 1910–1913.
 URL <http://dx.doi.org/10.1109/77.233588>
- [107] Mück, M., Dechert, J., Gail, J., Kreutzbeck, M., Schöne, S., & Weidl, R. (1995). Response of radio frequency superconducting quantum interference devices to electromagnetic interference. *Rev. Sci. Instr.*, **66**, 4690.
 URL <http://dx.doi.org/10.1063/1.1145308>
- [108] Clarke, J. & Braginski, A. I. (2004). *The SQUID Handbook Vol. I*. WILEY-VCH Verlag GmbH & Co. KGaA, Weinheim, Germany.
- [109] Ferrari, M. J., Kingston, J. J., Wellstood, F. C., & Clarke, J. (1991). Flux noise from superconducting $\text{YBa}_2\text{Cu}_3\text{O}_{7-x}$ flux transformers. *Appl. Phys. Lett.*, **58**, 1106–1108.
 URL <http://dx.doi.org/10.1063/1.104386>
- [110] Paladino, E., Galperin, Y. M., Falci, G., & Altshuler, B. L. (2014). $1/f$ noise: Implications for solid-state quantum information. *Rev. Mod. Phys.*, **86**, 361–418.
 URL <http://link.aps.org/doi/10.1103/RevModPhys.86.361>
- [111] De, A. (2014). Ising-Glauber Spin Cluster Model for Temperature-Dependent Magnetization Noise in SQUIDS. *Phys. Rev. Lett.*, **113**, 217002.
 URL <http://link.aps.org/doi/10.1103/PhysRevLett.113.217002>
- [112] Zahn, M. (2003). *Electromagnetic Field Theory: A Problem Solving Approach*. Krieger Publishing Company, Malabar, FL.

- [113] *FastHenry*, Computational Prototyping Group, Massachusetts Institute of Technology.
URL http://www.rle.mit.edu/cpg/research_codes.htm
- [114] Stan, G., Field, S. B., & Martinis, J. M. (2004). Critical Field for Complete Vortex Expulsion from Narrow Superconducting Strips. *Phys. Rev. Lett.*, **92**, 097003.
URL <http://link.aps.org/doi/10.1103/PhysRevLett.92.097003>
- [115] Bianchetti, R., Filipp, S., Baur, M., Fink, J., Lang, C., Steffen, L., Boissonneault, M., Blais, A., & Wallraff, A. (2010). Control and Tomography of a Three Level Superconducting Artificial Atom. *Phys. Rev. Lett.*, **105**, 223601.
URL <http://prl.aps.org/abstract/PRL/v105/i22/e223601>
- [116] Knill, E., Leibfried, D., Reichle, R., Britton, J., Blakestad, R. B., Jost, J. D., Langer, C., Ozeri, R., Seidelin, S., & Wineland, D. J. (2008). Randomized benchmarking of quantum gates. *Phys. Rev. A*, **77**, 012307.
URL <http://dx.doi.org/10.1103/PhysRevA.77.012307>
- [117] Chow, J. M., Gambetta, J. M., Tornberg, L., Koch, J., Bishop, L. S., Houck, A. A., Johnson, B. R., Frunzio, L., Girvin, S. M., & Schoelkopf, R. J. (2009). Randomized Benchmarking and Process Tomography for Gate Errors in a Solid-State Qubit. *Phys. Rev. Lett.*, **102**, 090502.
URL <http://dx.doi.org/10.1103/PhysRevLett.102.090502>
- [118] Kelly, J., Barends, R., Campbell, B., Chen, Y., Chen, Z., Chiaro, B., Dunsworth, A., Fowler, A. G., Hoi, I.-C., Jeffrey, E., Megrant, A., Mutus, J., Neill, C., O'Malley, P. J. J., Quintana, C., Roushan, P., Sank, D., Vainsencher, A., Wenner, J., White, T. C., Cleland, A. N., & Martinis, J. M. (2014). Optimal Quantum Control Using Randomized Benchmarking. *Phys. Rev. Lett.*, **112**, 240504.
URL <http://dx.doi.org/10.1103/PhysRevLett.112.240504>
- [119] Magesan, E., Gambetta, J. M., Johnson, B. R., Ryan, C. A., Chow, J. M., Merkel, S. T., da Silva, M. P., Keefe, G. A., Rothwell, M. B., Ohki, T. A., Ketchen, M. B., & Steffen, M. (2012). Efficient Measurement of Quantum Gate Error by Interleaved Randomized Benchmarking. *Phys. Rev. Lett.*, **109**, 080505.
URL <http://dx.doi.org/10.1103/PhysRevLett.109.080505>
- [120] Steffen, M., Vandersypen, L. M. K., & Chuang, I. L. (2000). Simultaneous soft pulses applied at nearby frequencies. *J. Magn. Reson.*, **146**, 369.
URL <http://dx.doi.org/10.1006/jmre.2000.2178>

- [121] Chow, J. M., Gambetta, J. M., Córcoles, A. D., Merkel, S. T., Smolin, J. A., Rigetti, C., Poletto, S., Keefe, G. A., Rothwell, M. B., Rozen, J. R., Ketchen, M. B., & Steffen, M. (2012). Universal Quantum Gate Set Approaching Fault-Tolerant Thresholds with Superconducting Qubits. *Phys. Rev. Lett.*, **109**, 060501.
URL <http://dx.doi.org/10.1103/PhysRevLett.109.060501>
- [122] Abdo, B., Sliwa, K., Shankar, S., Hatridge, M., Frunzio, L., Schoelkopf, R., & Devoret, M. (2014). Josephson Directional Amplifier for Quantum Measurement of Superconducting Circuits. *Phys. Rev. Lett.*, **112**, 167701.
URL <http://link.aps.org/doi/10.1103/PhysRevLett.112.167701>
- [123] Mutus, J. Y., White, T. C., Barends, R., Chen, Y., Chen, Z., Chiaro, B., Dunsworth, A., Jeffrey, E., Kelly, J., Megrant, A., Neill, C., O'Malley, P. J. J., Roushan, P., Sank, D., Vainsencher, A., Wenner, J., Sundqvist, K. M., Cleland, A. N., & Martinis, J. M. (2014). Strong environmental coupling in a Josephson parametric amplifier. *Appl. Phys. Lett.*, **104**, 263513.
URL <http://dx.doi.org/10.1063/1.4886408>
- [124] O'Brien, K., Macklin, C., Siddiqi, I., & Zhang, X. (2014). Resonant Phase Matching of Josephson Junction Traveling Wave Parametric Amplifiers. *Phys. Rev. Lett.*, **113**, 157001.
URL <http://dx.doi.org/10.1103/PhysRevLett.113.157001>
- [125] Hämäläinen, M., Hari, R., Ilmoniemi, R. J., Knuutila, J., & Lounasmaa, O. V. (1993). Magnetoencephalography—theory, instrumentation, and applications to noninvasive studies of the working human brain. *Rev. Mod. Phys.*, **65**, 413–497.
URL <http://link.aps.org/doi/10.1103/RevModPhys.65.413>
- [126] Parkkonen, L., Ilmoniemi, R., Lin, F.-H., & Espy, M. (2014). Ultra-Low-Field MRI and Its Combination with MEG. In Supek, S. & Aine, C. J., editors, *Magnetoencephalography*, pages 941–972. Springer Berlin Heidelberg.
URL http://dx.doi.org/10.1007/978-3-642-33045-2_46
- [127] Savukov, I., Zotev, V., Volegov, P., Espy, M., Matlashov, A., Gomez, J., & Jr., R. K. (2009). MRI with an atomic magnetometer suitable for practical imaging applications. *J. Magn. Reson.*, **199**, 188–191.
URL <http://dx.doi.org/10.1016/j.jmr.2009.04.012>
- [128] Kim, K., Begus, S., Xia, H., Lee, S.-K., Jazbinsek, V., Trontelj, Z., & Romalis, M. V. (2014). Multi-channel atomic magnetometer for magnetoencephalography: A configuration study. *NeuroImage*, **89**, 143–

151.

URL <http://dx.doi.org/10.1016/j.neuroimage.2013.10.040>

Appendices

Appendix A: KIM dynamic range

The general forms of the quadrature responsivities (pictured in Fig. 3 of Publication IV), where the carrier can be off-resonant, are

$$\left| \frac{\partial V_I}{\partial B_0} \right| \approx \frac{4|x|}{(1+4x^2)^2} \left| \frac{\partial V_{\text{out}}}{\partial B_0} \right|_{\omega_{\text{rf}}=\omega_r}, \quad (1)$$

$$\left| \frac{\partial V_Q}{\partial B_0} \right| \approx \frac{|1-4x^2|}{(1+4x^2)^2} \left| \frac{\partial V_{\text{out}}}{\partial B_0} \right|_{\omega_{\text{rf}}=\omega_r}. \quad (2)$$

The normalized frequency offset is $x = (\omega - \omega_r)/\kappa$, with Q_t evaluated at the screening current I_s of the operation point. The responsivity has decreased to 1/2 from its maximum [Eq. (3.8)] at frequencies $\omega_r(1 \pm 1/(2\sqrt{3}Q_t))$. The corresponding inductances are approximately $L_{\text{tot}}(1 \mp 1/(\sqrt{3}Q_t))$, and screening currents I_s^\pm . L_{tot} is also evaluated at the specific I_s . It follows that

$$(I_s^-)^2 + (I_s^+)^2 = 2I_s^2, \quad (3)$$

$$(I_s^-)^2 - (I_s^+)^2 = \frac{8L_{\text{tot}}}{\sqrt{3}Q_t L_{k0}}. \quad (4)$$

The equation for the dynamic range, by manipulation of Eq. (3.7), reads

$$\Delta B = \frac{(L_g + L_{k0})(I_s^- - I_s^+) + \frac{L_{k0}}{(I_s^*)^2}((I_s^-)^3 - (I_s^+)^3)}{A}. \quad (5)$$

At $I_s > 0$, where the KIM is responsive to the applied flux, it is relatively safe to approximate $I_s^- + I_s^+ \approx 2I_s$, and the final result from the combination of above formulae is

$$\Delta B \approx \frac{4L_{\text{tot}}I_s^{*2}}{\sqrt{3}Q_t A I_s} (1/\alpha_k + 3(I_s/I_s^*)^2). \quad (6)$$

Appendix B: Errata

- In the main text of Publication IV, the Cooper pair density should be $n_s/2$, that is, one half of n_s which is the density of paired electrons.
- In Publication IV, equation (3) should read

$$Z \approx \frac{Z_0 Q_{\text{ext}}}{2Q_i} (1 + j2Q_i(\omega - \omega_0)/\omega_0).$$

- In the Methods section of Publication IV, the kinetic inductance fraction α_k should be defined and included in the expression for the intrinsic quality factor: $Q_i = n_s/(\alpha_k n_{\text{qp}} \omega_0 \tau_{\text{qp}})$.
- In the Supplement of Publication V, the first line of equation (S8) should read

$$\Delta_a \hat{\Pi}_2^a + (\delta - \Delta_b) \hat{\Pi}_1^b + (2\delta - \Delta_b) \hat{\Pi}_2^b.$$

PUBLICATION I

**Josephson junction microwave amplifier
in self-organized noise
compression mode**

Sci. Rep. 2, 276.

Copyright 2012 Nature Publishing Group.
Reprinted with permission from the publisher.



Josephson junction microwave amplifier in self-organized noise compression mode

Pasi Lähteenmäki^{1*}, Visa Vesterinen^{2*}, Juha Hassel², Heikki Seppä², & Pertti Hakonen¹

¹Low Temperature Laboratory, Aalto University, P.O.Box 15100, 00076 AALTO, Finland, ²VTT Technical Research Centre of Finland, P.O. Box 1000, 02044 VTT, Finland.

SUBJECT AREAS:

ELECTRONIC MATERIALS
AND DEVICES

APPLIED PHYSICS

SUPERCONDUCTING MATERIALS

QUANTUM PHYSICS

Received
13 September 2011

Accepted
31 January 2012

Published
20 February 2012

Correspondence and
requests for materials
should be addressed to
P.L. (pasi.lahteenmaki@tll.tkk.fi)
or P.H. (pertti.hakonen@aalto.fi)

*These authors
contributed equally.

The fundamental noise limit of a phase-preserving amplifier at frequency $\omega/2\pi$ is the standard quantum limit $T_q = \hbar\omega/2k_B$. In the microwave range, the best candidates have been amplifiers based on superconducting quantum interference devices (reaching the noise temperature $T_n \sim 1.8T_q$ at 700 MHz), and non-degenerate parametric amplifiers (reaching noise levels close to the quantum limit $T_n \approx T_q$ at 8 GHz). We introduce a new type of an amplifier based on the negative resistance of a selectively damped Josephson junction. Noise performance of our amplifier is limited by mixing of quantum noise from Josephson oscillation regime down to the signal frequency. Measurements yield nearly quantum-limited operation, $T_n = (3.2 \pm 1.0)T_q$ at 2.8 GHz, owing to self-organization of the working point. Simulations describe the characteristics of our device well and indicate potential for wide bandwidth operation.

The goal of quantum limited amplification at microwave frequencies has become increasingly important for superconducting qubits and nanoelectromechanical systems¹. The lowest noise temperatures with respect to the quantum noise have been achieved using nondegenerate parametric amplifiers based on superconducting quantum interference devices (SQUIDS)²⁻⁴. They yield a noise temperature T_n of about $(1.0 - 1.6) T_q$. Other implementations of near-quantum limited amplification have been realized by means of Josephson ring oscillators⁵, DC-SQUIDS^{6,7}, and parametric amplifiers based on Josephson junction arrays^{2,8-11}. Devices based on photon-assisted tunneling SIS-mixers yield $T_n = 1.2T_q$ ¹². However, these devices lack power gain but they do have a large gain in photon number due to conversion from high to low frequency.

Negative differential resistance devices, in particular tunnel diodes, have been used in the past to construct oscillators and amplifiers for microwave frequencies. These devices are capable of very fast operation. They were among the first ones to be used at microwave frequencies because they display little or no excess noise in the negative resistance bias region¹³. Here, we propose a negative-resistance amplifier based on an unshunted, single Josephson junction (JJ) operating in a noise compression mode. Unshunted junctions have been analyzed and demonstrated to work in SQUID circuits at low frequencies by Seppä et al.¹⁴. We have developed analogous concepts for high frequency operation. The present device differs markedly from previous implementations using unshunted Josephson devices due to the modified impedance environment.

Unshunted junctions are attractive as low-noise devices since they minimize fluctuations by avoiding unnecessary dissipation in the junction environment. In voltage-biased (V_b) operation, these devices can be considered as mixers between the signal frequency (ω_s , around a few GHz) and the Josephson frequency ($\omega_J = (2e/\hbar) V_b = 2\pi \times 10 - 300$ GHz) including sidebands¹⁵. A frequency-dependent environmental impedance can be employed for controlling mixing strengths (because the Josephson junction is a phase driven current generator) and the impedance makes the conversion between these two quantities.

Results

The fundamental macroscopic principle of our single junction amplifier (SJA) is that the intrinsic resistance of a JJ is negative over time scales much longer than $1/\omega_J$ ¹⁴ (as shown in Fig. 1a). This is usually hidden in weakly damped JJs since the negative-resistance branch is unstable. On the other hand, for strongly damped junctions, the total dynamic resistance is positive. This can be seen from the current-voltage IV characteristics $v_b = \sqrt{i_b^2 - 1}$ for a Josephson junction with negligible capacitance (valid for $i_b > 1$). Here $v_b = V_b/I_c R$ denotes the voltage scaled with critical current I_c and the shunt resistance R while $i_b = I_b/I_c$ is the dimensionless current. Solving for the current through the junction alone, $i_{JJ} = i_b - v_b$ (illustrated by the black

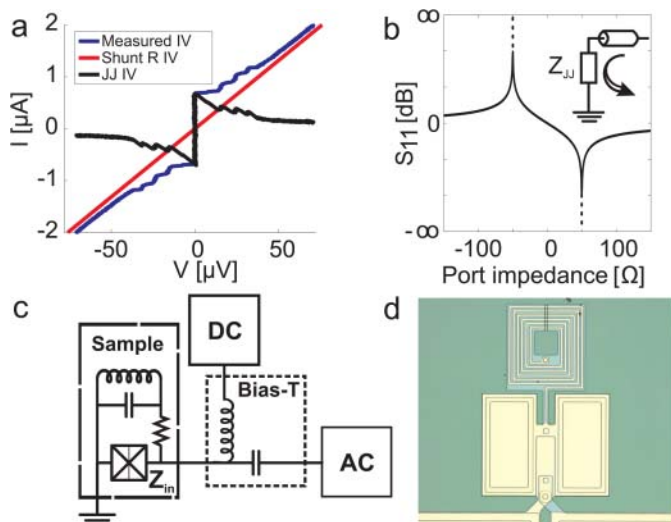


Figure 1 | a) Typical IV of a SJA (in blue); red and black curves indicate the division of I into shunt and junction currents, respectively. b) Reflection (scattering) amplitude S_{11} in a $Z_0 = 50 \Omega$ system as a function of the load impedance. c) Principal scheme of the SJA operation. d) Optical image of a SJA; the size of the image is approximately $270 \mu\text{m} \times 230 \mu\text{m}$.

curve in Fig. 1a), we get for the scaled dynamic resistance

$$r_d = \frac{R_d}{R} = \frac{1}{di_{JJ}/dv_b} = \frac{1}{di_b/dv_b - 1} \quad (1)$$

This yields $\sqrt{v_b^2 + 1}/(v_b - \sqrt{v_b^2 + 1})$, negative at all bias points.

The schematics of our SJA configuration is illustrated in Fig. 1c. To utilise the negative resistance of a JJ for amplification, stable operation has to be maintained by sufficient damping at all frequencies. The frequency-dependent damping is set in such a way that the external shunt damps the low ($\omega < \omega_s$, the signal frequency) and high ($\omega > \omega_s$) frequency dynamics, which ensures both stable DC bias and overdamped Josephson dynamics. In practice, we have realised this separation by mounting the shunt resistor in series with a bandstop filter whose center frequency is at the signal frequency ω_s ^{16,17}. The shunt capacitor is chosen large enough that it acts as a short at the Josephson frequency to ensure the high frequency dynamics and the IV curve are not modified. The stabilization in the stop band is provided by the postamplification circuit. The shunt circuit and the postamplification circuit together guarantee the stability of the device by generating a wide-band resistive environment for the JJ. Operated as a reflection amplifier, the power gain $|S_{11}(\omega)|^2 = |\Gamma(\omega)|^2$ is determined by the reflection coefficient

$$\Gamma(\omega) = (Z_{in}(\omega) - Z_0)/(Z_{in}(\omega) + Z_0), \quad (2)$$

where $Z_{in}(\omega)$ is the impedance of the JJ, the shunt and the series inductance; Z_0 is the impedance of the readout circuit. As seen from the curve in Fig. 1b, there is gain ($S_{11} > 0$ dB) at all values of negative resistance and a strong divergence around $Z_{in} = -Z_0$. In the stop-band of the shunt circuit, the input impedance $Z_{in}(\omega_s)$ consists of the JJ (and possibly of an LC impedance transformer): it is real and negative. For $|R_d| \gtrsim Z_0$, large gain with stable operation can be obtained. For operating conditions where $|R_d| \gg Z_0$ impedance transforming circuits are employed to change the reference level impedance Z_0 , e.g. from 50Ω typical for standard RF technology to a level of $1 \text{ k}\Omega$ which is a typical value of $|R_d|$ for small Josephson junctions at high bias voltages.

The dynamics of SQUID circuits can be analyzed using a Langevin type of differential equation for the phase variable φ across the Josephson junctions¹⁸. Good agreement of such Langevin analysis with measured experimental results has been obtained in the past^{19,20}.

In the semiclassical approach, the generalized Nyquist noise formula by Callen and Welton²¹ with the frequency dependence $0.5\hbar\omega \coth(\hbar\omega/2k_B T)$ is employed as the colored noise source in the differential equation^{19,22,23}. At the Josephson frequency, the semiclassical noise power per unit bandwidth is so large ($\propto \hbar\omega_j \gg k_B T$) that, after downmixing, it will have observable effects on the phase dynamics at the signal frequency ω_s . Since the noise at ω_s is cut off from the Josephson junction by the bandstop filter (see Fig. 1c), direct noise from the shunt is avoided and only the down-mixed noise is present in our device. The absence of direct noise ensures good noise characteristics for our SJA and this feature is one of the basic differences when comparing SJAs with traditional microwave SQUID amplifiers.

Experimental. Fig. 2 displays noise spectra measured on the device at different bias points. At low bias currents, the magnitude of the dynamic resistance $|R_d|$ is smaller than the environmental impedance in parallel to it, making the total damping impedance of the LC resonator in the shunt circuit negative. This leads to either spontaneous oscillations or saturation. The oscillations are highly nonlinear, which is manifested as higher harmonics in the spectra. The saturation shows up as vanishing response. As $|R_d|$ increases at higher bias points, the system is stabilized and the harmonics disappear since the device operates as a linear amplifier generating amplified noise at the output.

After finding the optimal stable bias point, the gain vs. frequency was recorded at several power levels. The maximum measured gain of the SJA was found to be 28.3 ± 0.2 dB. The measured power gain of the device is plotted in Fig. 3 at $P_{in} = -160$ dBm. The -1 dB compression point for P_{in} was found to be around -134 dBm; this yields a dynamic range of 70 dB as the input noise corresponds to -204 dBm. For the -3 dB bandwidth, we obtain $\text{BW} \approx 1$ MHz. However, the bandwidth depends very much on the bias voltage due to the variation of R_d along the IV-curve, indicating that fundamentally the device is capable of wideband gain. In the present experiments, we reached $|\Gamma|_{max} \times \text{BW} = 40$ MHz for the voltage gain - bandwidth product. The nominal parameters of the measured amplifier are given in Table I in the Methods section.

The inset in Fig. 3 displays the improvement of the signal to noise ratio when the SJA is switched on and operated at its maximum gain. Based on this improvement, we find that the input-referred noise power added by the amplifier is 220 ± 70 mK ($0.5\hbar\omega/k_B \coth(\hbar\omega/2k_B T) = 90$ mK originating from the source has been subtracted), which corresponds to $T_n \approx (3.2 \pm 1.0) T_q$. The best noise temperature was obtained at the largest gain of the SJA.

Theoretical. To theoretically model a single junction device with arbitrary, frequency-dependent environment with $0 < \beta_c = 2eR^2(\omega)I_c C/\hbar < 1$, we simulate numerically the electrical circuit on the basis of the DC and AC Josephson relations which define a nonlinear circuit element having the properties: $I_j = I_c \sin \varphi$ and $V = (\hbar/2e) \partial\varphi/\partial t$. We have compared our numerical simulations with analytic methods using an approximate model where we have adapted the resistively and capacitively shunted junction (RCSJ) approach to the modified environmental impedance of the SJA. Our numerical and analytic models take into account the Callen and Welton quantum noise from the environment semiclassically. Down-conversion of the noise at ω_j is the main quantity to be minimized for optimum performance.

The simulated power gain is included in Fig. 3 together with the experimental data. The theoretical gain curve is seen to follow the experimental behavior closely and it yields 42 MHz for the gain-bandwidth product. The simulated maximum gain amounts to 28.9 ± 0.5 dB. All these findings are in excellent agreement with the experimental data. Basically, the shape of the gain curve indicates that the amplification mechanism is based on mixing between ω_s and the sidebands of ω_j . This occurs along with the conversion from

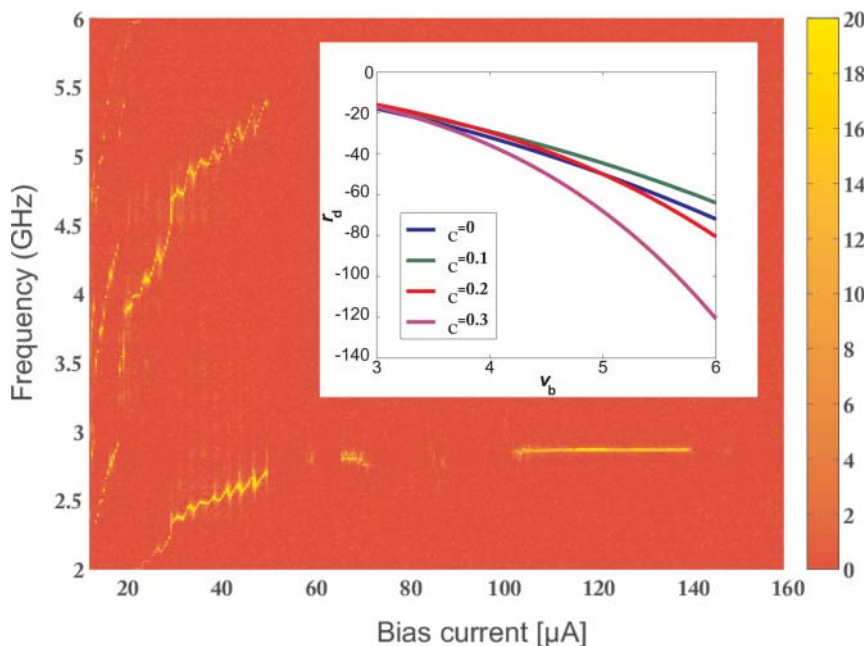


Figure 2 | Noise spectra of the device as function of the bias point; the reference level corresponds to $14 \text{ K } k_B$ and the power scale on the right is given in dB. The inset displays the dependence of r_d as a function of bias voltage for different values of β_C . Values between 0 and r_d^* lead to unstable behaviour; $r_d^* = -50$ without impedance transformer ($R = 1 \Omega$). There are no special features in the noise spectral density in the area below the inset.

down-mixed currents at ω_s to voltage by the shunt impedance (see the Supplementary material). For comparison, we have also calculated a linearized response curve where the Josephson junction has been replaced by a negative resistance of $R_d = -1370 \Omega$ from Eq. (1).

Our numerical simulations yield $T_n = 270 \pm 30 \text{ mK}$ which is close to the experimentally found $T_n = 220 \pm 70 \text{ mK}$. Hot-electron effects were taken into account by using the model of Ref. 24, on the basis of which we estimated the electronic temperature in the shunt to be $T_e \simeq 400 \text{ mK}$ instead of the base temperature 70 mK . The noise temperature is not very sensitive to hot electron effects when the shunt is fully blocked by the LC resonator at the center frequency. However, when going away from the center frequency, direct noise may leak

out from the shunt reducing the useful band to “a noise-temperature-limited” range. The simulated noise power spectrum and the corresponding T_n as a function of frequency are presented in Fig. 4.

In our analytic modeling, we have generalized the semiclassical treatment of Ref. 19 to finite capacitance C_J and combined the mixing analysis with the current-voltage characteristics derived in Ref. 23. For the noise analysis, we define a noise process $\varphi_s(t)$, band-limited near the signal frequency. Another noise process $\varphi_j(t)$ with $\langle \varphi_j(t)^2 \rangle \ll 1$ covers the Josephson frequency and one pair of sidebands ($\omega_j \pm \omega_s$). φ_j has a small variance because of the low impedance of the junction capacitor at high Josephson frequency. We expand $i_j = \sin \varphi(t) \approx \sin(\omega_j t + \varphi_s + \varphi_j)$ in order to describe the junction as a

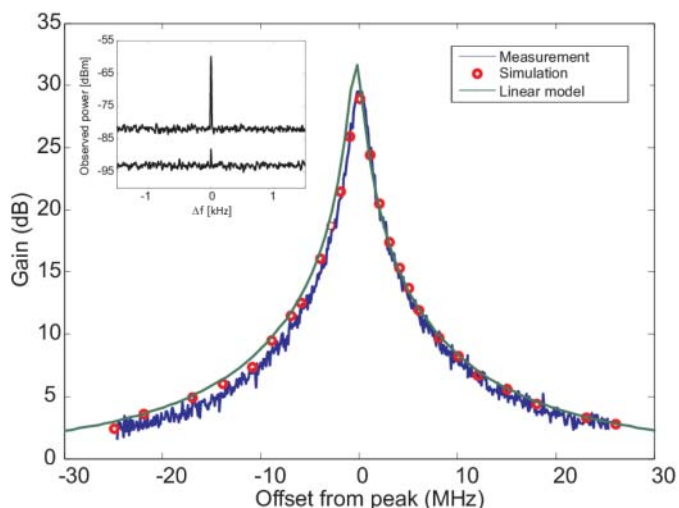


Figure 3 | Gain of the SJA as function of frequency at the optimal point of operation (blue, noisy curve). Results from our numerical simulation are denoted by open circles, while the smooth curve (green) illustrates the gain from a linearized electrical circuit model where the Josephson junction is replaced by a negative resistance of $R_d = -1370 \Omega$ from Eq. (1). Inset: Output noise spectra having the SJA off (lower trace) and on (at maximum gain).

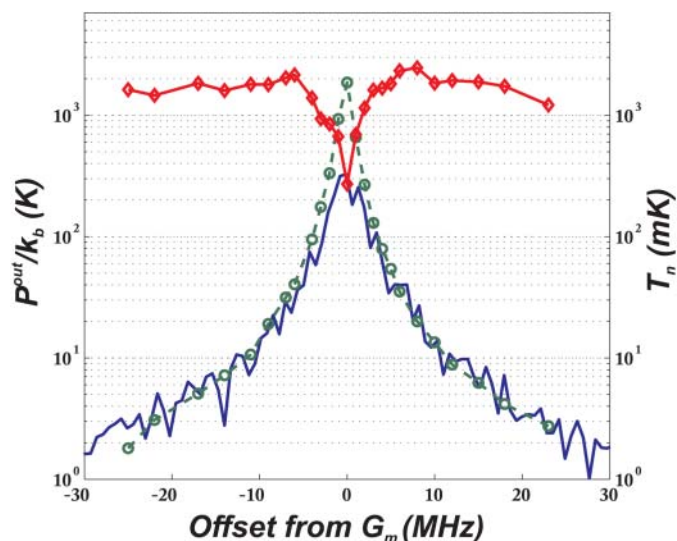


Figure 4 | The effective output noise temperature P_n^{out}/k_B (left scale) is compressed in the simulation (denoted by solid blue line) when compared with the product of the simulated gain ($G - 1$) and the uncompressed down-mixed noise of $2.4 \text{ K} \times k_B$ from Eq. 3 (○). After dividing the simulated output spectrum by the calculated gain, a clear dip is revealed in the input noise temperature (◇, right scale).

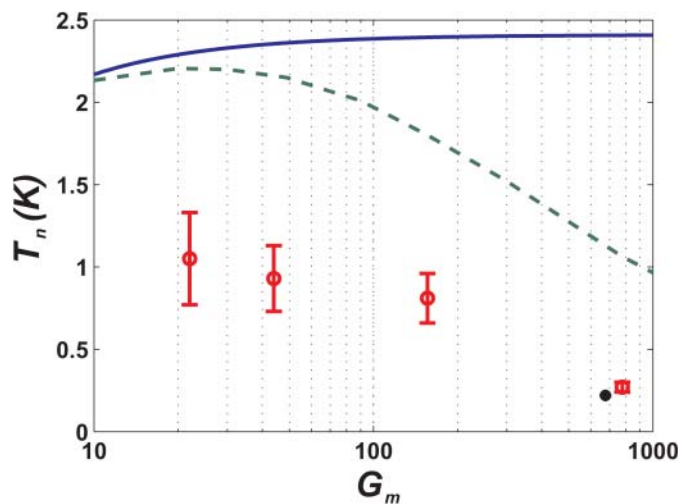


Figure 5 | Input noise temperature T_n vs. maximum gain of the SJA. The uncompressed T_n (Eq. (3) with $\xi = 1$, solid blue line) converges to 2.4 K at high gain. Compression suppressed T_n for the analytic model with two sidebands at $\omega_j \pm \omega_s$ is denoted by the dashed green line. Noise temperature from the simulations is depicted using open circles, and the error bars represent the statistical uncertainty in the simulated spectral density. The measurement result is marked by a filled circle (\bullet), while the standard quantum limit would be $T_q = \hbar\omega/2k_B = 70$ mK.

DC current generator plus two AC current noise generators: one at ω_s and the other around the Josephson frequency. In the Fourier plane, the AC Josephson relation and the impedance environments at low and high frequencies establish the down-mixing noise process. We denote the variance of the phase noise over the signal band by $\delta_s^2 = \langle \phi_s(t)^2 \rangle$. In our calculations, we expand $\exp(i\phi_s) \approx J_0(r) + i(2J_1(r)/r)\phi_s$ (which is a good approximation at small δ_s^2) but this breaks down when additional sidebands ($\omega_j \pm 2\omega_s$ and so on) become significant. These Bessel functions of the first kind have the phase noise amplitude r divided by the signal band. Ideally, r should follow the Rayleigh distribution. In our analysis, we treat separately the limit of small fluctuations, $\delta_s^2 \ll 1$, and the regime with $\delta_s^2 \geq 1$, in which noise compression effects appear. With large gain and resonantly boosted current-voltage conversion, the phase fluctuations will grow so much that the non-linearities begin to limit the gain, and the system is driven to a steady state where the down-mixing process becomes altered and significantly suppressed. The number of added quanta per unit band from mixed-down noise is derived in the Supplementary material:

$$\frac{k_B T_{\text{mix}}}{\hbar\omega_s} = \frac{N\xi(\delta_s^2)}{2} \left(\frac{1 + \beta_c^2 v_b^2}{1 + 3\beta_c^2 v_b^2} \right) \left(\frac{G_m - 1}{G_m} \right), \quad (3)$$

where $N = \omega_j/\omega_s$ and the factor $(G_m - 1)/G_m$ can be neglected at large gain. Noise suppression is denoted by the compression factor $\xi(\delta_s^2) \leq 1$ which equals unity at $\delta_s^2 \ll 1$ and decreases towards zero with growing variance. In our model with the sidebands $\omega_j \pm \omega_s$, we obtain $\xi(\delta_s^2) = \langle J_0^2(r) \rangle \sim \exp(-\delta_s^2)$. Hence, large improvement in noise performance can be achieved compared to the linear where $\xi(\delta_s^2) = 1$.

The role of noise compression in the operation of the SJA is illustrated in Fig. 4. For reference, we plot the uncompressed noise from Eq. (3) multiplied by the simulated gain. The output noise temperature from the actual simulation differs from it (an indication of noise compression). The simulated spectrum is rounded near the gain peak, which creates a dip in the input noise temperature.

In Fig. 5, the input noise temperature at G_m is plotted as a function of the gain. Linear theories predict convergence towards $T_n = 2.4$ K

at $G_m \gg 1$ (from Eq. (3) by taking $\xi = 1$). Above a threshold gain of ~ 13 dB, noise suppression sets in. From our analytic model with two sidebands $\omega_j \pm \omega_s$, we obtain $\xi = \langle J_0^2(r) \rangle = 0.44$ for the compression factor at $G_m = 28$ dB and the noise temperature reduces to $T_n = 1.0$ K. Compared with numerical simulations, the analytic model yields nearly 3–4 times larger value for T_n .

Discussion

The compression mechanism for noise is crucial for the high bias operation of the SJA since otherwise T_n would grow directly proportional to v_b (N in Eq. (3)). The operation with noise compression can be viewed as self-organization of the system. Microscopic degrees of freedom give rise to a macroscopic order which can be parametrized to describe the behavior of the system. In our device, the macroscopic ordering is dictated by the integrated noise over the amplified bandwidth. This parameter governs the macroscopic characteristics of the device (e.g. the effective critical current and the gain of the device for external signals). The actual value of the gain is set by the higher order terms present in the Josephson energy, which resembles that of the order parameter stabilization in regular phase transitions.

The bandwidth of our SJA is fundamentally limited below the Josephson and plasma frequencies, $\frac{1}{2} \min(\omega_J, \omega_p)$. It can be shown that the gain-bandwidth product is $|\Gamma|_{\text{max}} \times \text{BW} = 2/|R_d|(C + C_J)$ in our first-order filtering scheme. In the measured amplifier, the capacitance of the bandstop filter is $C \approx 4.3$ pF and $C_J = 0.35$ pF. Furthermore, using $R_d = -1370 \Omega$ as in our operating point of interest, the formula yields $|\Gamma|_{\text{max}} \times \text{BW} = 50$ MHz while ≈ 40 MHz is obtained experimentally. In general, stability of the amplifier requires that $C > C_J$. Reduction of the shunt capacitance facilitates improvement of the gain-bandwidth product but the boundary condition $R \gg (\omega_j C)^{-1}$ must be met. High bandwidth is predicted at small R_d too, which can be obtained most effectively by increasing the critical current. Also C_J controls the value of R_d so that the optimum for gain-bandwidth product is obtained for a small junction with a high critical current density.

Another possible low noise regime for the SJA is the limit of small ω_j . We analyzed a few devices at $v_b = 3$ ($N = 2.33$) with different β_c (see the Suppl.). We obtained analytically that the down-mixed noise contribution is around $\hbar\omega$ at $\beta_c = 0.3 - 0.5$ without any noise

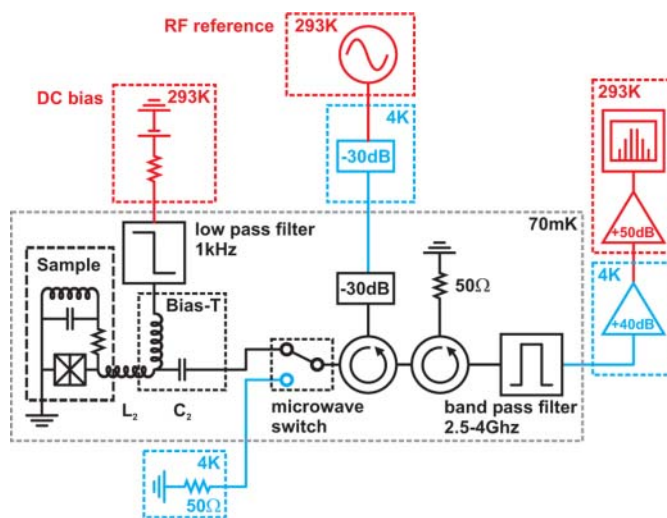


Figure 6 | Setup for measuring the SJA characteristics. The essential components of the SJA are located at 70 mK (indicated by the dashed black box). 60 dB of attenuation is employed to thermalize the incoming rf signal cable and two circulators eliminate the back action noise from the preamplifier. Noise temperature of the cooled preamplifier (including losses in front of the preamplifier) $T_n^{\text{HEMT}} = 14 \pm 3$ K at the center frequency of the SJA.



Table 1 | SJA parameters in the experiment and the simulation. Definitions: Z_0 , impedance of the source and the readout circuit; R , C and L the shunt resistance, capacitance and inductance, respectively; I_c , C_J , ω_p and β_c the critical current, the capacitance, plasma frequency and the Stewart-McCumber parameter of the junction, respectively; C_2 , L_2 the capacitance and the inductance in series with the SJA device (impedance transformer); ω_s the signal frequency; I_b and ω_J the bias current and the Josephson frequency at the optimal operating point

Parameter	Value	Parameter	Value
Z_0	50 Ω	I_c	17 μA
R	4.0 Ω	C_J	0.35 pF
C	4.26 pF	$\omega_p/(2\pi)$	61 GHz
L	702 pH	β_c	0.29
C_2	33 pF	I_b	140 μA
L_2	14.25 nH	$\omega_J/(2\pi)$	270 GHz
ω_s	2.865 GHz		

compression. This was verified in numerical simulations according to which 0.9 ± 0.2 quanta were added by our SJA. Addition of one quantum indicates that the noise behaviour of the SJA is reminiscent to that of heterodyne detection where the image frequency brings an extra noise of $\frac{1}{2}\hbar\omega$ to the detected signal²⁵, i.e. both sidebands of the Josephson frequency add $\frac{1}{2}\hbar\omega$ to the noise temperature.

The control of noise in our SJA is not fully optimized and several issues should be addressed in order to make the theoretical procedure for noise minimization more effective and transparent. Using numerical simulations, we reproduced the measured noise temperature $3.2T_q$ at high bias and found signs for the complex behavior of our device. Our analytical model mixes down noise only from two sidebands $\omega_J \pm \omega_s$, the consideration of which is sufficient at low Josephson frequency and small phase noise variance δ_s^2 . Consequently, the predictions of $T_n \sim \hbar\omega$ from our analytical modeling are reliable at low bias voltage. In the noise compression mode, $\delta_s^2 \geq 1$, our simulations show that the analytic model fails and an extension in the number of tracked sidebands is necessary. Moreover, further work will be needed to show whether pronounced noise compression can drive the SJA into the standard quantum limit T_q . Our analysis indicates that the concept of selectively shunted junction amplifier for microwaves is sound and that it provides the best route for quantum limited operation over large bandwidths.

Methods

Our experimental setup for the SJA measurements is shown in Fig. 6. The device is biased with a DC current which allows the effective value of the negative resistance to be tuned over a wide range of values. The incoming signal and the reflected signal are separated by circulators and the signal postamplification is performed by high electron mobility transistor (HEMT) based amplifiers at 4 K and at the room temperature. At the optimal operating point, the dynamic resistance R_d of the Josephson junction is -1370Ω in our amplifier. To get substantial gain according to Eq. 2, we apply impedance transformation by placing an inductor L_2 in series with the junction. This converts the input impedance $Z_{in}(\omega_s)$ close to -50Ω .

To measure the amplifier performance, we injected a reference signal and recorded the signal-to-noise (S/N) ratio while having the SJA ON and OFF. In the OFF state, the SJA acts like a pure inductance reflecting all the incoming power (passive mirror) and the noise in the S/N ratio measurement is fully specified by the HEMT preamplifier. The largest improvement in the S/N was found at the highest bias current $\sim 140 \mu\text{A}$ ($I_b = 8.2$). Using a source at 70 mK, the S/N ratio after the HEMT amplifier was improved by 17.2 ± 0.2 dB. Thanks to the microwave switch in the setup, the noise temperature of the HEMT amplifier could be carefully calibrated using the cold/hot load technique. The parameters of the investigated amplifier are collected into Table 1.

- Clerk, A. A., Devoret, M. H., Girvin, S. M., Marquardt, F. & Schoelkopf, R. J. Introduction to quantum noise, measurement, and amplification. *Rev. Mod. Phys.* **81**, 1155–1208 (2010).
- Hatridge, M., Vijay, R., Slichter, D. H., Clarke, J. & Siddiqi, I. Dispersive magnetometry with a quantum limited SQUID parametric amplifier. *Phys. Rev. B* **83**, 134501 (2011).

- Yurke, B., Corruccini, L. R., Kaminsky, P. G. & Rupp, L. W. Observation of parametric amplification and deamplification in a Josephson parametric amplifier. *Phys. Rev. A*, **39**, 2519–2533 (1989).
- Yurke, B. *et al.* A low-noise series-array Josephson junction parametric amplifier. *Appl. Phys. Lett.* **69**, 3078–3080 (1996)
- Bergeal, N. *et al.* Phase-preserving amplification near the quantum limit with a Josephson ring modulator. *Nature* **465**, 64–68 (2010).
- Mück, M., Kycia, J. B. & Clarke, J. Superconducting quantum interference device as a near-quantum-limited amplifier at 0.5 GHz. *Appl. Phys. Lett.* **78**, 967–969 (2001).
- Asztalos, S. J. *et al.* SQUID-based microwave cavity search for dark-matter axions. *Phys. Rev. Lett.* **104**, 041301 (2010).
- Castellanos-Beltran, M. A., Irwin, K. D., Hilton, G. C., Vale, L. R. & Lehnert, K. W. Amplification and squeezing of quantum noise with a tunable Josephson metamaterial. *Nature Physics* **4**, 929–931 (2008).
- Teufel, J. D., Donner, T., Castellanos-Beltran, M. A., Harlow, J. W. & Lehnert, K. W. Nanomechanical motion measured with precision beyond the standard quantum limit. *Nature Nanotech.* **4**, 820–823 (2009).
- Castellanos-Beltran, M. A. & Lehnert, K. W. A widely tunable parametric amplifier based on a SQUID array resonator. *Appl. Phys. Lett.* **91**, 083509 (2007).
- Spietz, L., Irwin, K., Aumentado, K. & Aumentado, J. Input impedance and gain of a gigahertz amplifier using a dc superconducting quantum interference device in a quarter wave resonator. *Appl. Phys. Lett.* **93**, 082506 (2008).
- Mears, C. A., *et al.* Quantum-limited heterodyne detection of millimeter waves using superconducting tantalum tunnel junctions. *Appl. Phys. Lett.* **57**, 2487–2489 (1990).
- Tiemann, J. J. Shot noise in tunnel diode amplifiers. *Proc. IRE*, **8**, 1418–1423 (1960).
- Seppä, H., Kiviranta, M., Grönberg, L. DC SQUID based on unshunted Josephson junctions: Experimental results. *IEEE Trans. Appl. Supercond.* **5**, 3248–3251 (1995).
- Likharev, K. K. *Dynamics of Josephson junctions and circuits* (Gordon and Breach, New York, 1986).
- Vystavkin, A., *et al.* One-frequency parametric amplifier using self-pumped Josephson junction. *Magnetics, IEEE Trans.* **13**, 233–236 (1977).
- Calander, N., Claeson, T. & Runder, S. Shunted Josephson tunnel junctions: High-frequency, self-pumped low noise amplifiers. *J. Appl. Phys.*, **53**, 5093–5103 (1982).
- Clarke, J. & Braginsky, A. I. eds., *The SQUID Handbook*, volume 1 (Wiley, Weinheim, 2004).
- Koch, R. H., Van Harlingen, D. J. & Clarke, J. Measurements of quantum noise in resistively shunted Josephson junctions. *Phys. Rev. B*, **26**, 74 (1982).
- Likharev, K. K. & Semenov, V. K. Fluctuation spectrum in superconducting point contacts. *Zh. Eksp. Teor. Fiz. Pis'ma* **15**, 625 (1972) *JETP Lett.* **15**, 442 (1972).
- Callen, H. B. & Welton, T. A. Irreversibility and generalized noise. *Phys. Rev.* **83**, 34–40 (1951).
- Levinson, Y., Quantum noise in a current-biased Josephson junction. *Phys. Rev. B* **67**, 184504 (2003).
- Brandt, F. T., Frenkel, J. & Taylor, J. C. Noise in resistively shunted Josephson junctions. *Phys. Rev. B* **82**, 014515 (2010).
- Wellstood, F. C., Urbina, C. & Clarke, J. Hot-electron effects in metals. *Phys. Rev. B* **49**, 5942–5955 (1994).
- Haus, H. A. *Electromagnetic noise and quantum optical measurements*, Ch. 8, (Springer, Berlin, 2000).

Acknowledgements

We thank Jari Penttilä for providing the Josephson junctions used in our experiments. We also thank Thomas Aref for his support during the writing of this article. This work was supported by Center of Excellence and Materials World Network grants of the Academy of Finland and by the European Science Foundation (ESF) under the EUROCORES Programme EuroGRAPHENE.

Author contributions

All authors took jointly part in the planning of this experimental work and the development of its theoretical interpretation. P. L. performed the experiments and V. V. made the numerical simulations and the analytical mixing analysis. P. L. and V. V. co-operatively wrote the first versions of the main manuscript and the Supplementary material. All authors contributed to editing of the manuscript.

Additional information

Supplementary information accompanies this paper at <http://www.nature.com/scientificreports>

Competing financial interests: The authors declare no competing financial interests.

License: This work is licensed under a Creative Commons Attribution-NonCommercial-NoDerivs 3.0 Unported License. To view a copy of this license, visit <http://creativecommons.org/licenses/by-nc-nd/3.0/>

How to cite this article: Lähteenmäki, P. *et al.* Josephson junction microwave amplifier in self-organized noise compression mode. *Sci. Rep.* **2**, 276; DOI:10.1038/srep00276 (2012).

Josephson junction microwave amplifier in the noise compression mode: Supplementary material

Pasi Lähteenmäki^{*†,1} Visa Vesterinen^{†,2} Juha Hassel,² Heikki Seppä,² and Pertti Hakonen¹

¹*Low Temperature Laboratory, Aalto University,
P.O.Box 15100, 00076 AALTO, Finland*

²*VTT Technical Research Centre of Finland,
P.O. Box 1000, 02044 VTT, Finland*

[†]These authors contributed equally.

CONTENTS

I. COMPUTATIONAL METHODS	3
II. ANALYTICAL METHODS	7
A. Direct noise	7
B. Down-mixed noise	8
C. Bandwidth	14
D. Stability	15
1. Input noise	15
2. Down-mixed noise	16
III. PRACTICAL CONSIDERATIONS IN THE SJA DESIGN	17
A. Limit of small fluctuations	17
B. Noise compression limit	18
IV. RESULTS	19
A. Reproduction of the experimental findings in the noise compression regime	19
B. Quantum limited amplifier without noise compression	21
References	23

Our Supplementary material is divided into chapters as outlined above. Ch. I details the circuit diagram of the single junction amplifier (SJA). The non-linear Josephson junction element and the semiclassical, quantum noise generators are defined, and we derive the Langevin system of differential equations that is solved numerically in the time domain. In Ch. II, we study the amplifier characteristics analytically by introducing a linear model where the Josephson junction is replaced by negative dynamic resistance R_d . In particular, the magnitude of R_d is linked to DC voltage bias and junction capacitance. Equations for down-mixed noise from the Josephson frequency are derived and analyzed in detail. Ch. III deals with guidelines for practical amplifier design and summarizes the constraints that limit the

parameter selection. Relations between gain, bandwidth, and stability are studied. Finally, Ch. IV presents the results. At high-bias operation point, the experiment is compared with the simulations of Ch. I and the analytic model of Ch. II. We also present numerical results of a nearly quantum limited amplifier at low bias, designed using principles given in Ch. III.

I. COMPUTATIONAL METHODS

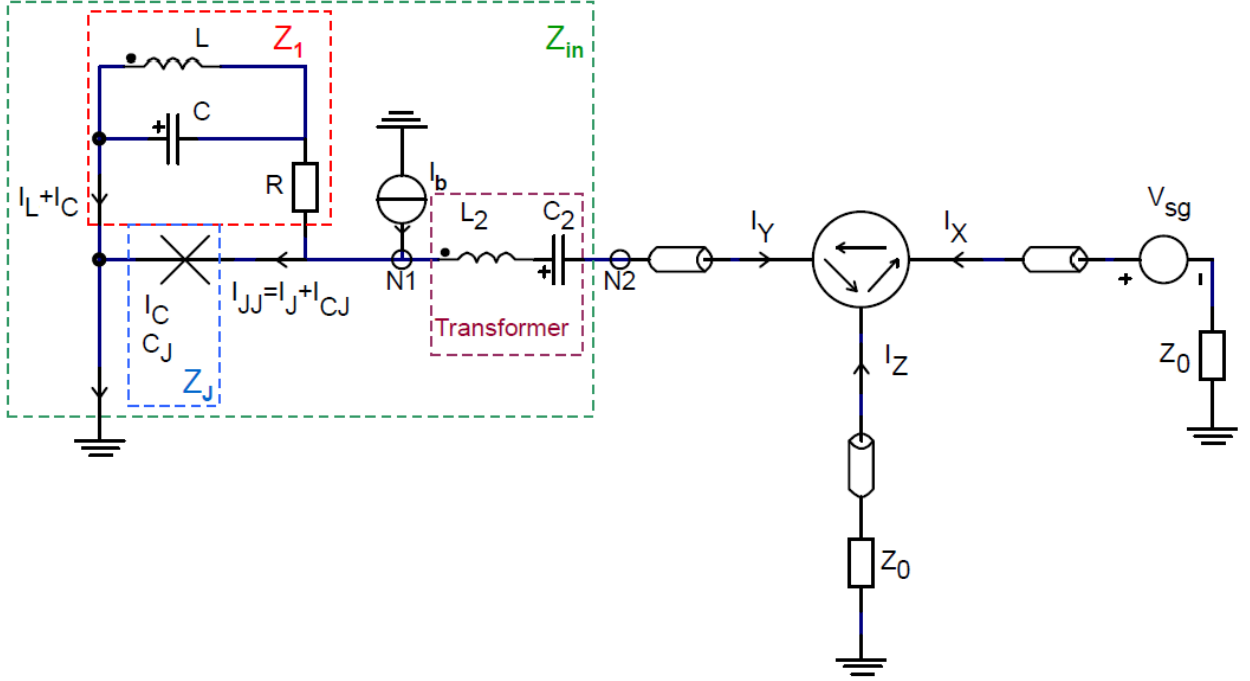


FIG. 1. Amplifier circuit with a Josephson junction denoted by the cross. Node $N1$ specifies the node to which the bias current I_b is fed. A circulator connects the branches X , Y , and Z in a manner denoted by the arrows; the amplifier input impedance Z_{in} is the impedance at $N2$ looking outward from port Y . The junction has internal capacitance C_J which is not drawn explicitly. For the variables, see text.

The circuit diagram of the analyzed SJA Josephson amplifier is presented in Fig. 1. Using the standard definitions for the Josephson current I_J and the voltage V

$$I_J = I_c \sin \varphi \quad (1)$$

$$V = \frac{\hbar}{2e} \frac{\partial \varphi}{\partial t} = \frac{\Phi_0}{2\pi} \frac{\partial \varphi}{\partial t}, \quad (2)$$

we can model the non-linear behavior of the junction in an otherwise regular electrical circuit.

The critical current I_c and the phase difference φ are measured across the junction. The constants e and \hbar denote the elementary charge and reduced Planck's constant, respectively; $\Phi_0 = \pi\hbar/e$ is the flux quantum. Other quantities in Fig. 1 are understood through

- C_J, I_{CJ} : junction capacitance and current flowing through it
- $R, I_R + \delta I$: resistance of the bandstop shunt and the current in it with fluctuation δI
- L, I_L, C, I_C : shunt inductor, capacitor, and the associated currents
- I_b, V_{sg} : current bias and signal voltage generators
- L_2, C_2 : LC transformer for impedance matching
- $I_X, I_Y \equiv -I_2, I_Z$: currents entering the three-port circulator (they sum up to zero)
- Z_0 : internal resistance of signal generator in branch X; matched load in branch Z.

Transformation into dimensionless variables written in lower case letters is defined as

$$\omega_p = \sqrt{2\pi I_c / (\Phi_0 C_J)} \text{ (plasma frequency)} \quad (3)$$

$$Q = \omega_p R C_J \text{ (quality factor)} \quad (4)$$

$$\tau = \omega_p t \quad (5)$$

$$i_J = I_J / I_c = \sin \varphi \quad (6)$$

$$v = V / (R I_c) = \frac{1}{Q} \frac{\partial \varphi}{\partial \tau} = \frac{\varphi'}{Q}. \quad (7)$$

Similarly, all currents are divided by I_c , and voltages by the product $R I_c$. The dynamics of the Josephson junction in the presence of finite $C_J > 0$ is often described using the dimensionless Stewart-McCumber parameter $\beta_C = Q^2 = 2eR^2 I_c C_J / \hbar$. Charges in capacitors become dimensionless when they are multiplied by ω_p / I_c . Dimensionless resistances r are multiples of R .

Kirchhoff's current law tells that

$$i_C + i_L = i_R + \delta i \text{ (in the shunt)} \quad (8)$$

$$i_2 + i = i_C + i_L + i_J + i_{CJ} \text{ (at node N1)} \quad (9)$$

$$i_X + i_Z = i_2 \equiv -i_Y \text{ (at the circulator)}. \quad (10)$$

Electric power must be conserved within the circulator. Using an ideal circulator, we obtain for the voltages and currents at the three ports:

$$v_X = \frac{v_{\text{sg}}}{2} \ \& \ i_X = \frac{Rv_{\text{sg}}}{2Z_0} \quad (11)$$

$$v_Y = v_{\text{sg}} - \frac{Z_0 i_2}{R} \quad (i_2 \text{ is a variable}) \quad (12)$$

$$v_Z = \frac{v_{\text{sg}}}{2} - \frac{Z_0 i_2}{R} \ \& \ i_Z = -\frac{Rv_Z}{Z_0}. \quad (13)$$

Kirchhoff's voltage law yields

$$v = v_{\text{sg}} - \frac{Z_0 i_2}{R} - \frac{L_2 \omega_p i_2'}{R} - \frac{q_2}{\omega_p R C_2} \quad (14)$$

(between nodes N1 and N2)

$$\frac{q}{\omega_p R C} = \frac{L \omega_p i_L'}{R} = v - i_R \quad (15)$$

(in the shunt),

where the primes denote time derivatives. The charges stored in the capacitors C and C_2 are related to the currents via $q' = i_C$ and $q_2' = i_2$, respectively. In the Josephson junction $q_J' = i_{C_J}$. We can gather all the information presented so far into a Langevin system of ordinary differential equations

$$\begin{pmatrix} \varphi' \\ q_J' \\ q' \\ i_L' \\ q_2' \\ i_2' \end{pmatrix} = A \begin{pmatrix} \varphi \\ q_J \\ q \\ i_L \\ q_2 \\ i_2 \end{pmatrix} + \begin{pmatrix} 0 \\ i_b - \delta i - \sin \varphi \\ \delta i \\ 0 \\ 0 \\ \frac{Rv_{\text{sg}}}{L_2 \omega_p} \end{pmatrix} \quad (16)$$

where matrix A is

$$\begin{pmatrix} 0 & 1 & 0 & 0 & 0 & 0 \\ 0 & -\frac{1}{Q} & \frac{C_J}{CQ} & 0 & 0 & 1 \\ 0 & \frac{1}{Q} & -\frac{C_J}{CQ} & -1 & 0 & 0 \\ 0 & 0 & \frac{\omega_0^2}{\omega_p^2} & 0 & 0 & 0 \\ 0 & 0 & 0 & 0 & 0 & 1 \\ 0 & -\frac{C_2 \omega_2^2}{C_J \omega_p^2} & 0 & 0 & -\frac{\omega_2^2}{\omega_p^2} & -\frac{Z_0}{L_2 \omega_p} \end{pmatrix}. \quad (17)$$

Eigenfrequencies are $\omega_0 = 1/\sqrt{LC}$ and $\omega_2 = 1/\sqrt{L_2 C_2}$.

Josephson frequency $\omega_J = 2eV_b/\hbar$, expressed through averaged Josephson voltage $V_b = \langle V \rangle$, is the quantity that determines the necessary bandwidth in the simulations. Two harmonics of ω_J fit inside $3\omega_J$, and the interval of digitally filtered noise samples is set to $6\omega_J$ because of Nyquist sampling theorem. For the shunt resistor, we included symmetrized quantum noise which has current spectral density

$$S_I(\omega) = \frac{2\hbar\omega}{R} \coth\left(\frac{\hbar\omega}{2k_B T_{\text{shunt}}}\right), \quad (18)$$

defined here as the variance of current per unit bandwidth at positive frequencies; k_B is Boltzmann's constant. The input noise, added to v_{sg} , had the voltage spectral density ($\omega > 0$)

$$S_V(\omega) = 2Z_0\hbar\omega \coth\left(\frac{\hbar\omega}{2k_B T_{\text{in}}}\right) \quad (19)$$

which corresponds to voltage variance per unit bandwidth. Input noise at temperature $T_{\text{in}} = 70$ mK was bandpass filtered to take the circulator bandwidth into account. It can be noticed that half a quantum of noise of $\hbar\omega/2$ enters the amplifier input even at zero temperature (consider the product $v_X i_X$ in Eq. (11)).

Simulation was started by setting voltages, charges and currents to zero. First, the bias current i_b was slowly turned on and swept linearly up to a point where stability could be observed. The bias was then swept down to the desired operation point ($i_b > 1$). Second, the amplifier was perturbed with a Gaussian input pulse from v_{sg} in order to confirm the stability. Finally, a sinusoidal input voltage was turned on, in the case when the reflection coefficient Γ of the system was to be evaluated. The coefficient gives the relation between input and output voltages: $v_Z(\omega) = \Gamma(\omega)v_X(\omega)$. The input impedance Z_{in} of the amplifier, or the impedance looking out from port Y, is easily obtained from

$$v_{\text{sg}} = \frac{Z_{\text{in}} + Z_0}{R} i_2. \quad (20)$$

The desired Fourier components of v_{sg} and i_2 are computed with FFT analysis on steady-state time traces. It turns out that

$$\Gamma(\omega) = \frac{Z_{\text{in}} - Z_0}{Z_{\text{in}} + Z_0} \quad (21)$$

as in regular microwave reflection measurements. Power gain of the amplifier can be estimated with $G = |\Gamma(\omega)|^2$, the squared modulus of the reflection coefficient. For more accurate

results, the spectral density of the output voltage v_Z is plotted in two distinct cases: (I) normal operation and (II) silent, unbiased situation with unity gain ($i_b = i_2 = 0$). Input noise is present on top of the sinusoidal signal in v_{sg} , see Eq. (13). The gain is computed as the ratio of spectral densities in the cases (I) and (II) at the input frequency.

Noise added by the Josephson amplifier was estimated after the gain peak $G(\omega)$ had been found. Nothing but quantum noise was present at input v_{sg} during this simulation. The spectral density of v_Z was scaled by $(RI_c)^2/(k_B Z_0)$ to get total noise power referred to the output. The noise added by the amplifier, as referred to the input, could be obtained by dividing the result by G and subtracting the contribution of v_{sg} . The equivalent noise power of fluctuations entering the amplifier was calculated as the product of $(RI_c)^2/(4k_B Z_0)$ and the spectral density of v_{sg} . The subtracted amount equals

$$\frac{\hbar\omega}{2k_B} \coth\left(\frac{\hbar\omega}{2k_B T_{in}}\right) \approx 90 \text{ mK}. \quad (22)$$

The intrinsic impedance of the Josephson junction, Z_J , could be estimated with steady-state FFT analysis of voltage v and total current $i_J + i_{CJ}$. We denote the dynamic resistance with R_d in equation

$$\frac{1}{Z_J} = i\omega C_J + \frac{1}{R_d} \quad (23)$$

which can be manipulated to obtain

$$R_d = -\frac{1}{\omega C_J} \cdot \frac{\Im\{Z_J\}}{\Re\{Z_J\}} = -\frac{\tan \phi_J}{\omega C_J}. \quad (24)$$

The phase difference between v and $i_J + i_{CJ}$ equals ϕ_J .

II. ANALYTICAL METHODS

A. Direct noise

The direct noise is defined as the noise generated at the shunt resistor R in the signal band. It is described by the current generator δi in parallel with R . We derived the linear transfer function from fluctuating resistor voltage $\delta v_R = \delta i$ to output voltage v_Z . The transfer function has the shunt impedance Z_1 in the denominator, see Figure 1. Exactly at the shunt eigenfrequency, $\omega_0 = 1/\sqrt{LC}$, the direct noise becomes negligible as $|Z_1| \rightarrow \infty$. After a small offset from ω_0 , the magnitude of the shunt reactance X_1 is finite but much

larger than R in the following equation:

$$Z_1 = R + (1/(i\omega L) + i\omega C)^{-1} = R + iX_1. \quad (25)$$

We may thus approximate

$$\frac{1}{Z_1} = \frac{R}{X_1^2} - \frac{i}{X_1}, \quad \omega \approx \omega_0, \quad (26)$$

and we obtain for the input-referred noise temperature

$$k_B T_{\text{direct}} = \frac{R|R_d|\hbar\omega}{2X_1^2} \coth\left(\frac{\hbar\omega}{2k_B T_{\text{shunt}}}\right), \quad R^2 \ll X_1^2$$

$$X_1 = \frac{\omega L}{1 - \omega^2 LC}. \quad (27)$$

B. Down-mixed noise

Here we present an analytic treatment for the noise generated in the shunt resistor at frequencies near the Josephson frequency and mixed down to signal frequency by Josephson dynamics. We divide the fluctuating phase over the Josephson junction $\varphi(t)$ into the three parts. First, φ_s is the noise close to the signal frequencies at the bandwidth determined by the frequency response of the environment, i.e., $Z_E(\omega)$. Second, φ_j describes the noise in the sidebands of the Josephson oscillation. Around the Josephson frequency, quantum noise φ_n is generated by the shunt resistance R which is the main source of dissipation there. In addition, the average phase varies as $\langle\varphi(t)\rangle = \omega_J t$ due to the voltage-driven Josephson oscillation at the high bias limit. The total phase can be written as

$$\varphi(t) = \omega_J t + \varphi_s(t) + \varphi_j(t) + \varphi_n(t). \quad (28)$$

Functions φ_s , φ_j are effectively band-limited due to the frequency-dependent environment. The simplest way to describe the noise spectra with narrow band is to use the envelope and phase representation [7], which leads to sinusoidal time dependence with a fluctuating amplitude and phase. For instance,

$$\varphi_s = r(t) \sin(\omega_s t + \psi(t)). \quad (29)$$

Using the sum rule of trigonometric functions, one can see that the random phase $\psi(t)$ only moves signal from one quadrature to the other, and this does not have any relevance for the

splitting of power between different frequencies. The spread of $r(t)$ is described by Rayleigh distribution which has the probability density function

$$f_R(r) = \frac{r}{\delta_s^2} e^{-r^2/(2\delta_s^2)} \quad (30)$$

where the variance of φ_s , or average power, is δ_s^2 . Thus, we have reduced the problem of band limited noise to sinusoidal behavior with an approximately defined amplitude.

The impedance $Z_E(\omega)$ seen by the signal frequency current fluctuation is given in our case by

$$Z_E(\omega) = \frac{R_d Z'_0(\omega)}{R_d + Z'_0(\omega)} \quad (31)$$

where $Z'_0(\omega)$ is the impedance in parallel to the junction (in our circuit Z_0 transformed close to $|R_d|$ by the series $L_2 C_2$ transformer). The resistance R of the bandstop filter is not visible in the signal band. Using $Z_E(\omega_s)$ for the conversion between current and voltage fluctuations at the signal frequency, we can easily calculate the input-referred noise temperature $k_B T_{mix} = Z_E^2 I_c^2 S_I(\omega_s) / (G Z'_0)$, where the power gain $G = |(R_d - Z'_0) / (R_d + Z'_0)|^2$ is responsible for the reduction to the input. We will move into the Fourier plane to obtain the dimensionless noise current generator $S_I(\omega_s)$ in parallel to the junction. The phase fluctuation φ_j in the Josephson band is assumed to be small: $\langle \varphi_j^2 \rangle \ll 1$. We expand the Josephson current $\sin \varphi(t)$ (total phase is in Eq. (28)) and set $\cos \varphi_j \approx 1$, $\sin \varphi_j \approx \varphi_j$. The currents at high frequencies and at the signal frequency become

$$i_j(t) = \cos(\omega_J t) \sin \varphi_s + \sin(\omega_J t) \cos \varphi_s \quad (32)$$

$$i_s(t) = \varphi_j \cos(\omega_J t) \cos \varphi_s - \varphi_j \sin(\omega_J t) \sin \varphi_s, \quad (33)$$

respectively. The phase-to-current relation in the Josephson band reads

$$\hbar \dot{\varphi}_j = 2eV_J \quad (34)$$

$$-I_c \dot{i}_j(\omega_J) = C_J \dot{V}_J + V_J/R, \quad (35)$$

in which V_J is the high-frequency part of Josephson voltage V . The current generators in parallel to the junction are $-i_s$ and $-i_j$. We adopt the Fourier transform convention $\hat{f}(\omega) = \int f(x) e^{-i\omega x} dx$. Since the Fourier transform of a product is a convolution, we obtain

the transforms

$$\begin{aligned}\hat{i}_j &= \frac{1}{2} \left(\widehat{\sin \varphi_s}(\omega - \omega_J) - i \widehat{\cos \varphi_s}(\omega - \omega_J) + \widehat{\sin \varphi_s}(\omega + \omega_J) + i \widehat{\cos \varphi_s}(\omega + \omega_J) \right) \\ &= \frac{i}{2} \left(-\widehat{e^{i\varphi_s}}(\omega - \omega_J) + \widehat{e^{-i\varphi_s}}(\omega + \omega_J) \right)\end{aligned}\quad (36)$$

$$\begin{aligned}\hat{i}_s &= \frac{1}{2} \left(\varphi_j \widehat{\cos \varphi_s}(\omega - \omega_J) + i \varphi_j \widehat{\sin \varphi_s}(\omega - \omega_J) + \varphi_j \widehat{\cos \varphi_s}(\omega + \omega_J) - i \varphi_j \widehat{\sin \varphi_s}(\omega + \omega_J) \right) \\ &= \frac{1}{2} \left(\widehat{\varphi_j e^{i\varphi_s}}(\omega - \omega_J) + \widehat{\varphi_j e^{-i\varphi_s}}(\omega + \omega_J) \right).\end{aligned}\quad (37)$$

Eqs. (34) and (35) now yield for the signal and Josephson bands

$$i\hbar\omega\hat{\varphi}_s = -2eZ_E I_c \hat{i}_s \quad (38)$$

$$|Z_E|^2(\omega) = |R_d|^2 |\sqrt{G(\omega)} - 1|^2 / 4 \quad (39)$$

$$i\hbar\omega\hat{\varphi}_j = \frac{2eRI_c}{1 + i\omega RC_J} \left(-\hat{i}_j + \hat{i}_n \right), \quad (40)$$

where i_n denotes the quantum noise from the shunt resistor; its spectral density reads $S_I(\omega) = 2\hbar\omega/(RI_c^2)$ in the dimensionless form. The spectrum of $\cos \varphi_s$ consists of a dc component and the even multiples of ω_s , whereas the spectrum of $\sin \varphi_s$ contains all odd harmonics of ω_s . We assume that Josephson frequency is large: $N = \omega_J/\omega_s \gg 1$. We write down explicitly the convolution in the first phase-to-current relationship:

$$\hat{i}_s = \frac{1}{4\pi} \int \left(\widehat{e^{i\varphi_s}}(s) \hat{\varphi}_j(\omega - \omega_J - s) + \widehat{e^{-i\varphi_s}}(s) \hat{\varphi}_j(\omega + \omega_J - s) \right) ds \quad (41)$$

$$\hat{\varphi}_j = \frac{2eRI_c}{i\hbar\omega(1 + i\omega RC_J)} \left(-\hat{i}_j + \hat{i}_n \right), \quad (42)$$

where (after neglecting some terms containing $2\omega_J$)

$$\hat{i}_j(\omega - \omega_J - s) = \frac{i}{2} \widehat{e^{-i\varphi_s}}(\omega - s) \quad (43)$$

$$\hat{i}_j(\omega + \omega_J - s) = -\frac{i}{2} \widehat{e^{i\varphi_s}}(\omega - s) \quad (44)$$

$$\hat{\varphi}_j(\omega - \omega_J - s) = \frac{2eRI_c(\hat{i}_n(\omega - \omega_J - s) - \frac{i}{2} \widehat{e^{-i\varphi_s}}(\omega - s))}{i\hbar(\omega - \omega_J - s)(1 + i(\omega - \omega_J - s)RC_J)} \quad (45)$$

$$\hat{\varphi}_j(\omega + \omega_J - s) = \frac{2eRI_c(\hat{i}_n(\omega + \omega_J - s) + \frac{i}{2} \widehat{e^{i\varphi_s}}(\omega - s))}{i\hbar(\omega + \omega_J - s)(1 + i(\omega + \omega_J - s)RC_J)}. \quad (46)$$

Here $\omega - s$ takes the values $0, \pm\omega_s, \pm2\omega_s, \pm3\omega_s$, etc, all of which are small compared with ω_J . We approximate $\omega \pm \omega_J - s \approx \pm\omega_J$ in the denominators.

Let us consider downmixing and upmixing separately, using only the first pair of sidebands. Then $\hat{\varphi}_j$ has nonzero contributions around $\omega_J - \omega_s, \omega_J, \omega_J + \omega_s$, and the corresponding negative frequencies. We expand the exponentials of φ_s using Bessel functions of

the first kind: $\exp(\pm i\varphi_s) \approx J_0(r) \pm i(2J_1(r)/r)\varphi_s$. φ_s is in the time domain here, while the Bessel terms are stochastic and will be time averaged later. Weak fluctuations in signal band are characterized by $r \approx 0$ and the exponential can be replaced by unity. In the limit of very strong fluctuations, additional terms with $J_2(r)$, $J_3(r)$, and so on may be required. As r is Rayleigh distributed, we obtain expectation values $\langle J_0(r) \rangle = \exp(-\delta_s^2/2)$ and $\langle 2J_1(r)/r \rangle = (1 - \exp(-\delta_s^2))/\delta_s^2$ (see Eq. (30) and Ref. [1]). Upmixing is described by

$$\begin{aligned}\hat{\varphi}_j(\omega_J + \omega) &\approx \frac{2eRI_c[\hat{i}_n(\omega_J + \omega) + ie^{i\varphi_s}(\omega)/2]}{i\hbar\omega_J(1 + ix)} \\ \hat{\varphi}_j(-\omega_J + \omega) &\approx \frac{2eRI_c[\hat{i}_n(-\omega_J + \omega) - ie^{-i\varphi_s}(\omega)/2]}{-i\hbar\omega_J(1 - ix)}.\end{aligned}\quad (47)$$

Fourier transforming,

$$\widehat{e^{\pm i\varphi_s}}(\omega) = 2\pi J_0(r)\delta(\omega) \pm i(2J_1(r)/r)\hat{\varphi}_s(\omega).\quad (48)$$

The Josephson frequency is converted to dimensionless bias voltage v_b via $\hbar\omega_J = 2eV_b = 2eRI_c v_b$. We note that $x = \omega_J RC_J = \beta_c v_b$ where $\beta_c = 2eR^2 I_c C_J / \hbar$. Downmixing is governed by

$$\hat{i}_s(\omega) = \frac{1}{4\pi} \int [(2\pi J_0\delta(s) + i\alpha\hat{\varphi}_s(s))\hat{\varphi}_j(\omega - \omega_J - s) + (2\pi J_0\delta(s) - i\alpha\hat{\varphi}_s(s))\hat{\varphi}_j(\omega + \omega_J - s)] ds\quad (49)$$

where α equals $2J_1(r)/r$. In order to make the analysis self-consistent, we plug in φ_j as a function of φ_s , see Eq. (47). After simplifying

$$\hat{\varphi}_j(\omega_s - \omega_J) + \hat{\varphi}_j(\omega_s + \omega_J) = \frac{1}{iv_b} \left(-\frac{\hat{i}_n(-\omega_J + \omega_s)}{1 - ix} + \frac{\hat{i}_n(\omega_J + \omega_s)}{1 + ix} - \frac{\alpha\hat{\varphi}_s(\omega_s)}{2} \left(\frac{1}{1 + ix} - \frac{1}{1 - ix} \right) \right),\quad (50)$$

we are left with

$$\hat{i}_s(\omega_s) = \frac{J_0}{2iv_b(1 + x^2)} \left((1 - ix)\hat{i}_n(\omega_J + \omega_s) - (1 + ix)\hat{i}_n(-\omega_J + \omega_s) \right).\quad (51)$$

By definition, the squared modulus of the Fourier transform is directly proportional to the power spectral density. We are interested in one-sided ($\omega > 0$) power spectral densities which receive contributions from positive and negative frequencies:

$$S_I(\omega) \propto |\hat{i}_s(\omega)|^2 + |\hat{i}_s(-\omega)|^2.\quad (52)$$

The total noise power from the sidebands is estimated by $S_I(\omega_J - \omega_s) + S_I(\omega_J + \omega_s) \approx 2S_I(\omega_J)$.

$$S_I(\omega_s) = \frac{J_0^2}{4v_b^2(1+x^2)} \cdot 2S_I(\omega_J). \quad (53)$$

Next, the stochastic term is time averaged: $J_0^2 \rightarrow \langle J_0^2 \rangle$. We take its expectation value with respect to the Rayleigh distributed noise amplitude in Eq. (30):

$$\langle J_0^2 \rangle = \int_0^\infty J_0^2(r) \frac{r}{\delta_s^2} e^{-r^2/(2\delta_s^2)} dr. \quad (54)$$

$\langle J_0^2 \rangle$ will differ significantly from unity only if phase variance is large, $\delta_s^2 > 1$, which would be a consequence of high gain. Interestingly, in the limit of vanishing capacitance ($x = \omega_J RC_J \approx 0$), high bias ($v_b \approx I_b/I_c$) and low gain ($\langle J_0^2 \rangle \approx 1$) we arrive at the Koch-Clarke formula [4] for down-mixed noise

$$S_I(\omega) = \frac{I_c^2 S_I(\omega_J)}{2I_b^2}. \quad (55)$$

We note that the DC current through the junction can be derived from the downmixing equation (49). It is essential that shunt capacitor C is not visible at Josephson frequency, otherwise the IV curve will change. Hence, we require $\omega_J RC \gg 1$ and study the limit $\omega_s \rightarrow 0$:

$$\begin{aligned} \hat{i}_s(0) &= \frac{1}{4\pi} \int \left[\widehat{e^{i\varphi_s}}(s) \left(\frac{2\pi J_0 \delta(s)}{2v_b(1-ix)} \right) + \widehat{e^{-i\varphi_s}}(s) \left(\frac{2\pi J_0 \delta(s)}{2v_b(1+ix)} \right) \right] ds \\ &= \frac{J_0}{4v_b} \left(\frac{\widehat{e^{i\varphi_s}}(0)}{1-ix} + \frac{\widehat{e^{-i\varphi_s}}(0)}{1+ix} \right) = \frac{J_0^2 \hat{1}}{2v_b(1+x^2)}. \end{aligned} \quad (56)$$

The DC current generator in parallel to the junction is $-\langle i_s \rangle = -\langle J_0^2 \rangle / (2v_b(1+x^2))$. As a consequence, the total bias current does not entirely flow through the shunt resistor. In the limit of small phase fluctuations, $\langle J_0^2 \rangle \approx 1$, the dynamic resistance of the junction at signal frequency will be

$$r_d = R_d/R = (d\langle i_s \rangle / dv_b)^{-1} = -\frac{2v_b^2(1+x^2)^2}{1+3x^2}. \quad (57)$$

We note that this result agrees with a previous study where the authors used perturbation theory to solve the IV curve for a resistively and capacitively shunted junction at high bias [6]. The result reads $v_b = i_b - [2i_b(1 + \beta_c^2 i_b^2)]^{-1}$. After differentiation,

$$r_d = \frac{1}{\left(\frac{\partial v_b}{\partial i_b} \right)^{-1} - 1} = -\frac{2v_b^2(1+x^2)^2 + 1 + 3x^2}{1+3x^2} \quad (58)$$

where $v_b^2 \approx i_b^2$. The two expressions for r_d differ by a factor -1 , which is negligible especially when $\beta_c > 0$. This is the first point where we observed discrepancy between the analytic model and the Langevin simulation. In the limit of large phase fluctuations, $\langle J_0^2 \rangle < 1$, the IV curve at DC should change according to analytic Eq. (56), but we did not notice any modification at variances up to $\delta_s^2 = 1.2$ in the simulation. We believe that the analytic model fails due to the inclusion of a single sideband pair only. The amplitudes of higher sidebands starting from $\omega_J \pm 2\omega_s$ are considerably large at high Josephson frequency as well as at large variance δ_s^2 .

In the conversion of Eq. (53) to input noise temperature, we keep the $\langle J_0^2 \rangle$ modification even though it appears to be incomplete in the limit of large phase fluctuations.

$$k_B T_{\text{mix}} = \frac{eI_c |R_d|}{2v_b} \left(\frac{G_m - 1}{G_m} \right) \frac{\langle J_0^2 \rangle}{1 + (\beta_c v_b)^2}. \quad (59)$$

The maximal gain is G_m . In the limit of high gain, $G_m \gg 1$, the term $(G_m - 1)/G_m \approx 1$ can be dropped out. At intermediate gain, on the other hand, we consider a cascade of similar amplifiers. Noise temperature from the Friis formula is

$$T_{\text{mix}} \left(1 + \frac{1}{G_m} + \frac{1}{G_m^2} + \dots \right) \rightarrow \frac{T_{\text{mix}}}{1 - 1/G_m} = \frac{G_m T_{\text{mix}}}{G_m - 1}. \quad (60)$$

As a consequence, the gain dependence vanishes in a multistage cascade. Our dynamic resistance for high bias (Eq. (57), $v_b \geq 3$) is inserted into Eq. (59), and we obtain

$$\frac{k_B T_{\text{mix}}}{\hbar\omega_s} = \frac{N\xi(\delta_s^2)}{2} \left(\frac{1 + \beta_c^2 v_b^2}{1 + 3\beta_c^2 v_b^2} \right) \quad (61)$$

which represents the number of added quanta at $N = \omega_J/\omega_s \gg 1$. The suppression of noise is included in the unknown function $0 < \xi(\delta_s^2) \leq 1$ which equals $\langle J_0^2 \rangle$ when noise is mixed down from the first pair of sidebands. It's obvious from Eq. (61) that low Josephson frequency and moderate junction capacitance improve the noise performance.

We have studied the breakdown of Eq. (61) at small N . The sideband pair will become asymmetric in phase and its spectral density. A correction term can be derived by starting from Eqs. (45) and (46) and retaining the antisymmetric $\omega_J - \omega_s$ and $\omega_J + \omega_s$ in the Josephson band:

$$\frac{N^2(1 + N^2 y^2)(1 + (N^2 + 3)y^2)}{(N^2 - 1)(1 + 2(N^2 + 1)y^2 + (N^2 - 1)^2 y^4)}, \quad (62)$$

where $y = \omega_s RC_J$. Eq. (61) must be multiplied by Eq. (62) which equals unity at high N . The correction term is significant at small N , and later we will show that the stan-

dard quantum limit, added noise of $\frac{1}{2}\hbar\omega_s$, cannot be reached in the limit of small phase fluctuations.

C. Bandwidth

The gain-bandwidth product of the SJA is $|\Gamma(\omega_s)|\Delta\omega_{-3\text{dB}}$. We postulate that the gain function $G(\omega) - 1$ has a peaked, Lorentzian form:

$$G(\omega) - 1 = \frac{G_m - 1}{1 + \left(\frac{2Q_s(\omega_s - \omega)}{\omega_s}\right)^2} \quad (63)$$

with the maximal gain of G_m . The full width at half maximum $\Delta\omega_{-3\text{dB}}$, or FWHM, is denoted by ω_s/Q_s where Q_s is the quality factor at the signal frequency. The integral over the Lorentzian peak equals

$$\int_0^\infty (G(\omega) - 1)df = \frac{1}{2\pi} \frac{\omega_s(G_m - 1)\pi}{Q_s} \frac{\pi}{2} = \frac{\omega_s(G_m - 1)}{4Q_s}. \quad (64)$$

The quality factor arises from the resonator $L, C + C_J$ which is loaded with the real part of Z_E .

$$Q_s = \Re\{Z_E\} \sqrt{\frac{C + C_J}{L}} \approx \omega_s |Z_E(\omega_s)| (C + C_J) = \frac{1}{2} |R_d| (\sqrt{G_m} - 1) \omega_s (C + C_J). \quad (65)$$

The minimal shunt capacitance is set by the shunt resistance and the Josephson frequency: $R = \alpha_C \cdot (\omega_J C)^{-1}$, $\alpha_C \gg 1$. Thus, we may write

$$C + C_J = \frac{\alpha_C}{\omega_J R} + C_J = \frac{\hbar(\alpha_C + x)}{2eR^2 I_c v_b}. \quad (66)$$

By using the Q-factor in Eq. (65) and the representation of the capacitance, Eq. (66), we obtain

$$|\Gamma(\omega_s)|\Delta\omega_{-3\text{dB}} = \frac{4eRI_c}{\hbar} \left(\frac{\sqrt{G_m}}{\sqrt{G_m} - 1} \right) \frac{v_b}{|r_d|(\alpha_C + x)} \approx \frac{N\omega_s\sqrt{G_m}}{\sqrt{G_m} - 1} \cdot \frac{1 + 3x^2}{v_b^2(1 + x^2)^2(\alpha_C + x)}. \quad (67)$$

Eq. (67) indicates that high bandwidth is reached when the critical current is large and the dynamic resistance $|r_d|$ is small; most effectively this is achieved by tuning down the dimensionless bias voltage.

D. Stability

In the stable operating mode of the amplifier, we do not allow zero crossings for the Josephson voltage fluctuations around the steady-state bias v_b . Instability of the amplifier is characterized by a spontaneous pattern of the Josephson voltage v at the signal frequency as well as extra harmonic content in the spectrum. We know that the origin of the fluctuations is either (i) noise from the amplifier input, (ii) down-mixed noise, or (iii) direct noise from the shunt resistor. We derive the variance of the dimensionless voltage noise for the first two cases, σ_{in}^2 and σ_{mix}^2 , respectively. The direct noise, discussed in Ch. II A, is small and it is neglected. Since these variances are uncorrelated and the standard deviation of the junction voltage becomes $\sigma = \sqrt{\sigma_{\text{in}}^2 + \sigma_{\text{mix}}^2}$. For stability reasons, there needs to be an operational margin for voltage fluctuations, which we approximate as $3\sigma < v_b$. We will later observe that this requirement leads to an upper bound for the available gain, since σ increases with gain.

1. Input noise

The voltage transfer function from the input to the junction is given by

$$\left| \frac{v}{v_{\text{sg}}} \right|^2 = \frac{|R_d|(G-1)}{4Z_0}. \quad (68)$$

The power spectral densities, S_g at the input and S_v at the junction, are linked in a similar fashion:

$$S_v = S_g \cdot \frac{|R_d|(G-1)}{4Z_0}. \quad (69)$$

The quantum noise at the input has the form

$$S_g = \frac{2Z_0\hbar\omega_s \coth(\hbar\omega_s/(2k_B T_{\text{input}}))}{R^2 I_c^2}. \quad (70)$$

The variance of the junction voltage, σ_{in}^2 , equals the power given by the integral of S_v over frequency, see Eq. (69).

$$\int S_v df = \sigma_{\text{in}}^2 = \frac{\hbar\omega_s |R_d|}{2R^2 I_c^2} \coth\left(\frac{\hbar\omega_s}{2k_B T_{\text{input}}}\right) \int (G(\omega) - 1) df. \quad (71)$$

The gain integral is evaluated in Eq. (64):

$$\int (G-1) df = \frac{\sqrt{G_m} + 1}{2|R_d|(C + C_J)}. \quad (72)$$

Finally, by combining the equations above,

$$\sigma_{\text{in}}^2 = \frac{\omega_s e v_b (\sqrt{G_m} + 1)}{2I_c (\alpha_C + \beta_c v_b)} \coth \left(\frac{\hbar \omega_s}{2k_B T_{\text{input}}} \right). \quad (73)$$

The central conclusion here is that the critical current I_c cannot be made small.

2. Down-mixed noise

We derive the phase noise variance δ_s^2 due to downmixing (cf. Eq. (51)) using frequency domain integrals. We observe from Eq. (38) that $\hbar^2 \omega^2 S_\varphi = (2eZ_E I_c)^2 S_I(\omega)$ which can be integrated with respect to frequency using Eq. (53) for $S_I(\omega)$:

$$\frac{\hbar \omega^2 S_\varphi}{2} = \left(\frac{eI_c}{2v_b} \right)^2 \frac{\langle J_0^2 \rangle \cdot 4Z_E^2}{1+x^2} S_I(\omega_J), \quad (74)$$

$$\frac{\hbar^2 \omega_s^2}{2} \int_0^\infty S_\varphi(\omega) df = \left(\frac{eI_c |R_d|}{2v_b} \right)^2 \frac{\langle J_0^2 \rangle}{1+x^2} \int_0^\infty (\sqrt{G(\omega)} - 1)^2 S_I(\omega_J) df \quad (75)$$

In Eq. (75) $(\sqrt{G} - 1)^2$ converges to zero more rapidly than a Lorentzian:

$$\int_0^\infty (\sqrt{G} - 1)^2 df = \int_0^\infty \left[(G - 1) + 2(1 - \sqrt{(G - 1) + 1}) \right] df < \int_0^\infty (G - 1) df. \quad (76)$$

We define a correction factor κ to write the result of the above integral in terms of the result of Eq. (64):

$$\int_0^\infty (\sqrt{G(\omega)} - 1)^2 df = \frac{\kappa \omega_s (G_m - 1)}{4Q_s}. \quad (77)$$

The correction factor κ , displayed in Fig. 2, approaches 1 at large gain, but at small gain $\kappa \ll 1$. Thus, we may separate out the ratio of the variance δ_s^2 to $\langle J_0^2 \rangle$:

$$\frac{\delta_s^2}{\langle J_0^2 \rangle} = \frac{\kappa e^3 I_c |R_d|^2 (G_m - 1)}{2Q_s \hbar^2 v_b (1+x^2) \omega_s} = \frac{4\kappa e^4 R^3 I_c^2 v_b^2 (\sqrt{G_m} + 1)(1+x^2)}{\hbar^3 \omega_s^2 (\alpha_C + x)(1+3x^2)}. \quad (78)$$

The variance is related to the voltage fluctuations via $\sigma^2 = \hbar^2 \omega_s^2 \delta_s^2 / (2eRI_c)^2$. Considering the limit $\langle J_0^2 \rangle = 1$,

$$\sigma_{\text{mix}}^2 = \frac{\kappa e |r_d| (\sqrt{G_m} + 1)}{4I_c R v_b (C + C_J)(1 + \beta_c^2 v_b^2)} = \frac{\kappa e^2 R |r_d| (\sqrt{G_m} + 1)}{2\hbar (1 + \beta_c^2 v_b^2) (\alpha_C + \beta_c v_b)}. \quad (79)$$

Most importantly, σ_{mix}^2 grows linearly with R , which has to be taken into account in the amplifier design.

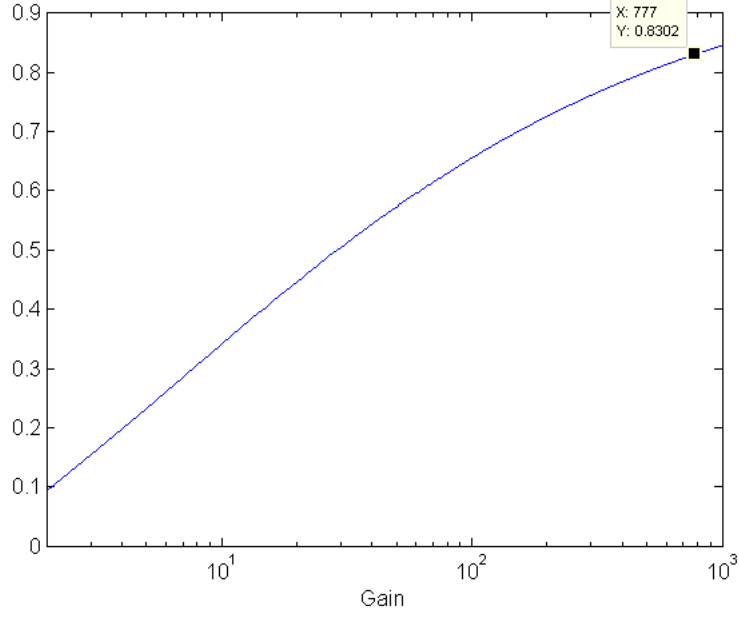


FIG. 2. Correction factor κ employed in expressing the integral Eq. (76) in terms of the result of Eq. (64).

III. PRACTICAL CONSIDERATIONS IN THE SJA DESIGN

The constraints that limit the available range of device parameters are listed in Table I. We extract some crucial relationships between R , I_c and C_J from the chapters above:

$$2eRI_c v_b = \hbar\omega_J = N\hbar\omega_s \quad (80)$$

$$N\omega_s RC_J = \beta_c v_b = x \quad (81)$$

$$|\Gamma(\omega_s)|\Delta\omega_{-3\text{dB}} \propto \frac{N(1+3x^2)}{v_b^2(1+x^2)^2} \quad (82)$$

$$\sigma_{\text{mix}}^2 \propto Rv_b^2(\sqrt{G_m} + 1) \quad (83)$$

$$\sigma_{\text{in}}^2 \propto \frac{v_b(\sqrt{G_m} + 1)}{I_c} \quad (84)$$

A. Limit of small fluctuations

The optimization in the case of small fluctuations $\delta_s^2 \ll 1$ begins with studying the down-mixed noise (Eq. (61) with $\xi = 1$). At low bias, the Josephson frequency is relatively small: N has to be a fraction, e.g. 2.5 or 3.5, because sidebands of the Josephson frequency (and its

TABLE I. SJA boundary conditions; Shunt $R-L-C$, Josephson frequency ω_J , junction capacitance C_J , plasma frequency ω_p , voltage bias v_b , critical current I_c , $\beta_c = 2eR^2I_cC_J/\hbar$.

Requirement	Solution
Shunt C not visible at ω_J	$\alpha_C = \omega_J RC = \beta_c v_b C / C_J > 1$
$\omega_p < \omega_J$	$\sqrt{\beta_c} v_b > 1$
$\omega_J > \omega_s$	$2eRI_c v_b > \hbar\omega_s$
Noise at ω_J is quantum	$2eRI_c v_b \gg k_B T_{\text{shunt}}$
$\hbar\omega_J$ is smaller than gap	$\hbar\omega_J < \Delta$
Stability	I_c is large enough, R is small enough
High bias	$v_b \geq 3$
Minimal direct noise	$\omega_s \approx 1/\sqrt{LC}$

harmonics) must not coincide with the signal frequency. Eq. (67) reveals that the bandwidth of the amplifier will suffer both from a small N and from a high $\beta_c v_b$ ($\beta_c = 2eR^2I_cC_J/\hbar$). Therefore, the noise optimization at $\delta_s^2 \ll 1$ is in conflict with a high bandwidth. The lower bound of v_b is found by (i) considering stability, i.e., forbidding zero crossings for the voltage fluctuations around v_b , (ii) remembering that high Josephson frequency (in practise, high v_b) was assumed in the calculations of Ch. II. By fixing N , the bias gives the product RI_c from Eq. (80). Stability can be improved by selecting a low R and a high I_c , because both σ_{in}^2 and σ_{mix}^2 will be decreased. Finally, fixing β_c gives x and the product RC_J . The disadvantages of a high RC_J will be discussed later. Guidelines for parameter selection are listed in Table II

B. Noise compression limit

The ultimate limit of noise compression, i.e., the exact form of $\xi(\delta_s^2)$, is unknown to us. It remains to be studied whether the standard quantum limit of added noise can be reached by means of compression. The non-linearities of the SJA will begin to limit the gain and alter the operation point when the variance of phase fluctuations grows beyond $\delta_s^2 = 1$. Here we analyze the simplest compression model $\xi(\delta_s^2) = \langle J_0^2 \rangle$, see Eq. (61). The ratio $\delta_s^2 / \langle J_0^2 \rangle$ grows linearly with $(\sqrt{G_m} + 1)$ as shown in Eq. (78). The procedure of estimating noise

TABLE II. SJA parameters at low ω_J and δ_s^2 . GBP is the gain-bandwidth product, σ^2 is the dimensionless variance of the Josephson voltage noise, and $\alpha_C = \omega_J RC$.

Parameter	Advantages	Disadvantages
Low R	Down-mixed noise stability σ_{mix}^2	Poor impedance matching
High I_c	Input noise stability σ_{in}^2	R becomes lower
Low N	Low down-mixed noise	Poor impedance matching, low GBP, shunt must be at low temperature
High β_c	Low down-mixed noise, $\omega_p \ll \omega_J$	Poor impedance matching, low GBP
High α_C	Stability, IV curve is accurate	Low GBP, direct noise grows rapidly when moving away from the shunt eigenfrequency

compression is numerical: there is a one-to-one correspondence between variance δ_s^2 and the ratio $\delta_s^2/\langle J_0^2 \rangle$. The latter is exactly known and we can read it from a graphical plot in Fig. 3, where we also depict δ_s^2 and $\langle J_0^2 \rangle$ separately. In the analytical modeling, we assume that the fluctuations of φ_s conform to a Rayleigh distributed amplitude (see Eq. (30)), although in the numerics there are observable deviations from this assumption. The compression factor is plotted as a function of gain in the lowest frame of Fig. 3. This graph defines the modification $0 < \langle J_0^2 \rangle \leq 1$ of the input noise temperature obtained for the investigated amplifier using linear models.

IV. RESULTS

A. Reproduction of the experimental findings in the noise compression regime

The bandwidth of the numerical simulation was 1 THz, and the input noise at $T_{\text{in}} = 70$ mK was bandpass filtered between 2.5 GHz and 3.5 GHz. The device parameters in the simulation are given in Table I of the main paper. The temperature of the shunt was set to $T_{\text{shunt}} = 400$ mK,

The dynamic resistance of the junction was -1370Ω in the simulation and -1350Ω analytically. A 28.9 dB power gain was observed at high L_2 (measured gain was 28.3 ± 0.2 dB). The gain-bandwidth-product was 42 MHz, and the added noise was 270 ± 30 mK (40

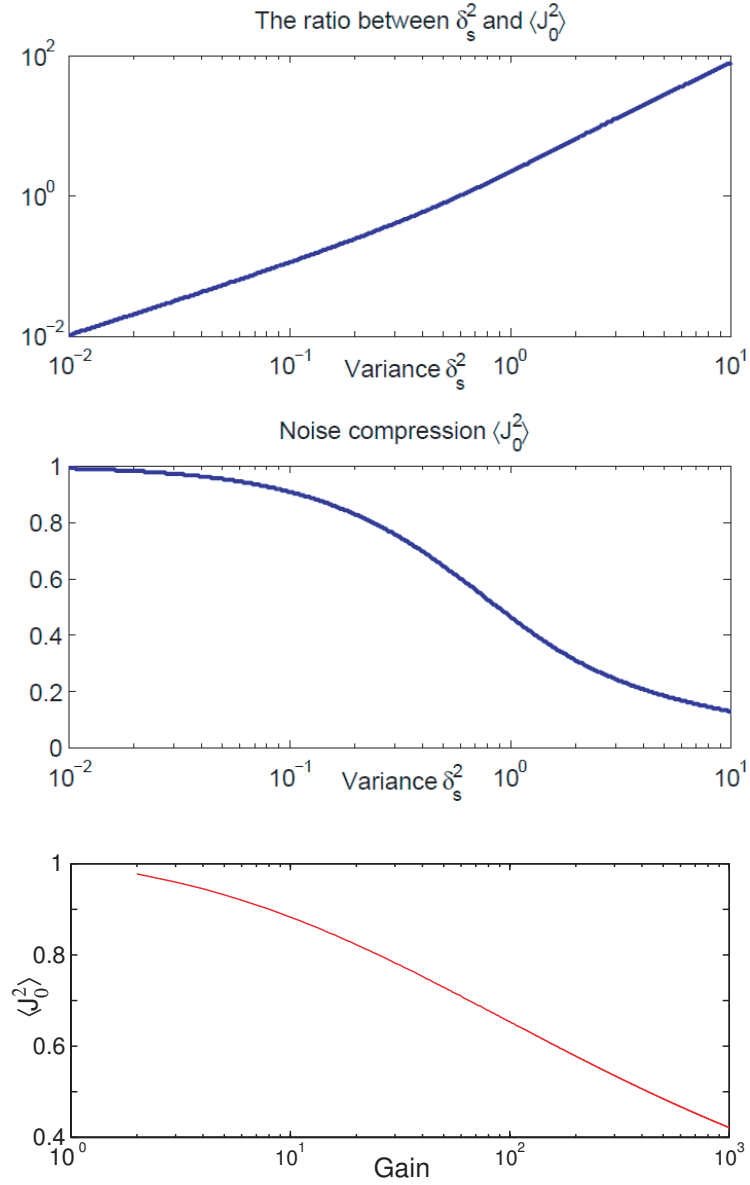


FIG. 3. Top frame: the ratio $\delta_s^2/\langle J_0^2 \rangle$ as a function of phase noise variance δ_s^2 in the signal band. Middle frame: noise compression as a function of the variance δ_s^2 . Lowest frame: the suppression factor $\langle J_0^2 \rangle$ vs. gain for the parameters used in the experiments (this suppression factor was employed in Fig. 5 in the main paper).

MHz and 220 ± 70 mK in the experiment, respectively). Altogether, the simulation was in good agreement with the experiment.

B. Quantum limited amplifier without noise compression

We minimized the down-mixed noise at low bias ($v_b \geq 3$) using Eqs. (61) and (62). In the best configurations, 0.9 noise quanta per unit band are added by the SJA. The optimum corresponds to $v_b = 3$, $\beta_c = 0.3 - 0.5$ and $N = 2.1 - 2.6$. The device parameters of the best simulated amplifier are listed in Table III. The shunt eigenfrequency was 3.0 GHz and the shunt temperature was set to 100 mK. The gain reached 14.5 ± 0.2 dB and the output

TABLE III. The best simulated SJA. For the parameter definitions, see Ch. I of this Supplementary material. $\alpha_C = \omega_J RC$.

Parameter	Value	Parameter	Value
Z_0	2.5Ω	I_c	$1 \mu\text{A}$
R	5Ω	C_J	4.6 pF
C	45 pF	$\omega_p/(2\pi)$	4.1 GHz
L	63 pH	β_c	0.35
C_2	33 pF	I_b	$3 \mu\text{A}$
L_2	0.69 nH	$\omega_J/(2\pi)$	7.0 GHz
ω_s	3.0 GHz	α_C	10

noise power was equivalent to 6.3 ± 0.3 K. Our numerical simulation yielded 0.9 ± 0.2 quanta for the added noise, in excellent agreement with the analytic model. We also simulated six other amplifiers at the bias $v_b = 3$. It was found that high RC_J may be responsible for the breakdown of the down-mixed noise model. The high RC_J modifies the phase differences induced by upmixing and downmixing processes. Several quanta of noise were added in some simulations at $\beta_c = 0.35 - 0.90$, even though the analytic expectation was about 1 quantum. At $\beta_c = 0.1$ the noise temperature was also very high, and we believe that this resulted from high plasma frequency $\omega_p > \omega_J$. Results consistent with our analytical model are plotted in Fig. 4.

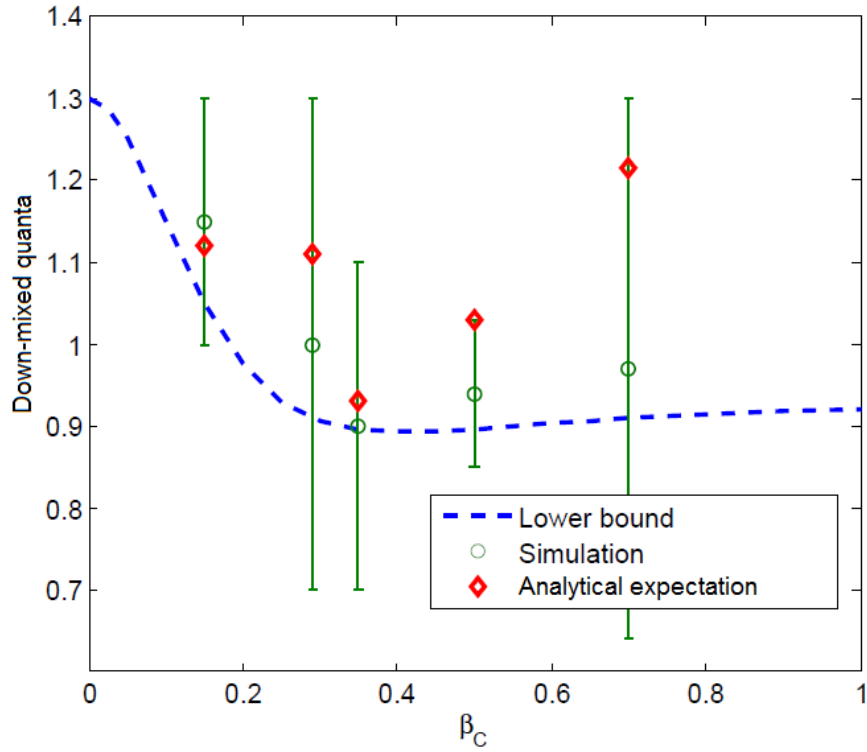


FIG. 4. Analytic model, Eqs. (61) and (62), yields a lower bound for added noise as a function of β_C . Several SJAs with varying parameters were simulated at $v_b = 3$. Gain was in the range $G_m = 11.2 - 24.5$ dB and $N = \omega_J/\omega_s = 2.3 - 5.6$. Our analytic model predicts accurately the down-mixed noise contribution provided that $\omega_J > \omega_p$ and RC_J is small.

-
- [1] M. Abramowitz and I. A. Stegun. *Handbook of Mathematical Functions with Formulas, Graphs, and Mathematical Tables*, U. S. Department of Commerce, 1972, Chap. 11.
- [2] K. K. Likharev and V. K. Semenov. Fluctuation Spectrum in Superconducting Point Junctions, *JETP Lett.* **15**, 442 (1972).
- [3] K. K. Likharev. *Dynamics of Josephson Junctions and Circuits*, Gordon and Breach, New York (1986).
- [4] R. H. Koch, D. J. van Harlingen, and J. Clarke. Quantum-Noise Theory for the Resistively Shunted Josephson Junction, *Phys. Rev. Lett.* **45**, 2132 (1980).
- [5] Y. Levinson. Quantum noise in a current-biased Josephson junction, *Phys. Rev. B* **67**, 184504 (2003).
- [6] F. T. Brandt, J. Frenkel, and J. C. Taylor. Noise in resistively shunted Josephson junctions, *Phys. Rev. B* **82**, 014515 (2010).
- [7] S. Haykin. *An Introduction to Analog and Digital Communications*, Wiley, New York, 1989.
- [8] G. Arfken. *Mathematical Methods for Physicists*, Academic Press, New York, 1970, p. 482.

PUBLICATION II

Tunable Impedance Matching for Josephson Junction Reflection Amplifier

IEEE Trans. Appl. Supercond. 23, 1500140.
Copyright 2013 IEEE.
Reprinted with permission from the publisher.

Tunable Impedance Matching for Josephson Junction Reflection Amplifier

Visa Vesterinen, Juha Hassel, and Heikki Seppä

Abstract—It has been recently demonstrated that a single Josephson junction with a properly engineered impedance environment can be used as a reflection amplifier approaching the quantum limit at microwave frequencies. In this article the authors describe an improved microwave setup for such a device. Voltage-tunable capacitors enable precise impedance matching across a wide range of operating points. Also, a branch-line coupler instead of a microwave circulator is used for the separation of the input and the output signals to make the system more compact and affordable. Furthermore, a custom-designed bias tee is introduced. The authors present characterization results of individual components as well as of the complete system. In particular, noise spectroscopy is used to study amplifier stability as a function of input matching.

Index Terms—Impedance matching, Josephson effect, microwave amplifiers.

I. INTRODUCTION

RECENT advances in quantum information processing have stimulated research on ultralow-noise amplifiers at microwave frequencies. In many experiments with, e.g., superconducting qubits and nanoelectromechanical resonators, weak microwave signals have to be amplified at cryogenic environment [1]–[4]. We have proposed an amplifier architecture (single junction amplifier, SJA) which takes advantage of the dissipationless and non-linear characteristics of the Josephson junction. Near-quantum-limited noise performance has recently been demonstrated [5]. Operated at finite voltage state enabled by DC current biasing, the junction exhibits negative differential resistance which is in many applications well hidden due to the resistive damping of the junction. In our case, the negative differential resistance is damped at low and high frequencies by a shunt resistor. The on-chip dissipation is blocked on the signal band by an LC bandstop filter in series with the shunt resistor, selectively revealing the negative differential resistance of the junction. Stability at signal frequency is provided by the damping from the external circuitry, in our system by the dissipative $Z_0 = 50 \Omega$ input of the second amplifying stage. Reflection power gain is generated by a transmission line terminated by the negative differential resistance.

The optimum operating condition for an SJA is such that the absolute value of the input impedance Z_{in} is real, negative

and in the order of Z_0 as reflection power gain is $|\Gamma|^2 = |(Z_{in} - Z_0)/(Z_{in} + Z_0)|^2$. However, in our practical circuits the magnitude of the negative differential resistance tends to be much larger than Z_0 whence impedance matching is required. This can be achieved by a resonant transformer. In practice, the signal band is set slightly off the center frequency of the LC bandstop filter to a point where $\text{Re}(Z_{in}) \approx -50 \Omega$ and compensating for the remaining reactive part is accomplished with additional reactive components. Previously, they were realized as passive components [5]. This made it laborious to find correct experimental parameters since parasitic components such as bonding wire inductance contribute significantly. Here we address this issue by applying varactor diodes enabling post-cooldown tuning of the matching circuit. We find suitable GaAs based varactor diodes maintaining their high-frequency performance at the cryogenic temperature. The effect of the tuning circuit on device stability is studied.

An additional challenge with reflection amplifiers is the decoupling of the amplified signal from the input. Non-reciprocal circulators are typically applied but they are often bulky and expensive. We study a simple branch-line coupler to replace the circulators. We present and characterize a complete microwave design including the tunable input circuit, the coupler as well as custom-designed DC block for biasing.

II. CIRCUIT DESIGN

We designed a printed circuit board which contains an amplifier sample on a chip, DC biasing circuitry, tunable impedance matching, and a branch-line coupler. Rogers RT/duroid 6002 is a suitable high-frequency laminate for cryogenic applications due to its temperature stability. The guided wavelength within microstrip structures is almost independent of temperature [6]. Our printed circuit board has a substrate 30 mils (0.76 mm) thick, and bulk permittivity is $\epsilon_r = 2.94$. The final design for 3 GHz signal band is pictured in Fig. 1.

In Fig. 1, input (IN) and output (OUT) are at branch-line coupler ports 1 and 4, respectively. The branch-line coupler is a four-port structure which comprises four units of transmission line with lengths of one quarter of guided wavelength at center frequency, and precisely engineered line impedances [7]. Reflective port 2 is named as sample branch and port 3 is a resistive termination. At the center frequency no input power is directly guided into the output ($S_{41} \approx 0$). S_{21} represents the transmission of input power to the reflective port and, due to symmetry $S_{34} = S_{21}$, the transmission of output back-action noise into a Z_0 termination. S_{42} is the transmission of the amplified signal into the output and, due to symmetry

Manuscript received October 9, 2012; accepted November 4, 2012. Date of publication November 15, 2012; date of current version December 8, 2012. This work was supported by the Academy of Finland.

The authors are with the VTT Technical Research Centre of Finland, 02044 VTT, Finland (e-mail: visa.vesterinen@vtt.fi).

Color versions of one or more of the figures in this paper are available online at <http://ieeexplore.ieee.org>.

Digital Object Identifier 10.1109/TASC.2012.2227653

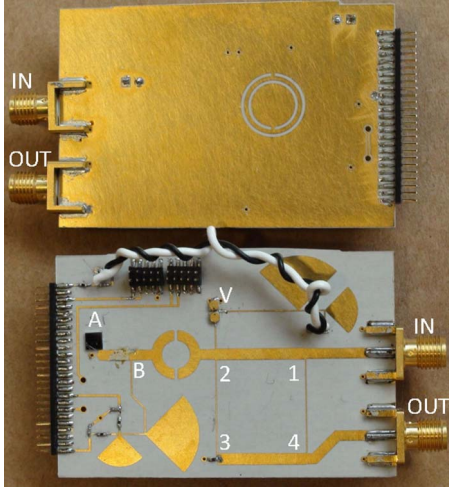


Fig. 1. Printed circuit board with microstrip structures. The rectangular dimensions are 62 mm \times 41 mm. The various symbols are: A, amplifier; B, bias-tee; V, varactors; 1-2-3-4, branch-line coupler. The ground plane features split-ring resonators. The radial stubs form RF chokes. The twisted pair of wire carries varactor diode supply voltage.

$S_{24} = S_{42} = S_{31}$, the transmission of output back-action noise into the reflective port. We denote coupler asymmetry with symbol r , the power split ratio $|S_{21}/S_{31}|^2$ at center frequency. Two parallel microstrip lines are given the same characteristic impedance $Z_0\sqrt{r}$ (vertical traces in Fig. 1) or $Z_0\sqrt{r/(1+r)}$ (horizontal traces in Fig. 1). Transmission magnitudes are

$$|S_{21}|^2 = r/(1+r) \quad (1)$$

$$|S_{31}|^2 = 1/(1+r). \quad (2)$$

Power entering at IN and leaving at OUT will experience the gain $|S_{21}\Gamma S_{31}|^2$, where Γ is the reflection coefficient of the sample branch. In Fig. 1 the branch is the parallel configuration of two terminations: varactor diodes (V) and the wire-bonded amplifier chip (A) in series with a bias-tee (B). The bias-tee consists of an RF choke which feeds in the DC biasing current for the amplifier; a similar choke based on radial stubs is supplying the reverse bias voltage for the varactor diodes. The bias-tee also features a high-pass filter the operation of which relies on split-ring resonators [8]. The block diagram containing the elements of Fig. 1 as well as external circuitry is in Fig. 2.

According to branch-line coupler equations the reflection coefficients, as referred to IN and OUT, are $|S_{21}\Gamma S_{21}|^2$ and $|S_{31}\Gamma S_{31}|^2$, respectively. These both should be minimized, but an immediate conflict appears: vanishing S_{21} and S_{31} suppress the gain provided for microwaves guided from IN to OUT. Such trade-offs are inherent in a reciprocal design in comparison with a circulator design. We decided to decouple OUT from the reflective port as well as possible, by increasing r [see also (2)]. In practice, the characteristic impedance $Z_0\sqrt{r}$ is increased until manufacturing constraints are reached: the higher the impedance, the narrower the microstrip trace width. On the other hand, S_{21} in (1) will approach unity, implying a maximal signal-to-noise ratio at the reflective port, an important property in the determination of the noise temperature, for example. The main trade-off here is the poor input matching. This is

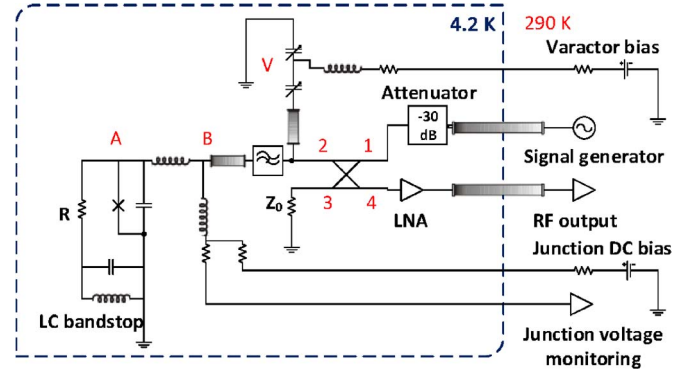


Fig. 2. Block diagram of our printed circuit board and the components connected into it. For the descriptions of symbols, see Fig. 1 and text. The amplifier chip contents are shown: the Josephson junction is symbolized with a cross and its intrinsic capacitance is drawn separately. In a linearized picture, which proved to be successful in [5], the junction can be replaced with a negative resistor at microwave frequencies. Bonding wire inductance between A and B should be noted. Low-noise amplifier (LNA) DC biasing is omitted for clarity. The DC return path of the lower varactor (tunable capacitance) follows the route through ports 2 and 3.

tolerable if the source impedance is real 50 Ω , which in our characterization measurements is achieved by placing a cold attenuator in front of the input port.

In Fig. 1 there are two additional precise lengths of microstrip line: one from port 2 to the varactors, and the other one from the high-pass filter to the amplifier chip. Their interplay, together with the range of capacitances available from the series connection of two varactors, is responsible for the impedance matching of the chip. We considered two scenarios: the chip introduces either a large or a negligible mismatch. The mismatch is typically large at high DC bias currents since the magnitude of negative differential resistance exceeds Z_0 there. At low biases, on the other hand, the SJA as such may appear as $Z_{in} \approx -Z_0$ over a wide band of frequencies. The parallel admittance Y determined by the section of microstrip line (characteristic impedance Z_V) and the varactor termination (effective capacitance C_{eff}) is [9]

$$Z_V Y = \frac{Z_V + \tan \theta / (\omega C_{eff})}{-i / (\omega C_{eff}) + i Z_V \tan \theta}$$

$$\Leftrightarrow Z_V Y = i \frac{\omega Z_V C_{eff} + \tan \theta}{1 - \omega Z_V C_{eff} \tan \theta} \quad (3)$$

Here ω is angular frequency, and θ is the phase 2π times the geometric length divided by guided wavelength. In the middle of capacitance range and at the intended signal frequency we set Y to either infinity or zero. Infinite admittance grounds the sample branch and at slightly lower and higher capacitances Y is able to cancel large reactances of the amplifier chip and the bonding wires. The condition for Y is $\theta = \arctan(\omega_s Z_V C_{eff})^{-1}$ (here ω_s is signal frequency and \bar{C}_{eff} is the capacitance averaged over the range of reverse bias voltages). Zero admittance represents an open circuit that does not interfere at all with the branch terminated by the chip. This is a useful feature if the chip needs minimal reactance cancellation. Zero admittance is achieved at the phase $\theta = \arctan(-\omega_s Z_V \bar{C}_{eff})$.

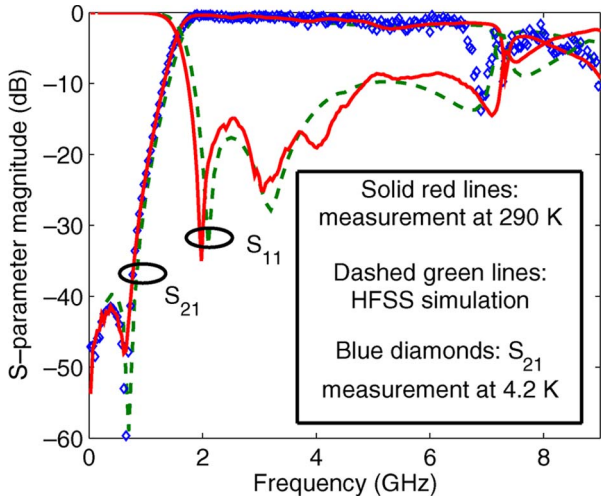


Fig. 3. Transmission and reflection characteristics of the microstrip high-pass filter. Insertion loss is 0.6 dB near the 3 GHz band, and return loss is better than 20 dB. Split-ring resonators are responsible for the 1.6–6.7 GHz -3 dB bandwidth at low temperature. The cooldown does not remarkably alter filter properties.

III. MEASUREMENTS

We cooled down some varactor diodes (M/A-COM, USA) and studied transmission S-parameter amplitude and phase to measure the capacitance. Two surface-mount diodes with nominal room temperature capacitances 1 pF and 10 pF were found to retain their properties at microwave frequencies at liquid helium temperature.

We tailored the high-pass filter response with Ansoft HFSS electromagnetic simulation software. The filter was implemented on an individual board which was measured with a network analyzer (Agilent E8362B) both at room temperature and when immersed in liquid helium. As pictured in Fig. 3, the simulation is in good agreement with the measured S-parameters, and we could verify that the cooldown induces negligible changes in the electrical properties of the board. It was essential to record the phase response as well (not shown) since it affects the functionality of the impedance matching elements.

The characterization of reflection amplifiers on printed circuit board was done in a liquid helium dewar through a dipstick. The usable bandwidth of the branch-line coupler was as large as 500 MHz and did not limit the amplifier operation. As visualized in Fig. 2, we placed a -30 dB cryogenic attenuator (Omni-Spectra, USA) at the input port, and a $+38$ dB cryogenic RF amplifier (Low Noise Factory LNC4_8A) at the output port. Rohde-Schwarz FSP30 spectrum analyzer could be connected to the output when needed. It was often accompanied by a $+42$ dB RF pre-amplifier Wenteq ABL-0600-01-4345. The first amplifier chip that we studied was identical to the one described in [5], except for the shunt resistor material (Mo instead of TiW). We cooled it down and measured the current-voltage characteristics (IV curve) to find critical current ($I_c \approx 12 \mu\text{A}$) and shunt resistance ($R \approx 3.5 \Omega$). The DC current bias was generated by a DC voltage generator in series with a large resistor. Josephson junction voltage was monitored with INA103 instrumentation amplifier at room temperature.

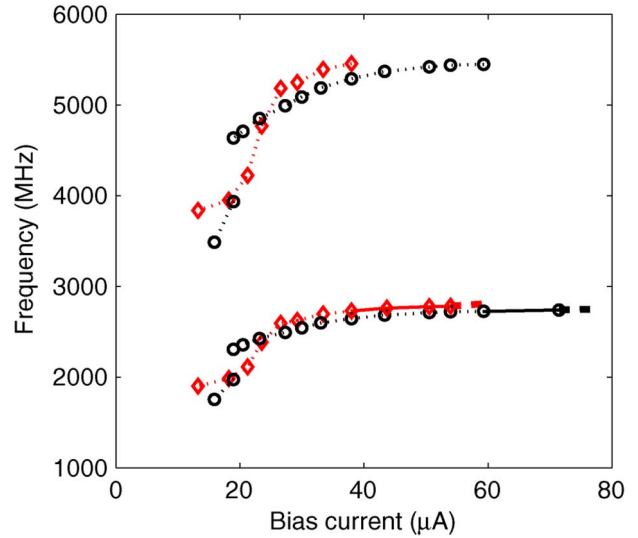


Fig. 4. Noise peak center frequencies. The datasets represent high (black circles) and low (red diamonds) varactor capacitance. The lower curves show the fundamental frequency of the amplifier and the upper curves show the first harmonic. The bias regime with harmonic content, marked with dotted traces, indicates unstable behaviour. The regime lacking harmonic content, marked with solid lines, provides stable gain that fades away at high bias. Bandwidth of the spectrum analysis was limited by the insertion loss of the high-pass filter, see Fig. 3.

In Figs. 1 and 2 the impedance matching circuitry follows the infinite admittance strategy described in the previous chapter. The power split ratio of the branch-line coupler is $r \approx 7.3$. Equation (3) was re-written for the branch containing the SJA and bias tee: the high-pass filter phase was contained in θ and the effect of the RF choke was ignored. We calculated the impedance mismatch for a handful of slightly different SJAs (assuming 3-nH bondwires) and searched for transmission line lengths which support impedance matching of the SJAs in question. The optimization established the following parameters: first, the trace preceding the varactors is 0.1 wavelengths long at 3 GHz and its characteristic impedance is 125Ω . Second, the $50\text{-}\Omega$ section between the high-pass filter and the chip is 0.15 wavelengths long. The performance of the impedance matching elements were experimentally tested with noise spectroscopy. The input was a Z_0 termination at room temperature: its purpose was to suppress parasitic resonances. The environmental noise level entering the port IN was set by the cold -30 dB attenuator. The output was connected to the spectrum analyzer. An indication of stable operation is that amplified thermal input noise is manifested as an output spectral peak representing the gain at signal band, whereas instabilities are typically manifested as highly non-linear oscillations having also higher harmonics in the spectra [5]. Resulting stability data obtained by sweeping the junction current bias and the varactor voltage bias are illustrated in Fig. 4. Changing the varactor capacitance shifts the range of junction biases which provide stable gain, an indication of successful circuit design. At the same time, the frequency of maximal gain is shifted as the magnitude of the impedance transformation determines the small offset from that determined by the LC bandstop filter. A more effective frequency tuning method would be to connect a varactor diode directly in parallel to the bandstop filter.

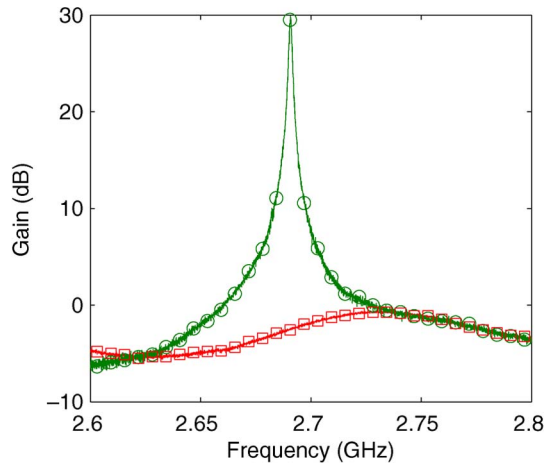


Fig. 5. Gain referenced to ideal reflection ($|\Gamma| = 1$) at the second port of the branch-line coupler, at -145 dBm input power entering port IN. The OFF state (red squares) is the zero voltage state of the Josephson junction. The ON state (green circles) is at bias point $54 \mu\text{A}$ and the varactor capacitance is low, see the red diamond curve of Fig. 4.

We selected a single bias point for more careful examinations with the network analyzer. Gain introduced by reflection from port 2 is visualized in Fig. 5: both the ON and OFF states of the amplifier are shown. The curves were calibrated with a separate printed circuit board where the reflective port is empty ($|\Gamma| = 1$ from an open circuit termination). It is not surprising that at the OFF state (zero voltage state of the Josephson junction) port 2 absorbs microwave power to some extent: microstrip losses, the insertion loss of the high-pass filter, and the parasitic series resistance of the varactor diodes are introducing dissipation. At the ON state (bias current about 4–5 times greater than I_c) we studied the gain as a function of input power, observed linearity at low powers, and found the -1 dB compression point -117 dBm. Assuming that the shunt and junction capacitances are $C = 4.3$ pF and $C_J = 0.4$ pF, respectively, we get some analytical estimates (see the theoretical work in [5]): negative differential resistance is $R_d \approx -130 \Omega$, and gain-bandwidth product from bandstop filter parameters is $2/(|R_d|(C + C_J)) \approx 2\pi \times 530$ MHz. In the measurement we observed at port 2 a five times smaller gain-bandwidth product, $2\pi \times 100$ MHz. We attribute this decrease to i) losses in the input matching network, and ii) intentional frequency response sharpness of the matching network, the line terminated with varactor diodes in particular.

IV. CONCLUSION

We developed and tested a controlled impedance environment for a single Josephson junction reflection amplifier. The stability was studied through noise spectroscopy, and the gain provided by Josephson junction negative differential resistance was extracted from transmission S-parameter measurements. High gains up to 30 dB were easily achieved with the aid of tunable impedance matching by varactor diodes. We described a realization of a complete microwave design on a single printed circuit board dedicated to signal frequencies around 3 GHz, but the design methods can be easily generalized to higher frequencies. We also employed a branch-line coupler as an alternative for circulators. The coupler is preferred due to its simplicity, modifiability and affordability. The drawback is input mismatch. It can be noted that the other components presented in this work (tunable matching circuit and DC block circuit) are applicable and useful also in circulator-based setups.

ACKNOWLEDGMENT

The authors would like to thank P. Lahteenmaki and P. Hakonen at the O. V. Lounasmaa Laboratory, Aalto University, for helpful discussions.

REFERENCES

- [1] M. Hatridge, R. Vijay, D. H. Slichter, J. Clarke, and I. Siddiqi, "Dispersive magnetometry with a quantum limited SQUID parametric amplifier," *Phys. Rev. B*, vol. 83, p. 134501, 2011.
- [2] N. Bergeal *et al.*, "Phase-preserving amplification near the quantum limit with a Josephson ring modulator," *Nature*, vol. 465, pp. 64–68, 2010.
- [3] M. Muck, J. B. Kycia, and J. Clarke, "Superconducting quantum interference device as a near-quantum-limited amplifier at 0.5 GHz," *Appl. Phys. Lett.*, vol. 78, pp. 967–969, 2001.
- [4] B. Abdo, F. Schackert, M. Hatridge, C. Rigetti, and M. Devoret, "Josephson amplifier for qubit readout," *Appl. Phys. Lett.*, vol. 99, p. 162506, 2011.
- [5] P. Lahteenmaki *et al.*, "Josephson junction microwave amplifier in self-organized noise compression mode," *Sci. Rep.*, vol. 2, p. 276, 2012. DOI:10.1038/srep00276.
- [6] N. Wade Falk *et al.*, "Cryogenic wide-band ultra-low-noise IF amplifiers operating at ultra-low DC power," *IEEE Trans. Microw. Theory Tech.*, vol. 51, no. 6, pp. 1705–1711, 2003.
- [7] R. E. Collin, *Foundations for Microwave Engineering*, 2nd ed. Hoboken, NJ: Wiley, 2001, pp. 432–434.
- [8] J.-C. Liu *et al.*, "Improved equivalent circuits for complementary split-ring resonator-based high-pass filter with C-shaped couplings," *IET Microw. Antennas Propag.*, vol. 2, no. 6, pp. 622–626, 2008.
- [9] D. M. Pozar, *Microwave Engineering*, 2nd ed. Hoboken, NJ: Wiley, 1998, ch. 2.

PUBLICATION III

**Submillimeter-wave kinetic
inductance bolometers
on free-standing nanomembranes**

Supercond. Sci. Technol. 27, 025002.
Copyright 2014 IOP Publishing Ltd.
Reprinted with permission from the publisher.

Submillimeter-wave kinetic inductance bolometers on free-standing nanomembranes

Andrey V Timofeev¹, Visa Vesterinen¹, Panu Helistö¹, Leif Grönberg¹, Juha Hassel¹ and Arttu Luukanen^{2,3}

¹ VTT Technical Research Center of Finland, PO Box 1000, FI-02044 VTT, Finland

² Millilab, VTT, Tietotie 3, Espoo, FI-02044, Finland

E-mail: andrey.timofeev@vtt.fi

Received 31 August 2013, revised 30 October 2013

Accepted for publication 12 November 2013

Published 12 December 2013

Abstract

We introduce a microwave submillimeter-wave detector based on an integrated micromesh absorber and superconducting kinetic inductance thermometer on a through-wafer released sub-micron thick membrane. Equilibrium operation achieved by thermal isolation through the membrane geometry enables operation at elevated thermal bath temperatures of 5–10 K. The bolometer operates in a phonon-noise limited regime with a measured noise equivalent temperature difference of below 10 mK at 1 s integration time, which is sufficient for radiometric imaging in terrestrial systems. We also measured and analyzed the bolometer frequency response in the band 0.1–1.4 THz. Performance improvements through further dimensional scale-down and temperature dependency are discussed.

Keywords: THz bolometer, kinetic inductance, membrane, frequency domain multiplexing, submillimeter-wave imaging

(Some figures may appear in colour only in the online journal)

1. THz imaging. Requirements for THz detectors and THz imaging systems

Radiometric imaging in the submillimeter-wave (THz) range allows for safe stand-off personnel security screening due to relatively good penetration of submillimeter waves through many dielectric materials [1]. The phenomenology of passive imaging is potentially less privacy intrusive compared, for example, with active imaging. This has triggered rapid developments of passive THz imaging systems and THz detectors with high resolution. Due to the low power levels of THz thermal signals governed by the Planck blackbody radiation law and a weak radiometric contrast between the objects and the human body (~ 10 K), passive submillimeter-wave imagers with radiometric resolution $\text{NETD} = 0.1\text{--}0.5$ K at video rate are required [2]. Such performance can be achieved with either broadband

superconducting, coherent heterodyne or direct preamplified THz detectors [1]. Most terrestrial applications would also benefit from near-diffraction limited angular resolution over a large field of view with tens of thousands of image pixels. This has until now been limited by the scalability of the focal plane detector technology. Recently developed prototypes of cryogenic THz imagers [3–5] utilize arrays of detectors in combination with scanning optics, compromising the need for a large number of pixels by optomechanical scanning. Scanning reduces the dynamic range of the image, increases the complexity, and reduces the reliability of the system. Therefore a passive THz imager would greatly benefit from a full 2D focal plane array (FPA). Multiplexed readout of such a 2D FPA is unavoidable, especially for cryogenic THz imagers. SQUID-based multiplexing of cryogenic detectors [6] is one solution, but it is somewhat complex manufacturing-wise and subject to electromagnetic interference in practice. Here we present microwave kinetic inductance bolometers operating at 4–10 K, meeting both sensitivity and scalability

³ Current address: Asqella Ltd, Kutomotie 18, 00380 Helsinki, Finland.

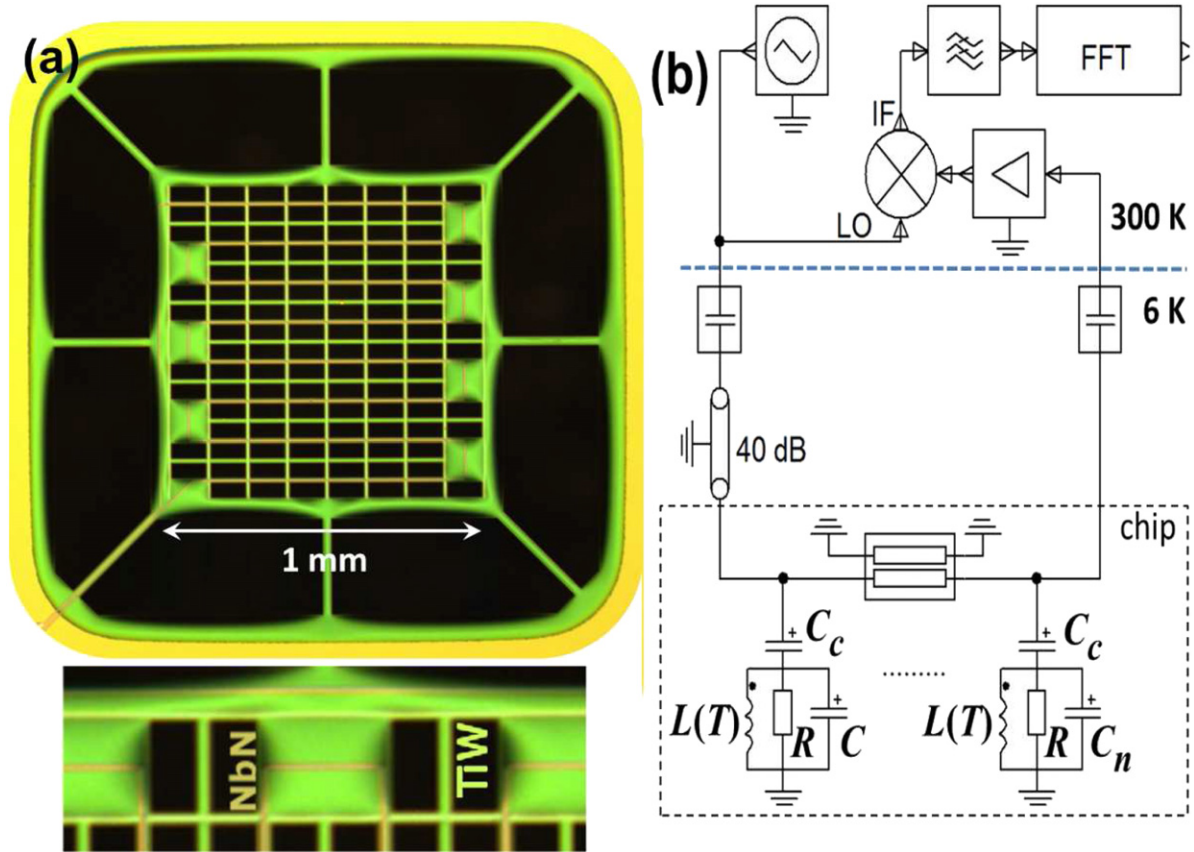


Figure 1. (a) Optical micrograph of the bolometer. Colors in the image from the camera of an optical microscope: SiN + SiO₂ membrane (green), NbN meandered line (light brown), TiW absorber (light yellow), Si substrate (dark yellow), holes (black). (b) Equivalent circuit of a microresonator bolometer array with microwave readout.

requirements for a superconducting submillimeter focal plane array. The concept and the first versions of superconducting kinetic inductance bolometers were proposed and realized [7] about two decades ago, and it has been also recently suggested [8] to revise this concept by using superconducting microwave resonators as they can be straightforwardly scaled up into frequency-multiplexed arrays. Here we present both a theoretical overview of the kinetic inductance bolometers and an experimental characterization of these devices, in line with the theory.

2. THz kinetic inductance bolometer. Theory overview

Our kinetic inductance bolometer (figure 1(a)) represents a superconducting NbN microresonator with a temperature T dependent inductive part $L(T)$ thermally coupled to a TiW grid absorber of THz radiation. The inductance has a long meander shape, and both meander and absorber films (each 100 nm thick), being separated by a 200 nm thick SiO₂ insulating film, are thermally isolated on a 200 nm thick SiN membrane mesh of about 1 mm² in area. The inductive meander is connected in parallel to a shunt capacitor C , forming a lumped superconducting LC-resonator with temperature-dependent resonant frequency $\omega_0(T) = 1/\sqrt{L(T)C}$ and impedance $Z(\omega_0(T))$. The resonator

is further connected to a superconducting transmission line of impedance $Z_0 = 50 \Omega$ through a series coupling capacitor C_c for microwave transmission $S_{21}(\omega) = (Z - i/\omega C_c)/(Z - i/\omega C_c + Z_0/2)$ readout, in the spirit of sub-Kelvin kinetic inductance detectors [9–11]. The minimum of S_{21} occurs at $\omega = 1/\sqrt{L(C + C_c)}$. In a thin superconducting film with a high normal-state resistivity, such as NbN in our case, kinetic inductance $L_k(T)$, being the measure of total inertia of charge carriers—Cooper pairs in a superconductor, can strongly dominate over the geometrical inductance L_g . At low frequencies $\omega_0 \ll \tau_{qp}^{-1}$, where τ_{qp}^{-1} is the rate of quasiparticle thermalization with a superconductor lattice, the total inductance $L(T)$ of the superconducting meander of length ℓ , width w and thickness t can be expressed as

$$L(T) = L_{k0}/[1 - (T/T_c)^a] + L_g. \quad (1)$$

Here T_c is superconducting transition temperature, $L_{k0} = \mu_0 \lambda_0^2 \ell / (wt)$, ($\ell \gg w \gg t$), and the zero-temperature magnetic penetration depth in the impure limit $\lambda_0 = \sqrt{\hbar \rho / (\mu_0 \pi \Delta_0)}$ is determined by the density of paired electrons $n_s(T) = n_{s0}$ at $T = 0$ through the normal-state resistivity $\rho = m / (n_{s0} e^2 \tau_e)$ (e is electron charge, m_e is the electron mass, μ_0 is the vacuum permeability, τ_e is the characteristic time of the electron mean free path, Δ_0 is the zero-temperature superconducting gap). Here $n_s(T)$ is assumed to obey the power law $n_s(T) = n[1 - (T/T_c)^a]$ [12] with the total density of conduction electrons

$n = n_s + n_{qp}$, including the density of quasiparticle thermal excitations n_{qp} . The intrinsic Q -factor of a superconducting resonator $Q_i = \frac{n_s}{n_{qp}} (\omega_0 \tau_{qp})^{-1}$ depends on temperature as

$$Q_i(T) = (\omega_0 \tau_{qp})^{-1} [(T/T_c)^{-a} - 1]. \quad (2)$$

The intrinsic thermal time constant of the bolometer $\tau_{th} = C_{th}/G$ is set by the membrane heat capacity C_{th} and the thermal conductance G of suspensions between the membrane and the substrate. Assuming for simplicity that only one component of the readout signal v_{out} is observed, the bolometer responsivity \mathcal{R} to the incident radiation power P_{rad} is defined as $\mathcal{R}_I = \eta^{-1} d(\text{Re}(v_{out}))/dP_{rad}$ and $\mathcal{R}_Q = \eta^{-1} d(\text{Im}(v_{out}))/dP_{rad}$ for in-phase (I-) and quadrature (Q-) components, where η is the quantum efficiency. The output voltage reads $v_{out} = S_{21} \sqrt{P_{rf} Z_0}$ (see appendix A) with the aid of equations (9)–(11) determining the resonator dynamics by the nonlinearity parameter $\alpha \propto P_{rf} \partial_T L$. In the linear regime $\alpha \ll 1$, \mathcal{R} can be increased by driving the resonator with a higher carrier microwave power P_{rf} . With a further increase of P_{rf} , α also increases, eventually breaking the assumptions of linear operation. In the nonlinear regime the thermal speed and the dynamic range can be traded off with the responsivity (equation (7)) as quantified by the thermal feedback loop gain $\beta = G^{-1} \partial_T P_m$ (equation (12)). Here, the experiments are carried out in the linear regime, whence the responsivity $\mathcal{R}_Q = \sqrt{\alpha a Z_0 / (2\omega_0 \tau_{qp} G T)}$ is limited by $\alpha \lesssim 0.1$ in practice.

The electrical noise equivalent power of the bolometer reads

$$\begin{aligned} \text{NEP}^2 = & \text{NEP}_{gr}^2 + \text{NEP}_{ph}^2 \\ & + \frac{4k_B (T + T_n) \text{Re}(Z_{||})}{2\mathcal{R}^2} \frac{Z_0^2}{|Z_0 + Z_{||}|^2}, \end{aligned} \quad (3)$$

with the phonon $\text{NEP}_{ph} = \sqrt{4k_B T^2 G}$ (assuming no thermal gradient across the membrane suspension legs [13]) and the quasiparticle generation–recombination $\text{NEP}_{gr} = (GT/a) \sqrt{\tau_{qp}/(Vn)} (T/T_c)^{-a/2}$ (equation (21)) noise equivalent powers. The last term in (3) represents the Johnson noise of the resistive elements, the detector dissipation and the feeding line, and the noise of the readout setup represented by noise temperature T_n referred to the impedance $Z_{||} = ((Z - i/\omega C_c)^{-1} + Z_0^{-1})^{-1}$. The prefactor 2 in front of \mathcal{R}^2 is due to the single quadrature case. As in thermal equilibrium the generation–recombination noise $\text{NEP}_{gr} \propto G \sqrt{\frac{\tau_{qp}}{Vn}}$ is significantly reduced, in contrast to the non-equilibrium case where it dominates ($\text{NEP}_{gr}^{\text{noneq}} \propto \sqrt{\frac{Vn}{\tau_{qp}}}$, V —superconductor volume), the bolometer operates in the phonon-noise limit provided \mathcal{R} is made large enough.

3. Measurements

3.1. Temperature dependence of kinetic inductance and quality factor

The superconductor material parameters were determined by measuring the transmission spectra S_{21} from 0.2 to

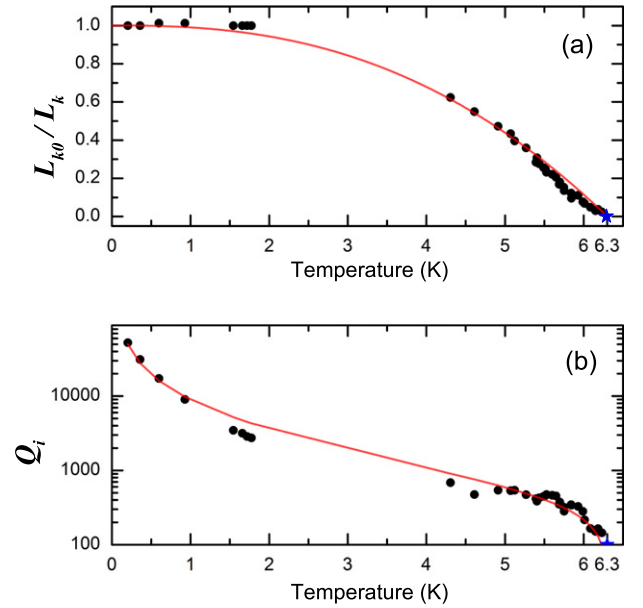


Figure 2. (a) Temperature dependence of the normalized kinetic inductance. (Inset) S_{21} transmission at 5.8 K. (b) Temperature dependence of the intrinsic quality factor Q_i . Data—dots, lines—data fits. $T_c = 6.3$ K used in the fits is shown by a blue star at the temperature axis.

6.2 K with a low carrier power P_{rf} . The data was fitted to equations (9) and (10) with $\alpha = 0$ to obtain Q_i and ω_0 . Nominal capacitances $C = 96$ pF and $C_c = 2.1$ pF were assumed. The geometric inductance $L_g = 3.0$ nH of the meander with $\ell = 4.2$ mm, $w = 5$ μm and $t = 100$ nm was determined by field simulation software. The low-temperature limit of kinetic inductance L_{k0} was found to be 7.8 nH, corresponding to $\lambda_0 \approx 860$ nm. Resulting $L(T)$ and $Q_i(T)$ data are shown in figure 2 along with the fits to equations (1) and (2), yielding $a = 2.5$ and $\tau_{qp} = 1.5$ ps. It was found, however, that the functional form of (2) was not valid at the lowest temperatures, whence a component of excess loss, empirically found inversely proportional to temperature, $Q_x = \xi/T$ was adopted, resulting in $\xi = 10\,300$ K. For the equilibrium regime of interest $T \gtrsim 0.8T_c$ the model (2) is sufficient.

3.2. Thermal conductance measurements

In the measurements presented below a similar bolometer device was tested, with slightly higher T_c and larger shunt capacitance $C = 105.2$ pF. The thermal conductance G was determined by applying DC power P to the resistive grid absorber. The resonant frequency $f_0 = \omega_0/2\pi$ was measured from $S_{21}(f)$, firstly as function of bath temperature (figure 3(b)) and secondly as function of DC power dissipated in the absorber on the membrane (figure 3(a)). The linear fits result in $df_0/dT = -224$ MHz K^{-1} and $df_0/dP = -1.23 \times 10^{16}$ Hz W^{-1} , yielding a thermal conductance $G = (df_0/dT)/(df_0/dP) = 18.2$ nW K^{-1} at 5.8 K. The thermal conductance contribution of NbN superconducting connections of the meander and the absorber is negligibly small.

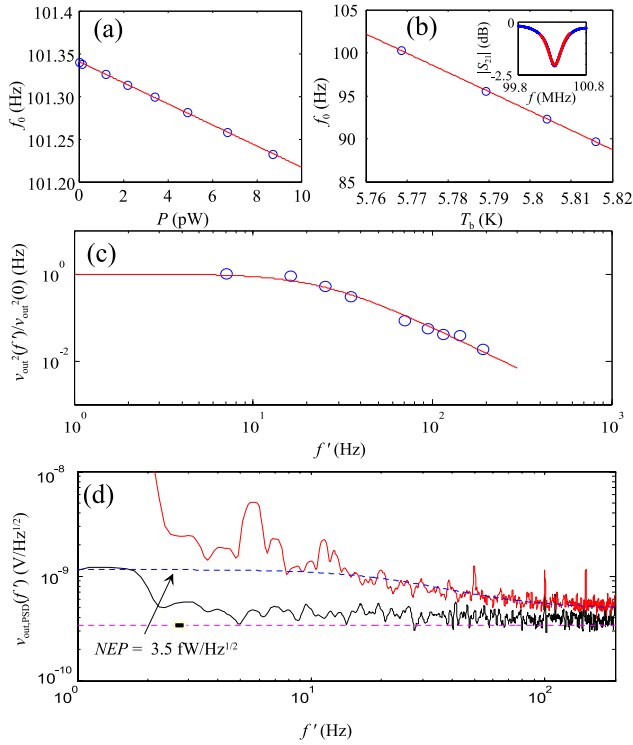


Figure 3. (a) Resonance frequency f_0 versus applied DC power to the absorber. (b) Resonance frequency f_0 versus bath temperature T_b . (c) Thermal cut-off measurements. Line shows a Lorentzian fit with $\tau_{th} = 6.4$ ms. (d) Noise spectra of bolometer IF signal referred to the input of the first preamplifier. Red solid line: Q-quadrature maximizing the responsivity. Black solid line: I-quadrature minimizing the responsivity. Dashed lines: fits to amplifier noise (red) and the sum of amplifier noise, bolometer noise and generator phase noise (blue).

3.3. Thermal time constant measurements

To determine the thermal cut off τ_{th} , the absorber was electrically excited at low frequencies f_{ext} , thus producing membrane temperature oscillations for the superconducting inductor at frequencies $f' = 2f_{ext}$. The resonator was driven at the frequency operating point $\omega = 1/\sqrt{L(C + C_c)}$ determined as the minimum of $S_{21}(\omega)$. The mixed-down IF signal $v_{out}^2(f')$ of the thermally excited resonator was recorded with a spectrum analyzer as a function of f' . The result is plotted in figure 3(c) along with a Lorentzian fit $v_{out}^2 \propto [1 + (2\pi f' \tau_{th})^2]^{-1}$, yielding thermal time constant $\tau_{th} = 6.4$ ms with a 3 dB cut off at 25 Hz.

The thermal isolation of the membrane is formed by 2.1 sheet squares of a bilayer film consisting of 200 nm thick amorphous SiN_x and SiO_2 , yielding a bilayer effective thermal conductivity $\kappa \approx 0.10$ W m⁻¹ K⁻¹, very close to literature values for both materials at our experimental temperature [14]. The membrane heat capacity yields $C_{th} = G\tau_{th} \approx 120$ pJ K⁻¹. The membrane mass, estimated from its dimensions (560×560 μm^2), the bilayer component thicknesses and material densities (2600 kg m⁻³ for SiO_2 and 3200 kg m⁻³ for Si_3N_4), is about 0.36×10^{-9} kg. This yields an effective specific heat capacity of the bilayer $c_p = 0.33$ J kg⁻¹ K⁻¹. Reference [14] gives $c_p/T^3 \approx$

10^{-3} J kg⁻¹ K⁻⁴ in the temperature range of interest for both materials, yielding $c_p \approx 0.20$ J kg⁻¹ K⁻¹ at 5.8 K, again in line with the experimental data.

3.4. Electrical NEP measurements

Measured output noise spectra referred to the amplifier input are shown in figure 3(d). The microwave frequency operating point is chosen at the point of minimum transmission and the spectra with maximal and minimal spectral densities obtained by rotating the reference phase are plotted. In accordance with the theory, the phase component (red line) maximizing the voltage spectral density is assumed to be the Q-component, while the 90° offset minimum (black line) is assumed to be the I-component. In addition to noise, thermal interference spikes at multiples of 1.4 Hz emerge from bath temperature oscillations due to pulse tube circulation. The noise levels are as expected, since the frequency operating point at the transmission minimum has a vanishing I-responsivity while the Q-responsivity \mathcal{R}_Q is maximized. Q-quadrature noise is also somewhat elevated above the thermal cut off, which is likely due to a phase jitter of the local oscillator with respect to the carrier signal. In figure 3(d) the fitted blue curve $(v_{out,PSD}^2 + v_0^2)^{1/2}$ to the Q-component voltage noise spectral density, $v_{out,PSD} \propto (1 + (\omega'\tau_{th})^2)^{-1/2}$, is obtained with $\tau_{th} = 6.4$ ms and a low-frequency limit of voltage noise spectral density of 1.2 nV Hz^{-1/2}. An additional constant term v_0 accounts for both amplifier noise and phase jitter noise of 0.35 nV Hz^{-1/2}.

To determine \mathcal{R}_Q the device parameters were fitted from the transmission curve as $L = 23.5$ nH and $Q_i = 420$, with nominal capacitances $C = 105.2$ pF and $C_c = 2.1$ pF (inset of figure 3(b)). $\partial \text{Im}(v_{out})/\partial f$ was calculated from equation (14) with $P_{rf} = 7.9$ pW. \mathcal{R}_Q results by multiplying this with df/dP obtained from the data of figure 3(a) as 3.45×10^5 V W⁻¹. This yields $NEP \approx (3.5 \pm 2.0)$ fW Hz^{-1/2}. The dominant uncertainty stems from the calibration of P_{rf} and the amplification chain (including preamplifier gain, mixer insertion loss and cable attenuation).

The measured NEP is in line with the theoretical phonon limited $NEP_{ph} = 5.8$ fW Hz^{-1/2} value determined from $NEP_{ph} = \sqrt{4k_B T^2 G}$ with the measured $G = 18.2$ nW K⁻¹ at 5.8 K. Thus we can conclude that the bolometer and the readout system are phonon-noise limited. Estimated generation–recombination noise $NEP_{gr}(\tau_{qp} < 1$ ns) $< 10^{-18}$ W Hz^{-1/2} and Johnson noise $NEP_{Johnson} \sim 10^{-17}$ W Hz^{-1/2} are negligibly small. It can also be noted that the readout criterion set by the experimental NEP corresponds to about $T_n \approx 4000$ K, whence the bolometer can be easily read out by a room-temperature low-noise microwave amplifier.

3.5. NETD and THz response measurements

For radiometric and THz response measurements we used an HDPE vacuum window and infrared blocking filters together with Zitex [15] filters installed at 50 and 4 K stages of

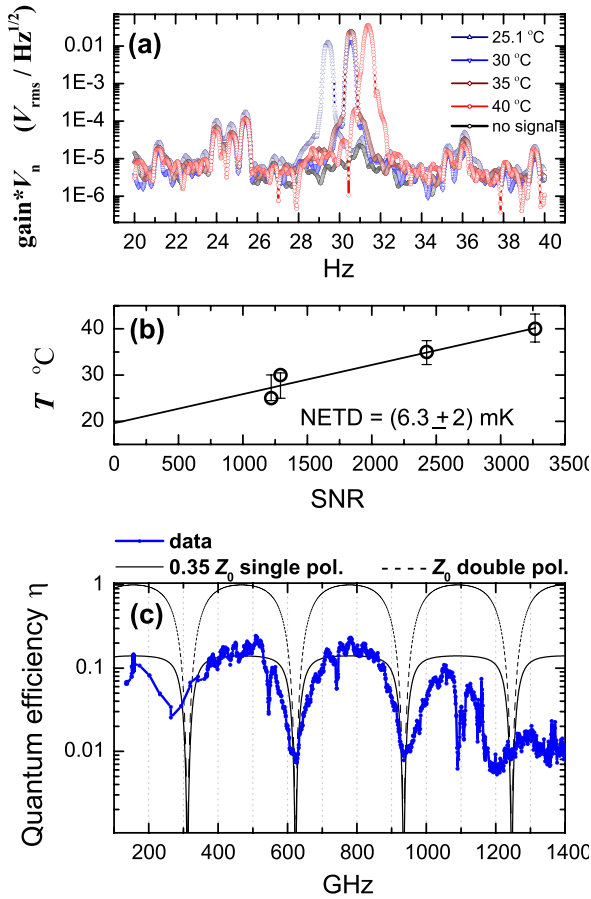


Figure 4. (a) Optical chopper signal at about 30 Hz at elevated black-body calibrator temperatures. A noise floor of $0.5 \times 10^{-5} \text{ V}_{\text{rms}} \text{ Hz}^{-1/2}$ is used to determine the SNR at 1 Hz. (b) Found from (a) SNR's at 1 Hz versus black-body calibrator temperatures. The linear fit yields $\text{NETD} = (6.3 \pm 2) \text{ mK}$. (c) The measured THz spectral response, data is normalized so that $\bar{\eta} = 0.111$ over 312–623 GHz. Solid line shows the result of a free-space impedance matching model assuming a single polarization absorber with $Z_{\text{abs}} = 0.35 \Omega \times 377 \Omega$, and the dashed line shows the result for dual polarization with $Z_{\text{abs}} = 377 \Omega$.

the cryocooler. A bolometer with a single polarization of the resistive meander absorber on the membrane was tested. The effective optical absorber impedance $Z_{\text{abs}} = 130 \Omega \approx 0.35 \Omega \times 377 \Omega$ is estimated from the geometrical filling factor of 0.04. NETD measurements (figure 4(b)) were performed by detecting an optomechanically chopped signal (at about 30 Hz) emitted from an aqueous broadband blackbody calibrator [16] placed right in front of the cryostat window. The reference blackbody of the chopper was Eccosorb AN-72 microwave absorbing material [17] attached to the chopper copper blades, whose radiometric temperature of 20°C is estimated from data in figure 4(b) at $\text{SNR} = 0$. A linear fit to the measured data (figure 4(b)) yields $\text{NETD} = (6.3 \pm 2) \text{ mK}$ at 1 Hz, with standard deviation error of 2 mK from linear regression.

The THz spectral response $\eta(\nu)$ was determined by illuminating the bolometer with circular-polarized THz waves using a photomixer which was tuned from 200 to 1400 GHz, and the amplitude was modulated at 30 Hz, whilst recording

the bolometer IF signal at the modulation frequency. The data was further normalized to that of a Golay cell (figure 4(c)) in order to calibrate for the frequency-dependent output power of the photomixer. Atmospheric water vapor absorption dips are clearly pronounced in the data at 542, 742 and 1090 GHz. A $\Delta\nu \approx 310 \text{ GHz}$ periodic detector response can be attributed to a $3\lambda/4 = 480 \mu\text{m}$ resonant optical cavity, in qualitative agreement with a simple model of free-space impedance matching of the absorber shunted with a cavity of a $3\lambda/4$ length. Deduced from the equation $\text{NEP} = 2\bar{\eta}k_{\text{B}}\text{NETD}\Delta\nu$ the average quantum efficiency yields $\bar{\eta} \approx 0.11$ for $\text{NEP} = 5.8 \text{ fW Hz}^{-1/2}$. This is in agreement with the average over 312–623 GHz band $\bar{\eta} = 0.111$ from the impedance matching model. The $\eta(\nu)$ data presented in figure 4(c) is normalized so that its average over 312–623 GHz is 0.111. Thus, for a dual polarization absorber with $Z_{\text{abs}} \approx 377 \Omega$, a quantum efficiency close to 1 is expected. The cavity length found of $480 \mu\text{m}$ as compared to its nominal value $450 \mu\text{m}$ (wafer thickness) indicates about 6% inaccuracy in THz beam-to-bolometer alignment.

4. Summary

We note that NEP (NETD) can be further improved by reducing G —by narrowing the suspensions and reducing the membrane thickness, as free-standing membranes down to $\lesssim 10 \text{ nm}$ thickness have been demonstrated [18, 19]. Also, a factor of about five improvement in NETD can be achieved simply by improving the optical matching of the absorber. Substantial improvement can be achieved by operating at lower temperatures (yet still above 1 K, with lower T_{c} superconductors) as NEP_{ph} improves as $\propto T^{2-2.5}$ depending on phonon heat transport mechanisms in low-dimensional bridges at low temperatures ($G \propto T^2$ for 2D or $G \propto T^3$ for 3D) [20]. The imaging speed is maintained or increased as C_{th} is approximately proportional to T^3 at low temperatures. Therefore, it appears possible to develop radiation detectors approaching the needs, for example, of astronomical imaging targeting cold objects of the Universe [21, 22], avoiding the usage of deep-cryogenic coolers.

In summary, we have demonstrated superconducting microwave kinetic inductance bolometers suitable for video-rate passive submillimeter imaging, for example, in security screening applications. The detectors are naturally adapted for frequency division multiplexing, making them attractive candidates for large focal plane imaging arrays. At the same time cryogenic requirements are modest, with an approximately 6 K operating temperature, and alleviated readout criteria enabling room-temperature electronics.

Acknowledgments

This work is financially supported by the Academy of Finland Grant No. 140484 (Cryogenic Microsensors), and Finnish Academy Program for Center of Excellence in Low Temperature Quantum Phenomena and Devices.

Appendix A. The responsivity

The time-dependent bolometer temperature $T(t)$ follows a differential equation including thermal feedback:

$$\partial_t T(t) = C_{\text{th}}^{-1} [P_{\text{rad}}(t) + P_m(T) - G(T(t) - T_b)], \quad (4)$$

where C_{th} is the heat capacity, P_{rad} is the absorbed radiation power, P_m is the share of carrier power absorbed on the membrane, G is the thermal conductivity, and T_b is the cryostat base temperature. For a steady-state temperature T_s with $P_{\text{rad}}(t) \ll P_m(T_s)$, and hence $\partial_t T = 0$, we get

$$T_s = P_m(T_s)/G + T_b. \quad (5)$$

Thus we can rewrite

$$\partial_t T(t) = C_{\text{th}}^{-1} [P_{\text{rad}}(t) + (\partial_T P_m - G)(T(t) - T_s)], \quad (6)$$

where we have additionally linearized P_m around T_s by setting $P_m(T(t)) - P_m(T_s) \approx \partial_T P_m(T(t) - T_s)$. This is readily converted into the frequency plane as

$$\Delta T(\omega') = \frac{1}{1 - \beta} \frac{\widehat{P}_{\text{rad}}(\omega')}{G} \left(\frac{1}{1 + i\omega'(1 - \beta)^{-1} \tau_{\text{th}}} \right), \quad (7)$$

where ΔT is the variation of temperature around the steady-state value T_s , as driven by the radiation signal \widehat{P}_{rad} , $\tau_{\text{th}} = C_{\text{th}}/G$ is the thermal cut off of the membrane and $\beta = G^{-1} \partial_T P_m$ describes thermal feedback in dissipative quadrature. The absorbed rf-carrier power is expressed as

$$\begin{aligned} P_m &= (1 - |S_{11}|^2 - |S_{21}|^2) P_{\text{rf}} \\ &= \frac{2Q^2 P_{\text{rf}}}{Q_i Q_e (1 + 4\delta^2)} \equiv \frac{P_{m0}}{1 + 4\delta^2}, \end{aligned} \quad (8)$$

in which P_{rf} is the total carrier power, Z_0 is the transmission line impedance, Q , Q_i and Q_e are correspondingly the total, intrinsic, and coupling quality factors, and δ is an offset frequency from S_{21} minimum (expressed in linewidths):

$$S_{21}(\delta) = (Q/Q_i + 2i\delta)/(1 + 2i\delta), \quad (9)$$

$$\delta = Q(\omega_{\text{rf}} - \omega_0)/\omega_0 + \frac{\alpha}{1 + 4\delta^2}, \quad (10)$$

$$\alpha = \frac{Q P_{m0}}{2G} \frac{1}{L} \frac{\partial L}{\partial T}. \quad (11)$$

It is to be noted that δ defines a frequency coordinate system that retains the linear properties of the resonator in the steady-state temperature T_s , whence it is also function of the total carrier power P_{rf} . The physical signal carrier frequency is ω_{rf} , and the resonant frequency ω_0 is evaluated at the bath temperature T_b . Thermal feedback is manifested as nonlinearity generated by α , where $\alpha < 0.8$ is the prerequisite for avoiding the onset of bifurcation due to the thermal feedback [23]. Parameter β depends on α as

$$\beta = \frac{-8\alpha\delta}{(1 + 4\delta^2)^2 + 8\alpha\delta} \quad (12)$$

$$\Rightarrow \frac{-\alpha}{\frac{4\sqrt{3}}{9} + \alpha} \leq \beta \leq \frac{\alpha}{\frac{4\sqrt{3}}{9} - \alpha}. \quad (13)$$

The inequality defines the limits of β . We assume that the preamplifier is matched to Z_0 . We also assume that

the intrinsic resonator dissipation is located ‘on-membrane’, which is likely the case of superconductor losses dominating the dissipation.

Bolometer output voltage measured across the input of the preamplifier is

$$v_{\text{out}}(\omega_{\text{rf}}, T) = S_{21} \sqrt{P_{\text{rf}} Z_0}. \quad (14)$$

The responsivities can now be calculated from equation (14) with the aid of equation (9). For example, if we choose to observe Q-quadrature (frequency quadrature) of v_{out} , $R_Q = d \text{Im}(v_{\text{out}})/dP_{\text{rad}} = (d \text{Im}(v_{\text{out}})/dT)(dT/dP_{\text{rad}})$. In the main text we have evaluated the responsivities by iteratively searching for the steady-state membrane temperatures. Typically the detectors are operated with negligible or near-negligible thermal feedback. It can be shown that the Q-quadrature responsivity at the S_{21} minimum ($\delta = 0$ in equation (10)) can in this case be expressed as

$$R_Q = \sqrt{\frac{\alpha}{G} \frac{1}{L} \frac{\partial L}{\partial T}} Q_i Z_0 \sqrt{\frac{Q_i}{Q_i + Q_e}}. \quad (15)$$

Looking at equation (10), this corresponds to selecting the carrier frequency from equation

$$\omega_{\text{rf}} = \omega_0(1 - \alpha/Q). \quad (16)$$

The extrinsic Q_e is typically set comparable to Q_i by choosing an appropriate value for the coupling capacitor C_c . Using equations (1) and (2) and setting $Q_i = Q_e$ we can rewrite equation (15) as

$$R_Q = \sqrt{\alpha \frac{aZ_0}{2\omega_0 \tau_{\text{qp}} G T}} \quad (17)$$

showing the dependency of responsivity on material and design parameters in a compact way.

Appendix B. NEP from generation–recombination processes

Generation–recombination noise can be expressed as the number fluctuation of quasiparticles as

$$S_{N_{\text{qp}}}(\omega') = \frac{4N_{\text{qp}} \tau_{\text{qp}}}{1 + (\omega' \tau_{\text{qp}})^2}. \quad (18)$$

We assume the limit where the responsivity is still limited by the thermal conductivity of the membrane, i.e. N_{qp} is represented by the equilibrium value of the membrane temperature, whence

$$\begin{aligned} N_{\text{qp}} &= N(N_{\text{qp}}/N) = N(T/T_c)^a \\ &= N \left[\left(\frac{\eta P_{\text{rad}}}{G} + T_b \right) / T_c \right]^a. \end{aligned} \quad (19)$$

The change in the number of quasiparticles around $P_{\text{rad}} = 0$ can be then expressed as

$$\frac{\partial N_{\text{qp}}}{\partial P_{\text{rad}}} = \frac{\eta a N}{G T_b} \left(\frac{T_b}{T_c} \right)^a. \quad (20)$$

In the limit $\omega \ll 1/\tau_{qp}$ this leads to noise equivalent power as limited by generation–recombination noise

$$\text{NEP}_{\text{gr}} = \eta S_{N_{qp}}^{1/2} \left(\frac{\partial P_{\text{rad}}}{\partial N_{qp}} \right) = \frac{GT_b}{a} \sqrt{\frac{\tau_{qp}}{Vn \left(\frac{T_b}{T_c} \right)^a}}, \quad (21)$$

where we have marked $N = nV$, with V denoting the volume of the inductive strip.

References

- [1] Luukanen A, Appleby R, Kemp M and Salmon N 2013 Millimeter-wave and terahertz imaging in security applications *Terahertz Spectroscopy and Imaging (Springer Series in Optical Sciences vol 171)* (Berlin: Springer) pp 491–520
- [2] Dietlein C R, Luukanen A, Meyer F, Popovic Z and Grossman E N 2006 Phenomenology of passive broadband terahertz images *4th ESA Workshop on Millimetre-Wave Technology and Applications* pp 405–9
- [3] Grossman E et al 2010 Passive terahertz camera for standoff security screening *Appl. Opt.* **49** E106–20
- [4] Heinz E et al 2011 Toward high-sensitivity and high-resolution submillimeter-wave video imaging *Opt. Eng.* **50** 113204
- [5] Luukanen A et al 2012 Measured performance of a high-resolution passive video-rate submillimeter-wave imaging system demonstrator for stand-off imaging *Proc. SPIE* **8362** 836209
- [6] Irwin K D et al 2012 Advanced code-division multiplexers for superconducting detector arrays *J. Low Temp. Phys.* **167** 588–94
- [7] McDonald D G 1987 *Appl. Phys. Lett.* **50** 775
Sauvageau J E and McDonald D G 1989 *IEEE Trans. Magn.* **25** 1331
Grossman E N, McDonald D G and Sauvageau J E 1991 Far-infrared kinetic-inductance detectors *IEEE Trans. Magn.* **27** 2677–80
Sauvageau J E, McDonald D G and Grossman E N 1991 Superconducting kinetic inductance radiometer *IEEE Trans. Magn.* **27** 2757–60
- [8] Zmuidzinas J 2012 *Annu. Rev. Condens. Matter Phys.* **3** 169–214
- [9] Day P L, LeDuc H G, Mazin B A, Vayonakis A and Zmuidzinas J 2003 A broadband superconducting detector suitable to use in large arrays *Nature* **425** 817–21
- [10] Doyle S, Mauskopf P, Naylon J, Porch A and Duncombe C 2008 Lumped element kinetic inductance detectors *J. Low Temp. Phys.* **151** 530–6
- [11] Baselmans J 2012 Kinetic inductance detectors *J. Low Temp. Phys.* **167** 292–304
- [12] Tinkham M 1965 *Superconductivity* (New York: Gordon and Breach)
- [13] Mather J C 1982 Bolometer noise: non-equilibrium theory *Appl. Opt.* **21** 1125–9
- [14] Zink B I and Hellman F 2004 Specific heat and thermal conductivity of low-stress amorphous SiN membranes *Solid State Commun.* **129** 199–204
- [15] Benford D J, Gaidis M C and Kooi J W 2003 Optical properties of Zitec in the infrared to submillimeter *Appl. Opt.* **42** 5118–22
- [16] Dietlein C R, Popovic Z and Grossman E N 2008 Aqueous blackbody calibration source for millimeter-wave/terahertz metrology *Appl. Opt.* **47** 5604–15
- [17] *Emerson and Cuming Microwave Products* www.eccosorb.com
- [18] Wang L et al 2012 Ultrathin oxide films by atomic layer deposition on graphene *Nano Lett.* **12** 3706–10
- [19] Shchepetov A et al 2013 *Appl. Phys. Lett.* **102** 192108
- [20] Kühn T and Maasilta I J 2007 Maximizing phonon thermal conductance for ballistic membranes *J. Phys.: Conf. Ser.* **92** 012082
- [21] Baselmans J et al 2008 Noise and sensitivity of aluminum kinetic inductance detectors for sub-mm astronomy *J. Low Temp. Phys.* **151** 524–9
- [22] Jackson B D et al 2012 The SPICA-SAFARI detector system: TES detector arrays with frequency-division multiplexed SQUID readout *IEEE Trans. Terahz. Sci. Technol.* **2** 12–21
- [23] Swenson L J 2013 Operation of a titanium nitride superconducting microresonator detector in the nonlinear regime *J. Appl. Phys.* **113** 104501

PUBLICATION IV

Kinetic Inductance Magnetometer

Nat. Commun. 5, 4872.

Copyright 2014 Nature Publishing Group.
Reprinted with permission from the publisher.

PUBLICATION V

**Mitigating information leakage
in a crowded spectrum of
weakly anharmonic qubits**

Submitted for publication:
Physical Review X.

Mitigating information leakage in a crowded spectrum of weakly anharmonic qubits

V. Vesterinen,^{1,2} O.-P. Saira,² A. Bruno,² and L. DiCarlo²

¹*VTT Technical Research Centre of Finland, P.O. Box 1000, 02044 VTT, Finland*

²*Kavli Institute of Nanoscience, Delft University of Technology,
P.O. Box 5046, 2600 GA Delft, The Netherlands*

(Dated: May 13, 2014)

A challenge for scaling up quantum processors using frequency-crowded, weakly anharmonic qubits is to drive individual qubits without causing leakage into non-computational levels of the others, while also minimizing the number of control lines. To address this, we implement single-qubit Wah-Wah control in a circuit QED processor with a single feedline for all transmon qubits, operating at the maximum gate speed achievable given the frequency crowding. Randomized benchmarking and quantum process tomography confirm alternating qubit control with $\leq 1\%$ average error per computational step and decoherence-limited idling of one qubit while driving another with a Wah-Wah pulse train.

Experimental quantum computing [1] seldom employs true qubits. Most architectures use effective qubits defined by a pair of energy levels within a multi-level quantum object (typically the ground and first excited states, labelled $|0\rangle$ and $|1\rangle$). Examples include non-spin-1/2 electron and nuclear spins [2], electronic levels in atoms and ions [3], photons with combined polarization, frequency and positional degrees of freedom [4], and most superconducting quantum circuits [5]. The transmon [6], phase [7] and capacitively-shunted flux [8] qubits are weakly anharmonic oscillators with logical transition frequency ω_{01} and nearest leakage transition frequency ω_{12} detuned by $|\Delta| = |\omega_{12} - \omega_{01}| \sim 0.1 \times \omega_{01}$. In these superconducting systems, temporarily occupying levels outside the computational subspace offers the key to fast and efficient multi-qubit operations such as conditional-phase [9, 10] and Toffoli gates [11, 12], and high-fidelity single-shot readout [13].

The benefits of using multi-level structures for quantum computing are balanced by more challenging single-qubit control. When driving an individual effective qubit with a resonant pulse at ω_{01} , the anharmonicity $|\Delta|$ imposes a practical limit on the maximum speed of gate operations, marking the transition from decoherence-to leakage-dominated errors. While theoretical optimal control has broken the speed limit using non-analytic pulses [14], analytic pulses with few tuning parameters are preferred by experimentalists for ease of implementation and tuning. Keeping leakage-induced errors below the 1% fault-tolerance threshold of modern error-correcting schemes [15] imposes the necessary but insufficient condition $t_g \gtrsim 2\pi/|\Delta|$ on the single-qubit gate time t_g . Interestingly, the standard Gaussian envelope is insufficient despite satisfying the minimal time-frequency uncertainty product. Proposed [14, 16, 17] DRAG (Derivative Removal by Adiabatic Gate) pulses combining Gaussian and derivative-of-Gaussian envelopes on the in- and out-of-phase quadratures have been widely adopted following validation with phase [18] and transmon [19] qubits in one- and two-qubit devices. To date, the com-

ination of DRAG and improved coherence has achieved average single-qubit gate errors of 0.08% in transmon qubits [20].

Moving forward, it is imperative to preserve high-quality single-qubit control as more effective qubits are crowded in a fixed frequency range. In architectures such as 2D [21] and 3D [22] circuit QED which exploit a common feedline or coupled resonator to drive multiple qubits, control drives couple almost equally to addressed and unaddressed qubits. In this regime of near-unity cross-talk, the absolute detuning $|\delta|$ between the logical transition of one qubit and the leakage transition of its frequency neighbor sets an even lower speed limit when $|\delta| < |\Delta|$. In order to ease coherence time requirements, it is therefore important to design analytic pulses with $t_g \sim 2\pi/|\delta|$ which avoid leakage in both the addressed qubit and its neighbor (henceforth termed internal and external leakage). To this end, Schutjens *et al.* [23] have recently developed Wah-Wah control (Weak AnHarmonicicity With Average Hamiltonian), combining DRAG with sideband modulation in a four-parameter pulse.

In this article, we present the experimental validation of leakage-avoiding Wah-Wah control at the speed limit of a multi-transmon 2D circuit QED processor. We create a bias condition with $\delta/2\pi = 57$ MHz and demonstrate avoidance of both external and internal leakage at gate times $16 \text{ ns} \leq t_g \leq 24 \text{ ns}$. Stroboscopic population measurements show that DRAG-only pulsing induces significant net population in the third level of the unaddressed transmon, while Wah-Wah ensures all population returns to the computational subspace by the end of the pulse. Using a variant of standard randomized benchmarking [24], we show alternating individual control of both qubits with 0.8 – 1.0% average error per computational step. Finally, we use quantum process tomography to demonstrate decoherence-limited idling of the unaddressed qubit as the other undergoes a Wah-Wah pulse train. Optimization of the four-parameter, analytic Wah-Wah pulse shape is straightforward and accelerated

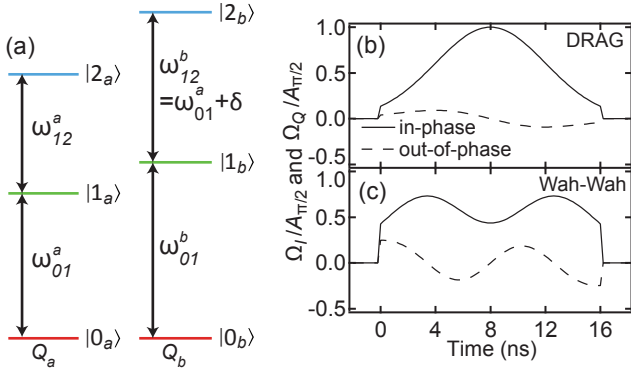


FIG. 1. (color online). (a) Energy level diagram for transmons Q_a and Q_b (not to scale). The ground $|0_k\rangle$ and first-excited $|1_k\rangle$ states of Q_k define a qubit subspace. The Q_a qubit transition frequency and the Q_b leakage transition frequency differ by $\delta = \omega_{12}^b - \omega_{01}^a = 2\pi \times 57$ MHz. (b-c) Comparison of in- and out-of-phase quadrature envelopes Ω_I and Ω_Q , respectively, for optimized DRAG and Wah-Wah $\pi/2$ pulses on Q_a (gate time $t_g = 16$ ns). For DRAG (b), Ω_I and Ω_Q are Gaussian and derivative-of-Gaussian, respectively [Eqs. (1)-(2) with $\sigma = 4$ ns, $A_m = 0$, $\beta = 0.6$ ns]. For Wah-Wah (c), $A_m = 0.9$, $\omega_m/2\pi = 25$ MHz, $\beta = 1.85$ ns.

by a simple model of the system Hamiltonian using independently measured parameters. Our results establish Wah-Wah control as an important tool for scalability, allowing control of frequency-crowded effective qubits at threshold without dedicated control lines.

We focus on two transmons (Q_a and Q_b) within a four-transmon, five-resonator 2D cQED processor of similar design to that of Ref. 25. Resonant control and readout pulses for all qubits are applied via one feedline coupling to readout resonators connecting to one qubit each. Using local flux control, we bias Q_a and Q_b to logical transitions $(\omega_{01}^a, \omega_{01}^b)/2\pi = (6.347, 6.750)$ GHz, and corresponding leakage transitions $(\omega_{12}^a, \omega_{12}^b)/2\pi = (5.980, 6.404)$ GHz, making $\delta = \omega_{12}^b - \omega_{01}^a = 2\pi \times 57$ MHz [Fig. 1(a)]. Thus, we expect [23] DRAG pulses [Fig. 1(b)] targeting Q_a to induce significant leakage from $|1_b\rangle$ to $|2_b\rangle$ for $t_g \lesssim 2\pi/\delta \sim 20$ ns. Indeed, we note that just four back-to-back Q_a DRAG π pulses already leak $\sim 50\%$ of the initial population in $|1_b\rangle$ to $|2_b\rangle$ for $t_g = 16$ ns (Fig. 2). Note that to within the few-percent accuracy limited by state preparation and measurement errors (SPAM), DRAG pulses do successfully avoid internal leakage in Q_a , as expected [14].

Using similar measurements, we now attempt to also avoid external leakage using the additional sideband modulation characteristic of Wah-Wah pulse envelopes [Fig. 1(c)] [23]:

$$\Omega_I(t) = A_\theta e^{-(t - \frac{t_g}{2})^2 / (2\sigma^2)} \left[1 - A_m \cos \left(\omega_m \left(t - \frac{t_g}{2} \right) \right) \right] \quad (1)$$

$$\Omega_Q(t) = \beta \dot{\Omega}_I(t). \quad (2)$$

Here, Ω_I and Ω_Q are the pulse envelopes in the in- and out-of-phase quadratures, and amplitude A_θ determines the rotation angle θ . The theory predicts that sideband modulation of the conventional Gaussian envelope in Ω_I can mitigate external leakage for suitably chosen modulation amplitude A_m and frequency ω_m . Just as in DRAG, keeping Ω_Q proportional to the time derivative of Ω_I should prevent internal leakage in Q_a upon optimizing the scaling parameter β . Figure 2 provides the experimental confirmation of external and internal leakage mitigation to within the accuracy allowed by SPAM. Q_a Wah-Wah π pulses with manually-optimized A_m , ω_m , A_π , and β populate $|2_b\rangle$ only temporarily, returning all population to $|1_b\rangle$ by the end of each pulse. (Details of the Wah-Wah pulse tune-up procedure are provided in the Supplement [26]). A numerical simulation of the system dynamics, which truncates the Hamiltonian at three levels per transmon, shows good correspondence with the manually optimized pulse parameters. To test its utility, we used the simulation to obtain first estimates of pulse parameters at two other Q_b bias points with even tighter separation of their logical frequencies ($\delta/2\pi = -60$ MHz and -80 MHz). We also obtained similar internal and external leakage mitigation for $t_g = 16$ ns (data not shown).

While Wah-Wah pulsing on Q_a successfully mitigates net leakage in Q_b , the temporary excursion of quantum amplitude from $|1_b\rangle$ to $|2_b\rangle$ induces a relative phase between levels $|0_b\rangle$ and $|1_b\rangle$, i.e., a z rotation in the Q_b qubit subspace. This induced phase is a deterministic function of the Q_a pulse parameters defined above. Thus, we can compensate it already in pulse synthesis by adjusting the phase of all subsequent Q_b pulses, in the style of virtual z gates [27]. To calibrate the phase shift, we embed several consecutive Wah-Wah Q_a pulses (either all π or $\pi/2$) into the second wait period in a standard echo sequence on Q_b ($\pi/2$, wait, π , wait, $\pi/2$). The final $\pi/2$ rotation translates the acquired phase into a population difference between $|0_b\rangle$ and $|1_b\rangle$. We observe that the induced Q_b phase is independent of rotation axis and linear in the number of Q_a pulses of a given type: 8.2° (38°) per $\pi/2$ (π) pulse. We perform a similar calibration of compensating z gates on Q_a for DRAG pulses applied to Q_b . Even though $(\omega_{12}^a - \omega_{01}^b)/2\pi = -770$ MHz and Q_b DRAG pulsing does not produce Q_a leakage (shown below), there is phase accrual in the Q_a qubit subspace: 2.5° (9.3°) per $\pi/2$ (π) pulse.

In order to test both leakage mitigation and phase compensation to higher accuracy than allowed by SPAM, we employ randomized benchmarking (RB). The single-qubit protocol first proposed and implemented by Knill *et al.* [24] (standard RB) provides a valuable baseline for gate errors on the addressed qubit, without concern for the unaddressed one. In standard RB [24, 28], one applies pseudo-random sequences of consecutive π and $\pi/2$ pulses to Q_k and measures the decay of fidelity to the

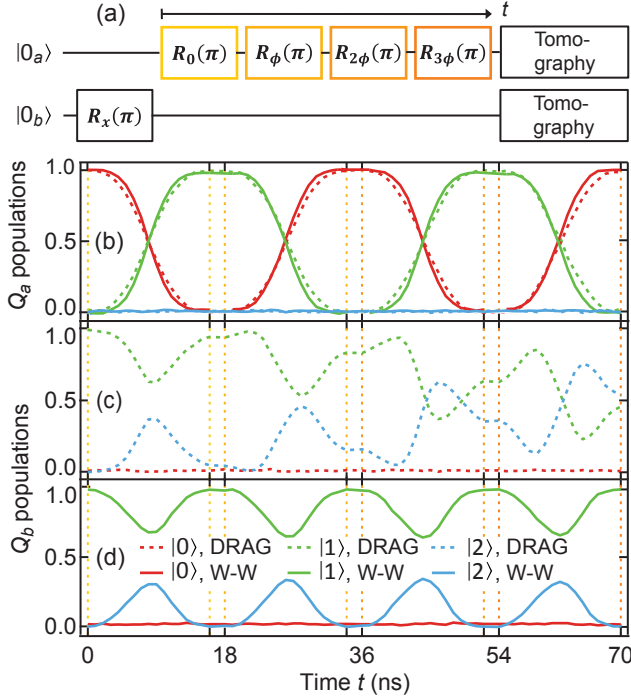


FIG. 2. (color online). Measured evolution of level populations in Q_a and Q_b during four consecutive Q_a π pulses with either DRAG and Wah-Wah envelopes ($t_g = 16$ ns). (a) Pulse sequence. Pulses are separated by a $t_b = 2$ ns buffer. Level populations at time t are obtained by truncating any ongoing Q_a pulse and commencing tomographic operations after a buffer time t_b . (b) Evolution of Q_a levels. Neither DRAG (dashed curves) nor Wah-Wah (solid curves) pulses drive the leakage transition in Q_a . (c-d) Evolution of Q_b levels during DRAG (c) and Wah-Wah (d) Q_a pulses. DRAG pulsing drives the Q_b leakage transition. The chosen relative phase $\phi = 237^\circ$ between subsequent π pulses exacerbates the net leakage. In contrast, Wah-Wah pulses populate $|2_b\rangle$ temporarily, returning the population to $|1_b\rangle$ by the end of each pulse.

ideal final state of that qubit (always $|0_k\rangle$ or $|1_k\rangle$) as the number of pulses is increased [Fig. 3(a)]. This decay allows extracting [26, 29] the average error per computational step (EPS), where computational step is defined as a pair of back-to-back π and $\pi/2$ pulses [24]. We extract EPS as a function of the step time $t_s = 2(t_g + t_b)$ by varying the buffer time t_b between pulses ($t_b \geq 2$ ns). To within statistical error, a linear fit of $\text{EPS}(t_s)$ for Q_a (Q_b) at short t_s extrapolates to the origin [Figs. 3(b)-(c)]. This observation suggests that the minimal 0.4% (0.4%) EPS is already decoherence limited.

With the EPS baselines from standard RB in place, we now employ alternating RB to investigate whether control of either qubit can remain decoherence limited when pulses are interleaved on the other. We apply an RB pulse on one qubit during the buffer ($t_b \geq t_g + 4$ ns) for the other, and perform virtual z -gate compensation

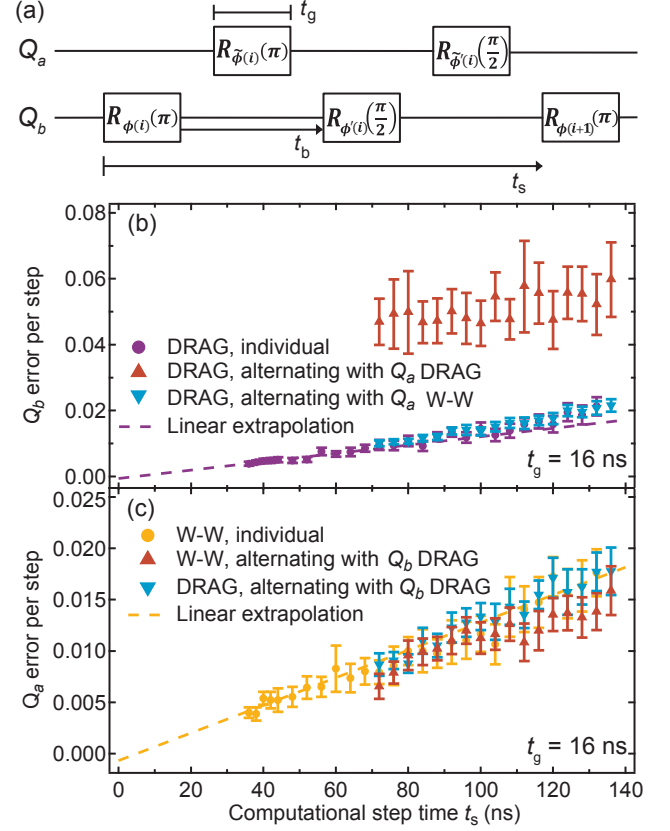


FIG. 3. (color online). Demonstration of decoherence-limited single-qubit control via individual and alternating randomized benchmarking. (a) Pseudo-random control pulses are applied to either one transmon or to both in alternating fashion. The average error per computational step (EPS) is extracted as a function of the computational step time $t_s = 2t_g + 2t_b$ (without and with a symmetrically timed RB pulse on the other transmon during buffer). (b) EPS for optimized Q_b DRAG pulses. The linear t_s dependence observed without Q_a pulses extrapolates to $(-6 \pm 9) \times 10^{-4}$ at $t_s = 0$, indicating decoherence-limited control. The fits are done to the first ten data points. The alternating EPS matches the individual EPS for Q_a Wah-Wah. In contrast, alternating with Q_a DRAG pulsing worsens the EPS to $\sim 5\%$. The large error bars reflect high sensitivity of $|2_b\rangle$ leakage to the particular sequence of Q_a rotations within the randomization. (c) EPS for optimized Q_a DRAG and Wah-Wah pulses. Overlapping results are obtained without and with alternating RB DRAG pulses on Q_b . The observed linear t_s dependence of EPS extrapolates to $(-7 \pm 9) \times 10^{-4}$ at $t_s = 0$, indicating that Q_a control is also decoherence limited.

for all pulses. Alternating RB performed with DRAG pulses on both Q_a and Q_b has no impact on Q_a , but increases the Q_b EPS to $\sim 5\%$ [Fig. 3(b)]. However, by using Wah-Wah pulses on Q_a , we recover the decoherence limited baselines simultaneously on both qubits. Similar results for $t_g = 20$ ns and 24 ns are presented in the Supplement [26].

As the final test of whether Wah-Wah pulsing on Q_a

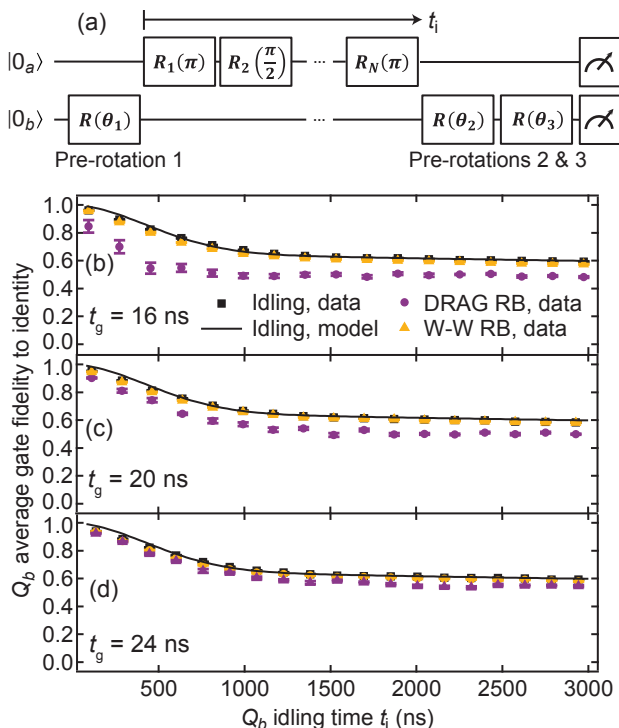


FIG. 4. (color online). Q_b average gate fidelity to the identity operation during various types of idling: no Q_a pulsing, Q_a DRAG RB, and Q_a Wah-Wah RB. (a) Pulse sequence. Initial and final rotations on Q_b are used for QPT of the evolution of Q_b qubit state to the three-level subspace. Results are shown for gate times (b) $t_g = 16$ ns, (c) 20 ns, and (d) 24 ns ($t_b = 2$ ns fixed). Model curves for true idling take into account the measured Q_b qubit relaxation and dephasing times [26]. The model assumes dephasing dominated by $1/f$ noise [30]. The Q_b average gate fidelity to identity during Q_a Wah-Wah RB (circles) is indistinguishable from that of true idling. In contrast, Q_a DRAG RB (triangles) deteriorates fidelity at shorter t_i .

affects Q_b , we perform quantum process tomography (QPT) of Q_b under various idling conditions: no pulses on Q_a (true idling), Q_a DRAG RB, and Q_a Wah-Wah RB (Fig. 4). The process map is a 9×4 transfer matrix [31] relating an initial reduced density matrix in the Q_b qubit subspace to a final reduced density matrix in the three-level [32] subspace. The Q_b average gate fidelity to identity for true idling decreases consistently with an analytic model [26] based on measured Q_b relaxation and dephasing rates. As expected, Q_b idling is compromised under Q_a DRAG RB, and worsens the shorter t_g . An analysis discerning contributions from population transfer and dephasing errors [26] confirms that the loss of idling fidelity is limited by induced leakage and not by imperfect z -gate compensation. Remarkably, the idling fidelity under Q_a Wah-Wah RB is nearly identical to the true idling fidelity for all t_g , further demonstrating the usefulness of the new control method.

In summary, we have shown experimentally, using level-population measurements, RB, and QPT, that Wah-Wah control [23] successfully mitigates crosstalk-induced leakage in a crowded spectrum of transmon qubits at gate times where the widely-adopted DRAG control fails. Wah-Wah control therefore represents a step towards scalability in multi-qubit architectures by allowing selective control of an increasing number of effective qubits without an equal addition of control lines. Wah-Wah builds sideband modulation to DRAG without sacrificing the analytic nature of the two-quadrature pulse shape, adding only two easily optimized parameters. Our demonstration in circuit QED takes place in the worst-case regime of unity crosstalk, with control pulses applied via one common feedline coupling equally to the addressed qubit and the unaddressed nearest-frequency neighbor. Looking forwards, as two-qubit gate and measurement times [33] decrease to that of single-qubit gates, the current restriction to non-overlapping control of frequency-neighboring qubits could ultimately bottleneck the clock cycle in surface-code quantum error correction [15]. A useful generalization of Wah-Wah, however, would allow simultaneous control of two qubits at small $|\delta|$.

We thank D. J. Egger, R. Schutjens and F. K. Wilhelm for many helpful discussions, N. K. Langford and D. Ristè for helpful comments on the manuscript, and D. J. Thoen and T. M. Klapwijk for NbTiN thin films. This work is funded by EU FP7 project SCALEQIT, the Netherlands Organization for Scientific Research (NWO, VIDI scheme), and a Marie Curie Career Integration Grant. V.V. was supported by the Research Foundation of Helsinki University of Technology.

-
- [1] T. D. Ladd, F. Jelezko, R. Laflamme, Y. Nakamura, C. Monroe, and J. L. O'Brien, *Nature*, **464**, 45 (2010).
 - [2] R. Hanson and D. D. Awschalom, *Nature*, **453**, 1043 (2008).
 - [3] C. Monroe and J. Kim, **339**, 1164 (2013).
 - [4] B. P. Lanyon, *et al.*, *Nature Phys.*, **5**, 134 (2009).
 - [5] M. H. Devoret and R. J. Schoelkopf, *Science*, **339**, 1169 (2013).
 - [6] J. Koch, *et al.*, *Phys. Rev. A*, **76**, 042319 (2007).
 - [7] J. M. Martinis, S. Nam, J. Aumentado, and C. Urbina, *Phys. Rev. Lett.*, **89**, 117901 (2002).
 - [8] M. Steffen, S. Kumar, D. P. DiVincenzo, J. R. Rozen, G. A. Keefe, M. B. Rothwell, and M. B. Ketchen, *Phys. Rev. Lett.*, **105**, 100502 (2010).
 - [9] F. W. Strauch, P. R. Johnson, A. J. Dragt, C. J. Lobb, J. R. Anderson, and F. C. Wellstood, *Phys. Rev. Lett.*, **91**, 167005 (2003).
 - [10] L. DiCarlo, *et al.*, *Nature*, **460**, 240 (2009).
 - [11] A. Fedorov, L. Steffen, M. Baur, M. P. da Silva, and A. Wallraff, *Nature*, **481**, 170 (2012).
 - [12] M. D. Reed, L. DiCarlo, S. E. Nigg, L. Sun, L. Frunzio, S. M. Girvin, and R. J. Schoelkopf, *Nature*, **482**, 382

- (2012).
- [13] F. Mallet, F. R. Ong, A. Palacios-Laloy, F. Nguyen, P. Bertet, D. Vion, and D. Esteve, *Nature Phys.*, **5**, 791 (2009).
- [14] F. Motzoi, J. M. Gambetta, P. Rebentrost, and F. K. Wilhelm, *Phys. Rev. Lett.*, **103**, 110501 (2009).
- [15] A. G. Fowler, M. Mariantoni, J. M. Martinis, and A. N. Cleland, *Phys. Rev. A*, **86**, 032324 (2012).
- [16] J. M. Gambetta, F. Motzoi, S. T. Merkel, and F. K. Wilhelm, *Phys. Rev. A*, **83**, 012308 (2011).
- [17] F. Motzoi and F. K. Wilhelm, *Phys. Rev. A*, **88**, 062318 (2013).
- [18] E. Lucero, *et al.*, *Phys. Rev. A*, **82**, 042339 (2010).
- [19] J. M. Chow, L. DiCarlo, J. M. Gambetta, F. Motzoi, L. Frunzio, S. M. Girvin, and R. J. Schoelkopf, *Phys. Rev. A*, **82**, 040305 (2010).
- [20] R. Barends, *et al.*, *Nature*, **508**, 500 (2014).
- [21] A. Wallraff, D. I. Schuster, A. Blais, L. Frunzio, R.-S. Huang, J. Majer, S. Kumar, S. M. Girvin, and R. J. Schoelkopf, *Nature*, **431**, 162 (2004).
- [22] H. Paik, *et al.*, *Phys. Rev. Lett.*, **107**, 240501 (2011).
- [23] R. Schutjens, F. Abu Dagga, D. J. Egger, and F. K. Wilhelm, *Phys. Rev. A*, **88**, 052330 (2013).
- [24] E. Knill, *et al.*, *Phys. Rev. A*, **77**, 012307 (2008).
- [25] O.-P. Saira, J. P. Groen, J. Cramer, M. Meretska, G. de Lange, and L. DiCarlo, *Phys. Rev. Lett.*, **112**, 070502 (2014).
- [26] See Supplementary Material.
- [27] M. Steffen, L. M. K. Vandersypen, and I. L. Chuang, *J. Magn. Reson.*, **146**, 369 (2000).
- [28] J. M. Chow, *et al.*, *Phys. Rev. Lett.*, **102**, 090502 (2009).
- [29] E. Magesan, J. M. Gambetta, and J. Emerson, *Phys. Rev. A*, **85**, 042311 (2012).
- [30] F. Yoshihara, K. Harrabi, A. O. Niskanen, Y. Nakamura, and J. S. Tsai, *Phys. Rev. Lett.*, **97**, 167001 (2006).
- [31] J. M. Chow, *et al.*, *Phys. Rev. Lett.*, **109**, 060501 (2012).
- [32] R. Bianchetti, S. Filipp, M. Baur, J. Fink, C. Lang, L. Steffen, M. Boissonneault, A. Blais, and A. Wallraff, *Phys. Rev. Lett.*, **105**, 223601 (2010).
- [33] D. Sank, *et al.*, arXiv:1401.0257 (2014).

Supplement to “Mitigating information leakage in a crowded spectrum of weakly anharmonic qubits”

V. Vesterinen,^{1,2} O.-P. Saira,² A. Bruno,² and L. DiCarlo²

¹ VTT Technical Research Centre of Finland, P.O. Box 1000, 02044 VTT, Finland

² Kavli Institute of Nanoscience, Delft University of Technology,
P.O. Box 5046, 2600 GA Delft, The Netherlands

(Dated: May 13, 2014)

EXPERIMENTAL DETAILS

Device

The chip is a four-transmon, five-resonator 2D cQED quantum processor of nearly identical design and fabrication as that presented in Ref. 1. An optical image of the device and detailed schematic of the setup are shown in Fig. S1. A high- Q resonator bus (5.16 GHz fundamental) couples to every transmon, while dedicated resonators, each dispersively coupled to one transmon, allow individual readouts via a common feedline. Transmon transition frequencies are individually controlled by dedicated flux-bias lines, each short-circuited near one transmon SQUID loop. Throughout this experiment, Q_a was biased at its flux-insensitive point, where $\omega_{01}^a/2\pi = 6.347$ GHz and $\Delta_a/2\pi = -357$ MHz. The Q_a readout resonator has a fundamental frequency of $\omega_r^a/2\pi = 7.7042$ GHz (for Q_a in $|0_a\rangle$), a coupling-limited linewidth of $\kappa_a/2\pi = 1.5$ MHz, and a dispersive coupling strength of $\chi_a/\pi = -1.3$ MHz. Three bias points were explored for Q_b (Table S1). The other two (inactive) transmons on the chip were biased at 4.31 GHz and 7.25 GHz throughout.

TABLE S1. Summary of Q_b -related device parameters at the three bias points explored.

Bias point	1	2	3
$\omega_{01}^b/2\pi$ (GHz)	6.750	6.636	6.616
$\Delta_b/2\pi$ (MHz)	-346	-349	-350
$\delta/2\pi$ (MHz)	57	-60	-81
$\omega_r^b/2\pi$ (GHz)	7.8181	7.8178	7.8177
$\kappa_b/2\pi$ (MHz)	1.8	N.A.	N.A.
χ_b/π (MHz)	-1.7	N.A.	N.A.

Additional device parameters at bias point 1

For bias point 1, where all shown data were taken, we calibrated several device parameters needed as input for simulation (discussed below). Measured relaxation and dephasing times of Q_a and Q_b are listed in Table S2. The Rabi frequencies of equal-amplitude drives resonant with the $|0\rangle \leftrightarrow |1\rangle$ and $|1\rangle \leftrightarrow |2\rangle$ transitions of each transmon are listed in Table S3, normalized to that of

TABLE S2. Measured qubit relaxation $T_{1(1\rightarrow 0)}$, Ramsey T_2^{Ramsey} , and echo T_2^{echo} times at bias point 1. The measured relaxation time $T_{1(2\rightarrow 1)}$ from second to first excited state in each transmon is also listed.

Transmon	Q_a	Q_b
$T_{1(1\rightarrow 0)}$ (μs)	7.65	5.65
$T_{1(2\rightarrow 1)}$ (μs)	4.18	3.66
T_2^{Ramsey} (μs)	2.13	0.64
T_2^{echo} (μs)	2.33	1.40

TABLE S3. Measured Rabi frequencies for equal-amplitude drives resonant with the $|0_k\rangle \leftrightarrow |1_k\rangle$ and $|1_k\rangle \leftrightarrow |2_k\rangle$ transitions, and estimated coupling strength of the ω_{01}^a drive to the four transitions. All values are normalized to that of the $|0_a\rangle \leftrightarrow |1_a\rangle$ transition.

Transmon Q_k	Q_a	Q_b
Rabi frequency at ω_{01}^k	1	0.90
Rabi frequency at ω_{12}^k	1.42	1.25
Coupling λ_1^k of ω_{01}^a drive to $ 0_k\rangle \leftrightarrow 1_k\rangle$	1	0.5
Coupling λ_2^k of ω_{01}^a drive to $ 1_k\rangle \leftrightarrow 2_k\rangle$	2.4	1.2

the $|0_a\rangle \leftrightarrow |1_a\rangle$ transition. From these, we estimate the relative coupling strength of a drive centered at ω_{01}^a to the four transitions by simulating the filter functions of the two readout resonators at ω_{01}^a using Microwave Office.

Transmon readout

Multiplexed readout. Simultaneous, independent readouts of Q_a and Q_b were performed by applying square-envelope tones (1 μs duration) at $\omega_m^a = \omega_r^a + 2\chi_a$ and $\omega_m^b \approx \omega_r^b + 2\chi_b$ to the feedline, respectively. To preserve the phase of measurement tones between experiment repetitions, we ensured that $\omega_m^\Delta = \omega_m^b - \omega_m^a$ was an integer multiple of $2\pi/t_{\text{rep}}$, where $t_{\text{rep}} = 100$ μs is the experiment repetition time. The amplified feedline output was demodulated by an IQ mixer, low-pass filtered (corner frequency 1.2 GHz) and digitized at $\delta t = 1$ ns sampling interval (see Fig. S1 for the complete readout chain). The mixer local oscillator frequency was chosen equal to ω_m^a . The two quadratures for Q_a readout were obtained by filtering the $I[n]$ and $Q[n]$ streams with an averager rejecting all multiples of ω_m^Δ . For Q_b readout,

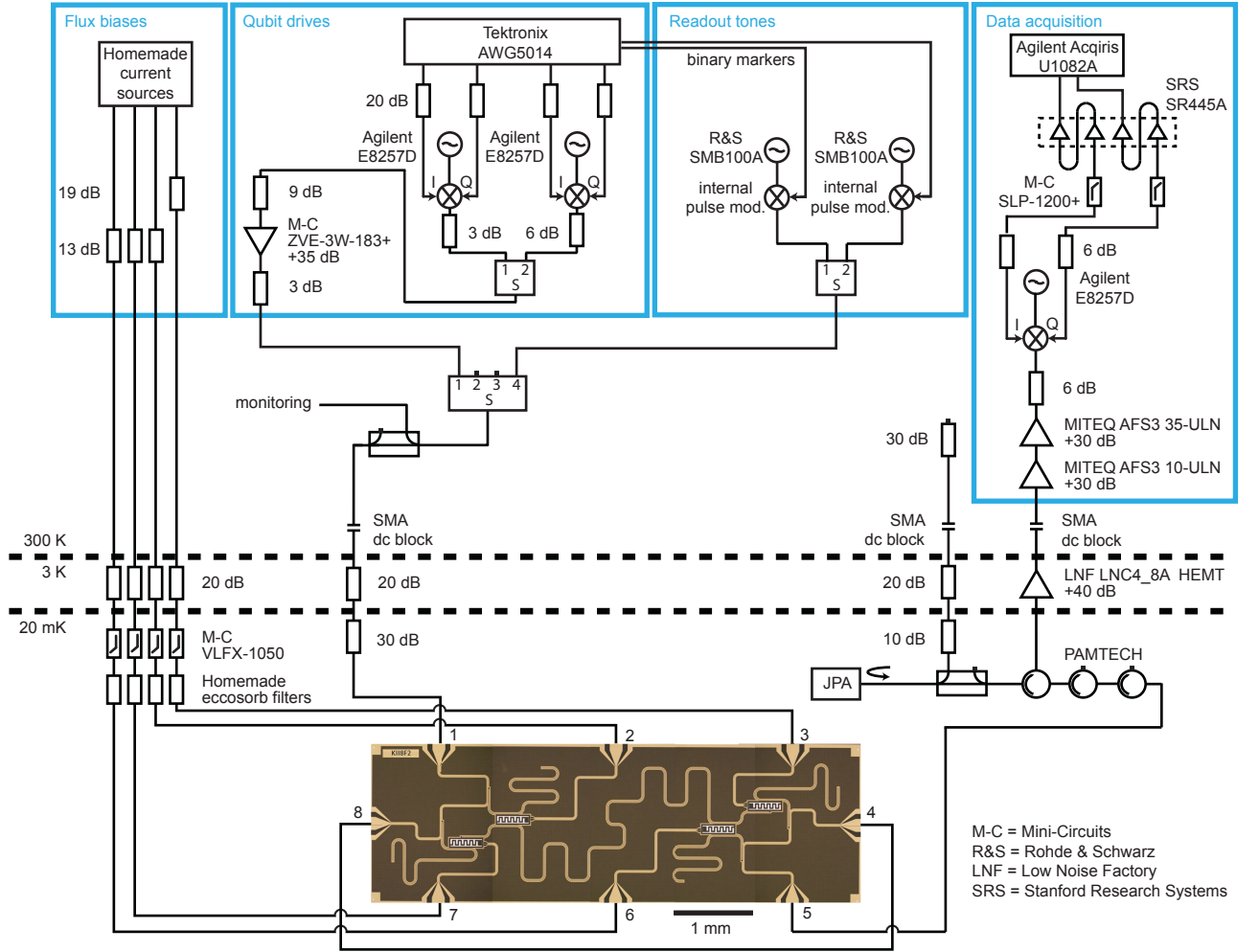


FIG. S1. Device and experimental setup. The $2 \text{ mm} \times 7 \text{ mm}$ chip is cooled to 20 mK in a $^3\text{He}/^4\text{He}$ dilution refrigerator (Leiden Cryogenics CF-450). The chip ports are labeled 1 through 8. Low-pass filtered d.c. currents generating static flux biases for the transmons enter through ports 2 (inactive transmon, transition frequency 4.31 GHz), 3 (Q_a), 6 (also inactive, transition frequency 7.25 GHz), and 7 (Q_b). All microwave control and readout pulses are applied at the single-feedline input port (1). Feedline ports 8 and 4 are externally connected by a short coaxial cable. Transmon readout is performed applying two simultaneous square-envelope pulses ($1 \mu\text{s}$ duration) near the fundamental frequencies of the dedicated resonators coupled to Q_a and Q_b . The transmitted feedline signal exiting at port 5 is routed by circulators (Pamtech) past a Josephson parametric amplifier (JPA, unpumped and unused) and into a HEMT amplifier (Low Noise Factory) at 3 K . Two room-temperature amplifiers (Miteq) further amplify the readout signals, which are subsequently demodulated with an IQ mixer (Marki Microwave). The mixer local oscillator frequency is chosen equal to the measurement frequency of one of the two readout resonators (thus, 0 Hz IF) and is 100 MHz offset from the second. The IF signals are amplified (Stanford Research Systems), digitized (Agilent), and homodyne detected digitally to complete the simultaneous readout of both transmons. DRAG and Wah-Wah pulse envelopes for resonant qubit control are generated by a Tektronix AWG5014 arbitrary waveform generator. We employ $\pm 50 \text{ MHz}$ single-sideband modulation to prevent spurious transmon driving by leakage of the local oscillator in the IQ mixers used for pulse up-conversion.

the two quadratures were derived from $I[n]$ by computing $I[n] \cos(\omega_m^\Delta n \delta t)$ and $I[n] \sin(\omega_m^\Delta n \delta t)$ and filtering with the averager. Finally, these four signals were integrated over the $1 \mu\text{s}$ interval to obtain the four voltages V_I^a , V_Q^a , V_I^b , and V_Q^b . The single-shot readout fidelities of Q_a and Q_b were 63% and 65% , respectively. We note that the parametric amplifier present in the readout chain was not employed as we did not require high readout fidelity

for this experiment.

Measurement model. We relate the average integrated voltages $\langle V_I^k \rangle$ and $\langle V_Q^k \rangle$ to the level populations of transmon Q_k using the model [2]

$$\langle V_i^k \rangle = \text{Tr}(\rho_k M_i^k),$$

where

$$M_i^k = \beta_{i0}^k \Pi_0^k + \beta_{i1}^k \Pi_1^k + \beta_{i2}^k \Pi_2^k, \quad (\text{S1})$$

$\hat{\Pi}_I^k = |l_k\rangle\langle l_k|$, and ρ_k the reduced qutrit density matrix of Q_k . We calibrate the coefficients $\beta_{i,j}^k$ by measuring $\langle V_i^k \rangle$ immediately after preparing $|0_k\rangle$, $|1_k\rangle$, and $|2_k\rangle$. We prepare the last two states using optimized DRAG pulses $R_{x,01}^k(\pi)$ and $R_{x,12}^k(\pi)R_{x,01}^k(\pi)$, respectively (see below for pulse details). Here, subscripts 01 and 12 indicate rotations in the $\{|0_k\rangle, |1_k\rangle\}$ and $\{|1_k\rangle, |2_k\rangle\}$ subspaces, respectively.

Extraction of level populations. To extract the level populations $P_j^k = \text{Tr}(\rho_k \hat{\Pi}_j^k)$ in transmon Q_k , we solve the set of three linear equations given by $\langle V_I^k \rangle$, $\langle V_Q^k \rangle$ and the (assumed) constraint $\sum_{i=0}^2 P_j^k = 1$. For the stroboscopic measurements in Figs. 2 and S2, we enhance the accuracy of Q_b level population measurements by increasing the number of linear equations to 7. We measure $\langle V_I^b \rangle$ and $\langle V_Q^b \rangle$ with measurement pre-rotations I , $R_{x,01}^b(\pi)$ and $R_{x,12}^b(\pi)$, and perform unweighted least-squares inversion. Q_a level population measurements in Fig. 2(b) are performed with Q_b pre-rotation I .

Pulse tuning

Tune-up of Q_a and Q_b pulses at each bias point and t_g began with a manual optimization of DRAG pulses on each transmon without concern for their effect on the other. To facilitate the fine tuning of the pulse amplitude A_θ ($A_{\pi/2} = A_\pi/2$) and the DRAG parameter β , we used a test sequence similar to those in Refs. 3 and 4. Each segment of the sequence applies one of 21 different pairs of pulses (each drawn from $\{I, R_{x,01}^k(\pi/2), R_{y,01}^k(\pi/2), R_{x,01}^k(\pi), R_{y,01}^k(\pi)\}$) to $|0_k\rangle$ and immediately performs measurement on Q_k . The pulse pairs are picked and ordered so that the Q_k qubit Bloch vector is ideally left at the north pole, equatorial plane or south pole of the Bloch sphere, in progression. The deviations from a three-level staircase in $\langle V_i^k \rangle$ provide a useful footprint of tune-up errors.

When turning on Wah-Wah pulsing of Q_a at bias point 1, we followed a manual optimization procedure. For each choice of sideband-modulation parameters A_m and ω_m , we first estimated the amplitude needed to preserve the area under the in-phase quadrature envelope. We multiplied the DRAG A_θ by $I_{\text{DRAG}}/(I_{\text{DRAG}} - A_m I_{\text{W-W}})$, where

$$I_{\text{DRAG}} = \int_0^{2\sigma} e^{-t^2/2\sigma^2} dt, \quad (\text{S2})$$

$$I_{\text{W-W}} = \int_0^{2\sigma} e^{-t^2/2\sigma^2} \cos(\omega_m t) dt. \quad (\text{S3})$$

We found this method to be accurate to $\pm 0.4\%$. Using the test sequence above (but implemented with Wah-Wah pulses), we next tuned β . Finally, similarly to Figs. 2 and S2, we measured the P_2^b produced by a sequence of four back-to-back Q_a Wah-Wah pulses. In this

way, we manually found the Wah-Wah parameters (A_θ , β , A_m , and ω_m) pulses that produce minimal P_2^b while performing the intended Q_a operation. The procedure was separately performed for $\theta = \pi$ and $\pi/2$ pulses. Once a good correspondence was established between manually optimized pulse parameters and those suggested by simulation, we increasingly relied on simulation to fix A_m and ω_m , and only manually tuned β . A summary of optimal Q_a DRAG, Q_a Wah-Wah, and Q_b DRAG pulse parameters at the three bias points and several t_g is provided in Table S4.

We finally note that to calibrate DRAG pulses in the $\{|1_k\rangle, |2_k\rangle\}$ subspace, we modified the test sequence to apply a pre-optimized $R_{x,01}^k(\pi)$ before applying the pulse pairs (each drawn from $\{I, R_{x,12}^k(\pi/2), R_{y,12}^k(\pi/2), R_{x,12}^k(\pi), R_{y,12}^k(\pi)\}$). No additional mixers were required for pulse up-conversion as both ω_{01}^k and ω_{12}^k could be reached by single-sideband modulation.

TABLE S4. Parameters of optimized Q_a and Q_b pulses at three bias points.

		Bias point			
		1	2	3	
$t_g = 16 \text{ ns}$	W-W $R_{\hat{n},01}^a(\pi)$	A_m	0.9	0.3585	-0.8
		$\omega_m/2\pi$ (MHz)	12.5	99.6	17.5
		β (ns)	0.9	0.2	0.2
	W-W $R_{\hat{n},01}^a(\pi/2)$	A_m	0.9	0.6743	0.5
		$\omega_m/2\pi$ (MHz)	25	76.5	25
		β (ns)	1.85	0.2	0.3
	DRAG $R_{\hat{n},01}^a(\theta)$	β (ns)	0.6	0.2	0.2
	DRAG $R_{\hat{n},01}^b(\theta)$	β (ns)	0.7	-0.1	-0.1
$t_g = 20 \text{ ns}$	W-W $R_{\hat{n},01}^a(\pi)$	A_m	0.23		
		$\omega_m/2\pi$ (MHz)	13.8		
		β (ns)	0.62		
	W-W $R_{\hat{n},01}^a(\pi/2)$	A_m	0.68		
		$\omega_m/2\pi$ (MHz)	23.8		
DRAG $R_{\hat{n},01}^a(\theta)$	β (ns)	0.6			
DRAG $R_{\hat{n},01}^b(\theta)$	β (ns)	0.68			
$t_g = 24 \text{ ns}$	W-W $R_{\hat{n},01}^a(\pi)$	A_m	-0.65		
		$\omega_m/2\pi$ (MHz)	15		
		β (ns)	0.6		
	W-W $R_{\hat{n},01}^a(\pi/2)$	A_m	0.45		
		$\omega_m/2\pi$ (MHz)	22.5		
DRAG $R_{\hat{n},01}^a(\theta)$	β (ns)	0.6			
DRAG $R_{\hat{n},01}^b(\theta)$	β (ns)	0.7			

Randomized benchmarking

The performance of optimized pulses was measured using randomized benchmarking (RB). In standard RB, random pairs of π and $\pi/2$ pulses are applied, all targeting the same transmon. The last $\pi/2$ pulse is chosen so that the targeted transmon ideally ends in either $|0\rangle$ or $|1\rangle$. For some sequences, this involves replacing the last $\pi/2$ with identity. The fidelity \mathcal{F} (squared overlap) of the final transmon state to the ideal final state is measured for each RB sequence. The average $\overline{\mathcal{F}}$ over all RB sequences is then plotted as function of the number of $\pi/2$ pulses, $N_{\pi/2}$.

In alternating RB, two standard RB sequences targeting different transmons are interleaved. Pulses targeting one transmon are applied during the buffer separating pulses targeting the other. Calibrated virtual z gates are applied both ways: to Q_a following a pulse on Q_b , and viceversa.

Pulse randomization. We briefly describe the pulse randomization procedure used to generate RB sequences. We first create at least 5 pseudo-random trains of $\pm\pi/2$ pulses around x and y (both signs and axes with equal probability), with enough pulses that the complete RB sequence would span 4 μs . Each $\pi/2$ pulse train is then interleaved with a train of $N_{\pi/2} + 1$ Pauli randomization pulses. Each Pauli randomization pulse is taken from the set $\{I, R_{x,01}^k(\pi), R_{x,01}^k(-\pi), R_{y,01}^k(\pi), R_{y,01}^k(-\pi)\}$ with equal probability $1/5$. We generate eight randomizations of the Pauli pulse train. Thus, interleaving the $\pi/2$ and Pauli pulse trains produces at least $5 \times 8 = 40$ RB sequences. After the experiment, we learned that the proper choice of Pauli randomization set would have been

$$\{I, R_{x,01}^k(\pi), R_{x,01}^k(-\pi), R_{y,01}^k(\pi), R_{y,01}^k(-\pi), R_{z,01}^k(\pi), R_{z,01}^k(-\pi)\},$$

with probability $1/4$ for I and $1/8$ for all others, and z -axis π rotations replaced with virtual z gates.

Extraction of average error per computational step. Following Ref. 5, we define a computational step as a pair of π and $\pi/2$ pulses including buffers [total step time $t_s = 2(t_g + t_b)$]. Our estimate of the average error per computational step, EPS, is obtained from a fit of $\overline{\mathcal{F}}(N_{\pi/2})$. In the absence of leakage, we expect [5, 6]

$$\overline{\mathcal{F}}(N_{\pi/2}) = (1 - A)e^{-\alpha N_{\pi/2}} + A,$$

with $A = 1/2$ and $\text{EPS} = (1 - e^{-\alpha})/2$. Note that $\overline{\mathcal{F}}(0) = 1$ because we correct for readout errors. This functional form fits very well the $\overline{\mathcal{F}}(N_{\pi/2})$ data for standard RB and for alternating RB with Q_a Wah-Wah pulses, with best-fit asymptotic fidelity $A = 0.50 \pm 0.05$ in all cases. EPS error bars in Figs. 3 and S4 represent 95% confidence intervals.

In the presence of leakage, we expect [7]

$$\overline{\mathcal{F}}(N_{\pi/2}) = \frac{1}{2}e^{-\alpha N_{\pi/2}} + \left(\frac{1}{2} - A\right)e^{-\gamma N_{\pi/2}} + A,$$

with reduced asymptotic fidelity $1/3 \leq A < 1/2$. We find good fits of this form to the Q_b $\overline{\mathcal{F}}$ data for alternating RB with Q_a DRAG pulses. For $t_g = 16$ ns, $t_s = 36$ ns, the best-fit $A = 0.33 \pm 0.02$ confirms strong leakage. Following Ref. 7, we use $(1 - e^{-\alpha})/2$ as estimator of EPS also in this case.

Quantum process tomography

We performed quantum process tomography (QPT) to fully characterize the evolution of Q_b under three idling scenarios: no applied pulses on Q_a , Q_a DRAG RB pulsing, and Q_a Wah-Wah RB pulsing.

In general, a quantum process is a linear, trace-preserving map of density matrices. The channel can be fully described by a transfer matrix \mathcal{R} connecting the input and output density matrices, each expanded in a suitable basis. The Pauli basis is a standard choice for processes confined to a qubit subspace [8]. In our case, the input and output spaces are the qubit and qutrit subspaces of Q_b . For the input space, we use the basis

$$P_1^{(2)} = \begin{pmatrix} 1 & 0 \\ 0 & 0 \end{pmatrix}, \quad P_2^{(2)} = \begin{pmatrix} 0 & 0 \\ 0 & 1 \end{pmatrix},$$

$$P_3^{(2)} = \frac{1}{\sqrt{2}} \begin{pmatrix} 0 & 1 \\ 1 & 0 \end{pmatrix}, \quad P_4^{(2)} = \frac{1}{\sqrt{2}} \begin{pmatrix} 0 & -i \\ i & 0 \end{pmatrix}.$$

For the output space, we use

$$P_1^{(3)} = \begin{pmatrix} 1 & 0 & 0 \\ 0 & 0 & 0 \\ 0 & 0 & 0 \end{pmatrix}, \quad P_2^{(3)} = \begin{pmatrix} 0 & 0 & 0 \\ 0 & 1 & 0 \\ 0 & 0 & 0 \end{pmatrix}, \quad P_3^{(3)} = \begin{pmatrix} 0 & 0 & 0 \\ 0 & 0 & 0 \\ 0 & 0 & 1 \end{pmatrix},$$

$$P_4^{(3)} = \frac{1}{\sqrt{2}} \begin{pmatrix} 0 & 1 & 0 \\ 1 & 0 & 0 \\ 0 & 0 & 0 \end{pmatrix}, \quad P_5^{(3)} = \frac{1}{\sqrt{2}} \begin{pmatrix} 0 & -i & 0 \\ i & 0 & 0 \\ 0 & 0 & 0 \end{pmatrix},$$

$$P_6^{(3)} = \frac{1}{\sqrt{2}} \begin{pmatrix} 0 & 0 & 1 \\ 0 & 0 & 0 \\ 1 & 0 & 0 \end{pmatrix}, \quad P_7^{(3)} = \frac{1}{\sqrt{2}} \begin{pmatrix} 0 & 0 & -i \\ 0 & 0 & 0 \\ i & 0 & 0 \end{pmatrix},$$

$$P_8^{(3)} = \frac{1}{\sqrt{2}} \begin{pmatrix} 0 & 0 & 0 \\ 0 & 0 & 1 \\ 0 & 1 & 0 \end{pmatrix}, \quad P_9^{(3)} = \frac{1}{\sqrt{2}} \begin{pmatrix} 0 & 0 & 0 \\ 0 & 0 & -i \\ 0 & i & 0 \end{pmatrix}.$$

The quantum process is fully characterized by a 9×4 real-valued matrix with elements \mathcal{R}_{pq} .

We used a four-step QPT protocol to extract \mathcal{R} for each idling scenario. The steps are: (i) state preparation,

(ii) idling for a time t_i , (iii) measurement pre-rotation, and (iv) measurement.

(i) For state preparation, a calibrated DRAG pulse U_n was applied to $|0_b\rangle$, taken from the set

$$\{I, R_{x,01}^b(\pi), R_{x,01}^b(\pi/2), R_{x,01}^b(-\pi/2), R_{y,01}^b(\pi/2), R_{y,01}^b(-\pi/2)\}.$$

(ii) The Q_a rotations during t_i were chosen according to the RB protocol described above. The QPT protocol was repeated for 64 distinct RB sequences (8 seeds, 8 Pauli randomizations per seed). The transfer matrix \mathcal{R} was computed as an average over these randomizations.

(iii) The measurement pre-rotations V_m on Q_b were chosen from the set

$$\begin{aligned} \{I, R_{x,01}^b(\pi/2), R_{x,01}^b(-\pi/2), R_{y,01}^b(\pi/2), R_{y,01}^b(-\pi/2), \\ R_{x,01}^b(\pi), R_{x,12}^b(\pi/2), R_{x,12}^b(-\pi/2), \\ R_{y,12}^b(\pi/2), R_{y,12}^b(-\pi/2), R_{x,01}^b(\pi)R_{x,12}^b(\pi/2), \\ R_{x,01}^b(\pi)R_{x,12}^b(-\pi/2), R_{x,01}^b(\pi)R_{y,12}^b(\pi/2), \\ R_{x,01}^b(\pi)R_{y,12}^b(-\pi/2), R_{x,01}^b(\pi)R_{x,12}^b(\pi)\}. \end{aligned}$$

Optimized DRAG pulses were used to implement all rotations. This set of pre-rotations augments that of Ref. [9] with redundant rotations in order to increase the stability of the inversion.

(iv) Using the dispersive readout described above, we obtain averaged integrated voltages $\langle V_I \rangle$ and $\langle V_Q \rangle$ for each (V_m, U_n) pair.

The averaged measurement $\langle V_i \rangle_{kl}$ for each (V_m, U_n) pair ($6 \times 15 = 90$ pairs total) is related to \mathcal{R} by

$$\langle V_i \rangle_{mn} = \sum_{pq} \mathcal{R}_{pq} \text{Tr}(V_m^\dagger M_i V_m P_p^{(3)}) \langle 0 | U_n^\dagger P_q^{(2)} U_n | 0 \rangle. \quad (\text{S4})$$

Combining all measurements, we arrive at a set of 180 linear equations for the 36 unknown \mathcal{R}_{pq} . We solve this over-determined set of linear equations by unweighted least-squares inversion.

As a measure of idling performance, we extract the average gate fidelity, F_g , of Q_b to identity [10, 11]. We find

$$\begin{aligned} F_g &= \sum_{j=\pm x, \pm y, \pm z} \text{Tr}[\rho_j \mathcal{E}(\rho_j)] \\ &= \frac{\mathcal{R}_{11} + \mathcal{R}_{22} + \mathcal{R}_{43} + \mathcal{R}_{54} - \mathcal{R}_{31} - \mathcal{R}_{32}}{6} + \frac{1}{3}. \end{aligned}$$

To gain further insight into the sources of infidelity, we decompose F_g as

$$F_g = \frac{F_1 + F_2 + 1}{3}, \quad (\text{S5})$$

where $F_1 = \frac{1}{2}(\mathcal{R}_{11} + \mathcal{R}_{22} - \mathcal{R}_{31} - \mathcal{R}_{32})$ and $F_2 = \frac{1}{2}(\mathcal{R}_{43} + \mathcal{R}_{54})$. F_1 is sensitive to errors in population

transfer. F_2 is sensitive to population transfer and also to pure dephasing within the qubit subspace. For true idling, we model

$$F_1(t_i) = \frac{1 + e^{-t_i/T_1(1 \rightarrow 0)}}{2}, \quad (\text{S6})$$

and

$$F_2(t_i) = e^{-t_i/(2T_1(1 \rightarrow 0))} e^{-t_i^2/T_\phi^2}. \quad (\text{S7})$$

The model F_2 reflects dominant pure dephasing by $1/f$ flux noise, as suggested by a non-exponential Ramsey fringe decay observed for Q_b .

SIMULATION

We perform a numerical simulation of the driven two-qubit system in order to: (a) validate the Wah-Wah modulation parameters manually optimized at bias point 1 and (b) speed-up the optimization of these parameters at other bias points. Following Ref. 12, we model the system Hamiltonian in a frame rotating with a resonant drive at ω_{01}^a , truncate at three lowest-energy levels per transmon, and make the rotating wave approximation:

$$\begin{aligned} \hat{H}/\hbar &= \Delta_a \hat{\Pi}_2^a + (\delta - \Delta_b) \hat{\Pi}_1^b + \delta \hat{\Pi}_2^b \\ &+ \frac{\Omega_I(t)}{2} [\lambda_1^a \hat{\sigma}_{x,1}^a + \lambda_1^b \hat{\sigma}_{x,1}^b + \lambda_2^a \hat{\sigma}_{x,2}^a + \lambda_2^b \hat{\sigma}_{x,2}^b] \\ &+ \frac{\Omega_Q(t)}{2} [\lambda_1^a \hat{\sigma}_{y,1}^a + \lambda_1^b \hat{\sigma}_{y,1}^b + \lambda_2^a \hat{\sigma}_{y,2}^a + \lambda_2^b \hat{\sigma}_{y,2}^b]. \end{aligned} \quad (\text{S8})$$

Here, $\sigma_{x,l}^k = |l_k\rangle \langle l-1_k| + |l-1_k\rangle \langle l_k|$, and $\sigma_{y,l}^k = i|l_k\rangle \langle l-1_k| - i|l-1_k\rangle \langle l_k|$. As defined in the main text, $\Delta_k = \omega_{12}^k - \omega_{01}^k$, $\delta = \omega_{12}^b - \omega_{01}^a$, and $\Omega_I(t)$ and $\Omega_Q(t)$ are the in- and out-of-phase pulse envelopes. Finally, λ_l^k is the coupling strength of the drive to the $|l-1_k\rangle \leftrightarrow |l_k\rangle$ transition. All model parameters are obtained from calibration measurements.

For each choice of gate time t_g , bias point, and Q_a pulse rotation angle $\theta \in \{\pi, \pi/2\}$, we identify a manifold of $(A_\theta, \beta, A_m, \omega_m)$ values performing a high-quality pulse on Q_a . For each (A_m, ω_m) pair in the range $A_m \in [-1, 1]$ and $\omega_m/2\pi \in [0, 100 \text{ MHz}]$, we find the A_θ and β achieving the desired rotation angle θ and minimizing internal leakage in Q_a . We then calculate the leakage P_2^b induced by four back-to-back Q_a pulses, starting from $(|0_b\rangle + i|1_b\rangle)/\sqrt{2}$. Similarly to Fig. 2, the phase of these Q_a pulses is increased in progression ($\phi, 2\phi, 3\phi$, and 4ϕ). We repeat for 200 values of ϕ between 0 and 2π . The simulation output consists of an image plot of $\max_\phi P_2^b$ as a function of A_m and ω_m .

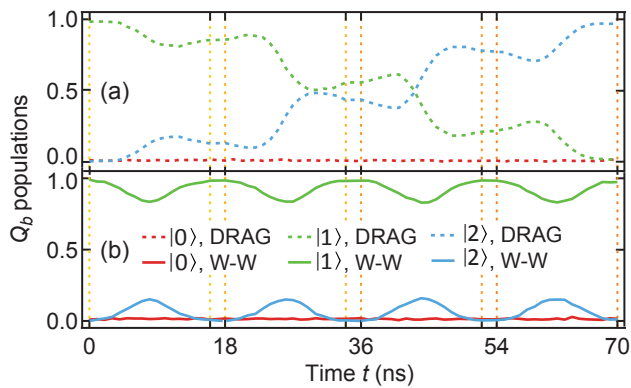


FIG. S2. Measured evolution of Q_b level populations during four back-to-back $\pi/2$ pulses on Q_a , with optimized DRAG and Wah-Wah envelopes ($t_g = 16$ ns). Panels (a) and (b) are dual to Figs. 2(c) and 2(d), respectively, but with $\pi/2$ instead of π pulses on Q_a . The phase of $\pi/2$ pulses is ϕ , 2ϕ , 3ϕ , and 4ϕ , in progression, with $\phi = 319^\circ$.

EXTENDED RESULTS

This section presents four figures lending further support to the main text claims. Complementing Fig. 2, Fig. S2 shows the evolution of level populations in Q_a and Q_b during repeated $\pi/2$ pulses on Q_a . Figure S3 compares measurements and simulation of $|2_b\rangle$ leakage induced by four back-to-back π or $\pi/2$ Wah-Wah pulses on Q_a . Image plots of leakage as a function of modulation parameters show good correspondence between the optimal Wah-Wah parameters found by simulation and

manually in experiment. Complementing Fig. 3, Fig. S4 shows standard and alternating randomized benchmarking results for longer gate times $t_g = 20$ ns and 24 ns. Finally, complementing Fig. 4, Fig. S5 helps identify dominant limitations to Q_b idling from decoherence, leakage error, and phase-compensation error.

- [1] O.-P. Saira, J. P. Groen, J. Cramer, M. Meretska, G. de Lange, and L. DiCarlo, *Phys. Rev. Lett.*, **112**, 070502 (2014).
- [2] S. Filipp, *et al.*, *Phys. Rev. Lett.*, **102**, 200402 (2009).
- [3] J. M. Chow, L. DiCarlo, J. M. Gambetta, A. Nunnenkamp, L. S. Bishop, L. Frunzio, M. H. Devoret, S. M. Girvin, and R. J. Schoelkopf, *Phys. Rev. A*, **81**, 062325 (2010).
- [4] M. Reed, *Entanglement and quantum error correction with superconducting qubits*, PhD Dissertation, Yale University (2013).
- [5] E. Knill, *et al.*, *Phys. Rev. A*, **77**, 012307 (2008).
- [6] E. Magesan, J. M. Gambetta, and J. Emerson, *Phys. Rev. A*, **85**, 042311 (2012).
- [7] J. M. Epstein, A. W. Cross, E. Magesan, and J. M. Gambetta, *ArXiv:1308.2928* (2013).
- [8] J. M. Chow, *et al.*, *Phys. Rev. Lett.*, **109**, 060501 (2012).
- [9] R. Bianchetti, S. Filipp, M. Baur, J. Fink, C. Lang, L. Steffen, M. Boissonneault, A. Blais, and A. Wallraff, *Phys. Rev. Lett.*, **105**, 223601 (2010).
- [10] A. Gilchrist, N. K. Langford, and M. A. Nielsen, *Phys. Rev. A*, **71**, 062310 (2005).
- [11] F. Motzoi, J. M. Gambetta, P. Rebentrost, and F. K. Wilhelm, *Phys. Rev. Lett.*, **103**, 110501 (2009).
- [12] R. Schutjens, F. Abu Dagga, D. J. Egger, and F. K. Wilhelm, *Phys. Rev. A*, **88**, 052330 (2013).

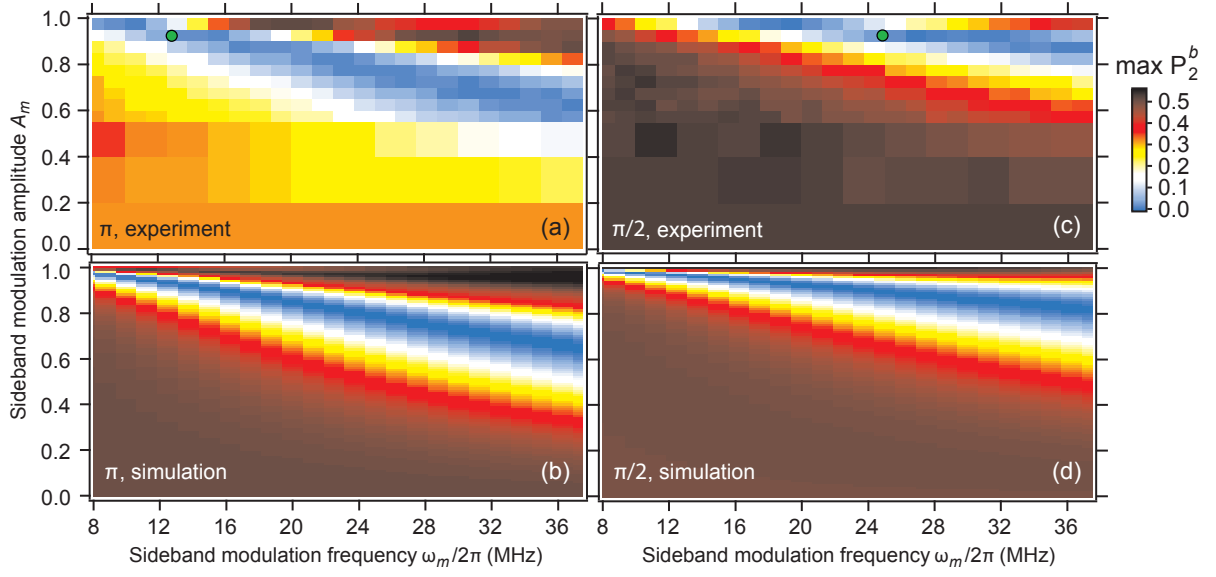


FIG. S3. Image plots of measured (a,c) and simulated (b,d) final population of $|2_b\rangle$, P_2^b , as a function of the modulation parameters A_m and ω_m in four consecutive π (a,b) or $\pi/2$ (c,d) Q_a Wah-Wah pulses ($t_g = 16$ ns). Transmons are initially in $|0_a\rangle$ and $(|0_b\rangle + i|1_b\rangle)/\sqrt{2}$. Similarly to Figs. 2 and S2, the phases of the pulses are ϕ , 2ϕ , 3ϕ , and 4ϕ , in progression. For each (A_m, ω_m) pair, we plot the maximal P_2^b measured over 80 values of ϕ between 0 and 2π . In experiment (a,c), we optimized the β coefficient at the left and right boundaries, and used linear interpolation with respect to ω_m (at fixed A_m) to set β inside. Markers indicate the manually found (A_m, ω_m) pairs minimizing P_2^b in experiment.

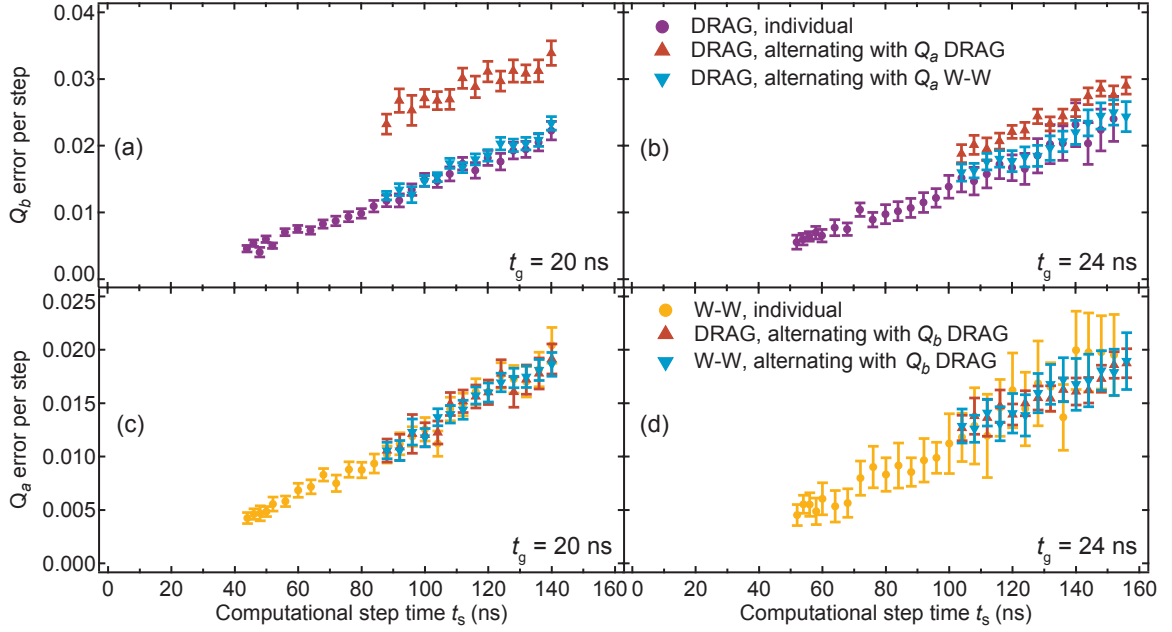


FIG. S4. Error per computational step, EPS, as a function of the computational step time $t_s = 2(t_g + t_b)$, obtained in standard and alternating randomized benchmarking. This figure is dual to Fig. 3, but with gate times $t_g = 20$ ns (a,c) and $t_g = 24$ ns (b,d), corresponding to $t_g|\delta|/2\pi \approx 1.1$ and 1.4 , respectively. As expected, the Q_b leakage induced by Q_a DRAG pulses is less severe the longer t_g . Optimized Q_a Wah-Wah pulsing allows achieving decoherence-limited EPS on Q_b .

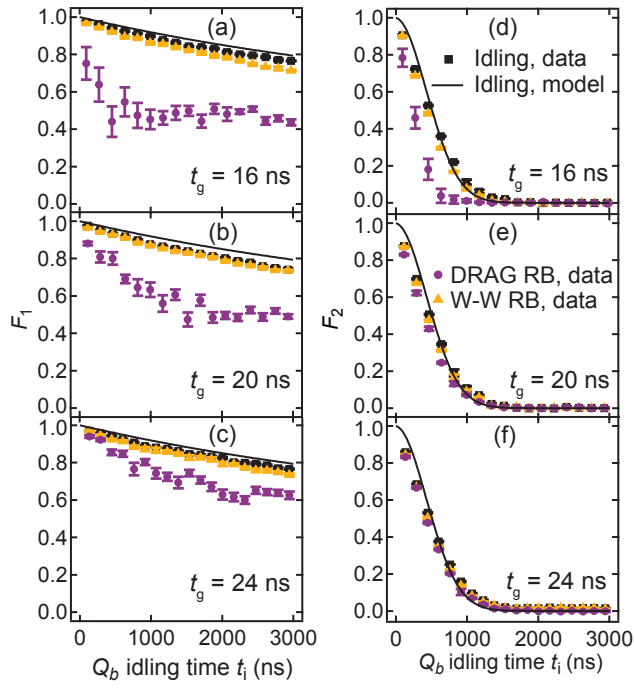


FIG. S5. Q_b average gate fidelity to the identity process as a function of idling time t_i , decomposed into components with different sensitivity to population transfer and to pure dephasing. (a-c) Fidelity F_1 is sensitive to relaxation within the qubit subspace and leakage out of the qubit subspace. (d-f) Fidelity F_2 is also sensitive to pure dephasing within the qubit subspace. Same raw data as in Fig. 4. Squares, circles, and triangles correspond to true idling (i.e., no pulses on Q_a), Q_a DRAG RB, and Q_a Wah-Wah RB, respectively. The combination of these plots allows two conclusions: Q_b idling for Q_a Wah-Wah RB is decoherence limited; Q_b idling for Q_a DRAG RB is dominated by leakage (rather than imperfect z -gate compensation). The large error bars for Q_a DRAG RB reflect the sensitivity of Q_b leakage to the randomization of Q_a DRAG pulses. See text for the details of the model for true idling (solid curves).

Title	Microwave-coupled superconducting devices for sensing and quantum information processing
Author(s)	Visa Vesterinen
Abstract	<p>Superconducting circuits and devices have unique properties that make them interesting from both theoretical and practical perspective. In a superconductor cooled below its critical temperature, electrons bound in Cooper pairs have the ability to carry current without dissipation. A structure where the Cooper pairs are coherently tunneling across a weak link is called a Josephson junction (JJ). The dissipationless and non-linear character of the JJ has found applications, e.g., in microwave amplifiers and quantum circuits. These two subjects are closely related since superconducting quantum bits (qubits) are artificial atoms with a transition spectrum in the microwave range. Mediated by microwave photons, qubit readout in circuit quantum electrodynamics (cQED) architecture requires signal boosting with a low-noise preamplifier. In this thesis, a new type of ultrasensitive JJ microwave amplifier was characterized and its noise performance was found to be close to a bound set by quantum mechanics. The amplifier uses the intrinsic negative differential resistance of a current-biased JJ.</p> <p>This work also addressed a challenge related to the scalability of the cQED architecture when the qubits are weakly anharmonic. In a frequency-crowded multi-qubit system, driving individual qubits may cause leakage into non-computational levels of the others. Leakage-avoiding single-qubit Wah-Wah control was implemented. At maximum gate speed corresponding to the frequency crowding, microwave control of two transmon qubits on a 2D cQED quantum processor was decoherence limited. The results disclose the usefulness of Wah-Wah in a future quantum computing platform.</p> <p>Quasiparticles are excitations from the paired superconducting ground state of conduction electrons. As the third topic, the generation-recombination dynamics of quasiparticles was employed in sensing. In electrodynamic terms, superconducting thin films have kinetic inductance from the inertia of the Cooper pairs and resistive dissipation from the quasiparticles. If the film is a part of an electrical resonator, quasiparticle density steers its microwave eigenfrequency and quality factor. In this work, submillimetre-wave radiation and external magnetic field were first converted into quasiparticle-generating temperature variations and screening currents in a superconductor, respectively. In the two devices called kinetic inductance bolometer and magnetometer, the corresponding changes in resonator parameters were read out to extract the encoded signal. Sensor characterization indicated potential for high sensitivity and low noise. Future applications of the bolometer and the magnetometer include security screening and biomagnetism, respectively. Here, multiplexability in frequency domain facilitates the scale-up to large sensor arrays.</p>
ISBN, ISSN	ISBN 978-951-38-8311-9 (Soft back ed.) ISBN 978-951-38-8312-6 (URL: http://www.vtt.fi/publications/index.jsp) ISSN-L 2242-119X ISSN 2242-119X (Print) ISSN 2242-1203 (Online)
Date	June 2015
Language	English, Finnish abstract
Pages	83 p. + app. 73 p.
Name of the project	
Commissioned by	
Keywords	superconductivity, Josephson junction, superconducting qubit, single-qubit control, quantum-limited amplifier, kinetic inductance, submillimetre-wave detector, magnetometer
Publisher	VTT Technical Research Centre of Finland Ltd P.O. Box 1000, FI-02044 VTT, Finland, Tel. 020 722 111

Nimeke	Mikroaalloille sovitettuja suprajohtavia laitteita anturisovelluksiin sekä kvantti-informaation käsittelyyn
Tekijä(t)	Visa Vesterinen
Tiivistelmä	<p>Suprajohtavilla piireillä ja laitteilla on ainutlaatuisia ominaisuuksia, jotka tekevät niistä kiinnostavia sekä teoreettisesta että käytännöllisestä näkökulmasta katsottuna. Suprajohteessa, joka on jäähdytetty kriittisen lämpötilansa alapuolelle, elektronit muodostavat Cooperin pareja, jotka kuljettavat sähkövirtaa häviöttömästi. Rakennetta, jossa Cooperin parit tunnelloituvat koherentisti heikon linkin yli kutsutaan Josephsonin liitokseksi (Josephson junction, JJ). Liitoksen häviötöntä ja epälineaarista luonnetta on käytetty esimerkiksi mikroaaltovahvistimissa sekä kvanttipiireissä. Nämä kaksi aihealuetta ovat lähellä toisiaan, sillä suprajohtavat kvanttibitit (kubitit) ovat keinoitekoisia atomeja, joiden transiitiospektri on mikroaaltoalueella. Kubitin luku, jota mikroaaltofotonit välittävät, tarvitsee matalakohinaisen esivahvistuksen silloin, kun operoidaan niin kutsutussa circuit quantum electrodynamics (cQED) –arkkitehtuurissa. Tässä väitöskirjassa uudentyypistä herkkää JJ-mikroaaltovahvistinta karakterisoitiin. Sen lisäämän kohinan todettiin olevan lähellä kvanttimekaniikan määräämää alarajaa. Vahvistin hyödyntää virtabiasoidulle liitokselle ominaista negatiivista differentiaali-resistanssia.</p> <p>Työssä vastattiin lisäksi haasteeseen, joka liittyy cQED-arkkitehtuurin skaalautuvuuteen, kun kubitit ovat lievästi epäharmonisia. Ahtaan taajuusvälin systeemissä yksittäisten kubittien ajaminen voi aiheuttaa vuotoa toisten kubittien energiatiloille, jotka sijaitsevat kubitti-aliavaruuden yläpuolella. Vuodon välttävä Wah-Wah -tekniikka yhden kubitin kontrollointiin toteutettiin käytännössä. Kvanttiportin maksiminopeudella, joka vastasi kokeen ahdasta taajuusväliä, mikroaaltokontrollin todettiin olevan dekoherenssin rajoittamaa. Systeeminä oli kaksi niin kutsuttua transmon-kubittia kaksiulotteisella cQED-kvanttiprosessorilla. Tulokset kertoivat Wah-Wah:in hyödyllisyydestä tulevaisuuden kvanttilaskenta-alustalla.</p> <p>Kvasipartikkelit ovat eksitaatioita suprajohteen johtavuuselektronien perustilalta. Työn kolmantena aihealueena oli kvasipartikkeliin syntymisen ja uudelleenyhdistymisen dynamiikka anturisovelluksissa. Sähködynamiikan termejä käyttäen suprajohtavassa ohutkalvossa on kineettistä induktanssia, joka on peräisin Cooperin parien inertiaasta, sekä resistiivista häviötä kvasipartikkeleista. Jos kalvo on osana sähköistä värähtelijää, kvasipartikkelitiheys ohjaa sen mikroaaltotaajuudella olevaa ominaistajuutta sekä hyvyyssukua. Tässä työssä alimillimetrialueen säteilyä muutettiin kvasipartikkeleita synnyttäväksi lämpötilavaihteluksi suprajohteessa, ja ulkoista magneettikenttää vastaavasti supravirraksi. Näissä kahdessa laitteessa, kutsumanimiltään kineettisen induktanssin bolometri ja magnetometri, aikaansaadut muutokset värähtelijän parametreissa luettiin hyötysignaalin erottamiseksi. Anturien karakterisaatio osoitti potentiaalia suurelle herkkyydelle sekä pienelle kohinalle. Tulevaisuuden sovelluksia bolometrille on esimerkiksi turva- ja valvontatekniikassa, ja magnetometrille biomagnetismin alalla. Tässä yhteydessä taajuusmultiplexointi helpottaa skaalaamista ylöspäin suuriin anturiryhmiin.</p>
ISBN, ISSN	ISBN 978-951-38-8311-9 (nid.) ISBN 978-951-38-8312-6 (URL: http://www.vtt.fi/publications/index.jsp) ISSN-L 2242-119X ISSN 2242-119X (Painettu) ISSN 2242-1203 (Verkkójulkaisu)
Julkaisu-aika	Kesäkuu 2015
Kieli	Englanti, suomenkielinen tiivistelmä
Sivumäärä	83 s. + liitt. 73 s.
Projektin nimi	
Rahoittajat	
Avainsanat	suprajohtavuus, Josephsonin liitos, suprajohtava kubitti, yhden kubitin kontrolli, kvanttirajoitteinen vahvistin, kineettinen induktanssi, alimillimetri-aallonpituusalueen ilmaisimien, magnetometri
Julkaisija	Teknologian tutkimuskeskus VTT Oy PL 1000, 02044 VTT, puh. 020 722 111

Microwave-coupled superconducting devices for sensing and quantum information processing

In a superconductor cooled below its critical temperature, electrons bound in Cooper pairs have the ability to carry current without dissipation. Quasiparticles, on the other hand, are excitations from the paired superconducting ground state.

In this work, the generation-recombination dynamics of quasiparticles in thin films was employed in sensing. Two studied devices, kinetic inductance bolometer and magnetometer, were designed to detect submillimetre-wave radiation and external magnetic fields, respectively. The superconducting sensing elements were complemented with a radio-frequency resonance to enhance the readout. Future applications of the sensitive bolometer and magnetometer include security screening and biomagnetism, respectively.

The second category of devices harnessed the Josephson effect where the Cooper pairs tunnel coherently across a weak link. Superconducting quantum bits (qubits) rely on this mechanism, and they are frequently operated in the circuit quantum electrodynamics (cQED) microwave architecture. This work addressed a challenge related to the scalability of multi-qubit cQED processors. The so-called Wah-Wah method was demonstrated to mitigate certain cross-talk effects of single-qubit control.

In addition, a new type of ultrasensitive Josephson microwave amplifier was characterized and its noise performance was found to be close to a bound set by quantum mechanics. Low-noise amplifiers are useful, e.g., in cQED setups where they improve the qubit readout fidelity.

ISBN 978-951-38-8311-9 (Soft back ed.)
ISBN 978-951-38-8312-6 (URL: <http://www.vtt.fi/publications/index.jsp>)
ISSN-L 2242-119X
ISSN 2242-119X (Print)
ISSN 2242-1203 (Online)

